TAMPEREEN TEKNILLINEN YLIOPISTO
TAMPERE UNIVERSITY OF TECHNOLOGY
Julkaisu 639 • Publication 639

Matti Eskola

Speed and Position Sensorless Control of Permanent Magnet Synchronous Motors in Matrix Converter and Voltage Source Converter Applications

Tampere 2006

Tampereen teknillinen yliopisto. Julkaisu 639
Tampere University of Technology. Publication 639

Matti Eskola

Speed and Position Sensorless Control of Permanent Magnet Synchronous Motors in Matrix Converter and Voltage Source Converter Applications

Thesis for the degree of Doctor of Technology to be presented with due permission for public examination and criticism in Rakennustalo Building, Auditorium RG202, at Tampere University of Technology, on the 1st of December 2006, at 12 noon.

Tampereen teknillinen yliopisto - Tampere University of Technology
Tampere 2006

ISBN 952-15-1687-9 (printed)
ISBN 952-15-1731-X (PDF)
ISSN 1459-2045

Abstract

In this thesis the sensorless control of a permanent magnet synchronous motor (PMSM) is studied. The study has two main purposes. The first is to find a simple and effective method to estimate the rotor position and angular speed of the PMSM. The second is to test the applicability of a matrix converter in sensorless PMSM drives.

A matrix converter (MC) enables a direct frequency conversion without DC-link with energy storage. In this thesis two matrix converter topologies, direct and indirect, are studied. The vector modulation and the current commutation strategies of a matrix converter are described.

Non-ideal properties of frequency converters such as dead times, overlapping times and voltage losses over semiconductors are disturbances for a control system and position estimator. These non-idealities are studied and the properties of a conventional voltage source inverter are compared to direct and indirect MC topologies.

The rotor position and angular speed of the PMSM can be estimated by various methods. Estimators can be divided into model based estimators and signal injection estimators. Model based estimators calculate mechanical quantities using the mathematical representation of the motor. Injection methods usually exploit the saliency of the PMSM. Injected voltage creates currents which are modulated by the rotor position. The position information can be extracted from measured currents. In this thesis the best features of model based and injection estimators are combined. In the proposed hybrid method signal injection is used at low speeds and the transition to model based estimator is performed when the speed increases. The estimator methods used in the hybrid estimator are selected by a comparative analysis and simulations. The most important criteria in the selection of the estimator method in this thesis are: simple algorithm and no need for modification of the modulator software or frequency converter.

The suitability of the proposed hybrid estimator is tested by simulations and experimental tests in various operating conditions. To test the performance of the matrix converter the experiments are carried out using both MC topologies and a conventional voltage source converter.

The results obtained show that a matrix converter can be used in PMSM drives where the speed and position of the PMSM are not measured. The proposed estimator method is stable over the nominal speed range including the zero speed region with full load torque.

Preface

This work was carried out at the Institute of Power Electronics at Tampere University of Technology (TUT) during the years 2001-2006. The research was funded by the Graduate School in Electrical Engineering, TUT, the Finnish Funding Agency for Technology and Innovation (TEKES) and industrial partners (ABB Oy Drives, Hyvinkään TechVilla, Kalmar Industries, KCI Konecranes Oyj, Kone Oyj, Vacon Oyj). I am also very grateful for the financial support in the form of personal grants from the Foundation of Technology (Tekniikan edistämissäätiö).

I express my gratitude to Professor Heikki Tuusa, the head of the Institute of Power Electronics, for supervising my thesis work and providing an excellent research enviroment. I thank all the staff in the Institute of Power Electronics for providing with me a pleasant working atmosphere. I am thankful to Tero Viitanen Dr. Tech. and Mikko Routimo Lic. Tech. for providing answers to my questions regarding voltage source converters. I also thank Mika Salo Dr. Tech. for the microcontroller support. Laboratory technician Pentti Kivinen built all the excellent test benches for the PMSM drives used in this thesis work, which is greatly appreciated. The matrix converter research of this thesis was done in collaboration with Matti Jussila Lic. Tech. Special thanks to Matti who built the matrix converter prototypes and did all the dirty work behind the results regarding MCs. Furthermore, I thank professors Jorma Luomi and Juha Pyrhönen for their comments and for reviewing this thesis.

I wish also to thank my parents and little brother for their encouragement and support during the past years. Above all, I express my deepest thanks to my wife, Mirkka, for her love, patience and understanding. And finally, very special thanks to our sunshine, Elsa, for many joyful moments during the completion of this thesis.

Helsinki, November 2006

Matti Eskola

Contents

List of symbols

a	Acceleration
AC	Alternating Current
b	Friction constant
BP	Band Pass
BS	Band Stop
d	Relative duration of vector in PWM
DC	Direct Current
DMC	Direct Matrix Converter
e	Back-emf (electromotive force)
EKF	Extended Kalman Filter
ELO	Extended Luenberger Observer
f	Frequency
i	Current
IGBT	Insulated Gate Bipolar Transistor
IMC	Indirect Matrix Converter
j	Imaginary unit
g	Gain parameter
k, K	Gain parameter
L	Inductance
LP	Low Pass
m	Modulation index
MC	Matrix Converter
p	Number of pole pairs
PI	Proportional and Integrating controller
PLL	Phase Locked Loop
PM	Permanent Magnet
PWM	Pulse Width Modulation
R	Resistance
SVM	Space Vector Modulation
sw	Switching function
t	Time
T	Torque
TF	Transfer Function
VSI	Voltage Source Inverter
VSC	Voltage Source (frequency) Converter
W	Energy
u	Voltage
x	Arbitrary quantity
Δ	Voltage error of a frequency converter
δ	Load angle
ε	Error signal
θ	Position angle
ρ	Coefficient used to determine poles of a PLL
ψ	Flux linkage
ω	Angular frequency

Subscripts

abc	Vector or matrix of a three-phase quantity

a,b,c	Input phases of the frequency converter, phases of three phase quantities
A,B,C	Ouput phases of the frequency converter
ave	Average value
c	Current model, overlapping
d	Real part of the space-vector in the rotor reference frame
de	Real part of the space-vector in the estimated rotor reference frame
e	Electrical quantity
i	A quantity oscillating with injection frequency, integration, input
id, iq	Real and imaginary parts of space-vector quantity with injection frequency in the rotor reference frame
ide, iqe	Real and imaginary parts of space-vector quantity with injection frequency in the estimated rotor reference frame
inv	Inverse transformation
L	Load
LL	Line-to-Line
on	On-state loss
q	Imaginary part of the space-vector in the rotor reference frame
qe	Imaginary part of the space-vector in the estimated rotor reference frame
mech	Mechanical quantity
mod	Modulation period
n	Nominal value
o	Output
p	Proportional
r	Electric rotor quantity (position angle, angular speed)
ref	Reference signal
s	Sample period
supply	Mains (three-phase distribution network)
sw	Switching period in PWM
α	Real part of the space-vector in the stationary reference frame
β	Imaginary part of the space-vector in the stationary reference frame
δ	Lead vector of the line bridge
γ	Lag vector of the line bridge
λ	Lead vector of the load bridge
κ	Lag vector of the load bridge
2	Output of the direct speed estimator

Superscripts

g	General reference frame (notation used with complex phasor, e.g. $\underline{i}^{g}$)
r	Rotor reference frame (notation used with complex phasor, e.g. $\underline{i}^{r}$)
re	Estimated rotor reference frame (notation used with complex phasor, e.g. $\underline{i}^{re}$)
s	Stationary reference frame
T	Transpose
*	Complex conjugate

Other notations

$\hat{x}$	Estimated value of x
$\tilde{x}$	Estimation error (x - $\hat{x}$) of x
$\mathbf{x}$	Matrix or vector $\mathbf{x}$
$\underline{x}$	Complex phasor, space-vector

1. Introduction

DC motor drives dominated the field of variable speed drives from the 19th century to the last decades of the 20th century. The controllability of DC drives was superior to those of AC drives. At the end of the 1960s K. Hasse introduced the field oriented control of AC motor. It was pointed out that in theory the induction motor can be controlled in the same way as the DC motor. The development of semiconductor power devices made it possible to build frequency converters for AC motors allowing a sinusoidal three-phase current supply with continuous frequency control. In the 1980s frequency converter fed AC drives using field oriented control were ready to challenge DC drives commercially. Since then the percentual share of DC drives has declined because the AC motor has several benefits compared to the DC motor. It is cheaper and needs much less maintenance because no mechanical commutator is needed. The speed range of the AC motor is wider and the machine size is smaller in the same power class. At present the frequency converter fed induction machine is the most common choice in industry when adjustable speed operation is required in power range from a few hundred W to a few MW.

The synchronous machines are the other group of AC machines and possess many of the advantages of induction machines. Traditionally the use of DC excited synchronous machines has been limited to generators and other high power applications. They cannot compete with induction motors in medium power range drives due to the higher price and more complex structure.

If DC excited rotor winding is replaced by permanent magnets, the synchronous machine has many attractive features compared to the induction motors. The excitation winding is not needed in the rotor. Thus the structure is greatly simplified. The copper losses are reduced because there are no current circuits in the rotor. This ensures higher efficiency and easier cooling compared to the induction motor. The use of modern rare-earth magnetic materials enables high flux densities and facilitates the construction of motors with unsurpassed power density. Permanent magnets can be manufactured in many shapes, which allows great flexibility for motor construction. The major drawback of the permanent magnet synchronous machine (PMSM) is the price. The stator structure is often similar to that of induction motors but the magnetic materials needed in the rotor are still fairly expensive. However, PMSMs are

becoming more popular and their application range is widening. Usually PMSMs are used in high performance low power servo applications. In recent years PMSMs have also been utilised in paper mills, wind-energy applications, elevators, ship propulsion drives and other high power applications. It is expected that in future PMSMs will continue replacing induction motors, also in conventional variable speed drives.

In variable speed PMSM drives the motor is controlled by a frequency converter. In the low and middle power ranges the most common solution in industry is to use a voltage source PWM inverter with diode rectifier. If the power quality is concerned the rectification is also carried out by an active PWM bridge. The active rectifier enables bi-directional power flow. This saves energy if the machine also operates in the regenerating region. In the case of the diode rectifier the power must be dissipated in a brake resistor if the machine is regenerating. In a DC link between the rectifier and an inverter the capacitor is used as an energy storage. Smoothening of the rectified voltage is the other purpose of the capacitor.

In recent years research on direct frequency conversion using a matrix converter (MC) has become more intense. The main reason for the interest in the matrix converter is that it provides a compact solution for a four-quadrant frequency converter, which produces sinusoidal input and output currents without a DC-link with passive components. The absence of the DC-link also has its disadvantages. Unfiltered input and output disturbances are carried through MC and output/input voltage ratio is smaller compared to the voltage source converter (VSC). MCs enabling the four-quadrant operation can be divided into direct and indirect topologies. The direct matrix converter (DMC) is a conventional MC circuit [Ven80] without the DC-link. Indirect matrix converter (IMC) consists of separated line and load bridges [Min93]. However, there exists no capacitor or inductor as an energy storage between the bridges.

The reduction of the size of the variable speed drive components is always an important goal in industry. In the future the frequency converter may be integrated into the motor. Due to the compact structure the integration of the matrix converter should be more realisable than the integration of conventional converters with DC-link. It will be interesting to see if MCs can challenge the VSC with an active rectifier. VSCs are mature technology but their size and costs have also been reduced due to the development of semiconductors and capacitors.

The field oriented control (FOC) originally introduced for induction machines is also the most common control strategy in PMSM drives. FOC is also called vector control [Nov00]. This term is used in this thesis. In vector control the torque of the machine is controlled via

controlling the stator current vector. The outer control system adjusting the speed and position gives the torque demand for the current control system.

Twenty years ago the direct torque control method (DTC) was introduced [Tak86]. This is the other widespread control method for AC drives. In a DTC drive the idea is to control the stator flux linkage and torque directly, not via controlling the stator current. This is accomplished by controlling the power switches using a predefined "optimum switching table" to select appropriate voltages for a motor. The selection of the switching states is made by the hysteresis comparators for torque and stator flux linkage. [Luu00] analyses the application of DTC to PMSMs. Direct torque control of the PMSM is beyond the scope of this thesis.

The vector control of a synchronous machine requires knowledge of the rotor position and angular speed. These mechanical quantities of a PMSM have usually been measured by shaft mounted motion sensors e.g. a tachometer, an encoder or a resolver. The presence of these sensors implies several disadvantages due to additional cost, a higher number of connections between the motor and the frequency converter and reduced robustness. In an industrial environment the sensors are vulnerable to mechanical impacts. Especially in lower power ranges the motion sensor can be the most expensive component in the entire drive system. For this reason several strategies to detect the speed and position without sensors have been developed for synchronous and asynchronous machines during the last twenty years.

If the speed and position are detected by estimator algorithms instead of motion sensors the control system of the AC machine is said to be sensorless. Sensorless control is a somewhat misleading term because only the speed/position control system is sensorless. The phase currents of the PMSM are measured for current control in vector control system. The term "indirect control" is also used in some publications [Yin03]. However, sensorless control is an established term in the literature and is also used in this thesis.

The position and speed estimators can be divided into two groups. The majority of the papers published describe methods based on the mathematical model of the PMSM [Bol99], [Jon89], [Mat96]. The main drawback of these model based estimators is insufficient performance at low speeds. To overcome low speed stability problems extensive research has been carried out to develop so-called injection estimators. In these methods a high frequency signal (voltage or current) is injected into the motor and the position angle and speed are determined by processing the resulting currents or voltages [Cor98], [Jan95], [Jan03], [Sil03].

The objective of this study has been to find a simple and effective method for on-line estimation of the rotor position angle and angular speed of the PMSM and to study the suitability of the matrix converter for the sensorless PMSM drives. The most promising speed and position estimators presented in the literature and meeting the following four requirements are compared.

1. Modification of the hardware of the frequency converter is not required.

2. Modification of the space-vector modulator software is not required.

3. The algorithm of the estimator should be as simple as possible.

4. The drive must be stable over the entire speed range including operation at zero speed.

Special attention was paid to zero speed region, which is the most problematic operating region for model based speed and position estimators. Injection estimators are stable at zero speed region. Therefore a combination of a model based method and an injection method is one of the goals of this thesis. The combination can exploit the strengths of both classes of estimators. The other goal is to empirically prove that the matrix converter can be applied in PMSM drive with sensorless control.

In Chapter 2, the modelling of the variable speed drive with PMSM is studied. The properties of the PMSMs are briefly discussed. The PMSM model taking the flux linkage harmonics into account is presented. The model is used in the simulations presented in Chapters 3 and 4. The voltage source frequency converter and matrix converter topologies and their non-ideal properties are studied [Jus06]. The vector control of the PMSM used in this thesis is described.

In Chapter 3, model based speed and position estimators (observers, flux estimators and back-emf estimators) are studied and the most promising methods are compared in simulations. The methods presented by Matsui [Mat90], [Mat92] were selected for further development. A new method which combines the best properties of Matsui's estimators is presented. This new algorithm is used in the hybrid estimator presented in Chapter 4.

In Chapter 4, signal injection estimators are studied. The high frequency signal injection methods are compared. The effect of the reference frame is studied. In addition to high frequency methods the low frequency estimator is studied [Esk05]. This method was introduced in 2001 for induction motors [Lep03] and is applied to PMSM drive in this study. The high frequency method where sinusoidal voltage is injected in the rotor reference frame is selected for the final implementation. At the end of Chapter 4 the model based estimator and

signal injection estimator are combined to achieve stable operation over the entire speed range of the PMSM.

In Chapter 5, the experimental setup is presented. The performance of the proposed sensorless control method is verified in Chapter 6. The matrix converter fed speed and position sensorless PMSM drive is tested experimentally. Some tests are also carried out by the voltage source converter and the results are compared to those achieved by MCs. Chapter 7 concludes the study.

The contributions of this thesis are summarized below.

- The analysis and comparison of output voltage non-idealities of matrix converters (Chapter 2). The results were published in [Jus06]. The author's contribution was developing the simulation model in collaboration with Jussila and programming of the control software for the PMSM drive used in experimental tests.
- A novel model based estimator algorithm is presented in Section 3.4.5. The proposed algorithm is based on the work of Matsui [Mat90], [Mat92]. In this thesis the best features of Matsui's estimators are combined.
- Problems arise due to the saliency when the low frequency injection is used to estimate the speed and position of the PMSM. The saliency effect is theoretically analysed and a simple compensation method is proposed (Chapter 4). The performance of the compensation method is verified experimentally. The results were published in [Esk05]. Speed and position estimator using the low frequency injection was originally presented for induction motors in [Lep03].
- The proposed hybrid estimator is proven to be stable in the speed range from zero to nominal speed.
- It is shown by measurements in Chapter 6 that matrix converters can be applied in PMSM drives where the rotor angular speed and position are not measured. Both MC topologies are experimentally tested. The PMSM drive fed by the direct MC topology with sensorless control has been reported in [Ari04] and [Liu03]. The indirect MC topology with sensorless control was tested first time in [Esk04].

2. Frequency converter fed PMSM drive

2.1 Permanent magnet synchronous machines

Permanent magnet synchronous machines can be divided into brushless DC machines (BLDC) and sinewave machines. The following ideal characteristics of BLDC are given in [Hen94].

- Distribution of magnet flux in the airgap is rectangular,
- The current waveform of three phase BLDC is a 120° squarewave. Two phases are conducting at any and every instant,
- Stator windings are concentrated.

The ideal characteristics of sinewave PMSM are:

- Sinusoidal distribution of magnet flux in the airgap,
- Sinusoidal current waveforms,
- Sinusoidal distribution of stator conductors.

The control of a power electronic device feeding the BLDC is easier than the control of a converter using PWM techniques. Demands for semiconductor switches and control electronics are lower compared to a frequency converter capable of producing sinusoidal currents. The development of semiconductors and integrated circuits has increased the popularity of sinewave machines. A sinewave machine fed by a modern frequency converter has clearly better torque characteristics compared to BLDC drive. BLDC drives are not discussed further in this study.

PMSMs can be categorized based on the mounting of the permanent magnets. Fig. 2.1a shows one possible rotor structure with two pole pairs. The magnets are mounted on the surface of the rotor (SPMSM). Fig. 2.1b shows one possible structure where magnets are buried inside the rotor (IPMSM). More detailed information from different magnet mounting strategies and rotor structures will be found in [Hen94].

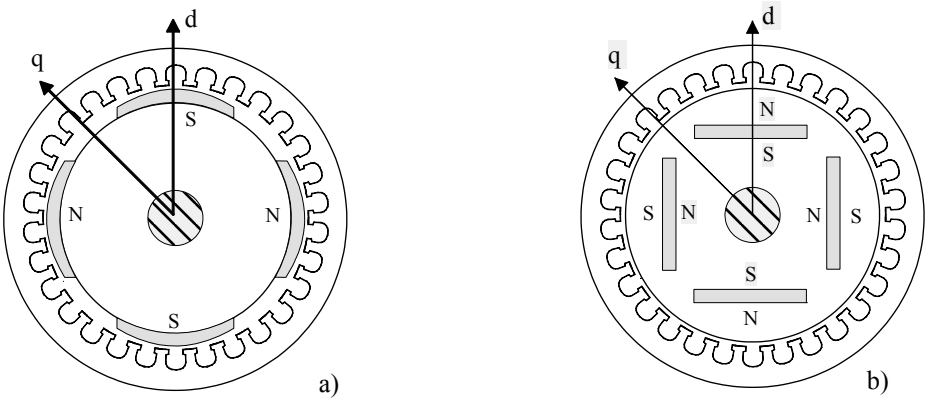

Fig. 2.1 a) PMSM with surface mounted magnets, two pole pairs. b) PMSM with interior mounted magnets, two pole pairs.

In Fig. 2.1 arrows with "d" and "q" denote direct and quadrature axes of the PMSM. d-axis is the magnetic axis of the rotor and the arrow indicates the positive direction of the rotor flux. The mechanical angle between d and q axes is $\pi/(2p)$ where p is the number of pole pairs.

If the magnets are mounted on the rotor surface the effective air gap is rather large because the permeability of permanent magnets is low, typically close to that of air [Hen94]. Due to the large air gap the inductances of the SPMSMs are smaller. The difference between the direct and quadrature axis inductances (L_d and L_q) is usually small. However, there is always some saliency because the strong magnetic fields saturate the iron, especially the stator teeth. This makes the effective air gap larger in the d-axis direction. Thus $L_d < L_q$. Due to the relatively small inductances PMSMs with surface mounted magnets are not suitable for drives where strong field weakening is required.

In the case of IPMSMs there are flux paths in the d axis direction where the reluctance is high due to the low permeability of the permanent magnet material, Fig. 2.1b. Thus the inductance is clearly larger in the q axis direction. The buried magnet placement enables a small air gap. Thus the inductances are larger compared to a SPMSM.

PMSMs can be also categorized on the basis of the direction of the flux. Fig. 2.1 and Fig. 2.2a show the structure of a radial flux machine, which is the common structure for AC machines. The flux created by the permanent magnets crosses the air gap in a radial direction to link the rotor flux with stator windings. The stator structure of the radial flux PMSM is basically same as in the case of the induction machines. The flux can also cross the air gap in parallel direction with the rotor shaft, Fig. 2.2b. These machines are called axial flux machines.

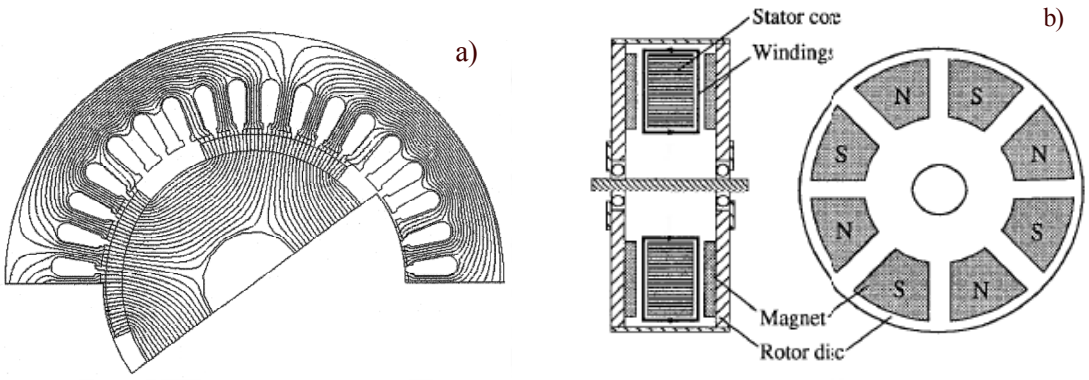

Fig. 2.2 a) Radial flux structure and b) axial flux structure.

A small length/diameter ratio is typical of axial flux machines. This structure makes possible a high number of pole pairs. Axial flux machines are often used in high power solutions where angular speeds are rather small, e.g. elevators, generators and ship propulsion drives. Radial flux machines compete with induction motors in variable speed drives in industrial applications and are extensively used in small power servo drives.

2.2 Modelling of the PMSM

At the beginning of Section 2.2.1 three-phase voltage and flux linkage equations of the PMSM are given. Section 2.2.1 also provides a short introduction to space-vector theory and its application on modelling of PMSMs. Section 2.2.2 deals with the PMSM model, where the effects of flux linkage harmonics are taken into account.

2.2.1 Modelling of the voltage equations using the space-vector theory

The voltage equations of the three-phase PMSM in a phase variable form are [Vas92], [Nov00]

$$\begin{aligned} u_\mathrm{a} &= Ri_\mathrm{a} + \frac{d\psi_\mathrm{a}}{dt} \\ u_\mathrm{b} &= Ri_\mathrm{b} + \frac{d\psi_\mathrm{b}}{dt} \\ u_\mathrm{c} &= Ri_\mathrm{c} + \frac{d\psi_\mathrm{c}}{dt} \end{aligned} \tag{2–1}$$

The flux linkages can be written

$$\begin{aligned} \psi_\mathrm{a} &= L_\mathrm{sa}(\theta_\mathrm{r})i_\mathrm{a} + L_\mathrm{m,ab}(\theta_\mathrm{r})i_\mathrm{b} + L_\mathrm{m,ac}(\theta_\mathrm{r})i_\mathrm{c} + \psi_\mathrm{m}\cos(\theta_\mathrm{r}) \\ \psi_\mathrm{b} &= L_\mathrm{sb}(\theta_\mathrm{r})i_\mathrm{b} + L_\mathrm{m,ba}(\theta_\mathrm{r})i_\mathrm{a} + L_\mathrm{m,bc}(\theta_\mathrm{r})i_\mathrm{c} + \psi_\mathrm{m}\cos(\theta_\mathrm{r} - 2\pi/3) \\ \psi_\mathrm{c} &= L_\mathrm{sc}(\theta_\mathrm{r})i_\mathrm{c} + L_\mathrm{m,ca}(\theta_\mathrm{r})i_\mathrm{a} + L_\mathrm{m,cb}(\theta_\mathrm{r})i_\mathrm{b} + \psi_\mathrm{m}\cos(\theta_\mathrm{r} + 2\pi/3) \end{aligned} \tag{2–2}$$

where $L_{sa,}$ L_{sb} and L_{sc} are self inductances of the stator windings and $L_{m,ca}$, $L_{m,ab}$ ans $L_{m,bc}$ are mutual inductances between the windings. ψ_m is a permanent magnet (PM) flux. Due to the saturation effects and mechanical structures of PMSMs the inductances are functions of the electric rotor position angle θ_r. The electric rotor position angle is the direction of the rotor flux (North Pole of the rotor magnets). The zero angle is the direction of phase a. The relation between the mechanical and the electrical rotor position is

$$\theta_r = p\theta_{mech} \tag{2–3}$$

where p is the number of pole pairs.

In a general case the inductances of the PMSM (2–2) can be expressed with Fourier series [Low96], [Pet01]. The inductances consist of a constant component and a sum of even harmonics when the rotor position θ_r changes.

In the literature on controlled AC drives the following assumptions are commonly made [Vas92].

- The stator windings are assumed to be perfectly sinusoidally distributed,
- The effect of the discrete nature of the stator structure is neglected. Therefore stator windings produce a sinusoidal magneto-motive-force,
- In the case of the PMSM the radial flux-density distribution produced by the rotor permanent magnets is perfectly sinusoidal and the flux linkage from the rotor in the stator windings contains only the fundamental component,
- The effect of the magnetic saturation is ignored.

With these assumptions the inductance variation has only a one sinusoidal component. The inductance of the phase is at its minimum when the rotor flux direction (d axis in Fig. 2.1) is in alignment with the phase. Thus the phase inductances are functions of the angle $2\theta_r$. If only this single sinusoidally distributed saliency is assumed, the self inductances and the mutual inductances of a synchronous motor are written [Vas92]:

$$\begin{aligned} L_{sa}(\theta_r) &= L_{s0} + L_{s2}\cos(2\theta_r) \\ L_{sb}(\theta_r) &= L_{s0} + L_{s2}(\theta_r - 2\pi/3) \\ L_{sc}(\theta_r) &= L_{s0} + L_{s2}(\theta_r + 2\pi/3) \end{aligned} \tag{2–4}$$

$$\begin{aligned} L_{m,ab}(\theta_r) &= L_{m0} + L_{m2}\cos(2\theta_r - 2\pi/3) \\ L_{m,ca}(\theta_r) &= L_{m0} + L_{m2}\cos(2\theta_r + 2\pi/3) \\ L_{m,bc}(\theta_r) &= L_{m0} + L_{m2}\cos(2\theta_r) \end{aligned} \tag{2–5}$$

where L_{s0} and L_{m0} are the average components of the self and the mutual inductances. L_{s2} and

L_{m2} are the amplitudes of the sinusoidal components. In the case of PMSMs $L_{s2}<0$ and $L_{m2}<0$.

In a general case the flux linkages created by the permanent magnets consist of a fundamental sinusoidal component and the sum of odd harmonics. If the assumptions given above are valid the three-phase flux linkage created by the PM flux has only the fundamental component as written in (2–2).

2.2.1.1 Space-vector theory

In the theory and analysis of AC systems a commonly used approach is to represent the three-phase quantities as a function of time by complex phasors. These phasors are called space-vectors in the literature. This section gives a short introduction to space-vector theory. More detailed information will be found in many textbooks, e.g. [Vas92], [Kra02], [Nov00].

The Park transformation matrix **K** transforms the three phase quantity x into a complex phasor called a space-vector. x denotes any three phase quantity, current, flux linkage or voltage. Subscripts α and β denote real and imaginary parts of the space-vector.

$$\begin{bmatrix} x_\alpha \\ x_\beta \\ x_0 \end{bmatrix} = \underbrace{\frac{2}{3}\begin{bmatrix} \cos\theta & \cos(\theta-2\pi/3) & \cos(\theta+2\pi/3) \\ -\sin\theta & -\sin(\theta-2\pi/3) & -\sin(\theta+2\pi/3) \\ 1/2 & 1/2 & 1/2 \end{bmatrix}}_{\mathbf{K}} \begin{bmatrix} x_a \\ x_b \\ x_c \end{bmatrix} \tag{2–6}$$

In (2–6) θ denotes the angle of the real axis of the complex plane compared to the direction of the phase a. This angle of the reference frame can be freely selected. It may be constant or a function of time. The coefficient 2/3 in front of the transformation matrix means that the non-power invariant form of coordinate transformation is used. In that case the length of the space-vector $x_\alpha + jx_\beta$ is equal to the peak value of the sinusoidal three phase quantity x. This method is used throughout this study. The other common form of transformation [Vas92] is to replace 2/3 by its square root. In that case the amplitude is changed but the power and torque equations in space-vector form need no additional coefficients. When the non-power invariant (amplitude invariant) form is used the inverse transformation is

$$\begin{bmatrix} x_a \\ x_b \\ x_c \end{bmatrix} = \underbrace{\begin{bmatrix} \cos\theta & -\sin\theta & 1 \\ \cos(\theta-2\pi/3) & -\sin(\theta-2\pi/3) & 1 \\ \cos(\theta+2\pi/3) & -\sin(\theta+2\pi/3) & 1 \end{bmatrix}}_{\mathbf{K}_{inv}} \begin{bmatrix} x_\alpha \\ x_\beta \\ x_0 \end{bmatrix} \tag{2–7}$$

In this thesis the star connection is used in all machines. If the neutral point is not connected the zero sequence component x_0 has non-zero value only under fault conditions.

Fault conditions are not covered in this work. If x is voltage in (2–7) the sum of the fundamental frequency components of u_a, u_b and u_c is approximately zero. In PWM operation the instantaneous sum of the phase voltages is not zero because at every instant each three motor phases are connected to either lower or higher voltage level. As will be explained in Section 2.3 these two voltage levels can be DC-buses or phase voltages of the supply network. This zero sequency voltage component varying with high frequency is not interesting when sensorless control methods are analysed. Therefore x_0 is assumed to be zero throughout this study.

In PMSM drives the typical choices for the angle of the reference frame θ (2–6) are 0 and the rotor position angle θ_r. If the angle is zero the transformation is made to the stator reference frame, where the real axis is aligned in the direction of phase a. Because the position angle is constantly zero it is also called a stationary reference frame. In the original Park transformation the real axis of the complex plane is tied to the rotor position θ_r. In this thesis it is called rotor reference frame.

When sensorless control methods are studied θ_r is unknown. In that case θ_r is replaced by its estimate $\hat{\theta}_r$ in (2–6). The real and imaginary parts of the space-vector are denoted by the subscripts d and q in the rotor reference frame and by de and qe in the estimated rotor frame. In the stationary frame the real and imaginary parts are marked by α and β. In the literature they are also denoted by D and Q. The coordinate transformations are illustrated in Fig. 2.3 .

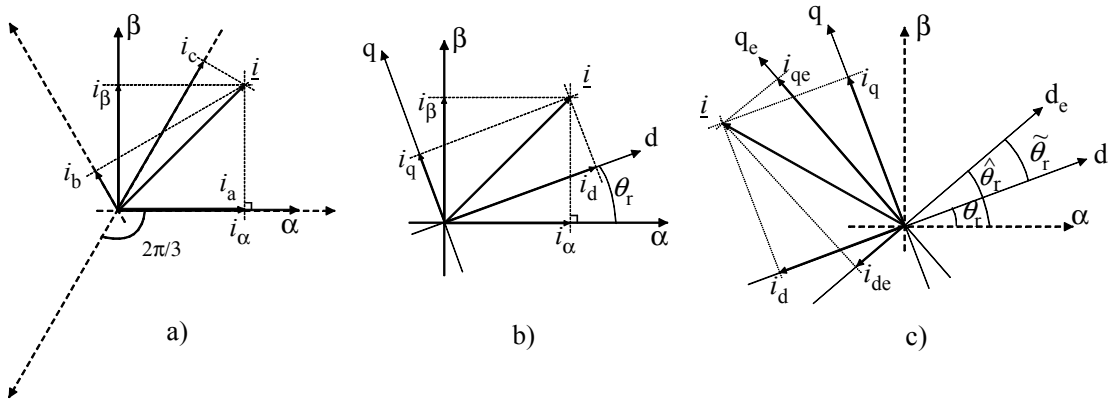

Fig. 2.3 a) Composition of the current vector from three phase form to space-vector representation. b) Transformation from stationary to rotor reference frame. c) Transformation between actual and estimated rotor reference frames.

If a complex phasor notation is used the transformation to stationary frame can be written using (2–6) with $\theta = 0$.

$$\underline{i}^s = \frac{2}{3}(i_a + i_b e^{j2\pi/3} + i_c e^{j4\pi/3}) = \frac{2}{3}\left(i_a + \frac{1}{2}(-i_b - i_c)\right) + j\left(\frac{i_b - i_c}{\sqrt{3}}\right) = i_\alpha + j i_\beta \qquad (2–8)$$

where i_a, i_b and i_c are phase currents. A similar expression can also be written for voltage and flux linkages. If no zero-sequence currents exist $i_\alpha = i_a$. Using complex quantities the transformation between stationary and rotating reference frames can be written

$$\begin{aligned} \underline{i}^{\mathrm{r}} &= \underline{i}^{\mathrm{s}} e^{-j\theta_{\mathrm{r}}} = i_{\mathrm{d}} + \mathrm{j}i_{\mathrm{q}} = (i_\alpha \cos\theta_{\mathrm{r}} + i_\beta \sin\theta_{\mathrm{r}}) + \mathrm{j}(i_\beta \cos\theta_{\mathrm{r}} - i_\alpha \sin\theta_{\mathrm{r}}) \\ \underline{i}^{\mathrm{s}} &= \underline{i}^{\mathrm{r}} e^{j\theta_{\mathrm{r}}} = i_\alpha + \mathrm{j}i_\beta = (i_{\mathrm{d}} \cos\theta_{\mathrm{r}} - i_{\mathrm{q}} \sin\theta_{\mathrm{r}}) + \mathrm{j}(i_{\mathrm{q}} \cos\theta_{\mathrm{r}} + i_{\mathrm{d}} \sin\theta_{\mathrm{r}}) \end{aligned} \tag{2–9}$$

The superscripts s and r of the phasors in (2–8) - (2–9) indicate the reference frame. In the literature on AC motors s and r often indicate stator and rotor quantities when used as subscripts. This thesis deals with PMSMs without damper windings. Thus there is no confusion even if the subscripts s and r are omitted in the case of three-phase quantities.

2.2.1.2 Space-vector representation of voltage and flux linkage equations

The model of the PMSM is simplified if the three-phase voltage model (2–1) is transformed to a space-vector form using (2–6). In rotor reference frame the voltage equation of the PMSM is:

$$\begin{aligned} u_{\mathrm{d}} &= Ri_{\mathrm{d}} + \frac{d\psi_{\mathrm{d}}}{dt} - \omega_{\mathrm{r}}\psi_{\mathrm{q}} \\ u_{\mathrm{q}} &= Ri_{\mathrm{q}} + \frac{d\psi_{\mathrm{q}}}{dt} + \omega_{\mathrm{r}}\psi_{\mathrm{d}} \end{aligned} \tag{2–10}$$

Flux linkage components ψ_{d} and ψ_{q} are achieved by transforming (2–2) to the rotor reference frame. If the inductances (2–4), (2–5) contain only the sinusoidal component varying as a function of $2\theta_{\mathrm{r}}$ the flux linkage in the rotor reference frame is

$$\begin{aligned} \psi_{\mathrm{d}} &= \psi_{\mathrm{m}} + L_{\mathrm{d}} i_{\mathrm{d}} \\ \psi_{\mathrm{q}} &= L_{\mathrm{q}} i_{\mathrm{q}} \end{aligned} \tag{2–11}$$

where $L_{\mathrm{d}} = L_{\mathrm{s0}} - L_{\mathrm{m0}} + L_{\mathrm{s2}}/2 + L_{\mathrm{m2}}$ and $L_{\mathrm{q}} = L_{\mathrm{s0}} - L_{\mathrm{m0}} - L_{\mathrm{s2}}/2 - L_{\mathrm{m2}}$. When (2–11) is substituted into (2–10) the voltage equation of the PMSM can be written

$$\begin{aligned} u_{\mathrm{d}} &= Ri_{\mathrm{d}} + L_{\mathrm{d}} \frac{di_{\mathrm{d}}}{dt} - \omega_{\mathrm{r}} L_{\mathrm{q}} i_{\mathrm{q}} \\ u_{\mathrm{q}} &= Ri_{\mathrm{q}} + L_{\mathrm{q}} \frac{di_{\mathrm{q}}}{dt} + \omega_{\mathrm{r}} (\psi_{\mathrm{m}} + L_{\mathrm{d}} i_{\mathrm{d}}) \end{aligned} \tag{2–12}$$

The voltage equation (2–12) is usually applied in the literature. It is accurate enough when the performance of the control system is analysed. A more accurate voltage model of the PMSM

is studied in Section 2.2.2. The equations of the electromagnetic torque and mechanics are given in Section 2.2.2.3.

About the notations

The three-phase equations transformed into the space-vector form can be written using the matrix notation or the complex phasor notation. The complex phasor form is possible only if the parameters of the phases are equal. In the case of an AC motor this means that R and L are equal in each phase and do not vary as a function of rotor position. The basic stator voltage equation of the symmetric PMSM in the rotor frame is used as an example. It can be written using the complex phasor notation as follows

$$\underline{u}^{\mathrm{r}} = R\underline{i}^{\mathrm{r}} + L\frac{d\underline{i}^{\mathrm{r}}}{dt} + \mathrm{j}\omega_{\mathrm{r}}(L\underline{i}^{\mathrm{r}} + \psi_{\mathrm{m}}) \tag{2–13}$$

In (2–12) the direct and quadrature axis inductances are not equal. Now the aforementioned simple notation cannot be used. The voltage equation can be written in matrix form:

$$\mathbf{u}^{\mathrm{r}} = \mathbf{R}\mathbf{i}^{\mathrm{r}} + \mathbf{L}\frac{d}{dt}\mathbf{i}^{\mathrm{r}} + \omega_{\mathrm{r}}\mathbf{T}(\mathbf{L}\mathbf{i}^{\mathrm{r}} + \boldsymbol{\psi}_{\mathrm{m}}) \tag{2–14}$$

$$\mathbf{u}^{\mathrm{r}} = \begin{bmatrix} u_{\mathrm{d}} \\ u_{\mathrm{q}} \end{bmatrix}, \mathbf{i}^{\mathrm{r}} = \begin{bmatrix} i_{\mathrm{d}} \\ i_{\mathrm{q}} \end{bmatrix}, \mathbf{R} = \begin{bmatrix} R & 0 \\ 0 & R \end{bmatrix}, \mathbf{L} = \begin{bmatrix} L_{\mathrm{d}} & 0 \\ 0 & L_{\mathrm{q}} \end{bmatrix}, \mathbf{T} = \begin{bmatrix} 0 & -1 \\ 1 & 0 \end{bmatrix}, \boldsymbol{\psi}_{\mathrm{m}} = \begin{bmatrix} \psi_{\mathrm{m}} \\ 0 \end{bmatrix}$$

or the real and imaginary parts are written separately as in (2–12). The matrix notation (2–14) is compact and often used in many papers to save space. It is the opinion of the author that Equation (2–12) is more informative because the real and imaginary parts are written separately. In this study the style of Equation (2–12) is preferred.

2.2.2 A PMSM model with higher order flux linkage harmonics

The assumptions given in the beginning of Section 2.2.1 can be made if the PMSM is modelled for control system analysis. If the electric angular speed $\omega_{\mathrm{r}} = p\omega_{\mathrm{mech}}$ and the position angle of the rotor θ_{r} are measured using a sensor the modern high performance closed-loop control techniques compensate most of the effects of non-ideal machine structure. In the literature the non-ideal properties of the PMSMs are usually analysed in papers addressing torque ripple minimization in high performance drives with speed and position sensors [Col99], [Hol96], [Low90], [Qia04].

In this thesis sensorless control is applied. This means that the speed and position are

determined using current and voltage information. These electrical quantities contain the harmonics caused by non-ideal properties of the machine and the frequency converter. To understand the performance and the problems of sensorless methods a more accurate PMSM model must be used.

The model now presented is still simplified compared to the real PMSM.

- The effects of magnetic saturation and motor temperature are ignored,
- Slot harmonics (cogging torque) are not modelled. The reluctance of the magnetic circuit varies when the edges of the rotor magnets pass the stator teeth. Torque pulsation occur at a frequency $\omega_{\mathrm{mech}} \times$ number of slots,
- The phase resistances are assumed to be identical,
- Geometric symmetry of the stator and rotor poles is assumed.

2.2.2.1 Phase inductances of the PMSM

If all the simplifications given above and in Section 2.2.1 are used the phase inductances contain only the average value $L_{\mathrm{s0}} = (L_{\mathrm{q}} + L_{\mathrm{d}})/2$ and sinusoidal component with frequency $2\omega_{\mathrm{r}}$ and amplitude $L_{\mathrm{s2}} = (L_{\mathrm{d}} - L_{\mathrm{q}})/2$. This sinusoidal component is called main saliency. If a more accurate model is needed the higher order saliencies must be included. In a general case the self inductances of phases are [Low96], [Pet01]

$$\begin{aligned} L_{\mathrm{sa}}(\theta_{\mathrm{r}}) &= L_{\mathrm{s0}} + \sum_{n=1}^{\infty} L_{\mathrm{s},2n} \cos(2n\theta_{\mathrm{r}}) \\ L_{\mathrm{sb}}(\theta_{\mathrm{r}}) &= L_{\mathrm{sa}}(\theta_{\mathrm{r}} - 2\pi/3) \\ L_{\mathrm{sc}}(\theta_{\mathrm{r}}) &= L_{\mathrm{sa}}(\theta_{\mathrm{r}} + 2\pi/3) \end{aligned} \tag{2–15}$$

where the zero rotor angle θ_{r} is the direction of the phase a. Similarly, the mutual inductances between the phases can be written [Pet01]

$$\begin{aligned} L_{\mathrm{m,ab}}(\theta_{\mathrm{r}}) &= L_{\mathrm{m,0}} + \sum_{n=1}^{\infty} L_{\mathrm{m},2n} \cos(2n\theta_{\mathrm{r}} - n2\pi/3) \\ L_{\mathrm{m,ca}}(\theta_{\mathrm{r}}) &= L_{\mathrm{m,0}} + \sum_{n=1}^{\infty} L_{\mathrm{m},2n} \cos(2n\theta_{\mathrm{r}} + n2\pi/3) \\ L_{\mathrm{m,bc}}(\theta_{\mathrm{r}}) &= L_{\mathrm{m,0}} + \sum_{n=1}^{\infty} L_{\mathrm{m},2n} \cos(2n\theta_{\mathrm{r}}) \end{aligned} \tag{2–16}$$

2.2.2.2 Flux linkage and voltage equations in the rotor reference frame

The flux linkage from the rotor magnets in the stator winding can be expressed as a sum of odd cosines [Hen94].

$$\boldsymbol{\psi}_{\mathrm{m,abc}} = \sum_{n=1}^{\infty} \psi_{\mathrm{m},(2n-1)} \begin{bmatrix} \cos((2n-1)\theta_{\mathrm{r}}) \\ \cos((2n-1)(\theta_{\mathrm{r}} - 2\pi/3)) \\ \cos((2n-1)(\theta_{\mathrm{r}} + 2\pi/3)) \end{bmatrix} \tag{2–17}$$

The amplitude of (2n-1)th harmonic component decreases rapidly when n increases. The amplitudes of flux harmonics $\psi_{\mathrm{m(2n-1)}}$ are dependent on the specific shape of the PM magnets and stator winding structure. Usually in the literature only the first component $\psi_{\mathrm{m,1}}$ is included. It is denoted as ψ_{m} [Vas92]. This parameter is also called a back-emf constant. The back-emf is the voltage induced in the stator windings by the variable magnetic field in the airgap. In this thesis back-emf is the voltage induced by the rotor magnets when the rotor is rotating. With the more general definition the back-emf also includes the mutually and self-induced voltage between windings [Pro03].

Using (2–15) - (2–17) the fluxes of the PMSM can be written

$$\boldsymbol{\psi}_{\mathrm{abc}} = \mathbf{L}_{\mathrm{abc}}\mathbf{i}_{\mathrm{abc}} + \boldsymbol{\psi}_{\mathrm{m,abc}} \tag{2–18}$$

where $\mathbf{L}_{\mathrm{abc}} = \begin{bmatrix} L_{\mathrm{sa}}(\theta_{\mathrm{r}}) & L_{\mathrm{m,ab}}(\theta_{\mathrm{r}}) & L_{\mathrm{m,ac}}(\theta_{\mathrm{r}}) \\ L_{\mathrm{m,ba}}(\theta_{\mathrm{r}}) & L_{\mathrm{sb}}(\theta_{\mathrm{r}}) & L_{\mathrm{m,bc}}(\theta_{\mathrm{r}}) \\ L_{\mathrm{m,ca}}(\theta_{\mathrm{r}}) & L_{\mathrm{m,bc}}(\theta_{\mathrm{r}}) & L_{\mathrm{sc}}(\theta_{\mathrm{r}}) \end{bmatrix}, \mathbf{i}_{\mathrm{abc}} = \begin{bmatrix} i_{\mathrm{a}} \\ i_{\mathrm{b}} \\ i_{\mathrm{c}} \end{bmatrix}$

After the three-phase flux linkage equation (2–18) is transformed to the rotor reference frame the d and q axis components of the flux linkage are

$$\begin{aligned} \psi_{\mathrm{d}} &= \psi_{\mathrm{md}} + L_{\mathrm{dd}} i_{\mathrm{d}} + L_{\mathrm{dq}} i_{\mathrm{q}} \\ \psi_{\mathrm{d}} &= \psi_{\mathrm{mq}} + L_{\mathrm{qq}} i_{\mathrm{q}} + L_{\mathrm{dq}} i_{\mathrm{d}} \end{aligned} \tag{2–19}$$

where [Low90], [Col99]

$$\begin{aligned} L_{\mathrm{dd}} &= L_{\mathrm{d}} + \sum_{n=1}^{\infty} L_{\mathrm{dd},6n} \cos(6n\theta_{\mathrm{r}}) \\ L_{\mathrm{qq}} &= L_{\mathrm{q}} + \sum_{n=1}^{\infty} L_{\mathrm{qq},6n} \cos(6n\theta_{\mathrm{r}}) \\ L_{\mathrm{dq}} &= \sum_{n=1}^{\infty} L_{\mathrm{dq},6n} \sin(6n\theta_{\mathrm{r}}) \\ \psi_{\mathrm{md}} &= \psi_{\mathrm{m}} + \sum_{n=1}^{\infty} \psi_{\mathrm{md},6n} \cos(6n\theta_{\mathrm{r}}) \\ \psi_{\mathrm{mq}} &= \sum_{n=1}^{\infty} \psi_{\mathrm{mq},6n} \sin(6n\theta_{\mathrm{r}}) \end{aligned} \tag{2–20}$$

A more detailed description of the formation of the inductance harmonics can be found in [Pet01]. It can be seen in (2–20) that the stator flux linkages in the d,q frame contain the

average component and multiples of the sixth harmonics. In stationary frame the flux linkages contain harmonics of the order 5,7,11,13,17,19…

Here (2–20) is truncated to contain only the 6th harmonic (n = 1). For modelling purposes this can be done because the amplitudes of 6nth harmonics decrease rapidly when n increases. Equation (2–20) is the general case where $L_{dd,6}$, $L_{qq,6}$ and $L_{dq,6}$ have different values. To further simplify the model, Equations (2–15) and (2–16) are truncated to contain harmonics up to the 4th order (n = 2), [Wal04b]. In that case $L_{dd,6} = -L_{qq,6} = -L_{dq,6} = L_{s4}/2 + L_{m4}$. This inductance component in the rotor reference frame is denoted here as L_6.

In the PM flux linkage equation (2–17) the 5th and 7th harmonics (n = 3, n = 4) are included. Using the aforementioned simplifications (2–20) can be written.

$$\begin{aligned}
L_{dd} &= L_d + L_6\cos(6\theta_r)\\
L_{qq} &= L_q - L_6\cos(6\theta_r)\\
L_{dq} &= -L_6\sin(6\theta_r)\\
\psi_{md} &= \psi_m + (\psi_{m,5} + \psi_{m,7})\cos(6n\theta_r) = \psi_m + \psi_{md,6}\cos(6n\theta_r)\\
\psi_{mq} &= (-\psi_{m,5} + \psi_{m,7})\sin(6n\theta_r) = \psi_{mq,6}\sin(6n\theta_r)
\end{aligned} \tag{2–21}$$

Using (2–19) and (2–21) we can write the voltage model (2–10) of the PMSM in the rotor reference frame where harmonics of 6th order are included.

$$\begin{aligned}
u_d &= Ri_d + L_d\frac{di_d}{dt} - \omega_r L_q i_q + L_6\cos(6\theta_r)\frac{di_d}{dt} - L_6\sin(6\theta_r)\frac{di_q}{dt}\\
&- 5\omega_r L_6\sin(6\theta_r)i_d - 5\omega_r L_6\cos(6\theta_r)i_q - 6\omega_r\psi_{md6}\sin(6\theta_r) - \omega_r\psi_{mq6}\sin(6\theta_r)\\
u_q &= Ri_q + L_q\frac{di_q}{dt} + \omega_r(L_d i_d + \psi_m) - L_6\cos(6\theta_r)\frac{di_q}{dt} - L_6\sin(6\theta_r)\frac{di_d}{dt}\\
&+ 5\omega_r L_6\sin(6\theta_r)i_q - 5\omega_r L_6\cos(6\theta_r)i_d + 6\omega_r\psi_{mq6}\cos(6\theta_r) + \omega_r\psi_{md6}\cos(6\theta_r)
\end{aligned} \tag{2–22}$$

If only first three components on the right hand side of (2–22) are included the voltage model reduces to the fundamental frequency model (2–12) used in textbooks.

In the literature on torque ripple the inductances are often assumed to contain only the average components L_d and L_q [Hol96], [Low90], [Qia04]. This means that only the main saliency is included in the analysis. In that case the stator flux linkage harmonics are caused only by the non-sinusoidal distribution of the rotor flux. This assumption may be valid when the torque ripple is analysed because the contribution to the torque by the stator winding inductances is smaller than that of the rotor PM flux [Low90]. In this thesis the modelling of the PMSM is based on (2–22) when the non-ideal properties are studied. Thus the effect of inductance variation in the rotor frame is also modelled.

2.2.2.3 Equations of the electromagnetic torque and mechanics

The equation of the electromagnetic torque can be derived from the expression of the energy stored in the field coupling the electric and mechanical systems, stator and rotor [Vas92], [Nov00], [Kra02]. If linear magnetic conditions are assumed, the following three-phase expression can be written for the energy stored to the coupling field of the PMSM [Kra02].

$$W_{\text{field}}(i,\theta_{\text{r}}) = \frac{1}{2}\mathbf{i}_{\text{abc}}^{\text{T}}\mathbf{L}_{\text{abc}}(\theta_{\text{r}})\mathbf{i}_{\text{abc}} + \mathbf{i}_{\text{abc}}^{\text{T}}\boldsymbol{\psi}_{\text{m,abc}}(\theta_{\text{r}}) \tag{2–23}$$

The losses of the coupling field are ignored because the energy of the field is stored mainly in the air gap of the PMSM. It is shown in [Kra02] that under these assumptions the rate of change of the mechanical energy of the PMSM is the same as the change of the energy stored in the coupling field in the air gap. The rate of change of the mechanical energy is the torque produced by the PMSM.

$$T_{\text{e}}(\mathbf{i}_{\text{abc,}},\theta_{\text{r}}) = p\frac{\partial W(\mathbf{i}_{\text{abc}},\theta_{\text{r}})}{\partial\theta_{\text{r}}} = p\left(\frac{1}{2}\mathbf{i}_{\text{abc}}^{\text{T}}\frac{\partial\mathbf{L}_{\text{abc}}(\theta_{\text{r}})}{\partial\theta_{\text{r}}}\mathbf{i}_{\text{abc}} + \mathbf{i}_{\text{abc}}^{\text{T}}\frac{\partial\boldsymbol{\psi}_{\text{m,abc}}(\theta_{\text{r}})}{\partial\theta_{\text{r}}}\right) \tag{2–24}$$

p is the number of pole pairs. (2–24) is transformed to the rotor reference frame using (2–7).

$$T_{\text{e}}(\theta_{\text{r}}) = p\left(\frac{1}{2}(\mathbf{K}_{\text{inv}}\mathbf{i}^{\text{r}})^{\text{T}}\frac{\partial\mathbf{L}_{\text{abc}}}{\partial\theta_{\text{r}}}\mathbf{K}_{\text{inv}}\mathbf{i}^{\text{r}} + (\mathbf{K}_{\text{inv}}\mathbf{i}^{\text{r}})^{\text{T}}\frac{\partial\boldsymbol{\psi}_{\text{m,abc}}}{\partial\theta_{\text{r}}}\right) \tag{2–25}$$

where $\mathbf{i}^{\text{r}} = [i_{\text{d}}\ i_{\text{q}}]^{\text{T}}$ and $\mathbf{K}_{\text{inv}}$ is the transformation matrix from rotor frame to stationary (2–7) frame. The cogging torque is not included. If the expression of the electromagnetic torque is truncated to contain harmonics up to 6th order (2–25) can be written

$$\begin{aligned} T_e = {} & \frac{3}{2}p\{\psi_{\text{m}}i_{\text{q}} + (L_{\text{d}} - L_{\text{q}})i_{\text{d}}i_{\text{q}} - 2L_6((i_{\text{d}}^2 - i_{\text{q}}^2)\sin(6\theta_{\text{r}}) + 2i_{\text{d}}i_{\text{q}}\cos(6\theta_{\text{r}})) \\ & + i_{\text{q}}\cos(6\theta_{\text{r}})(\psi_{\text{md,6}} + 6\psi_{\text{mq,6}}) - i_{\text{d}}\sin(6\theta_{\text{r}})(\psi_{\text{mq,6}} + 6\psi_{\text{md,6}})\} \end{aligned} \tag{2–26}$$

The first component $3/2p\,\psi_{\text{m}}i_{\text{q}}$ is the main torque producing component. The second one is the reluctance torque caused by the main saliency. The other terms arise due to the harmonics in inductances and rotor flux linkage. They are dependent on the rotor position.

In a general case the load torque, friction and inertia of the PMSM drive can be a function of time, rotor position and angular speed. In this thesis the inertia J and friction coefficients are assumed to be constants during the test sequences. Thus the equation of motion can be written

$$T_e - T_L = J\frac{d\omega_{mech}}{dt} + b\omega_{mech} + \frac{F\omega_{mech}}{|\omega_{mech}|} \quad (2–27)$$

In (2–27) T_L is the load torque, J is the inertia of the drive, ω_{mech} (= ω_r/p) is the mechanical angular speed of the rotor and b is the friction constant. F denotes the Coulomb friction component. Usually F is ignored because it makes (2–27) non-linear. Between the angular speed and the rotor position holds

$$\theta_r = \int \omega_r dt + \theta_0 \Leftrightarrow \omega_r = \frac{d\theta_r}{dt} \quad (2–28)$$

Now all the equations required to build the model of the PMSM have been introduced. The Simulink model based on Equations (2–22), (2–26) - (2–28) is presented in Chapter 3.

2.3 Pulse width modulated frequency converters

If controlled operation is required the AC machine must be supplied by a frequency converter. The most common frequency converter structure in industry is the voltage source converter (VSC) which contains a rectifier, a DC-link with a capacitor, and an inverter. The power switches of the inverter bridge are usually IGBTs.

The possibility of using current source PWM technology for frequency conversion has also been studied [Sal02]. Positive features of the PWM current source converter (PWM-CSC) are inherent AC current production and almost sinusoidal inverted voltages. However, the commercial applications of PWM-CSC are minimal compared to voltage source technology. The main disadvantages of the CSCs are the bulky inductor in the DC-link and the more complex control of the AC currents due to the LC filter resonance. In this thesis current source technology is not studied.

Direct frequency conversion using PWM technology is possible using a matrix converter. A matrix converter is a forced commutated converter which uses an array of controlled bi-directional switches to create a variable output voltage with unrestricted frequency. The idea of the matrix converter was introduced in the 1970s [Gyu76]. The name “matrix converter” was introduced in 1980 by Venturini and Alesina [Ven80]. They presented the main circuit as a matrix of bi-directional power switches. They also significantly developed modulation methods and mathematical analysis of the MC. The comprehensive list of important steps in the development of the MCs is presented in [Whe02].

In an MC the power can flow in both directions. An MC does not have a DC-link circuit.

The absence of the DC-link components enables small size and reliable operation. Compared to PWM-VSC the maximum output/input voltage ratio of the MC is smaller and the disturbances between input and output are not filtered due to the absence of the DC-link with energy storage.

This section contains an introduction to VSC and MC topologies. The VSC and its PWM modulation strategies are presented very briefly because the frequency conversion using three phase PWM inverter is well known technology. Detailed information on PWM-VSC can be found in several textbooks, e.g. [Hol03], [Nov00]. The properties of the MC are explained in more detail because MCs are an emerging technology. The properties of VSC and MC important for sensorless control methods are compared. The disturbances caused by the voltage losses of the main circuit components are analysed in the case of both converter structures.

2.3.1 Voltage source converter

The VSC consists of a rectifier, a DC-link and an inverter. In Fig. 2.4 the rectifier is a three-phase diode bridge. In this thesis the rectifier is called a line bridge. The capacitor in the DC-link is the energy storage which supplies the three-phase inverter circuit called a load bridge. The capacitor also filters the DC-voltage. In the load bridge the power can flow from the DC-link to the motor (motoring operation) or from the motor to the DC-link (regenerating operation). Power flow is not possible from the DC-link to the supply network if a diode rectifier is used. Therefore the power must be dissipated in the brake resistor if the load is regenerating.

If the diode rectifier is replaced by an active line bridge, Fig. 2.5, the brake resistor is not needed. The other benefits are sinusoidal currents in the supply network, unity input power factor and the option to compensate the reactive power. In this thesis the VSC used in experimental tests is the type in Fig. 2.4.

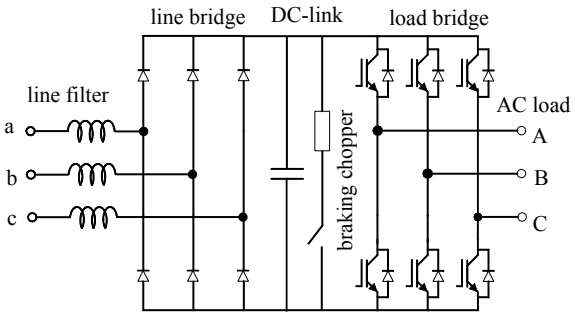

Fig. 2.4 Main circuit of the VSC with a diode rectifier.

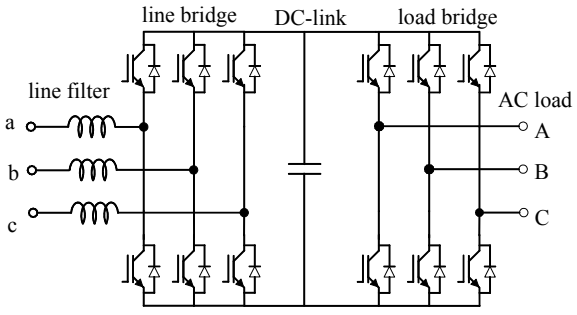

Fig. 2.5 Main circuit of theVSC with an active IGBT-rectifier.

The line filter improves the quality of the input current of the converter. In the case of an active rectifier, Fig. 2.5, simple L filter can be replaced by LCL filter [Oll93]. LCL filter removes high frequency current ripple more efficiently and the dimensions of the filter may be reduced. However, the control of the rectifier with LCL filter is more challenging due to the resonance properties of the filter.

2.3.1.1 Space-vector modulation of the voltage source converter

The PWM signal was formerly generated using carrier based methods. Modulator was realised using analogue devices. Nowadays the modulator is usually implemented using an integrated digital circuit. The modulator algorithm is based on the space-vector theory. In contrast to the carrier based modulators there are no separate modulators for each phase. The space-vector modulator (SVM) calculates the switching times using the space-vector presentation of the stator voltage reference $\underline{u}_{o,ref}$.

The switching functions for output phases are sw_A, sw_B and sw_C. They have a value of 1 if the phase is connected to the positive DC-bus and of -1 if connected to the negative bus. Switching functions are substituted into Equation (2–8) and the result is multiplied by the virtual midpoint of DC-link voltage $u_{DC}/2$. The space-vector presentation of the output voltage is

$$\underline{u}_o = \frac{2}{3}\left(sw_A \frac{u_{DC}}{2} + \left(-\frac{1}{2} + j\frac{\sqrt{3}}{2} \right) sw_B \frac{u_{DC}}{2} + \left(-\frac{1}{2} - j\frac{\sqrt{3}}{2} \right) sw_C \frac{u_{DC}}{2} \right) = \underline{sw}_o \frac{u_{DC}}{2} \quad (2–29)$$

where $\underline{sw}_o$ is the space-vector of the switching functions of the inverter bridge in the stationary reference frame. The possible voltage vectors and the composition of the output voltage reference are illustrated in Fig. 2.6. A three phase, two-level inverter of the VSC, Fig. 2.4, provides six active and two zero voltage vectors. For example, the vector $\underline{u}_2(1,1,-1)$ in Fig. 2.6 means that phases a and b are connected to the positive DC-bus and phase c to the negative bus. Zero voltage vector is achieved by connecting all phases to negative or positive DC-bus. The output voltage reference vector $\underline{u}_{o,ref}$ is sampled with fixed clock frequency and is obtained by switching two adjacent active vectors and zero vectors during the modulation period t_{mod}. $\underline{u}_{o,ref}$ can be written

$$\underline{u}_{o,ref} = d_\kappa \underline{u}_\kappa + d_\lambda \underline{u}_\lambda = \underline{sw}_{o,ave} \frac{U_{DC}}{2} \quad (2–30)$$

where $\underline{sw}_{o,ave}$ is an average switching function (d_λ $\underline{sw}_\lambda$ + d_κ $\underline{sw}_\kappa$) during t_{mod} and U_{DC} is the

average DC-link voltage. Lead vector $\underline{u}_\lambda$ is the next active vector in the direction of rotation and lag vector $\underline{u}_\kappa$ is the active vector behind $\underline{u}_{o,ref}$. Relative durations d_λ and d_κ of the lead and lag vectors respectively are

$$d_\lambda = \underbrace{\frac{\sqrt{3}|\underline{u}_{o,ref}|}{U_{DC}}}_{m} \sin(\theta_o) \tag{2–31a}$$

$$d_\kappa = \underbrace{\frac{\sqrt{3}|\underline{u}_{o,ref}|}{U_{DC}}}_{m} \sin(\frac{\pi}{3} - \theta_o) \tag{2–31b}$$

$$d_{zero} = d_0 + d_7 = 1 - d_\lambda - d_\kappa \tag{2–31c}$$

The coefficient m is called a modulation index. The actual durations are achieved by multiplying d_λ and d_κ by t_{mod}. d_κ, d_λ and zero vectors are taken symmetrically in respect of the centre of the modulation period, Fig. 2.7. $d_\kappa = d_1$ and $d_\lambda = d_2$. θ_o is the angle between a voltage reference vector $\underline{u}_{ref}$ and lag vector, Fig. 2.6. In the literature half of t_{mod} is usually analysed instead of the full modulation period. In this thesis vector durations are calculated for t_{mod} to make the equations comparable to those of matrix converters.

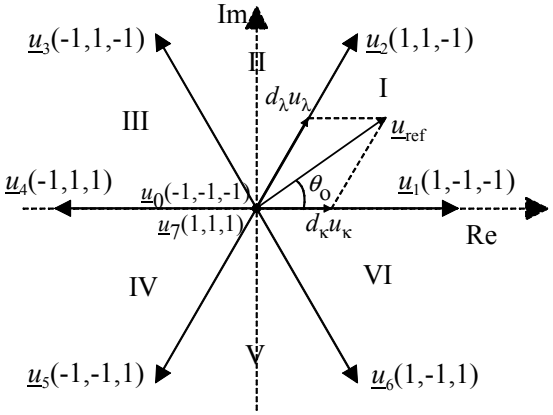

Fig. 2.6 Voltage vectors of VSI. $\underline{u}_{o,ref}$ is formed in sector I.

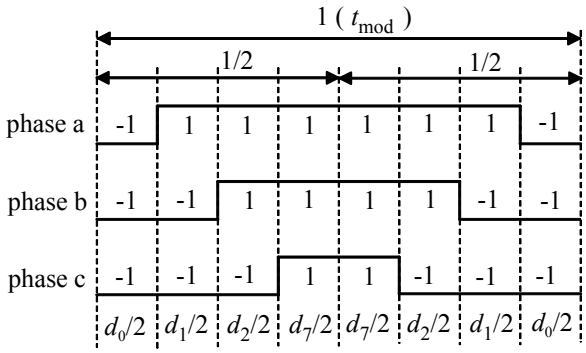

Fig. 2.7 Vector placements during one modulating period in the first voltage sector.

If the modulation index $m \leq 1$ the amplitude of the voltage reference vector $\underline{u}_{o,ref}$ equals the mean output voltage during t_{mod}. The modulation is then said to be linear, meaning $|\underline{u}_{o,ref}| \leq U_{DC}/\sqrt{3}$. In this thesis the modulation is performed only in the linear range, $0 \leq m \leq 1$.

The durations of u_7(1,1,1) and u_0(-1,-1,-1) and their placements are dependent on the modulation strategy. In this thesis the placement of the zero vector of the voltage source inverter (VSI) is symmetrical, Fig. 2.7. Each half modulation period begins and ends at the zero vector. The active vector is chosen so that the state of switches in only one phase has to

be changed during the vector transition. In linear modulation range this method has a harmonic performance and maximum output voltage rather similar to conventional carrier based PWM methods with third harmonic injection, [Hol03].

If the VSC is loaded the voltage over DC-link capacitor is the average of the three phase diode rectifier output: $U_{DC} = (3\sqrt{2}/\pi)\times U_{LL,supply}$ (540 V in the case of 400 V supply network). The maximum output/input voltage ratio of the VSC in the case of linear modulation is $(U_{DC}/\sqrt{3})/(U_{LL,supply}/\sqrt{3/2}) = 3/\pi \approx 0.955$. With active rectifier, Fig. 2.5, the output voltage is limited by the maximum voltage of the DC-link capacitor and switching components.

2.3.1.2 Current commutation

In the case of VSI the upper and lower switches of one output phase cannot be conducting at the same time because the DC-link would be short circuited. This is prevented by a dead time. During the dead time both switches of the phase are opened and the diodes allow safe conducting paths for current. The commutation between switches is always forced and the control of switches requires no information about currents. The commutation is illustrated in Fig. 2.8, where the active voltage vector of the VSI is changed from vector $\underline{u}_1$ to $\underline{u}_2$. The conducting components are drawn as a straight line.

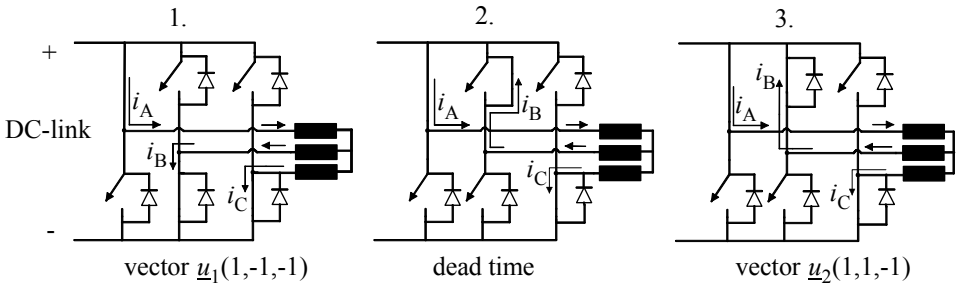

Fig. 2.8 Current commutation between switches in a voltage source inverter.

2.3.2 Matrix converter

Fig. 2.9a illustrates a conventional 3×3 matrix converter topology [Ven80] where nine bi-directional switches are implemented using IGBTs. This topology is also called a direct matrix converter (DMC). The conventional vector modulated DMC, may be replaced by a vector modulated indirect matrix converter (IMC), which consists of separated line and load bridges as presented in Fig. 2.9b, [Min93], [Iim97], [Mur01], [Wei01]. This structure is also called a two-stage matrix converter. In the IMC there are only six active bi-directional switches instead of nine in the DMC. The load bridge of the IMC is a conventional inverter

bridge of a voltage source converter. In theory DMC and IMC have similar properties. However, the performance of these two topologies is not identical. The differences are discussed in the following sections.

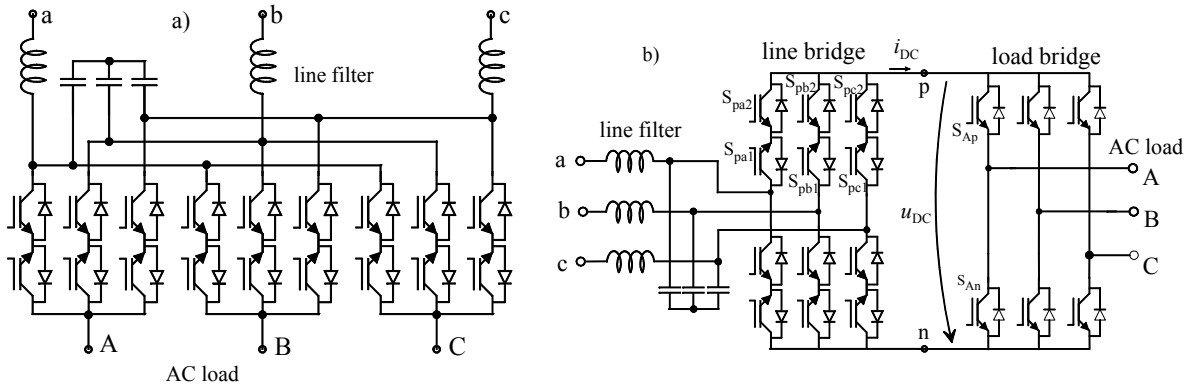

Fig. 2.9 a) Direct matrix converter (DMC), b) Indirect matrix converter (IMC).

Every input phase of the matrix converter can be connected to any of the output phases. Power flow in both directions requires that the switches are bi-directional. Normally, the MC is fed by a voltage source and, for this reason, the input phases a,b,c should not be short circuited. If the MC supplies an AC machine which is an inductive load the output phases A,B,C must never be opened.

In theory nine switches of 3×3 MC have 2^9 switching states. The aforementioned constraints limit the possible switching states to 27. The line filter of the MC is usually an LC circuit. The capacitors provide paths for the currents of the input phases when the phase is not connected to load. Multistage LC has also been investigated but the simple LC filter is found to be the best alternative considering cost and size [Whe94].

In the following sections the structure and control of bi-directional switches of MC are discussed. Current commutation of MC and VSI are compared. A space-vector modulator for the matrix converter is presented using "fictitious DC-link" method.

2.3.2.1 Bi-directional switches

In this study the bi-directional switch is implemented using IGBTs. Fig. 2.10 illustrates three switch combinations [Nie96], [Whe02], [Jus05]. Fig. 2.10a shows a common emitter configuration with a central connection. This switch structure is available as an integrated IGBT module. The benefit of the integrated structure is the minimised stray inductance.

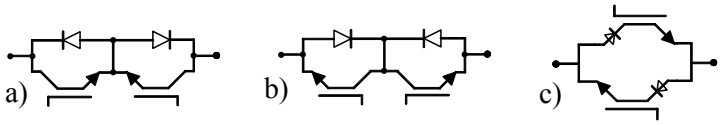

Fig. 2.10 Bidirectional switch cells: a) common emitter, b) common collector, c) reverse blocking IGBT.

Fig. 2.10b illustrates the common collector configuration. The conduction losses are the same as for the common emitter configuration. Using the common collector configuration the number of isolated power supplies can be minimised [Whe02]. Six isolated supplies are needed if the emitters of three IGBTs connected to each input and output phase are connected to the same potential. In the case of common emitter switch cell nine isolated supplies are required. However, if the emitter of three IGBT is connected to the same potential the stray inductances can cause problems due to the long connections. This is naturally a problem only if the MC is implemented using discrete components. If the full matrix converter circuit is integrated into one module the stray inductances are small and the common collector configuration is a more attractive switch cell structure than the common emitter configuration [Bru01].

Fig. 2.10c illustrates a switch cell with two reverse blocking IGBTs [Lin01], [Ito04] connected in antiparallel. This could be the switch cell commonly used in the near future if reverse blocking IGBTs are further developed.

2.3.2.2 Current commutation

In the MC a short circuit between input phases must be avoided and the output phases (load phases) must be always connected to some of three input phases. Thus the commutation must be actively controlled at all times with respect to these basic rules. Each group of three bi-directional switches connected to each output phase, Fig. 2.9a, is controlled independently in a such way that the input is not short circuited and the load phases are not opened. This requires rather complicated commutation strategies compared to VSI.

The commutation is first explained for direct topology (DMC). Commutation techniques are based on the knowledge of the load current direction [Whe02] or the knowledge of the voltage over bi-directional switch [Emp98], [Whe04]. An attempt is made to solve the commutation problem using soft switching techniques but these methods increase the component count and conduction losses [Whe02]. In this thesis only the load current direction based commutation methods are discussed.

The first load current direction based method was the four-step commutation [Bur89]. The four-step commutation from input phase a to input phase b in the case of load phase A is shown in Fig. 2.11. Similar principles also hold for switches of phases B and C.

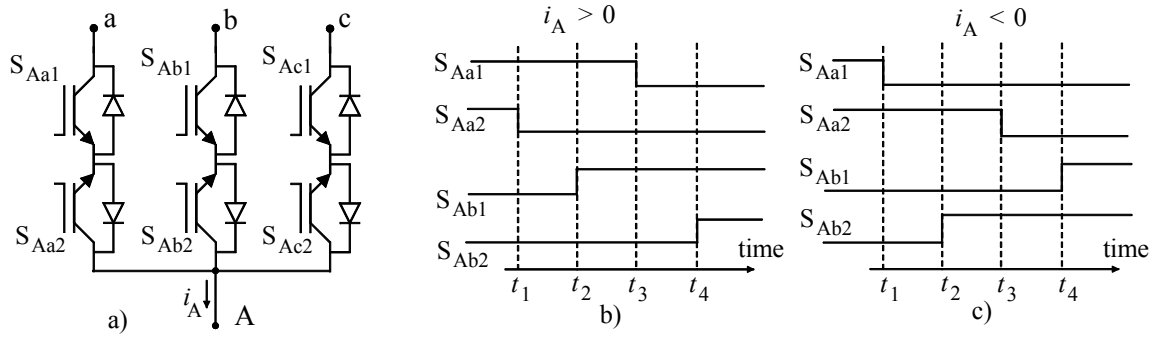

Fig. 2.11 Four-step commutation. a) Switch group of output phase A, b) timing diagram for gate signals, positive load current, c) timing diagram for gate signals, negative load current.

In Fig. 2.11a the positive current direction is from input (a,b,c) to output A. If $i_A > 0$, Fig. 2.11b, the commutation process begins at the instant t_1 when switch S_{Aa2} is turned off. S_{Aa2} is not conducting. The next step (t_2) is to ensure a conducting path for the current from input phase b) by turning S_{Ab1} on. If $u_b > u_a$ the current commutates naturally between phases a and b at this point. If $u_b < u_a$ the commutation is forced at the instant t_3 when S_{Aa2} is turned off. The last step (t_4) is to turn S_{Ab2} on to allow current reversals. Fig. 2.11c shows the timing diagram in the case of negative i_A. The delays between the switching instants are dependent on the characteristics of the semiconductor devices used in the bi-directional switches.

The four-step commutation can be reduced to three-step if $t_2 = t_3$. S_{Aa1} is turned off at the same instant as S_{Ab1} is turned on. This method requires that the turn-off delay of the switch device is longer than the turn-on delay [Whe04]. In the opposite case the conduction path opens and an overvoltage occurs. In the two-step strategy [Swe91], [Emp98] only the conducting component of the bi-directional switch is turned on. Thus no switching at instants t_1 and t_4 is performed. One-step strategy is similar to two-step but there is no delay between the switching of S_{Aa1} and S_{Ab1}. Similar to three step strategy, this requires the turn-off time to be longer than the turn-on time. In this thesis the four-step commutation is applied.

Indirect matrix converter

The indirect matrix converter, Fig. 2.9b, can be considered as a 3×2 matrix converter and voltage source inverter connected in series. The output voltage between two phases of the line bridge (3×2 DMC) is controlled to be a DC voltage. Thus the voltage between the two outputs can be considered as a DC-link even if there is no energy storage. IMC produces a three phase output voltage from DC-link similar to VSI. The commutation of the line bridge of the IMC is performed using similar principles as explained for the DMC. The difference is that the input phases a,b,c are not connected to the load phases directly but to the two DC-buses. The commutation of the VSI was explained above and it is similar to the commutation of the load

bridge of the IMC.

2.3.2.3 Space-vector modulation of the matrix converter

Several modulation strategies have been proposed for the matrix converter. The most important methods are discussed and references given in [Whe02]. In this thesis only the space-vector modulation [Hub89], [Hub95], [Nie96], [Cas02], [Jus05] is discussed.

The direct matrix converter (DMC) has 27 allowed switching states [Hub95]. The allowed states can be classified into three groups [Whe02].

Group I: Each output phase A,B,C is connected to a different input phase a,b,c. These vectors rotate at the frequency of the supply network and have a constant amplitude.

Group II: Two output phases are connected to a common input line and the remaining one is connected to one of the other input lines. These space-vectors have a fixed direction but varying amplitude.

Group III: All output phases are connected to the same input phase. The output vectors have zero amplitude.

In the SVM method discussed in this study the Group I vectors are not used. The desired output voltage is synthesized from Group II active vectors and Group III zero vectors.

The SVM is also called an indirect modulation method because it is often derived using ideal IMC topology, Fig. 2.12, with "fictitious DC-link". This is possible if the vectors of

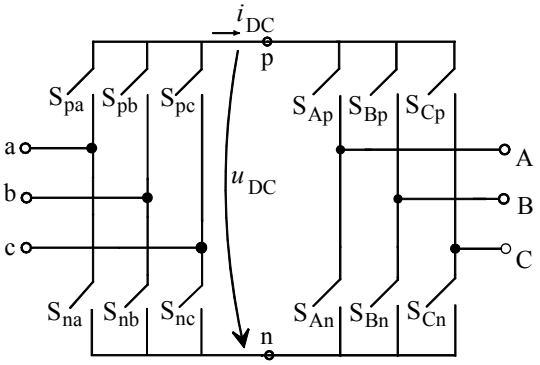

Fig. 2.12 Ideal IMC used in the space-vector modulation analysis.

Group I are not used. The line and load bridges are analysed separately and finally the results are combined. The input voltages and voltage references of the load are assumed to be constant during one modulation period.

Line bridge

Let us first define switching functions sw_a, sw_b, sw_c for each input phase. They can have values –1, 0 and 1. $sw_a = 0$ means that the input phase a is not connected to DC-bus. $sw_a = 1$ means that the phase a is connected to bus p, which means the ideal switch S_{pa}, Fig. 2.12, is

conducting. If $sw_a = -1$ the S_{na} is conducting. The same principles also hold for phases b and c. To prevent the short circuit only one input phase can be connected to each bus. Thus

$$sw_a + sw_b + sw_c = 0 \tag{2–32}$$

The phase currents are: $i_a = sw_a i_{DC}$, $i_b = sw_b i_{DC}$, $i_c = sw_c i_{DC}$. Using (2–8) the space-vector of the input current in stationary reference frame is

$$\underline{i}_i = (2/3)\left(sw_a i_{DC} + \left(-\frac{1}{2} + j\frac{\sqrt{3}}{2}\right) sw_b i_{DC} + \left(-\frac{1}{2} - j\frac{\sqrt{3}}{2}\right) sw_c i_{DC} \right) = \underline{sw}_i i_{DC} \tag{2–33}$$

The combinations allowed by (2–32) are illustrated in Fig. 2.13 for positive and negative i_{DC}. For example $\underline{i}_1(1,0,-1)$ means $sw_a = 1$, $sw_b = 0$, $sw_c = -1$.

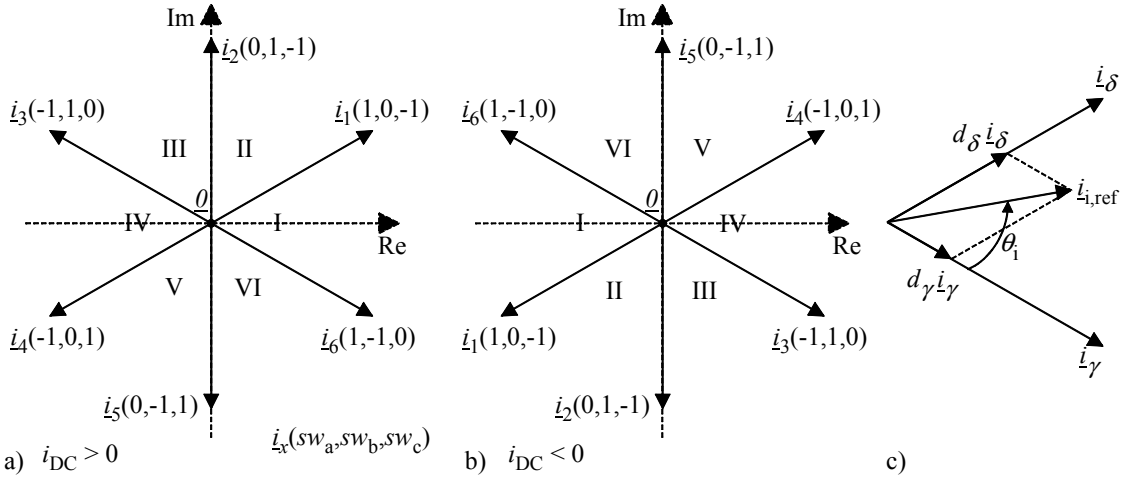

Fig. 2.13 Input current sectors and allowed switching state vectors for a) $i_{DC} > 0$, b) $i_{DC} < 0$, c) composition of the current vector in sector I.

The current reference vector $\underline{i}_{i,ref}$ is sampled with fixed clock frequency and is obtained by switching two adjacent active vectors during the modulation period t_{mod}, Fig. 2.13c. Thus the main principle is similar compared to the composition of the voltage vector in the case of VSC, Fig. 2.6. The input current vector during t_{mod}, Fig. 2.13c, can be written

$$\underline{i}_{i,ref} = d_\gamma \underline{i}_\gamma + d_\delta \underline{i}_\delta \tag{2–34}$$

where $d_\gamma = \frac{|\underline{i}_{i,ref}|}{|i_{DC}|}\sin\left(\frac{\pi}{3} - \theta_i\right)$, $d_\delta = \frac{|\underline{i}_{i,ref}|}{|i_{DC}|}\sin(\theta_i)$

d_γ and d_δ are relative on-durations for active current vectors. γ and δ denote lag and lead vector respectively.

If the line bridge is ideal the DC-link power is $(3/2)\mathrm{Re}\{\underline{u}_i \underline{i}_i^*\} = u_{DC} i_{DC}$ [Vas92]. $\underline{u}_i$ is the space-vector representing the three-phase input voltage. The input current vector from (2–33)

is substituted into the expression of the DC-link power and both sides are divided by i_{DC}. The instantaneous DC-link voltage can be written as

$$u_{DC} = \frac{3}{2}\mathrm{Re}\left\{\underline{u}_i \underline{sw}_i^*\right\} \tag{2–35}$$

The average of the switching function vector $\underline{sw}_i$ during a modulation period t_{mod} is the sum of two vectors, Fig. 2.13c, $\underline{sw}_{i,ave} = d_\gamma \underline{sw}_{i,\gamma} + d_\delta \underline{sw}_{i,\delta}$. The average DC-link voltage during t_{mod} can be written

$$U_{DC} = \frac{3}{2}\mathrm{Re}\left\{\underline{u}_i \underline{sw}_{i,ave}^*\right\} = \frac{3}{2}\left(d_\gamma \mathrm{Re}\left\{\underline{u}_i \underline{sw}_{i,\gamma}^*\right\} + d_\delta \mathrm{Re}\left\{\underline{u}_i \underline{sw}_{i,\delta}^*\right\}\right) \tag{2–36}$$

Load bridge

The load bridge in Fig. 2.12 is the same circuit as the VSI. Therefore Equations (2–30)-(2–31) also hold for the load bridge of the IMC. In this thesis the zero vector placement of the MC is not the same as that used with VSI, Fig. 2.7. The switching strategy of the MC is explained later in this section. The active output voltage vectors of the IMC and the composition of $\underline{u}_{o,ref}$ are presented in Fig. 2.14.

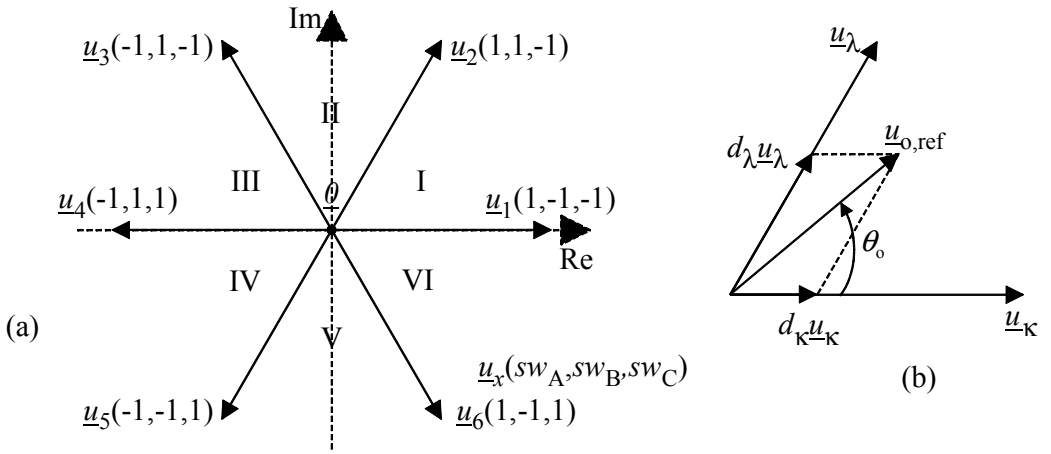

Fig. 2.14 a) Output voltage vectors, b) composition of the output voltage in sector I.

Synthesis of the line and load bridges

The space-vector modulation of the MC is achieved by combining the equations of the line and load bridges [Hub95]. During t_{mod} the reference voltage vector $\underline{u}_{o,ref}$ (2–30) is composed of two active vectors, Fig. 2.14. Similarly the average output switching function during t_{mod} is: $\underline{sw}_{o,ave} = d_\kappa \underline{sw}_\kappa + d_\lambda \underline{sw}_\lambda$. When $\underline{sw}_o$ is replaced by $\underline{sw}_{o,ave}$ in (2–29) and the expression of U_{DC} (2–36) is substituted into (2–29) the average output voltage during t_{mod} can be written

$$\begin{aligned}\underline{u}_{\mathrm{o,ave}} &= \frac{3}{4}\underline{sw}_{\mathrm{o,ave}}\left(d_\gamma \,\mathrm{Re}\left\{\underline{u}_\mathrm{i}\,\underline{sw}_\gamma^*\right\} + d_\delta \,\mathrm{Re}\left\{\underline{u}_\mathrm{i}\,\underline{sw}_\delta^*\right\}\right) \\ &= \frac{3}{4}\left(d_\kappa d_\gamma \underline{sw}_\kappa \,\mathrm{Re}\left\{\underline{u}_\mathrm{i}\,\underline{sw}_\gamma^*\right\} + d_\kappa d_\delta \underline{sw}_\kappa \,\mathrm{Re}\left\{\underline{u}_\mathrm{i}\,\underline{sw}_\delta^*\right\} + d_\lambda d_\gamma \underline{sw}_\lambda \,\mathrm{Re}\left\{\underline{u}_\mathrm{i}\,\underline{sw}_\gamma^*\right\}\right. \\ &\left. + d_\lambda d_\delta \underline{sw}_\lambda \,\mathrm{Re}\left\{\underline{u}_\mathrm{i}\,\underline{sw}_\delta^*\right\}\right)\end{aligned} \tag{2–37}$$

If the load bridge is ideal $\underline{u}_{\mathrm{o,ave}} = \underline{u}_{\mathrm{o,ref}}$. Now the direct relation between output and input voltage is obtained. It can be seen from (2–37) that the output voltage is composed using four active voltage vectors. There are two DC voltage levels, $(3/4)\mathrm{Re}\{\underline{u}_\mathrm{i}\underline{sw}_\gamma^*\}$ and $(3/4)\mathrm{Re}\{\underline{u}_\mathrm{i}\underline{sw}_\delta^*\}$. The output voltage is obtained using both of them with load bridge states $\underline{sw}_\kappa$ and $\underline{sw}_\lambda$. The relative on-durations of the active vectors are

$$\begin{aligned} d_{\kappa\gamma} &= d_\kappa d_\gamma = m\sin(\pi/3-\theta_\mathrm{o})\sin(\pi/3-\theta_\mathrm{i}) \\ d_{\kappa\delta} &= d_\kappa d_\delta = m\sin(\pi/3-\theta_\mathrm{o})\sin(\theta_\mathrm{i}) \\ d_{\lambda\gamma} &= d_\lambda d_\gamma = m\sin(\theta_\mathrm{o})\sin(\pi/3-\theta_\mathrm{i}) \\ d_{\lambda\delta} &= d_\lambda d_\delta = m\sin(\theta_\mathrm{o})\sin(\theta_\mathrm{i}) \end{aligned} \tag{2–38}$$

The time reserved for zero vectors is

$$d_0 = 1 - d_{\kappa\gamma} - d_{\kappa\delta} - d_{\lambda\gamma} - d_{\kappa\delta} \tag{2–39}$$

Maximum output voltage

The maximum output voltage of the MC can be calculated using (2–36). Fundamental frequency components of the input voltage and the average switching function $\underline{sw}_{\mathrm{i,ave}}$ are used. $\omega_1 t$ is the angle of the fundamental frequency input voltage vector $\underline{u}_{\mathrm{i,1}}$. The angle of the fundamental frequency input current $\underline{i}_{\mathrm{i,1}}$ and average switching function $\underline{sw}_{\mathrm{i,ave}}$ is then $\omega_1 t$ - $\varphi_{\mathrm{i,1}}$ where $\varphi_{\mathrm{i,1}}$ is the fundamental displacement angle of the input. The average DC-link voltage during t_{mod} is

$$U_{\mathrm{DC}} = \frac{3}{2}\mathrm{Re}\left\{\left|\underline{u}_{i,1}\right| e^{j\omega_1 t}\left|\underline{sw}_{\mathrm{i,ave}}\right| e^{-j\omega_1 t+\varphi_{\mathrm{i,1}}}\right\} \tag{2–40}$$

$|\underline{sw}_{\mathrm{i,ave}}|$ denotes current ratio $|\underline{i}_{\mathrm{i,1}}|/i_{\mathrm{DC}}$ which cannot have values greater than unity. Thus the average DC-link voltage during t_{mod} in the case of unity ($|\underline{i}_{\mathrm{i,1}}|/i_{\mathrm{DC}}$) is

$$U_{\mathrm{DC}} = \frac{3}{2}\left|\underline{u}_{\mathrm{i,1}}\right|\cos(\varphi_{\mathrm{i,1}}) \tag{2–41}$$

The maximum value of the modulation index ($m = \sqrt{3}\,|\underline{u}_{\mathrm{o,ref}}|/U_{\mathrm{DC}}$) of the load bridge is unity in linear modulation (see Section 2.3.1.1). If (2–41) is substituted into the equation of the

duration of the active output vector of the VSI (2–31) the modulation index m can be written:

$$m = \frac{2\left|\underline{u}_{\mathrm{o,ref}}\right|}{\sqrt{3}\left|\underline{u}_{\mathrm{i,1}}\right|\cos\varphi_{\mathrm{i,1}}} \tag{2–42}$$

Thus the maximum theoretical output/input voltage ratio in the case of linear modulation is $\sqrt{3}/2 \approx 0.866$ (m = 1) and is achieved when the displacement power factor of the input is unity. In this thesis $\cos\varphi_{\mathrm{i,1}}$ = 1. In the case of VSC with diode rectifier the maximum output/input voltage ratio is approximately 0.95 [Hol03].

Switching strategy

In this study the switching states during one modulation period are arranged applying the following principles [Jus05], [Nie96]:

1. Only one output phase changes its state when the switching state vector is changed.
2. Active vectors are taken symmetrically in respect of the centre of the modulation period.
3. Zero vector is taken in the middle of the modulation period.

This strategy gives small switching losses. [Cha03] has presented a strategy where the losses are further reduced.

Now the zero vector is not divided as was the case with VSC, Fig. 2.7. The strategy is clarified in Table 1. Examples of four current and voltage sector combinations are presented.

Let us consider the case when the input current vector and the output voltage vector are in sector I. It can be seen in Fig. 2.13 and Fig. 2.14 that the state $\underline{sw}_{\kappa\gamma}$ connects output phase A to input phase a. B and C are connected to b. This state is denoted abb (state 1 in Table 1). State $\underline{sw}_{\lambda\gamma}$ gives aab and so on. This is illustrated in Fig. 2.15. It is important to note that if the sum of the current and voltage sectors is an odd number, the order of load bridge switching states is changed. The output zero vector requires no changes in switches of the fictitious line bridge because the conducting path of the input current is opened anyway when all output phases are connected to the same bus, Fig. 2.15.

In [Apa03], [Cas02] the zero vector of MC is divided into three parts. In that case every $t_{\mathrm{mod}}/2$ period begins and ends with zero vector. This method was already explained in the case of VSI in Section 2.3.1. This strategy decreases the high frequency harmonics in the input and low frequency harmonics in the output [Apa03]. It also increases the switching losses compared to zero vector placement of Table 1 because the number of switching events is increased.

Table 1. Switching states and on-durations in four cases during one modulation period.

u_{sec}	i_{sec}	state 1	state 2	state 3	state 4	state 5	state 6	state 7	state 8	state 9
I	I	abb	aab	aac	acc	ccc	acc	aac	aab	abb
I	II	aac	acc	bcc	bbc	bbb	bbc	bcc	acc	aac
II	I	bab	aab	aac	cac	ccc	cac	aac	aab	bab
II	III	cbc	bbc	bba	aba	aaa	aba	bba	bbc	cbc
durations		$t_{\gamma(\kappa,\lambda)}/2$	$t_{\gamma(\lambda,\kappa)}/2$	$t_{\delta(\lambda,\kappa)}/2$	$t_{\delta(\kappa,\lambda)}/2$	t_0	$t_{\delta(\kappa,\lambda)}/2$	$t_{\delta(\lambda,\kappa)}/2$	$t_{\gamma(\lambda,\kappa)}/2$	$t_{\gamma(\kappa,\lambda)}/2$
Input vector		$\underline{sw}_\gamma$		$\underline{sw}_\delta$					$\underline{sw}_\gamma$	
Output vector: odd ($u_{sec}+i_{sec}$)		sw_λ	$\underline{sw}_\kappa$		$\underline{sw}_\lambda$	$\underline{0}$	$\underline{sw}_\lambda$	$\underline{sw}_\kappa$		$\underline{sw}_\lambda$
Combined state		$\underline{sw}_{\lambda\gamma}$	$\underline{sw}_{\kappa\gamma}$	$\underline{sw}_{\kappa\delta}$	$\underline{sw}_{\lambda\delta}$	$\underline{0}$	$\underline{sw}_{\lambda\delta}$	$\underline{sw}_{\kappa\delta}$	$\underline{sw}_{\kappa\gamma}$	$\underline{sw}_{\lambda\gamma}$
Output vector: even ($u_{sec}+i_{sec}$)		$\underline{sw}_\kappa$	$\underline{sw}_\lambda$		$\underline{sw}_\kappa$	$\underline{0}$	$\underline{sw}_\kappa$	$\underline{sw}_\lambda$		$\underline{sw}_\kappa$
Combined state		$\underline{sw}_{\kappa\gamma}$	$\underline{sw}_{\lambda\gamma}$	$\underline{sw}_{\lambda\delta}$	$\underline{sw}_{\kappa\delta}$	$\underline{0}$	$\underline{sw}_{\kappa\delta}$	$\underline{sw}_{\lambda\delta}$	$\underline{sw}_{\lambda\gamma}$	$\underline{sw}_{\kappa\gamma}$
		← $t_{mod}/2$ →					← $t_{mod}/2$ →			

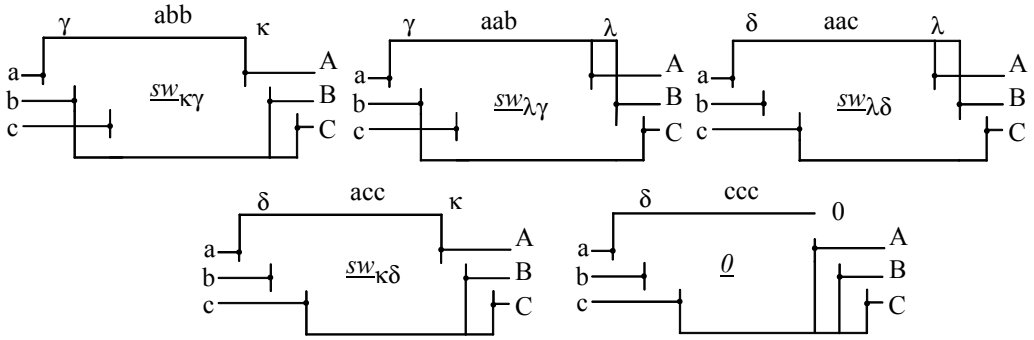

Fig. 2.15 Switching states of MC during $t_{mod}/2$. u_{sec} = I and i_{sec} = I (Table 1).

Indirect matrix converter

The analysis presented above was for the DMC topology, Fig. 2.9a. The line and load bridges are fictitious for DMC but real circuits in the case of IMC, Fig. 2.9b. If the switches are ideal both topologies have similar performance. In practice the losses and output waveforms of DMC and IMC are not identical. The on-state losses of the IMC are higher because there are more components in the current path, Fig. 2.9. In DMC the output voltage is composed by switching the sinusoidal line-to-line supply voltages. In IMC the output voltage is formed from DC-link voltage which has a PWM waveform. In the case of the IMC the zero vector is formed by connecting all the load phases to the upper or lower DC bus. During the zero vector the input current vector is active (2–33) but i_{DC} is zero because the output phases are connected to the same bus, Fig. 2.15.

2.4 Comparison of non-ideal properties of VSC and MC

In the ideal case the voltage reference vector $\underline{u}_{o,ref}$ equals the mean output voltage produced during each modulation period. This requires linear modulation range and ideal components in the main circuit. In practice the voltage drop over semiconductors causes power losses and distorts the output waveform of the converter. The necessary switching strategies (dead times and overlapping times) to prevent short circuits and overvoltages are the other source of distortion. In this section these non-ideal properties of the voltage source converters and matrix converters are compared.

In many sensorless control methods the motor input voltage should be known as accurately as possible. The PWM voltage is not usually measured because the number of sensors would be increased and the sampling rate is limited. Therefore the estimator algorithms use the voltage reference vector as the output voltage information. The differences between $\underline{u}_{o,ref}$ and the true output voltage in the VSCs and MCs are studied in this section. Power losses are briefly discussed.

Modelling of the non-linear properties of the voltage source inverter bridge has been widely studied in the literature [Hol02], [Mun99], [Hol02]. Therefore only the basic principles are presented here. The non-linear properties of DMC have been studied in [Lee04b] but IMC has not been analysed earlier. Jussila and the author have compared the non-linear properties of DMC and IMC using a vector form in [Jus06].

2.4.1 Non-linear model of the bi-directional switch

Fig. 2.16 shows the forward characteristics of SKM75GA123D IGBT module. This module is used in the DMC prototype (Appendix B) and in the line bridge of the IMC prototype. In the analysis of the non-linear properties of the VSI and MC, diodes and IGBTs are linearized using a constant threshold voltage U_{th} and constant resistance r_d, Fig. 2.16. In the literature [Mun99], [Hol02] the average value of the IGBT and the diode U_{th} and r_d are used. Therefore only one value for U_{th} and r_d is needed. This simplification is also done in this thesis.

In the DMC and in the line bridge of the IMC the bi-directional switches contain an IGBT and a diode connected in series. Therefore U_{th} and r_d are threshold voltages and resistances for two devices connected in series. In the load bridge of the IMC and in the VSI U_{th} and r_d are for one device. To avoid confusion between MC topologies U_{th} and r_d are denoted as $U_{th,i}$, $r_{d,i}$ in the line bridge of the IMC. The load bridge quantities of the IMC are marked $U_{th,o}$, $r_{d,o}$.

In this study the 5 kVA prototype MCs feed a 3.5 kW PMSM, Appendix A. Due to the low power level the operating area is in the non-linear part of the Fig. 2.16. The selection of U_{th} and r_d for the simulation model is therefore rather difficult.

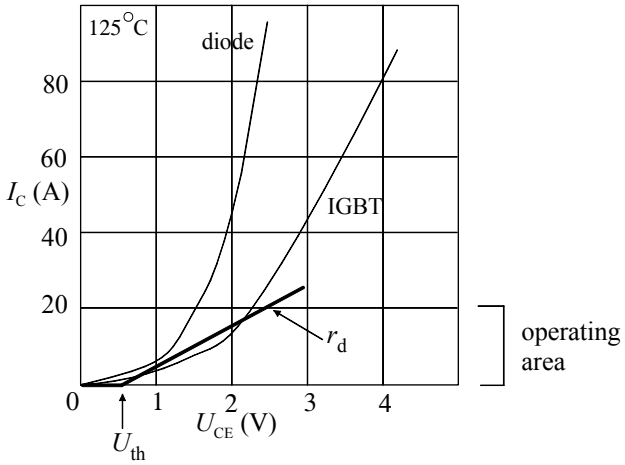

Fig. 2.16 Forward characteristics of the power devices in SKM75GA123D module.

2.4.2 Non-linear model of the VSI

Fig. 2.17a illustrates the control of phase A of the VSI. A short circuit is avoided using a delay t_d called dead time. The block t_d in Fig. 2.17a delays the rising edges of the signals controlling the switches S_{Ap} and S_{An}.

The gate signal, on and off durations of the switches of phase A, are shown in Fig. 2.17b during one modulation period. The voltage between the output and fictitious central point 0 of the DC-link is also shown in the case of negative and positive current directions. U_d and U_I denote an on-state voltage drop over diode and IGBT respectively. Let us consider the case $i_A < 0$. In the beginning S_{An} conducts i_A to bus n. During the first half of t_{mod} S_{An} is turned off and after dead time t_d S_{Ap} is turned on. The output A is connected to negative bus via S_{An} until the current is commutated from S_{An} to diode d_p. The commutation is complete after the turn off delay t_{off}. When phase A is connected to the negative bus via S_{An} the voltage $U_{A0} = -U_{DC}/2 + U_I$. When i_A flows to a positive bus through d_p: $U_{A0} = U_{DC}/2 + U_d$. The next transition begins when sw_a changes its state from 1 to -1. d_p conducts until the dead time and the turn-on delay t_{on} of S_{An} are over. Finally the output A is again connected to a negative bus via S_{an}. The rate of change of the voltage over the semiconductors is assumed to be infinite.

It can be seen in Fig. 2.17b that with a negative current the area above the zero voltage level is increased compared to the desired voltage pulse $U_{A0,ref}$. For positive current the area is decreased by the same amount. In the analysis the average on-state voltage drop $(U_d + U_I)/2$ is used [Hol02] and is denoted $U_{on} = U_{th} + r_d i$. The difference between U_d and U_I is assumed to

have a vanishing effect on the voltage error [Mun99].

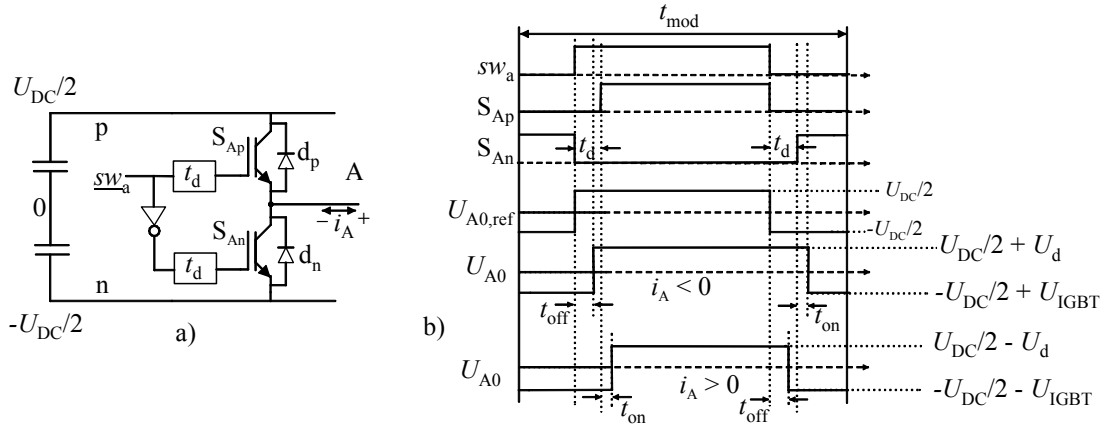

Fig. 2.17 a) Control of output phase A of the VSC, b) On and Off times during t_{mod}.

Using Fig. 2.17, it is possible to write the expression for the average voltage error between the ideal and the actual phase voltages during one modulation period.

$$sw_A \frac{U_{DC}}{2} - u_{A0} = \Delta_{uA} = \text{sign}(i_A)\left(\underbrace{\frac{\overbrace{t_d + t_{on} - t_{off}}^{U_{dead}}}{t_{mod}} U_{DC} + U_{th}}_{\text{non-linear part}}\right) + r_d i_A \tag{2–43}$$

The voltage error Δ_{uA} is caused by the dead time $U_{dead} = U_{DC}(t_d + t_{on} - t_{off})/t_{mod}$ and on-state voltage drop over the semiconductors. The on-state voltage drop is also a function of temperature because parameters U_{th} and r_d are temperature dependent.

Expressions similar to (2–43) can also be written for phases B and C. If they are substituted into (2–6) a voltage error vector in the stationary reference frame can be written:

$$\begin{aligned} \underline{\Delta}_u &= \frac{2}{3}\left(U_{dead} + U_{th}\right)\left(\text{sign}(i_A) + e^{j2\pi/3}\text{sign}(i_B) + e^{j4\pi/3}\text{sign}(i_C)\right) + r_d \underline{i}^s \\ &= \underbrace{\frac{4}{3}\left(U_{dead} + U_{th}\right)\underline{\text{sec}\,i}^s}_{\text{non-linear part}} + r_d \underline{i}^s \end{aligned} \tag{2–44}$$

$$\text{where } \underline{\text{sec}\,i}^s = 1/2\left(\text{sign}(i_A) + e^{j2\pi/3}\text{sign}(i_B) + e^{j4\pi/3}\text{sign}(i_C)\right)$$

$\underline{\text{sec}\,i}^s$ is the current sector indicator. Its magnitude is unity and it has six discrete locations in the complex plane.

In sensorless control methods based on the model of the PMSM, r_d can be taken into account by increasing the stator resistance of the model. The non-linear part $U_{dead} + U_{th}$ is a more problematic disturbance. It distorts the output voltage waveform and causes a voltage drop which is difficult to compensate. Compensation can be achieved by a separate inverter model [Hol02]. However, accurate compensation is difficult to achieve due to the temperature

dependency and non-linear nature of semiconductors, Fig. 2.16.

Fig. 2.18 illustrates the effect of the non-linear properties of the VSI. The resistive voltage drop is omitted. Fig. 2.18a shows the voltage drop in one phase (2–43). The real and imaginary parts of the non-linear voltage vector in the stationary reference frame and the length of the vector are shown in Fig. 2.18b, c. In the simulations of Fig. 2.18 $(t_d+t_{on}-t_{off})/t_{mod}$ = 0.003, U_{th} = 0.3 V and U_{DC} = 540 V.

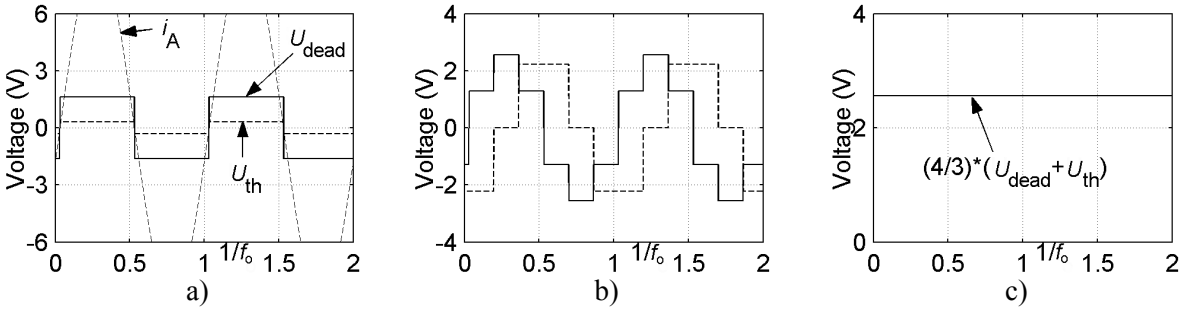

Fig. 2.18 a) Voltage components in one phase caused by the U_{dead} and U_{th}. b) Components of the non-linear voltage vector in stationary reference frame. c) Length of the voltage vector.

2.4.3 Non-linear model of the IMC

In the VSI the source voltage for the load is the DC-link voltage. In the matrix converter the source voltages are the line-to-line voltages of the supply network. In the case of the IMC the voltage errors of the line and load bridges are discussed separately.

2.4.3.1 Line bridge

The commutation of the current in the line bridge of the IMC is illustrated in Fig. 2.19. Fig. 2.19a shows the four-step commutation in the switch group of bus p between phases a and b in the input current sector 2, Fig. 2.13, in the case of positive current direction in the DC-link. The positive current direction is from the line side to the load, Fig. 2.12. Fig. 2.19b shows the same with a negative i_{DC}. In sector 2 the bus n is connected to the phase c and the positive bus p is connected either to phase a or b. The switches S_{pa1}, S_{pa2}, S_{pb1}, S_{pb2} of the input phases were illustrated in Fig. 2.9b.

As discussed earlier, the commutation is forced or natural depending on the values of phase voltages taking part in the process. During one modulation period one commutation is natural and the other is forced. If the commutation is forced the connection of bus p and the new phase is delayed by the overlapping time t_c plus the turn-off delay t_{off}. In natural commutation the current transfers to the new phase after turn-on delay t_{on}. In Fig. 2.19 the on-state voltage drop of the bi-directional switch is denoted as U_{on} and consists of the threshold

voltage $U_{\mathrm{th,i}}$ and resistive voltage drop $r_{\mathrm{d,i}}i_{\mathrm{DC}}$.

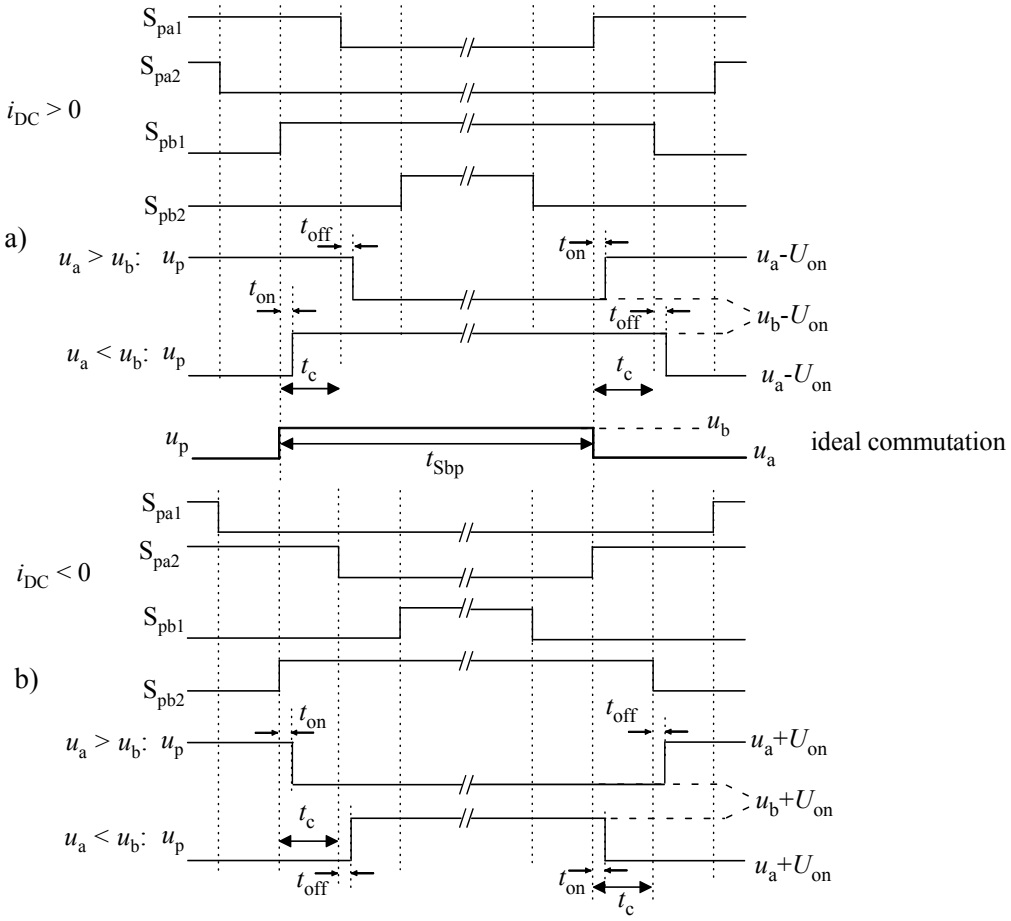

Fig. 2.19 Four-step commutation in switch group of bus p between phases a and b in current sector 2. a) i_{DC} flows in a positive direction, b) i_{DC} flows in a negative direction. t_{Sbp} denotes the desired time when bus p is connected to phase b.

The average voltage error during one modulation period between the ideal and real DC-link voltage can be defined by subtracting the voltage with losses and delays from ideal p bus voltage u_{p}, Fig. 2.19, given in (2–36). The average voltage used in the generation of the active output voltage vectors during one modulation period is [Jus06]

$$U_{\mathrm{DC}} = \frac{3}{2}\mathrm{Re}\left\{\underline{u}_{\mathrm{i}}\,\underline{sw}^{*}_{\mathrm{i,ave}}\right\} - \Delta_{\mathrm{ui}} = \frac{3}{2}\left(d_{\gamma}\,\mathrm{Re}\left\{\underline{u}_{\gamma}\,\underline{sw}^{*}_{\mathrm{i}\gamma}\right\} + d_{\delta}\,\mathrm{Re}\left\{\underline{u}_{\delta}\,\underline{sw}^{*}_{\mathrm{i}\delta}\right\}\right) - \Delta_{\mathrm{ui}} \tag{2–45}$$

$$\text{where } \Delta_{\mathrm{ui}} = -\mathrm{sign}(i_{\mathrm{DC}})\left(\frac{t_{\mathrm{c}} + t_{\mathrm{off}} - t_{\mathrm{on}}}{t_{\mathrm{mod}}}\left|u_{\mathrm{LL,med}}\right| - (U_{\mathrm{th,i}} + r_{\mathrm{d,i}}\left|i_{\mathrm{DC}}\right|)\right) \tag{2–46}$$

Δ_{ui} is the voltage component produced by the non-ideal line bridge. $u_{\mathrm{LL,med}}$ is the is the line-to-line voltage with the middlemost amplitude. In current sector 2 the commutation occurs between phases a and b, Fig. 2.13 ($\cos\varphi_{\mathrm{i}} = 1$). Therefore the voltage error is dependent on the amplitude of the line-to-line voltage u_{ab} which is $u_{\mathrm{LL,med}}$ in sector 2. In the other sectors the voltage error is similarly dependent on $u_{\mathrm{LL,med}}$. The voltage component Δ_{ui} during one

fundamental period of the input voltage is illustrated in Fig. 2.20. f_{in} is the frequency of the supply network. The DC-link voltage contains the multiples of the sixth harmonics of the supply frequency. The amplitudes of these harmonics are small compared to the average u_{DC} (2–40).

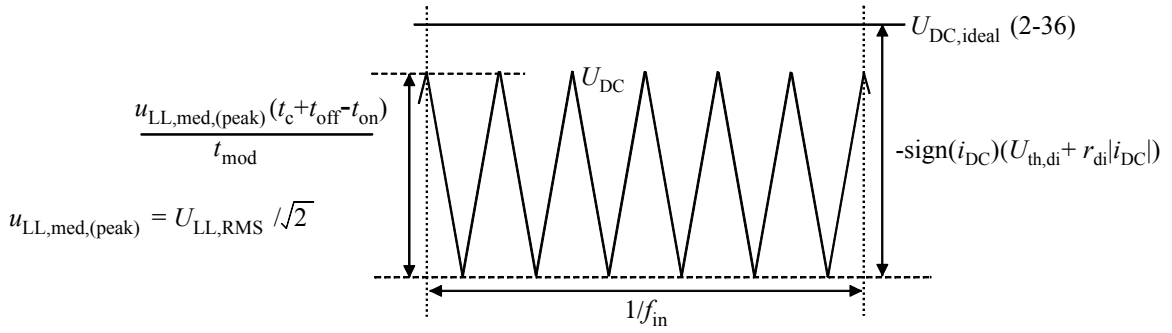

Fig. 2.20 $U_{DC,ref}$ of the IMC and the actual U_{DC} (2-45). i_{DC} flows to positive direction.

It can be seen in (2–46) that the overlapping time boosts the DC-link voltage if $i_{DC} > 0$. It is also easy to see in Fig. 2.19 where the bus p is connected to a higher input voltage longer than the desired time t_{Sbp}. Overlapping has an opposite effect compared to dead time (2–43). i_{DC} is positive when the displacement power angle of the load is between $-\pi/6$ and $\pi/6$ [Kol02].

2.4.3.2 Load bridge

The load bridge of the IMC is similar to the VSI. However, the control of the switches of the load bridge is not similar in this thesis. In the case of the VSI every phase is switched twice during t_{mod}, Fig. 2.7. In the case of IMC one output phase is switched twice, one four times and one is not switched during one modulation period. The number of state transitions of the switch depends the sector of the output voltage [Jus06]. It can be seen in Table 1 and in Fig. 2.15 that the output phase C is not switched during one modulation period if the output voltage reference is in sector 1. Therefore the voltage error in one phase caused by the dead time is a function of the sign of the current and also a function of the sector of the voltage reference $\underline{u}_{o,ref}$, Table 2. In Table 2 U_{dead} is the voltage error in the case of two switchings during t_{mod}: $U_{dead} = \text{sign}(i_{phase})U_{DC}(t_d + t_{on} - t_{off})/t_{mod}$ (2–43).

Table 2. Dead time effect of the load bridge of the IMC.

Sector of $\underline{u}_{o,ref}$	U_{dA}($\times U_{dead}$)	U_{dB}($\times U_{dead}$)	U_{dC} ($\times U_{dead}$)
1	1	2	0
2	2	1	0
3	0	1	2
4	0	2	1
5	2	0	1
6	1	0	2

Compared to the VSI the non-linear threshold voltage U_{th} in the bi-directional switches of the IMC have a similar effect on the output voltage. Instead of (2–30) the output voltage vector during the modulation period is:

$$\underline{u}_{\text{o}} = \underline{sw}_{\text{o,ave}} \frac{U_{\text{DC}}}{2} - \underline{\Delta}_{\text{uo}} \tag{2–47}$$

where $$\underline{\Delta}_{\text{uo}} = \frac{2}{3}\left(\Delta_{\text{uoA}} + \Delta_{\text{uoB}} e^{j2\pi/3} + \Delta_{\text{uoC}} e^{j4\pi/3}\right) \tag{2–48}$$

$\underline{\Delta}_{\text{uo}}$ is the non-linear voltage error vector produced by the IMC load bridge where

$$\begin{aligned}
\Delta_{\text{uoA}} &= \text{sign}(i_{\text{A}})\left(\frac{t_{\text{d}} + t_{\text{on}} - t_{\text{off}}}{t_{\text{mod}}} U_{\text{DC}} U_{\text{dA}} + U_{\text{th,o}}\right) + r_{\text{d,o}} i_{\text{A}} \\
\Delta_{\text{uoB}} &= \text{sign}(i_{\text{B}})\left(\frac{t_{\text{d}} + t_{\text{on}} - t_{\text{off}}}{t_{\text{mod}}} U_{\text{DC}} U_{\text{dB}} + U_{\text{th,o}}\right) + r_{\text{d,o}} i_{\text{B}} \\
\Delta_{\text{uoC}} &= \text{sign}(i_{\text{C}})\left(\underbrace{\frac{t_{\text{d}} + t_{\text{on}} - t_{\text{off}}}{t_{\text{mod}}}}_{\text{effect of the dead time}} U_{\text{DC}} U_{\text{dC}} + U_{\text{th,o}}\right) + r_{\text{d,o}} i_{\text{C}}
\end{aligned} \tag{2–49}$$

U_{dA}, U_{dB}, U_{dC} are coefficients with value 0, 1 or 2 from Table 2.

The non-linear error voltage caused by dead times and threshold voltages is illustrated in Fig. 2.21. In the simulations of Fig. 2.21 $(t_{\text{d}}+t_{\text{on}}-t_{\text{off}})/t_{\text{mod}}$ = 0.003, $U_{\text{th,o}}$ = 0.3 V and U_{DC} = 489 V. The output voltage vector leads the current vector 0.2 rad. As can be seen in Table 2, the non-linear voltage caused by dead times has five possible levels. In VSI the voltage levels were $\pm(U_{\text{dead}}+U_{\text{th}})$. The amplitude of the non-linear voltage vector has two levels, Fig. 2.21c. If the current displacement angle of the PMSM is smaller than π/6 rad the durations of lower and higher voltage levels are equal. If the angle between output voltage and current is increased over π/6 rad the duration of the lower level decreases. If the displacement angle is smaller than π/6 the average voltage error of IMC load bridge is smaller

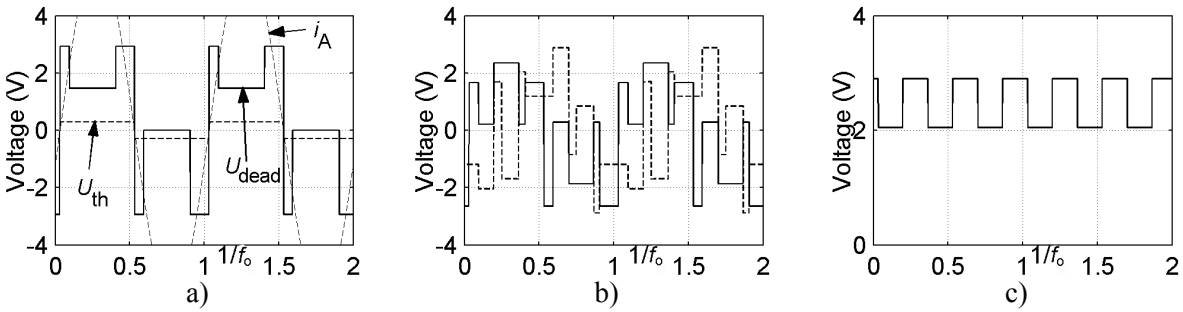

Fig. 2.21 a) Voltage components in one phase caused by the U_{dead} and $U_{\text{th,o}}$. Output voltage vector leads the current vector 0.2 rad b) Components of the non-linear voltage vector in stationary reference frame. c) Length of the non-linear voltage drop vector.

compared to VSI due to the smaller DC-link voltage.

2.4.4 Non-linear model of the DMC

During every modulation period two output phases of the DMC change their state twice and one four times, Table 1. The sector of the output voltage reference determines the phase switched four times [Jus06]. As explained in Section 2.3.2.2 the commutation principle of the DMC and the line bridge of the IMC is similar. Thus the voltage error of one phase caused by one forced and one natural commutation during t_{mod} has the form $u_{LL}(t_c + t_{off} - t_{on})/t_{mod}$, also in the case of DMC. u_{LL} is the line-to-line input voltage taking part in the forming of the output phase voltage. As discussed in Section 2.4.3.1 the overlapping time t_c increases the output voltage (2–46), Fig. 2.19. This also holds for the output voltage of the DMC.

Let us assume that $\underline{u}_{o,ref}$ and $\underline{i}_{i,ref}$ both lie in their sector 1. It can be seen in Table 1 and Fig. 2.15 that phase A is formed from the input phases a and c. C is formed using b and c. The input phase connected to A and C is changed twice during t_{mod}. The input phase connected to the output B is changed four times during t_{mod}. u_B is formed using line-to-line voltages u_{ab} and u_{ca}. When the current and voltage references are in sector 1, u_{ab} is the highest of the line-to-line voltages. u_{ca} is the lowest one and u_{bc} is the middlemost. The same principle also holds for other current-voltage sector combinations, Table 3. The voltage error in one phase caused by the non-linear properties of the DMC topology is dependent on the highest u_{LL}, the lowest u_{LL}, the middlemost u_{LL} or the voltage (highest u_{LL} - lowest u_{LL}).

Table 3. Line-to-line input voltages determining the non-linear voltage error of the DMC.

Sector of $\underline{u}_{o,ref}$	Sector of $\underline{i}_{i,ref}$	Phase A	Phase B	Phase C
1	Odd	$\lvert u_{LL,min}\rvert$	$u_{LL,max} - u_{LL,min}$	$\lvert u_{LL,med}\rvert$
	Even	$\lvert u_{LL,med}\rvert$	$u_{LL,max} - u_{LL,min}$	$u_{LL,max}$
2	Odd	$u_{LL,max} - u_{LL,min}$	$\lvert u_{LL,min}\rvert$	$\lvert u_{LL,med}\rvert$
	Even	$u_{LL,max} - u_{LL,min}$	$u_{LL,med}$	$u_{LL,max}$
3	Odd	$\lvert u_{LL,med}\rvert$	$\lvert u_{LL,min}\rvert$	$u_{LL,max} - u_{LL,min}$
	Even	$u_{LL,max}$	$\lvert u_{LL,med}\rvert$	$u_{LL,max} - u_{LL,min}$
4	Odd	$\lvert u_{LL,med}\rvert$	$u_{LL,max} - u_{LL,min}$	$u_{LL,min}$
	Even	$u_{LL,max}$	$u_{LL,max} - u_{LL,min}$	$\lvert u_{LL,med}\rvert$
5	Odd	$u_{LL,max} - u_{LL,min}$	$\lvert u_{LL,med}\rvert$	$\lvert u_{LL,min}\rvert$
	Even	$u_{LL,max} - u_{LL,min}$	$u_{LL,max}$	$\lvert u_{LL,med}\rvert$
6	Odd	$\lvert u_{LL,min}\rvert$	$\lvert u_{LL,med}\rvert$	$u_{LL,max} - u_{LL,min}$
	Even	$\lvert u_{LL,med}\rvert$	$u_{LL,max}$	$u_{LL,max} - u_{LL,min}$

Using the equation of the ideal output voltage of the VSI (2–29) and the equation of the fictitious DC-link voltage (2–36) the output voltage vector of the DMC can be written

$$\underline{u}_o = \underline{sw}_o \frac{3}{4} \mathrm{Re}\left\{\underline{u}_i \underline{sw}^*_{i,ave}\right\} - \underline{\Delta}_u \qquad (2–50)$$

$\underline{\Delta}_u$ is the non-linear voltage vector produced by the DMC. $\underline{\Delta}_{uo}$ can be written

$$\underline{\Delta}_u = \frac{2}{3}\left(\Delta_{uA} + \Delta_{uB}e^{j2\pi/3} + \Delta_{uC}e^{j4\pi/3}\right) \tag{2–51}$$

where

$$\begin{aligned}
\Delta_{uA} &= -\text{sign}(i_A)\left(\frac{t_c - t_{on} + t_{off}}{t_{mod}} u_{LL}(\text{sec}_u, \text{sec}_i)_A - U_{th}\right) + r_d i_A \\
\Delta_{uB} &= -\text{sign}(i_B)\left(\frac{t_c - t_{on} + t_{off}}{t_{mod}} u_{LL}(\text{sec}_u, \text{sec}_i)_B - U_{th}\right) + r_d i_B \\
\Delta_{uC} &= -\text{sign}(i_C)\left(\underbrace{\frac{t_c - t_{on} + t_{off}}{t_{mod}} u_{LL}(\text{sec}_u, \text{sec}_i)_C}_{U\text{overlapping}} - U_{th}\right) + r_d i_C
\end{aligned} \tag{2–52}$$

The voltages $u_{LL}(\text{sec}_u,\text{sec}_i)_{A,B,C}$ are selected from Table 3. Error voltages of the phases of the DMC have a structure similar to IMC line bridge error equation (2–46). The effect of the overlapping boosts the output voltage.

The non-linear error voltage of the DMC caused by the overlapping and U_{th} is illustrated in Fig. 2.22. The output frequency is 75% of the input frequency (supply). The voltage leads the current by 0.2 rad. In the simulations of Fig. 2.22 $(t_c\text{-}t_{on}+t_{off})/t_{mod} = 0.003$, $U_{th} = 0.6$ V and $u_{LL} = 400$ V (supply). The threshold voltage is now doubled compared to Fig. 2.21 because there are two devices in series.

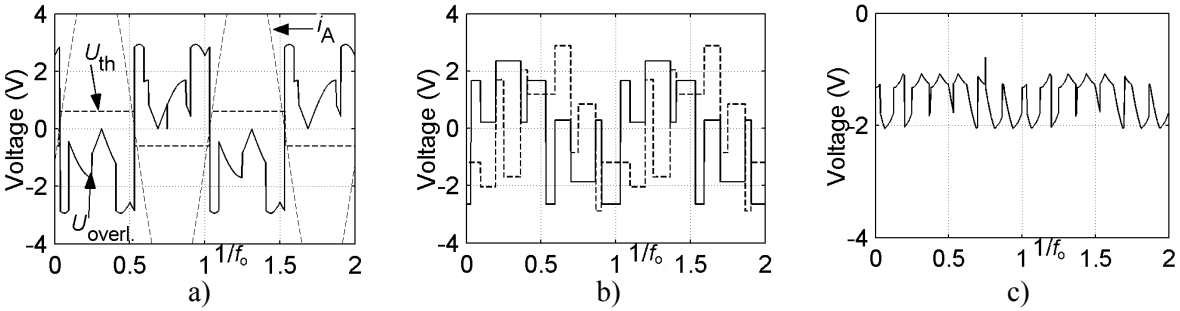

Fig. 2.22 a) Voltage components in one phase caused by the $U_{overlapping}$ and U_{th}. Voltage leads current 0.2 rad and the output frequency is 75% of the f_{in} b) Components of the non-linear voltage vector ($U_{overl.} + U_{th}$) in the stationary reference frame. c) Length of the non-linear voltage drop vector.

In Fig. 2.22 the boosting effect of the overlapping time is greater than U_{th}. Therefore the non-linear properties of the converter increase the output voltage compared to the reference. However, the final terminal voltage of the PMSM is smaller than the voltage reference $\underline{u}_{o,ref}$ if $r_d i$ is also included.

2.4.5 Comparison of topologies

In this section the non-ideal properties of VSI and MC topologies are compared by simulations and measurements (MCs only). The comparison is based on the steady state measurements with the PMSM drive. The PMSM used in the tests is machine A (Appendix A). 5 kVA IMC and DMC prototypes and the experimental set-ups are discussed in detail in Chapter 5. In both prototypes IGBTs made by Semikron® are used. The load bridge of the IMC consists of a six-pack module SKM40GD123D (max. current 40 A, max. voltage 1200 V). The line bridge of the IMC consists of IGBT modules with an antiparallel diode and a freewheeling diode, SKM75GAL123D (max. current 75 A, max voltage 1200 V). In the DMC prototype all IGBTs are the same type as in the IMC line bridge. They are packed in the modules SKM75GAL123D and SKM75GB123D.

2.4.5.1 Simulation results

The simulations of voltage losses are performed with Matlab® Simulink software. The voltage generation model of IMC is based on (2–45) - (2–49). The model of the DMC is based on (2–50)-(2–52). To study the output voltage error generated by non-ideal switches, both models are formed ignoring the modulation frequency components. The load is modelled by setting the load current magnitude and displacement angle to the same value as in the measurements presented in the next section. The simulations are performed using the same frequencies and voltage references as were used in the measurements. The parameters used in the simulation are based on the datasheets and the measurements of the semiconductors used. The parameter values are presented in Table 4. Tables 5 and 6 give the simulation results for IMC and DMC respectively. The voltage drop Δu_o in Tables 5 and 6 denotes the difference between the amplitudes of the voltage reference and the simulated output voltage.

Table 4. Parameters of switches used in the simulations.

	$U_{th,i}$	$r_{d,i}$	$U_{th,o}$	$r_{d,o}$	$(t_d + t_{on} - t_{off})/t_{mod}$	$(t_c - t_{on} + t_{off})/t_{mod}$
IMC	1 V	0.3 Ω	0.5 V	0.2 Ω	0.0035 (load bridge)	0.002 (line bridge)
DMC	—	—	1 V	0.3 Ω	—	0.002

Table 5. Simulated output quantities of the IMC supplying PMSM.

speed	f_o (Hz)	Load	$\lvert\underline{u}_{o,ref}\rvert$ (V)	$\lvert\underline{i}_o\rvert$ (A)	$\lvert\underline{u}_o\rvert$ (V)	Δu_o (V)	$\Delta u_o / \lvert\underline{u}_{o,,ref}\rvert$ (%)
5%	3.75	0	13	0.3	10.8	2.2	17
		Nominal	28	10.0	24	4	14.3
50%	37.5	0	122	0.5	120.1	0.9	0.7
		Nominal	137	10.1	132.8	4.2	3.1
100%	75	0	243	0.5	241.5	1.5	0.6
		Nominal	260	10.3	254.5	5.5	2.1

Table 6. Simulated output quantities of the DMC supplying PMSM.

speed	f_o (Hz)	Load	$\lvert\underline{u}_{o,ref}\rvert$ (V)	$\lvert\underline{i}_o\rvert$ (A)	$\lvert\underline{u}_o\rvert$ (V)	Δu_o (V)	$\Delta u_o / \lvert\underline{u}_{o,,ref}\rvert$ (%)
5%	3.75	0	11	0.3	10.7	0.3	2.7
		Nominal	25	10.0	21.8	3.2	12.8
50%	37.5	0	119	0.5	118.6	0.4	0.3
		Nominal	134	10.2	130,8	3.2	2.4
100%	75	0	238	0.5	237.5	0.5	0.2
		Nominal	254	10.3	250.7	3.3	1.3

The simulations are also conducted with the voltage source inverter model, Table 7. The DC-link voltage is assumed to be constant 540 V in all simulations. The parameters of the VSI are similar to the parameters of the load bridge of the IMC, Table 4. $\lvert\underline{u}_{o,ref}\rvert$ and $\lvert\underline{i}_o\rvert$ are similar to the IMC simulations, Table 5.

Table 7. Simulated output quantities of the VSI supplying PMSM.

speed	f_o (Hz)	Load	$\lvert\underline{u}_{o,ref}\rvert$ (V)	$\lvert\underline{i}_o\rvert$ (A)	$\lvert\underline{u}_o\rvert$ (V)	Δu_o (V)	$\Delta u_o / \lvert\underline{u}_{o,,ref}\rvert$ (%)
5%	3.75	0	13	0.3	10.7	2.3	17.7
		Nominal	28	10.0	22.5	5.5	19.6
50%	37.5	0	122	0.5	119.6	1.4	1.1
		Nominal	137	10.1	131.5	5.5	4
100%	75	0	243	0.5	240.6	2.4	1
		Nominal	260	10.3	254.5	5.5	2.1

Compared to IMC the voltage error is greater in VSI simulations at low speeds. This is an expected result because the dead time effect is slightly stronger in VSI due to the higher U_{DC}.

2.4.5.2 Measured results

Machine A (Appendix A) was driven by the IMC and DMC prototypes. The motor was controlled using the vector control in the rotor reference frame. The angular speed and position of the PMSM are measured. Steady state measurements are performed at speeds of 5%, 50% and 100% (nominal speed) with no-load and nominal load. Tables 8 and 9 give the amplitude of the voltage reference vector, measured output voltage and current of MCs. The voltage drop Δu_o in Tables 8 and 9 denotes the amplitude difference between the fundamental frequency components of the voltage reference and the measured output voltage.

Table 8. Measured output quantities of the IMC supplying PMSM.

Speed	f_o (Hz)	Load	$\lvert\underline{u}_{o,ref}\rvert$ (V)	$\lvert\underline{i}_o\rvert$ (A)	$\lvert\underline{u}_o\rvert$ (V)	Δu_o (V)	$\Delta u_o / \lvert\underline{u}_{o,,ref}\rvert$ (%)
5%	3.75	0	12.7	0.3	12.1	0.6	4.7
		Nominal	28.3	10	22.5	6.0	21
50%	37.5	0	122.3	0.5	120.7	1.6	1.3
		Nominal	136.9	10.1	131.6	5.3	3.8
100%	75	0	242.5	0.5	240.8	1.7	0.7
		Nominal	260.4	10.3	252.9	7.5	2.9

Table 9. Measured output quantities of the DMC supplying PMSM.

Speed	f_o (Hz)	Load	$\lvert\underline{u}_{o,ref}\rvert$ (V)	$\lvert\underline{i}_o\rvert$ (A)	$\lvert\underline{u}_o\rvert$ (V)	Δu_o (V)	$\Delta u_o / \lvert\underline{u}_{o,ref}\rvert$ (%)
5%	3.75	0	11.3	0.3	11.5	-0.2	-1.8
		Nominal	24.9	10.0	21.4	3.5	14.1
50%	37.5	0	119.0	0.5	118.4	0.6	0.5
		Nominal	133.7	10.2	130.5	3.2	2.4
100%	75	0	237.5	0.5	236.7	0.8	0.3
		Nominal	254.3	10.3	251.1	3.2	1.3

It can be seen in Tables 8 and 9 that the DMC generates output voltage more accurately than the IMC. The spectra of u_{AB} in the case of nominal load and 50% speed are illustrated in Fig. 2.23 and Fig. 2.24.

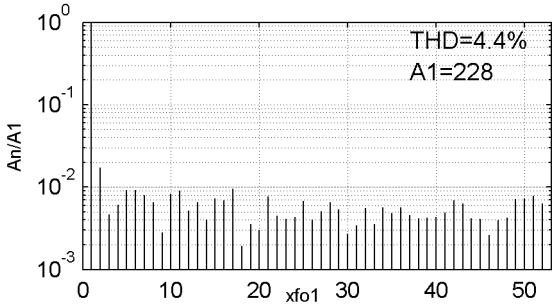

Fig. 2.23 IMC: Spectrum of u_{AB} with resolution of load frequency (37.5 Hz).

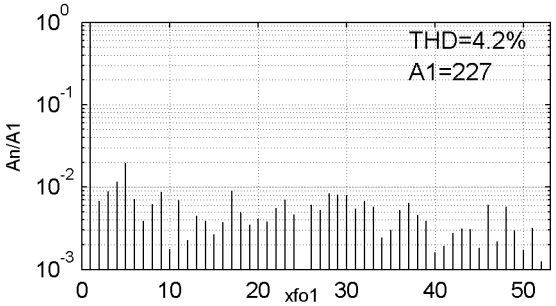

Fig. 2.24 DMC: Spectrum of u_{AB} with resolution of load frequency (37.5 Hz).

The measured results are in agreement with the simulated results. The most remarkable difference is found in the case of 3.75 Hz output frequency and zero load. The modelling of the bi-directional switch is not accurate in the case of small currents because the forward characteristics of the semiconductors used are very non-linear.

2.4.5.3 Conclusion

Speed and position estimators based on the PMSM model need information about the stator voltage. Because this is usually not measured the voltage reference is used instead. Therefore in this thesis the most interesting non-ideal property of the converters is the difference between the voltage reference and the actual output voltage. Measurements and simulations show that the DMC gives the smallest voltage error. This was expected because the overlapping in the commutation process boosts the output voltage. In the VSI and the load bridge of the IMC the effect of the dead time is the opposite. IMC and VSI have quite similar voltage error properties due to the similar inverter bridge.

In this thesis the space-vector modulation methods of VSI and MCs were different. The symmetric zero vector placement [Hol03], Fig. 2.7, which minimizes the output harmonics was used in the case of VSI. The modulation strategy used with MCs, Table 1, gives small switching losses.

The harmonic content of the output voltages of IMC and DMC were shown in Fig. 2.23 and Fig. 2.24. THD of the $\underline{u}_o$ was slightly smaller in the case of the DMC. In [Jus05] IMC and DMC were compared in several measurements and simulations and it was found that in general the THD of the output current and the voltage are smaller in the case of the DMC.

Even if the modulation strategy was similar in both MCs there are differences in the voltage steps caused by the converter when the sector of the output current vector is changed. In IMC the effect of the threshold voltage and the dead time voltage have a same sign (2–49). In DMC the effect of the threshold voltage decreases the non-linear effect of overlapping (2–52). This is important when signal injection position estimators are applied. The non-linear voltages caused by the threshold voltages and commutation process disturb the estimator when the output current vector is close to the sector boundary [Lin02], [Lin03b].

On-state power losses are not compared in this study because they are not important from the perspective of the sensorless control system. However, it is easy to see from the main circuits that there are three semiconductor devices in the current path of the IMC and two devices when DMC or VSI are used. Therefore the efficiency of the IMC is usually poorer.

The direct matrix converter topology seems to be more ideal for sensorless control purposes than the indirect topology. The voltage error between the reference and the actual voltage is smaller. Voltage steps when phase currents change their signs are smaller. If the supply is ideal the DMC also outperforms the VSI which has a line bridge similar to IMC. In practice the quality of the output voltage and the current may be better when a VSI is used due to the energy storage in the DC-link.

2.5 Control system of the PMSM

In this thesis the control system used in the simulations and the experimental tests is the vector control [Nov00], [Vas98]. The speed of the PMSM is controlled by a cascaded structure where the inner loop controls the current (torque) of the PMSM and the outer loop controls the angular speed ω_r.

The speed reference signal is compared to the measured or the estimated speed, Fig. 2.25. In this thesis the speed is controlled by a PI type algorithm. The output of the speed controller is the reference signal for the quadrature axis current i_q. The flux of the PMSM can be affected by i_d.

Measured currents are transformed to the synchronous reference frame and the differences between the real and imaginary axis current references and actual current components are

inputs for the current controllers. In this thesis PI type controllers are used. In steady state the current error is driven to zero because the components of the current vector reference are DC-signals.

The outputs of the current controllers are real and imaginary components of the voltage reference vector $\underline{u}_{o,ref}$, which is realized by a PWM converter. The PWM modulator contains another coordinate transformation because the actual voltages are sinusoidal. Fig. 2.25 shows the sensorless control system performed in the rotor reference frame tied to the estimated rotor position $\hat{\theta}_r$. In Fig. 2.25 $\hat{\omega}_r$ denotes the estimated rotor angular speed. Subscripts de and qe in Fig. 2.25 denote current vector components in an estimated rotor reference frame.

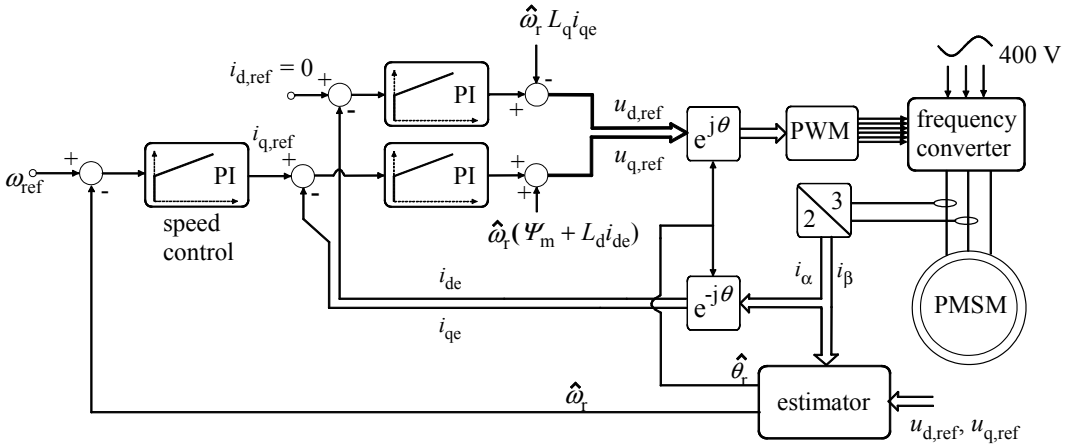

Fig. 2.25 Vector control of the PMSM in the rotor reference frame. ω_r and θ_r are estimated.

In servo drives the controlled quantity is often the rotor position. The position control loop is not shown in Fig. 2.25. It would be the outermost control loop and the output of the position control is the speed reference signal.

The coordinate transformation to the rotor reference frame does not linearize the PMSM equations. The voltage equations of the PMSM in the rotor frame are coupled by the rotational voltages $\omega_r \psi_d$ and $\omega_r \psi_q$ (back-emfs where total flux linkages are included) (2–12). Therefore i_d and i_q are not independently controlled. The cross-coupling effect is removed if d and q axis rotational voltages are added to the outputs of the q and d axis current controllers respectively, Fig. 2.25. This is called a feedforward compensation [Nov00].

Current control can also be performed in the stationary reference frame. Only one coordinate transformation is then needed. Stationary frame control is sometimes required if the speed and the position estimation is based on the sinusoidal signals. The drawback of the stationary frame control is the steady state error due to the sinusoidal references if separate PI controllers are used as in Fig. 2.25. However, it is possible to construct a current control in the stationary frame with an identical performance to the control system of Fig. 2.25 [Nov00],

[Row86]. This current control system is illustrated in Fig. 2.26 where k_p and t_i are gain and the integration time of the PI controller respectively. A cross-coupling between α and β controllers is required. The decoupling of the back-emf (rotational voltages) requires trigonometric operations in the stationary frame. Because the structure of the current control is more complicated in the stationary frame the synchronous frame control is usually preferred.

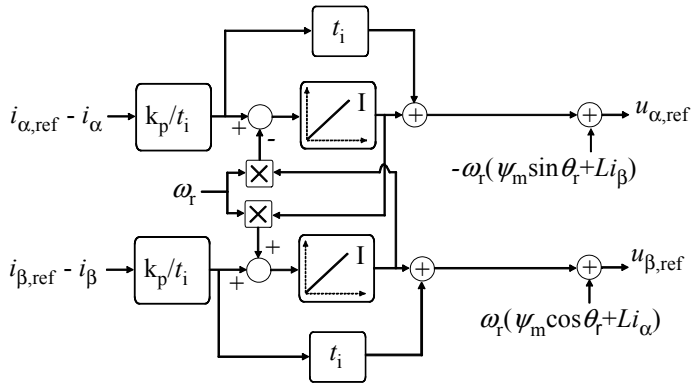

Fig. 2.26 Current control of the PMSM in the stationary reference frame.

Control of i_d

If the PMSM is driven above the nominal speed the magnetic field is weakened by negative direct axis current to prevent too high stator voltages. In this thesis PMSMs are not driven above their nominal speeds. Field weakening below the nominal speed may be reasonable when relative values of the inductances are large. In that case a significant amount of the stator flux linkage is produced by the stator current. High load torques (clearly over nominal) may require excessive stator voltages when operated around the nominal speed if the d axis flux is not weakened.

If the effect of the reluctance torque $(L_d - L_q)i_d i_q$ (2–26) is also taken into account in the current control it is possible to produce a maximum torque with a certain current vector length [Jah86]. The effect of the saliency in torque producing is often insignificant. The machines studied in this thesis, Appendix A, have rather small inductance difference $(L_d - L_q)$. Therefore the maximum torque per ampere control is not used.

In this thesis the average value of $i_{d,ref}$ is zero in all simulations and measurements. This is done to simplify the analysis of the estimators. However, the algorithms of the model based methods, studied in Chapter 3, do not require zero i_d. Performance of the estimator may be impaired if the field weakening is used. In the estimator algorithms i_d is multiplied by motor parameters which are not accurately known. Therefore i_d is an additional source of errors.

In the case of signal injection estimators, studied in Chapter 4, problems may arise when

the d axis flux is weakened using negative i_d and a PMSM with surface mounted magnets is applied. The saliency is then mainly induced by the saturation of the stator iron in the d axis direction. Weakening of the d axis flux may remove the saliency which can lead to unstable operation because most of the injection estimators can not operate with saliency ratio near unity.

Discrete-time implementation of PI controllers

PI controllers must be transformed into a discrete-time form before they are implemented in a microcontroller. In this thesis a time-continuous PI controller is discretized using a Backward difference method [Åst97] where the Laplace variable s is replaced by $(z-1)/zt_s$. The discrete-time transfer function of the PI controller is

$$G(z) = \frac{zk_p(1 + t_s / t_i) - k_p}{z - 1} \tag{2–53}$$

where t_s, k_p and t_i are sample time, gain and the integration time respectively. The anti-windup PI algorithm based on (2–53) can be expressed as

$$\begin{aligned} &y(k) = y(k-1) + k_p(1+t_s/t_i)u(k) - k_p u(k-1) \\ &\text{if}(y(k) > y_{max});\ y(k) = y_{max} \\ &\text{if}(y(k) < y_{min});\ y(k) = y_{min} \end{aligned} \tag{2–54}$$

where y and u denote output and input respectively. $y(k)$ is the output of the current sampling period and $y(k-1)$ is the previous output. If the output exceeds the limit value the integration is stopped. This algorithm is used in the current and speed control, Fig. 2.25. The anti-windup controller is illustrated in Fig. 2.27. The length of the delay Δ is t_s. The saturation of the PI controllers in Fig. 2.26 is prevented by setting the inputs of the integrators at zero if the output exceeds the limit value.

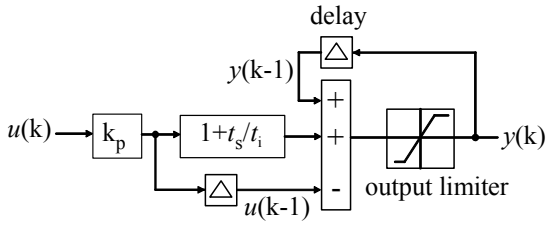

Fig. 2.27 Anti-windup discrete-time PI controller used in speed and current control.

3. Model based estimators

This chapter deals with estimator methods based on the model of the PMSM. At the beginning of this chapter a short introduction to sensorless methods in general is provided. The main categories are introduced and the principle for classifying the methods in this study is explained. The rest of the chapter concentrates on model based estimator methods and their comparison.

3.1 Introduction to speed and position estimators

Sensorless control means that the mechanical quantities of the AC machine are not measured but estimated on-line using some convenient algorithm. This is done to reduce costs and to increase the robustness of the variable speed drive. A sensorless control is composed of the control system and estimator algorithm which calculates mechanical feedback information, position angle θ_r and the rotor angular speed ω_r in the case of the PMSM. The control system used here is the conventional vector control [Vas98], [Nov00], Fig. 2.25.

Speed and position estimators can be allocated to three main categories.

1. Model based estimators. These methods use the model of the machine and the measured electrical quantities to determine the rotor position and speed. The motor model is usually based on Equations (2-12), (2-26), (2-27) and (2-28). The measured electrical quantity is usually the stator current of the AC machine. Here model based methods are divided into the following subcategories.

a State observers

b. Back-emf methods

c. Flux linkage methods

2. Signal injection estimators. An additional signal (voltage or current) is injected into the motor and the position angle and speed are determined by processing the resulting currents or voltages. Injection methods can be divided into two groups.

a. High frequency methods. These estimators exploit the magnetic saliency (anisotropy) of the machine. In the literature the frequency of the injection signal is from a few hundred Hz to kHz region.

b. Low frequency methods. These estimators are based on the mechanical vibration of the

rotor. The injection frequency is usually from a few Hz to a few hundred Hz.

3. Soft computing estimators. Soft computing methods use neural networks, fuzzy logic or genetic algorithms to estimate the speed and position. Neural networks learn the properties of the particular machine using predetermined training data. After training the neural network should estimate the position and speed. The inputs of the network are currents and voltages. Neural networks can also learn the properties of the machine during the actual drive sequence. Fuzzy logic estimators are based on the linguistic rules determined by a human expert.

Chapter 3 concentrates on category 1. Signal injection estimators are discussed in Chapter 4. Soft computing methods are not studied in this thesis. More information about soft computing estimators can be found in [Vas99].

3.1.1 Basic properties of the estimators

3.3.1.1 Model based methods

In this study the model based methods are divided into state observers (category 1a) and voltage model methods (1b and 1c). A state observer is an algorithm implemented to reconstruct the inaccessible states in a system using the accessible states [Bro91], [Gre93]. Accessible states are usually the components of the measured current vector of the PMSM. However, this definition is valid for most model based estimators. In this study the state observer is an estimator which uses a state-space representation of PMSM based on the voltage model (2-12) and mechanical equations (2-27) - (2-28). The state observer estimates the unknown mechanical states θ_r and ω_r using the error between the measured current space-vector and the estimated current vector.

The flux linkage estimators and back-emf estimators are based on the voltage model of PMSM (2-12). In categories 1b and 1c the primary estimated quantities are the back-emf and the stator flux linkage. The estimates contain speed and position information. This information can be calculated directly from flux and emf estimates or obtained with a suitable tracking algorithm. Here the tracking algorithm is a phase locked loop (PLL) discussed in Section 3.3.

All model based methods need a back-emf to track the rotor position. If $\omega_r = 0$ the back-emf is zero and the currents are DC signals. Zero back-emf and DC currents contain no information about rotor position. Therefore model based estimators cannot operate at zero speed. In practice a low speed region is also problematic due to the parameter errors.

3.3.1.2 Signal injection estimators

During the last ten years extensive research has been carried out to develop estimators where these problems at low speeds can be avoided. The methods also suitable for the zero speed operation are called “injection methods”. In these methods a high frequency signal (voltage or current) is injected into the motor and the position angle and speed are determined by processing the resulting currents or voltages. The injection signal is usually superimposed on the voltage references of the PMSM. Injection can be continuous when a sinusoidal signal is added to voltage references and the space-vector modulation is not interrupted. In discontinuous injection the normal modulation operation is stopped at regular intervals and test pulses are injected into the motor.

Most of injection estimators belong to group 2a. They exploit the magnetic saliency (anisotropy) of the machine. High frequency methods have no stability problems at zero or in low speed region and they need no information on the parameters of the PMSM. High frequency methods are not suitable for machines with saliency ratio L_d/L_q close to unity. In that case the error signal amplitude is small and high performance current measurement and signal processing are required to extract useful position information.

In the case of low frequency signal injection estimator the injected signal creates mechanical oscillation if the position is not correctly estimated. The voltage model (2-12) is used to calculate the estimated back-emf signal. This signal contains information on position error. The estimator also needs the voltage and parameter information. Therefore it is a mixture of a model based and an injection estimator. The major drawbacks are slow dynamics due to the low injection frequency and problems in the case of high inertia. The small saliency ($L_d \approx L_q$) is not a problem. Signal injection methods are studied in Chapter 4.

3.1.2 Principles of the comparison of the estimators in this study

In this study the goal is to find a sensorless control system which gives stable operation over the speed range of the PMSM. Field weakening region is not discussed. It would be very difficult to find a universally best sensorless method because the demands for an estimator depend on the PMSM itself and the variable speed solution in which the PMSM is used. Here the speed and position estimator must meet the following requirements.

1. No modification of the hardware of the frequency converter is required.

2. No modification of the space-vector modulator software is required.

3. The algorithm of the estimator should be as simple as possible.

4. The drive must be stable over the entire speed range including operation at zero speed.

Requirement 1 means that the frequency converter used in vector controlled variable speed drive with motion sensors must also be suitable for sensorless drives without hardware modifications. In practice this means that no additional measurements are needed. In the VSC with a diode rectifier the currents of the PMSM and DC-link voltage are the only measured quantities. In MC line currents are also measured. Sensorless methods requiring additional measurements, e.g. voltage measurements or current sign detector circuits, are not discussed.

Requirement 2: To decrease the software modifications estimators which require modified vector modulator are not accepted. The idea again is to keep things simple.

Requirement 3: There are two reasons why simple estimator algorithms are preferred to mathematically more sophisticated methods. Understanding the straightforward methods requires no profound knowledge of mathematics or control theory. Complicated algorithms also need more time to compute. This may not be a problem in the future due to the development of integrated circuits. However, in industry there is usually a tendency to use low cost circuits. Therefore it may take quite a long time until the computation time is not a problem when control systems of AC motors are developed. The requirement for a simple algorithm also means that parameter estimators should be avoided.

Soft computing methods are not discussed here because they cannot be considered to be simple methods. The other problem is the tuning of the soft computing algorithms. The characteristics of the PMSM must be taught to the neural network. There is no universal rule about how to select optimal teaching data or the optimal structure for the neural network. Tuning of a fuzzy-logic algorithm is time consuming because the algorithm contains more tuning parameters compared to estimators based on conventional control theory. Parameters must be chosen by trial and error. There is no unified theory to help to select suitable fuzzy rules and tuning parameters for a particular application [Vas99].

Requirement 4: A stable sensorless control system cannot be achieved using only model based methods. Model based estimators have good performance in high and medium speed regions while signal injection methods are superior at low speeds. The goal of this study is to use a hybrid estimator which exploits the benefits both of these. In the case of model based estimators starting properties or operation at very low speeds are not considered in this thesis.

3.2 State observers

State observers were the first methods proposed to estimate the position and speed of the AC machine. [Ued75] is one of the first papers where unknown variables (states) of the

synchronous machines were estimated by an observer. In this Section 3.2 several of the state observer methods presented in the literature to estimate the speed and position angle of the PMSM are briefly considered. Section 3.2.1 concentrates on deterministic observers based on the linearized PMSM model. In Section 3.2.2 an "exact linearization" state observer is discussed. Section 3.2.3 deals with a stochastic observer i.e. Kalman filter. This section is concluded with discussion on the properties of state observers when used in sensorless control of PMSM.

3.2.1 State observers using a linearized PMSM model

The general state-space model of a linear time-invariant system is

$$\begin{aligned} \frac{d\mathbf{x}}{dt} &= \mathbf{A}\mathbf{x} + \mathbf{B}\mathbf{u} \\ \mathbf{y} &= \mathbf{C}\mathbf{x} \end{aligned} \tag{3–1}$$

where **x** is the state vector, **u** is the input vector and **y** is the output vector. **x**, **u** and **y** are functions of time. To simplify the equations notation **x**(t) is replaced by **x** in this study. **A** is an n×n square matrix and **B** is an n×m matrix. n is the number of states and m is the number of inputs. **A** and **B** are constant coefficient matrices. **C** is a k×n matrix where k is the number of outputs.

A state observer for linear systems was introduced by Luenberger in the 1960's. Some of the state variables are not measurable. The observer estimates the unknown states using the error between the measured and estimated output. The state-space model of the Luenberger observer is

$$\frac{d\hat{\mathbf{x}}}{dt} = \mathbf{A}\hat{\mathbf{x}} + \mathbf{B}\mathbf{u} + \mathbf{K}(\mathbf{y} - \mathbf{C}\hat{\mathbf{x}}) \tag{3–2}$$

where **K** is a matrix with constant gains. If $\tilde{\mathbf{x}} = \mathbf{x} - \hat{\mathbf{x}}$ and (3–2) is subtracted from (3–1) it follows that

$$\frac{d\tilde{\mathbf{x}}}{dt} = (\mathbf{A} - \mathbf{K}\mathbf{C})\tilde{\mathbf{x}} = \mathbf{F}\tilde{\mathbf{x}} \tag{3–3}$$

The estimation error approaches asymptotically zero as time approaches infinity provided that the eigenvalues of the gain matrix (poles of the system) **F** (3–3) are located in the left of the complex frequency plane [Lue71]. Observers where the gain matrix **K** is chosen by the pole placement technique are called deterministic observers. The observer (3–2) where measured

states are also estimated is called a full-order observer. In reduced order observers the measured states are not estimated. Therefore the dimensions of the observer are reduced [Bro91], [O're83]. The theory of the reduced order observer is not presented here because the basic idea of how the unknown states are estimated is similar to full order observers.

State-space model of the PMSM

In the case of PMSM the state vector $\underline{x}$ is usually $[i_d \;\; i_q \;\; \theta_r \;\; \omega_r]^T$ or $[i_\alpha \;\; i_\beta \;\; \theta_r \;\; \omega_r]^T$ if the estimation is performed in the stationary frame. The PMSM is modelled by (2-12), (2-27) and (2-28). In synchronous reference frame the state-space representation of the PMSM is

$$\underbrace{\frac{d}{dt}\begin{bmatrix} i_d \\ i_q \\ \omega_r \\ \theta_r \end{bmatrix}}_{\mathbf{x}} = \underbrace{\begin{bmatrix} (-Ri_d + \omega_r L_q i_q)/L_d \\ (-Ri_q - \omega_r L_d i_d - \psi_m \omega_r)/L_q \\ \frac{3p^2\psi_m}{2J} i_q - \frac{b}{J}\omega_r \\ \omega_r \end{bmatrix}}_{f(\mathbf{x})} + \underbrace{\begin{bmatrix} 1/L_d & 0 & 0 & 0 \\ 0 & 1/L_q & 0 & 0 \\ 0 & 0 & -p/J & 0 \\ 0 & 0 & 0 & 0 \end{bmatrix}}_{\mathbf{B}} \underbrace{\begin{bmatrix} u_d \\ u_q \\ T_L \\ 0 \end{bmatrix}}_{\mathbf{u}} \tag{3–4a}$$

$$\mathbf{y} = \underbrace{\begin{bmatrix} 1 & 0 & 0 & 0 \\ 0 & 1 & 0 & 0 \end{bmatrix}}_{\mathbf{C}} \begin{bmatrix} i_d \\ i_q \end{bmatrix} \tag{3–4b}$$

PMSM is a non-linear system. States i_d and i_q are multiplied by state ω_r in rows 1 and 2. In the stationary frame the state-space model is more complicated because the state vector $f(\mathbf{x})$ contains trigonometric functions. If the control theory for linear systems is applied the PMSM model must be linearized using the system Jacobian matrix $\mathbf{A}_J$ [Vas98]. For (3–4a) the Jacobian matrix is

$$\mathbf{A}_J = \frac{\partial f}{(\partial i_d, \partial i_q, \partial \omega_r, \partial \theta_r)} = \begin{bmatrix} -R/L_d & \omega_r L_q/L_d & i_q L_q/L_d & 0 \\ -\omega_r L_d/L_q & -R/L_q & -i_d L_d/L_q & 0 \\ 0 & (3p^2\psi_m)/2J & -b/J & 0 \\ 0 & 0 & 1 & 0 \end{bmatrix} \tag{3–5}$$

3.2.1.1 Extended Luenberger observers (ELO)

In [Orl89], [Du95] and [Elm96] the extended Luenberger observer (ELO) was used for speed, position and parameter estimation of AC machines. "Extended observer" has two meanings in the motor control literature.

1) Linear observer (3–1) is used to estimate the states of a non-linear system. The non-linear model is linearized every time the estimator algorithm is computed [Bol99], [Vas98].
2) In addition to 1) the parameters of the model are also estimated [Orl89], [Du95].

If the estimation error $\tilde{\mathbf{x}}$ is assumed to be small, the non-linear model can be replaced by $\mathbf{A}_J$ (3–5) [Du95], [Elm96]. The discrete time equation of the full order ELO [Du95] is presented in (3–6). The derivation of (3–6) can be found in [Du95], [Elm96], [Orl89], [Son00].

$$\hat{\mathbf{x}}(k+1 \mid k) = \hat{\mathbf{x}}(k \mid k-1) + t_S \left(\underbrace{\left(\mathbf{A}_J(k) - \mathbf{K}(k)\mathbf{C}\right)}_{=\mathbf{L}(k)} \hat{\mathbf{x}}(k \mid k-1) \right) + t_S \left(\mathbf{B}\mathbf{u}(k) + \mathbf{K}\mathbf{y}(k) + \mathbf{g}(k) \right) \qquad (3\text{–}6)$$

The notation $\mathbf{x}(k|k-1)$ means that the value of vector $\mathbf{x}$ at time instant k is based on the information from the previous sampling period. The states of the PMSM are estimated by the ELO using a following four step algorithm:

1. Specify observer poles. Construct a suitable observer matrix $\mathbf{L}(k)$ (3–6) with specified poles. $\mathbf{L}$ has the same purpose as $\mathbf{F}$ in the linear observer (3–3). This step can be done off-line.

2. Calculate $\mathbf{g}(k) = f(\mathbf{x})(k) - \mathbf{A}_J(k)$. $\mathbf{g}$ is the error between the nonlinear model and the linearized model.

3. Solve $\mathbf{K}$ from $\mathbf{L}(k) = \mathbf{A}_J(k) - \mathbf{K}(k)\mathbf{C}$.

4. Calculate the state vector at the next sampling period, (3–6).

It is easy to see that the computational requirements of the ELO algorithm are demanding. $\mathbf{A}_J$ is updated at every sampling interval. Therefore the gain matrix $\mathbf{K}$ is also constantly calculated, step 3. Solving $\mathbf{K}$ from $\mathbf{L}(k)$ is a time consuming operation. In practice the estimator structure can be greatly simplified without considerable losses in the dynamic performance. The following section gives a few examples of simplified deterministic observers.

3.2.1.2 Examples of simplified state observers for speed and position tracking

In [Jon89] the non-linear model of the PMSM in synchronous reference frame (3–4) was directly used in the observer equation (3–2). $\mathbf{Ax}$ was replaced by $f(\mathbf{x})$ in (3–2). It was stated that the large signal stability of the estimator is difficult to prove. However, it was found in the simulations that the linearized model predicted the behaviour of the non-linear observer with a good accuracy. Compared to the ELO the estimator algorithm was greatly simplified.

In [Sep92] the observer of [Jon89] was further developed. The gain matrix **K** was constant in [Jon89] but in [Sep92] gain scheduling was used. **K** was not updated in every sampling period. However, a different gain matrix was used in the low and high speed regions.

In [Low93] the PMSM model in the rotor reference frame (3–4) was linearized using measured currents i_d and i_q. It is possible now to write a state-space model where **A** (3–1) is time-variant but linear.

$$\underbrace{\frac{d}{dt}\begin{bmatrix} i_d \\ i_q \\ \omega_r \end{bmatrix}}_{\mathbf{x}} = \underbrace{\begin{bmatrix} -R/L_d & 0 & i_q L_q / L_d \\ 0 & -R/L_q & (-\psi_m - i_d L_d)/L_q \\ 0 & \frac{3p^2\psi_m}{2J} & -b/J \end{bmatrix}}_{\mathbf{A}} \underbrace{\begin{bmatrix} i_d \\ i_q \\ \omega_r \end{bmatrix}}_{\mathbf{x}} + \underbrace{\begin{bmatrix} 1/L_d & 0 & 0 \\ 0 & 1/L_q & 0 \\ 0 & 0 & -p/J \end{bmatrix}}_{\mathbf{B}} \underbrace{\begin{bmatrix} u_d \\ u_q \\ T_L \\ 0 \end{bmatrix}}_{\mathbf{u}} \quad (3\text{–}7)$$

$$\frac{d\theta_r}{dt} = \omega_r \qquad \mathbf{y} = \mathbf{C}\mathbf{x} = [1 \quad 1 \quad 0]\mathbf{x}$$

The position estimate is obtained by integrating the estimated ω_r. (3–7) can be directly used in the equation of the linear full-order observer (3–2). After the eigenvalues of the error dynamics (3–3) have been chosen the gain matrix **K** must be determined. Now **A** is a function of currents. Therefore **K** (3–2) must be updated on-line. A simple method is to use a look-up table. In practice **A** is a function of i_q only because i_d is usually small or controlled to zero. Thus only a one-dimensional table is needed.

3.2.2 Non-linear state observer

The observer based speed and position estimators described above are based on linear control theory. There are also techniques where the process is linearized using a suitable feedback structure. No gradient matrix calculations are needed. One of the non-linear strategies is the “exact linearization” technique [Isi85]. Using this method it is possible to construct a speed control system for a PMSM where the non-linear effects such as cross coupling between d and q axis equations are eliminated [Sol00]. This model based non-linear state-feedback control requires information on all four states of the PMSM (3–4). If mechanical states are not measured they can be estimated using a full-order [Sol00], [Guc01] or reduced-order [Sol96] observer also based on the “exact linearization” theory. This non-linear method can also be used to estimate speed and position for conventional vector control [Sol95].

The state observer based on "exact linearization" theory is presented in (3–8) [Sol00]. The observer algorithm is performed in the stationary reference frame. It is an extended version because the load torque is also estimated.

$$\frac{d}{dt}\begin{bmatrix}\hat{i}_\alpha\\ \hat{i}_\beta\\ \hat{\omega}_r\\ \hat{\theta}_r\\ \hat{T}_L\end{bmatrix}=\underbrace{\begin{bmatrix}(-R\hat{i}_\alpha+\psi_m\hat{\omega}_r\sin\hat{\theta}_r)/L+u_\alpha/L\\ (-R\hat{i}_\beta-\psi_m\hat{\omega}_r\cos\hat{\theta}_r)/L+u_\beta/L\\ \frac{3p^2\psi_m}{2J}(-\hat{i}_\alpha\sin\hat{\theta}_r+\hat{i}_\beta\cos\hat{\theta}_r)-\frac{\hat{T}_L}{J}-\frac{b}{J}\hat{\omega}_r\\ \hat{\omega}_r\\ 0\end{bmatrix}}_{f(\mathbf{x})+\mathbf{Bu}}+\begin{bmatrix}\multicolumn{2}{c}{\boldsymbol{\Gamma}\mathbf{K}}\\ g_1\sin\hat{\theta}_r & -g_2\cos\hat{\theta}_r\end{bmatrix}\begin{bmatrix}i_\alpha-\hat{i}_\alpha\\ i_\beta-\hat{i}_\beta\end{bmatrix} \quad (3\text{–}8)$$

where $\boldsymbol{\Gamma}=\begin{bmatrix}1 & 0 & 0 & 0\\ 0 & 1 & 0 & 0\\ 0 & 0 & L\sin\hat{\theta}_r\psi_m^{-1} & -L\cos\hat{\theta}_r\psi_m^{-1}\\ 0 & 0 & L\cos\hat{\theta}_r/(\psi_m\hat{\omega}_r) & L\sin\hat{\theta}_r/(\psi_m\hat{\omega}_r)\end{bmatrix}$

K is 4×2 constant matrix. g_1 and g_2 are also constant gains. A tedious derivation of the non-linear gain matrix **Γ** and the proof of stability using Lyapunov's theory is presented in [Guc01], [Sol95], [Sol00].

Compared to ELO (3–6) the algorithm is computationally much more effective. There is no need for complicated matrix operations or gain scheduling. The "exact linearization" method is mathematically elegant compared to the observers presented above. The stability of the observer can be proven. Gains **K**, g_1 and g_2 are constants and need not to be updated.

3.2.3 Stochastic state observer (Kalman filter)

Kalman filter is a state observer which gives a linear and minimum error variance algorithm to optimally estimate the unknown states of a dynamic system from noisy data taken at a discrete time. The structure of the Kalman filter is similar to (3–2). In the Kalman filter the selection of gain **K** is based on the stochastic properties of the system [Gre93], [Vas98]. The model is usually presented in a discrete form.

$$\begin{aligned}\mathbf{x}(k+1)&=\mathbf{x}(k)+t_s(\mathbf{A}\underline{x}(k)+\mathbf{Bu}(k))+\mathbf{w}(k)\\ \mathbf{y}(k)&=\mathbf{Cx}(k)+\mathbf{v}(k)\end{aligned} \quad (3\text{–}9)$$

w and **v** are zero mean Gaussian noises with covariance matrices **Q** and **R**. The system noise **w** takes into account the system disturbances (unknown load torque) and parameter errors of the model. **v** represents the measurement noise. Noise vectors **w** and **v** are independent of the

system state vector **x** if **v** is not correlated with a process noise **w**. **Q** is a 4×4 diagonal matrix and **R** is a 2×2 diagonal matrix in the case of the PMSM.

A linear Kalman filter is a two-stage algorithm

$$\begin{aligned}\hat{\mathbf{x}}(\mathrm{k}\mid \mathrm{k}\text{-}1) &= \hat{\mathbf{x}}(\mathrm{k}\text{-}1\mid \mathrm{k}\text{-}1) + t_\mathrm{S}\left(\mathbf{A}\hat{\mathbf{x}}(\mathrm{k}\text{-}1\mid \mathrm{k}\text{-}1) + \mathbf{B}\mathbf{u}(\mathrm{k}\text{-}1)\right)\\ \hat{\mathbf{x}}(\mathrm{k}\mid \mathrm{k}) &= \hat{\mathbf{x}}(\mathrm{k}\mid \mathrm{k}\text{-}1) + \mathbf{K}(\mathbf{y}(\mathrm{k}) - \mathbf{C}\hat{\mathbf{x}}(\mathrm{k}\mid \mathrm{k}\text{-}1))\end{aligned} \tag{3–10}$$

where the next value for **x** is first predicted using the previous value of input vector **u** and state vector **x**. The predicted state vector $\hat{\mathbf{x}}(\mathrm{k}\mid \mathrm{k}-1)$ is then corrected using the error between the measured output and the predicted output $\mathbf{C}\hat{\mathbf{x}}(\mathrm{k}\mid \mathrm{k}-1)$. For Kalman gain **K** can be written

$$\mathbf{K} = \mathbf{P}\mathbf{C}^\mathrm{T}(\mathbf{C}\mathbf{P}\mathbf{C}^\mathrm{T} + \mathbf{R})^{-1} \tag{3–11}$$

P is a state covariance matrix [Gre93], [Vas98]. In the linear case **K** is a predetermined constant matrix. In the non-linear case **K** and **P** are updated between prediction and correction steps (3–10) at every sampling interval. The algorithm is called an extended Kalman filter (EKF). The software implementation is a similar type multistep algorithm as that presented in Section 3.2.1.1. If an EKF is used to estimate the states of the PMSM the matrix **A** (3–10) is replaced by $f(\mathbf{x})$ (3–4). Jacobian matrix $\mathbf{A}_\mathrm{J}$ (3–5) is needed when the state covariance matrix **P** is updated.

Detailed information about EKF can be found in [Bol99], [Bol01], [Bol03], [Dha91], [Gre93]. Calculations of **K** and **P** are time consuming operations. The computational burden is comparable to an extended Luenberger observer.

Tuning of the Kalman filter is done by adjusting the coefficients of **Q** and **R**. Matrices **Q** and **R** affect both the transient performance and steady state operation. The following tuning principles are given in [Vas98]: If elements of **Q** are increased a greater uncertainty in the machine model is assumed. Large **Q** increases **K**. The measurements will be more heavily weighted. If elements of **R** are increased the measurements are assumed to be noisy and will be weighted less by the EKF. The elements of **K** will decrease resulting in a lower transient performance.

In [Bol03] the selection of **Q**, **R** and initial value of **P** were studied through experimental tests and simulations. It was found that the per unit values of the current and motor parameters of surface magnet PMSM vary in a narrow range regardless of motor size. Therefore it is possible to find covariance matrices suitable for all standard PMSM drives. In practice some fine tuning should be done but it is claimed in [Bol03] that an effective and general initial guess has been found for EKF settings in sensorless PMSM drives.

3.2.4 General properties of state observers in sensorless control of PMSM

Several state observers where speed and position were estimated by tracking the measured stator currents were briefly discussed in Sections 3.2.1 – 3.2.3. ELO, EKF and the observer based on the "exact linearization" (3–8) were compared by simulations in [Esk02]. There were no significant differences between the performances of the methods tested. However, the computations required by those three full order observers are different.

Computations required by the non-linear observer (3–8) are: two divisions, 36 multiplications and 17 additions. The algorithm contains several trigonometric operations. Sine and cosine of the rotor position may be taken from predetermined tables. Using the look-up tables is a fast operation compared to time consuming approximation algorithms. In EKF algorithm there are 125 multiplications and 78 additions. In both methods parameter dependent constants are calculated off-line and multiplications with zero are eliminated. If the parameters are estimated on-line they can be updated in the slower time level compared to the estimator algorithm.

Computational requirements were also compared with Matlab running in the personal computer with Intel Pentium processor. Both algorithms were driven 10^5 times in a for-loop. Time was measured using Matlab's timer functions.

If the relative duration of the "exact linearization" for-loop is 1, the time needed by EKF is approximately 3.6. This ratio is in agreement with the number of computations of these methods. ELO was also tested using the same method and was ten times slower than EKF. However, this result is not valid in practice because the gain matrix **K** (3–6) was solved by Matlab's PLACE function which is not designed for real-time applications.

The non-linear observer would be fairly easy to implement using common microcontrollers. EKF and ELO require more optimization of algorithms if they are applied in practice.

Although the algorithms discussed above have their own features there are also properties and problems common to all state observers.

1. Instability at zero speed. Theoretically this means that the PMSM model is not observable if ω_r is zero [Åst97]. This is a common property for all model based estimators. If currents and voltages are DC-signals there is not enough information on rotor position.

2. The Need for the mechanical model. The states are corrected using the error between measured states and their estimates. All four states [i_d i_q θ_r ω_r] of the PMSM are needed to

construct the error signal between the measured current and the estimated current. This leads to the following drawbacks.

- Computational requirements are increased,
- Instead of three electrical parameters (L, R and ψ_m) mechanical parameters J and b should also be known. Load torque T_L is an additional unknown input for the system. However, it was pointed out in [Jon89], [Low93] that state observers tolerate fairly large errors in J, b or T_L.

3. Steady state errors in speed estimate due to the parameter errors. The reason can be seen by observing the model of the PMSM (3–4). For example, if the estimated ψ_m is greater than the actual PM flux, the observer must decrease the estimated ω_r to keep the estimated i_q equal to the measured one. This leads to an increased actual speed. Resistance errors also cause steady state speed error. This is illustrated in Fig. 3.1 and Fig. 3.2, where EKF and the "exact linearization" observer are simulated in the case of overestimated ψ_m [Esk02].

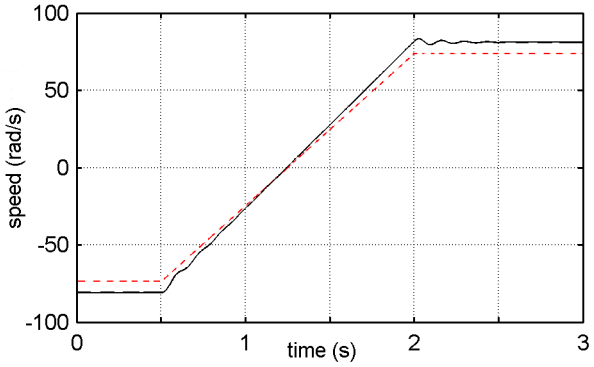

Fig. 3.1 EKF: Speed reference (dashed), simulated speed (solid). +10% error in estimated ψ_m [Esk02].

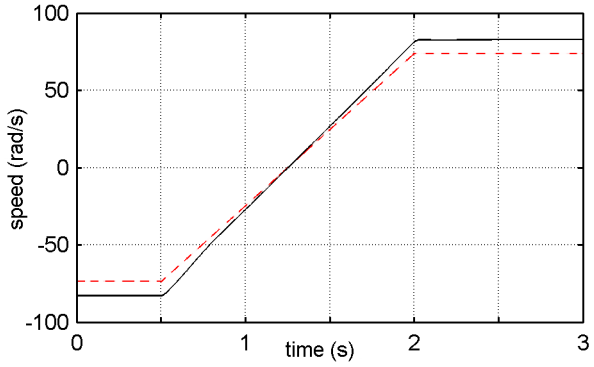

Fig. 3.2 Non-linear observer: Speed reference (dashed), simulated speed (solid). +10% error in estimated ψ_m [Esk02].

This is a problem if the steady state speed needs to be known accurately. To overcome these problems the parameters should be estimated. This increases the computational burden and complexity of the system.

Apart from computationally heavy methods (ELO, EKF), the major drawbacks of the state observers are steady state speed errors and the need for modelling of the mechanics. Therefore state observers are not further discussed.

3.3 Phase locked loop structure in sensorless control of PMSM

A phase locked loop is a device or an algorithm which causes one signal to track another one [Hsi96], [Ste97]. In this section the use of a PLL in sensorless control of the PMSM is discussed. The basic structure of the PLL suitable to estimate the speed and the position of the

PMSM is illustrated in Fig. 3.3. The phase detector block calculates the error signal ε, which is a function of the estimation error. The phase detector embodies the control system, the model of the motor and the measured quantities used to calculate the error signal ε. As will be seen in the following sections, the position estimation error $\tilde{\theta}_\mathrm{r} = \theta_\mathrm{r} - \hat{\theta}_\mathrm{r}$ causes an error signal which can be written in the form:

$$\varepsilon = K \sin(\tilde{\theta}_\mathrm{r}) \tag{3–12}$$

where K is an application specific gain parameter. The error ε can be used to force the position estimate to its true value using the following non-linear algorithm [Har00]

$$\frac{d\hat{\omega}_\mathrm{r}}{dt} = \mathrm{k}_1 \varepsilon \tag{3–13}$$

$$\frac{d\hat{\theta}_\mathrm{r}}{dt} = \hat{\omega}_\mathrm{r} + \mathrm{k}_2 \varepsilon \tag{3–14}$$

where k_1 and k_2 are gain parameters. The structure of the algorithm (3–13), (3–14) can be considered as a PI controller and an integrator connected in series, Fig. 3.3. The basic structure shown in Fig. 3.3 can be used in the case of model based and injection estimators. Every estimation method has its own phase detector system.

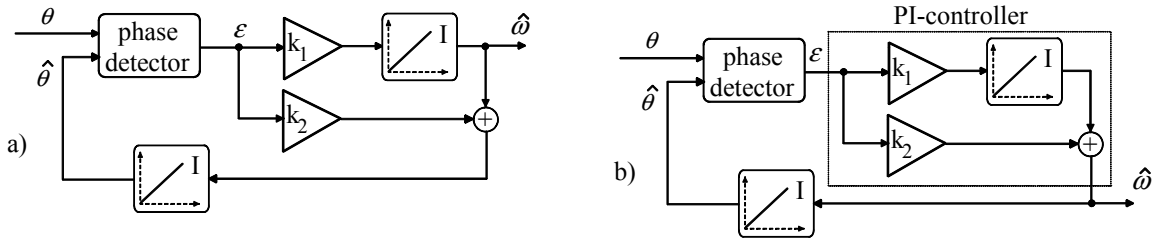

Fig. 3.3 Speed and position estimator using PLL structure. a) Speed estimate is an integral of the position error, b) speed estimate is the output of the PI controller.

Dynamics of the PLL

The estimate of angular speed of the PMSM can be taken from the output of the integral branch [Har00], Fig. 3.3a, or from the output of the PI-controller, Fig. 3.3b. The latter is faster and commonly used in the literature, [And99], [Lee04a], [Mat90]. In this study the slower version is preferred because it is less sensitive to noise.

To make the analysis of the PLL easier the error ε is linearized by assuming $\sin(\theta_\mathrm{r} - \hat{\theta}_\mathrm{r}) \approx \theta_\mathrm{r} - \hat{\theta}_\mathrm{r} = \tilde{\theta}_\mathrm{r}$. This is a valid assumption if the estimation error is small. It is also assumed that ε is calculated correctly and without delay. (3–13) and (3–14) are now written as

$$\frac{d\hat{\omega}_\mathrm{r}}{dt} = \mathrm{k}_1 K\tilde{\theta}_\mathrm{r} \tag{3–15}$$

$$\frac{d\hat{\theta}_\mathrm{r}}{dt} = \hat{\omega}_\mathrm{r} + \mathrm{k}_2 K\tilde{\theta}_\mathrm{r} \tag{3–16}$$

Using these linearized equations transfer functions for the estimated speed can be written:

$$\frac{\hat{\omega}_\mathrm{r}(s)}{\omega_\mathrm{r}(s)} = \frac{\mathrm{k}_1 K}{s^2 + \mathrm{k}_2 K s + \mathrm{k}_1 K} \qquad \text{(Fig. 3.3a)} \tag{3–17}$$

$$\frac{\hat{\omega}_\mathrm{r}(s)}{\omega_\mathrm{r}(s)} = \frac{\mathrm{k}_2 K s + \mathrm{k}_1 K}{s^2 + \mathrm{k}_2 K s + \mathrm{k}_1 K} \qquad \text{(Fig. 3.3b)} \tag{3–18}$$

In both cases the transfer function between the estimated and the actual position θ_r is similar to (3–18). In order to gain robustness and avoid oscillations both poles are placed at the real axis: $s = -\rho$, where ρ is a positive constant. This type of a pole placement is mostly used in this study. The characteristic polynomial is then $s^2 + 2\rho s + \rho^2$, so the gain parameters k_1 and k_2 should be chosen as

$$\mathrm{k}_1 = \frac{\rho^2}{K},\ \mathrm{k}_2 = \frac{2\rho}{K} \tag{3–19}$$

where k_2 is the gain k_p of the PI controller and k_1 is $\mathrm{k}_\mathrm{p} / t_\mathrm{i}$, Fig. 3.3. In [Har00] the properties of the PLL type estimator are studied in detail when the parameters of the PI part were chosen as described above. The analysis is not repeated here. Step responses of (3–17) and (3–18) are shown in Fig. 3.4.

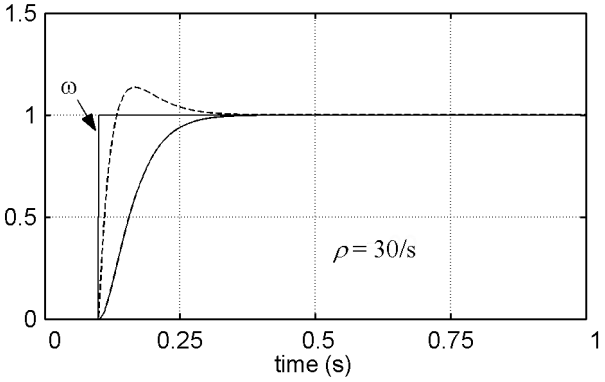

Fig. 3.4 Step response of the PLL. Speed is estimated using (3–17) (solid line) and (3–18) (dashed line).

Let us is assume that the actual speed ω_r is constant. (3–15) and (3–16) are subtracted from $\mathrm{d}\omega_\mathrm{r}/\mathrm{d}t$ (=0) and $\mathrm{d}\theta_\mathrm{r}/\mathrm{d}t$. If a small estimation error is assumed the following differential

equations for estimation error can be written where the noise component n is added to the linearized error component $K\tilde{\theta}_\mathrm{r}$.

$$\frac{d\tilde{\omega}_\mathrm{r}}{dt} = -\frac{\rho^2}{K}(K\tilde{\theta}_\mathrm{r} + n) \tag{3–20}$$

$$\frac{d\tilde{\theta}_\mathrm{r}}{dt} = \tilde{\omega}_\mathrm{r} - \frac{2\rho}{K}(K\tilde{\theta}_\mathrm{r} + n) \tag{3–21}$$

When the angle error is solved from (3–21) and substituted into (3–20) we obtain the relation between disturbance n and estimation errors for speed and position.

$$\tilde{\omega}_\mathrm{r} = -\frac{\rho^2}{K}\left(\frac{s}{(s+\rho)^2}\right)n \tag{3–22}$$

$$\tilde{\theta}_\mathrm{r} = -\frac{\rho}{K}\left(\frac{2s^2 + 5\rho s + 2\rho^2}{(s+2\rho)(s+\rho)^2}\right)n \tag{3–23}$$

The relation between the speed error and noise is a band pass filter with centre frequency ρ (3–22). The steady state speed error is zero if disturbance n is a DC-signal. This means that slowly varying disturbances like parameter uncertainties do not produce a speed error in steady state. This is a clear advantage compared to the observers discussed in previous sections. Transfer function between position error and noise is a low pass filter with non-zero DC-gain (3–23). Thus the parameter errors can create a position error in steady state operation.

3.4 Back-emf estimators

This section deals with estimators where the primary estimated quantity is the back-emf of the PMSM. First the idea of speed and position estimation directly from voltage equations of the PMSM (2-12) is discussed in Chapter 3.4.1. Some examples taken from the literature are presented. Direct estimation from voltage equations is a simple task but leads to problems with steady state errors if parameters are not accurately known. Therefore the rest of Chapter 3.4 concentrates on methods where a PLL type algorithm is used to remove the steady state errors. The error signal of the PLL (3–12) in the case of PMSM drive is derived in Section 3.4.2. Section 3.4.3 deals with estimators where the speed is estimated directly from voltage equations and the effect of parameter errors is corrected by a PLL algorithm. Section 3.4.4

deals with the current tracking estimator. This method is also based on the estimated back-emf information but the error between measured and estimated current is used instead of the voltage error. The best properties of estimators discussed in Sections 3.4.3 and 3.4.4 are combined in one algorithm in Section 3.4.5. In this Section 3.4, L_d and L_q do not vary as a function of the rotor position. The effect of non-sinusoidal flux linkage and inductance variations are studied by simulations in Section 3.6.

3.4.1 Direct speed and position estimation

A very straightforward strategy to estimate the angular speed ω_r of the PMSM is presented below. The speed is solved directly from the imaginary component of the voltage equation in the rotor frame (2-12).

$$u_q = Ri_q + L_q \frac{di_q}{dt} + \omega_r (L_d i_d + \psi_m) \Rightarrow \hat{\omega}_r = \frac{u_{qe} - \hat{R} i_{qe} - \hat{L}_q \frac{di_{qe}}{dt}}{\hat{\psi}_m} \tag{3–24}$$

The subscripts de and qe denote quantity in the estimated rotor reference frame (control system reference frame). The position estimate is obtained by integrating the estimated speed.

If parameters, currents and voltages are accurately known the PLL algorithm would be unnecessary because (3–24) gives a correct estimate for the speed. In transients the estimate would be slightly delayed due to the current control. In practice ω_r estimated by (3–24) always contains a steady state error. Using the actual motor quantities (3–24) can be written in steady state (current derivatives are zero):

$$\hat{\omega}_2 = (u_{qe} - \hat{R} i_{qe}) / \hat{\psi}_m = (u_q \cos\tilde{\theta}_r + u_d \sin\tilde{\theta}_r - \hat{R} i_q \cos\tilde{\theta}_r - \hat{R} i_d \sin\tilde{\theta}_r) / \hat{\psi}_m \tag{3–25}$$

The subscript 2 in ω denotes the output of the direct speed estimator. The current seen by the control system is

$$\underline{i}^{re} = \underline{i}^{r} e^{j\tilde{\theta}_r} \Leftrightarrow i_{de} = i_d \cos\tilde{\theta}_r - i_q \sin\tilde{\theta}_r, i_{qe} = i_q \cos\tilde{\theta}_r + i_d \sin\tilde{\theta}_r \tag{3–26}$$

The current control drives the average of i_{de} to zero (in this thesis $i_{d,ref} = 0$). The steady state d axis current is

$$i_d = i_q \tan\tilde{\theta}_r \tag{3–27}$$

The rotor frame voltage equation (2-12) and (3–27) are substituted into (3–25). Now the speed estimate in steady state is:

$$\hat{\omega}_2 = \omega_r \left(\frac{\psi_m}{\hat{\psi}_m} \cos\tilde{\theta}_r + \frac{(L_d - L_q)}{\hat{\psi}_m} i_q \sin\tilde{\theta}_r \right) + \frac{\tilde{R}}{\hat{\psi}_m} (i_q \cos\tilde{\theta}_r + i_d \sin\tilde{\theta}_r) \quad (3–28)$$

The system is unstable without PLL correction if parameter errors force $|\hat{\omega}_2|$ to be smaller than $|\omega_r|$. Let us consider the case when $\omega_r > 0$, $i_q > 0$, $\psi_m - \hat{\psi}_m < 0$ and $\tilde{R} = 0$. The position error is initially zero. The estimate given by (3–28) is smaller than ω_r and the speed control tries to drive the speed error to zero by increasing the q axis current reference. The position estimate is the integral of the speed estimate. Now the position error $\tilde{\theta}_r$ increases because (3–28) gives too small estimate for speed. Increased position error further decreases the estimated speed. This creates a positive feedback. If $\tilde{R} < 0$ the effect is similar. In the opposite case the system is stable but a steady state position error remains. If parameter errors increase the absolute value of the speed estimate $\hat{\omega}_2$ the system stabilizes to the operating point where the left and right hand sides of (3–28) are equal. The speed error is zero in steady state. Analytical solution of the steady state position error would lead to a very complicated expression. It can be checked by simulations that rather small parameter errors create significant steady state position errors.

This parameter sensitivity is the main reason why the real part of the voltage model (2-12) should be also exploited. As will be explained in the next section (3.4.2) the d axis voltage equation contains position error information.

Estimators in the literature

In [Pii04] the speed is estimated directly using the q axis voltage model (3–24). The parameter sensitivity of the estimator was decreased by an additional PM flux estimator. The total estimator algorithm is simple and the performance in experimental tests was fairly satisfactory [Pii04]. However, the position error can be significant if the R and ψ_m are not accurately known.

The paper published by Kim and Sul [Kim97] is a widely cited publication where the speed and position are determined directly from the estimated back-emf in the estimated synchronous reference frame. A non-salient PMSM was assumed. If $L_d = L_q = L$ the voltage model in the estimated rotor frame can be approximated as

$$u_{\mathrm{de}} \approx Ri_{\mathrm{de}} + L\frac{di_{\mathrm{de}}}{dt} - \hat{\omega}_{\mathrm{r}} Li_{\mathrm{qe}} - \underbrace{\omega_{\mathrm{r}}\psi_{\mathrm{m}} \sin\tilde{\theta}}_{e_{\mathrm{de}}}$$
$$u_{\mathrm{qe}} \approx Ri_{\mathrm{qe}} + L\frac{di_{\mathrm{qe}}}{dt} + \hat{\omega}_{\mathrm{r}} Li_{\mathrm{de}} + \underbrace{\omega_{\mathrm{r}}\psi_{\mathrm{m}} \cos\tilde{\theta}}_{e_{\mathrm{qe}}} \qquad (3\text{–}29)$$

Flux components Li_{d}, Li_{q} are multiplied by the estimated speed because it is the derivative of the position angle of the estimated reference frame. Equation (3–29) will be further discussed in Section 3.4.2. In [Kim97] current derivatives were removed using the idea of "electrical steady state". Current sampling and control of currents were performed more frequently than the speed control and the estimator. The longer time interval is called an "estimation period". Current samples from the end of the estimation period are used. It was assumed that even in speed transients the currents are constants at the end of the estimation period. Thus $d\underline{i}^{\mathrm{re}}/dt = 0$. The estimated position used in current control was fixed to a constant for one estimation period. If the estimated angle is constant $d\hat{\theta}_{\mathrm{r}} / dt = \hat{\omega}_{\mathrm{r}} = 0$. Now the derivatives are removed from (3–29) and it can be written for the position error

$$\frac{e_{\mathrm{de}}}{e_{\mathrm{qe}}} = \frac{-u_{\mathrm{de}*} + Ri_{\mathrm{de}}}{u_{\mathrm{qe}*} - Ri_{\mathrm{qe}}} = \frac{\psi_{\mathrm{m}}\omega_{\mathrm{r}} \sin\tilde{\theta}_{\mathrm{r}}}{\psi_{\mathrm{m}}\omega_{\mathrm{r}} \cos\tilde{\theta}_{\mathrm{r}}} = \tan\tilde{\theta}_{\mathrm{r}} \approx \tilde{\theta}_{\mathrm{r}} \qquad (3\text{–}30)$$

In (3–30) voltages $u_{\mathrm{de}*}$ and $u_{\mathrm{qe}*}$ are not the same as steady state voltages of (3–29) because the estimated speed is zero. Position error (3–30) is added to the previous estimate at each estimation interval. Thus it can be considered an input of the discrete time integrator. The position is calculated:

$$\hat{\theta}_{\mathrm{emf}}(\mathrm{k}) = \hat{\theta}_{\mathrm{emf}}(\mathrm{k}\text{-}1) + \tilde{\theta}_{\mathrm{r}} = \hat{\theta}_{\mathrm{emf}}(\mathrm{k}\text{-}1) + \hat{\omega}_{\mathrm{r}} t_{\mathrm{s}} \qquad (3\text{–}31)$$

where t_{s} is the sample time. It should be noted that $\pi/2$ rad must be subtracted from the angle θ_{emf} to obtain the estimate of the rotor position.

This position estimator is a tracking type method where the actual error signal is $-u_{\mathrm{de}*} + Ri_{\mathrm{de}}$. If the position estimate is smaller than the actual position the error ($\tilde{\theta}_{\mathrm{r}} = \theta_{\mathrm{r}} - \hat{\theta}_{\mathrm{r}} > 0$). The position estimate (3–31) will also be too large. As a result e_{de} increases and the estimated position will be corrected toward the actual value during the next sampling period. The same idea natually works when the position estimate is leading the actual position.

If i_{de} is small the parameter R in the denominator of (3–30) only changes the gain of the position error signal (3–31) if it is not accurately known. Therefore parameter errors have no significant influence on the steady state position estimate.

In [Kim97] the speed is estimated using a separate algorithm where the length of the estimated back-emf is divided by PM flux. The speed estimate is naturally sensitive to errors of ψ_m and R. The estimate of ψ_m is corrected by a fairly simple algorithm. The estimated speed is compared to the speed estimated directly from the position error, $\hat{\omega}_r = \tilde{\theta}_r / t_s$ (3–31). This signal is noisy but in steady state its average is equal to the actual speed. The difference between the speed estimates is the input for a PI controller and the output of the controller is used to correct the estimated ψ_m.

The algorithm introduced in [Kim97] has a simple structure and good position tracking properties. The main drawbacks are the parameter sensitive speed estimator and the need for parameter correction.

In [Bat00] the rotor position of the PMSM is estimated by a state observer based on the voltage equation in stationary frame. This method suffers from the same drawbacks as the state observers discussed in previous sections. In the position estimator the gain matrix should be updated when ω_r changes. The estimated speed contains steady state errors if R or ψ_m are not correctly estimated. The position estimate has been reported to be rather insensitive to parameter errors [Bat00].

3.4.2 Voltage equations in the estimated synchronous reference frame

The voltage equation of the PMSM is analysed in steady state conditions. The control and estimator algorithms are performed in the estimated synchronous reference frame. The frequency converter is assumed to be ideal. There is no voltage error between the voltage reference and the actual stator voltage. Higher order harmonics of flux linkage and inductances are ignored. In that case voltages u_{de} and u_{qe} are the voltage reference signals $u_{de,ref}$ and $u_{qe,ref}$. These signals are the outputs of the d and q axis current controllers. The voltage equations of the PMSM in the actual rotor frame are

$$\begin{aligned} u_d &= Ri_d + L_d \frac{di_d}{dt} - \omega_r L_q i_q \\ u_q &= Ri_q + L_q \frac{di_q}{dt} + \omega_r (L_d i_d + \psi_m) \end{aligned} \tag{3–32}$$

Current derivatives can be ignored because steady state operation is analysed. The voltage equation (3–32) is transformed into the estimated rotor reference frame, $\underline{u}^{re} = \underline{u}^{r} e^{j\tilde{\theta}_r}$, Fig. 3.5a. The voltage components in the estimated d,q frame are

$$
\begin{aligned}
u_{\mathrm{de}} &= Ri_{\mathrm{de}} - \hat{\omega}_{\mathrm{r}}\left(i_{\mathrm{de}}\cos\tilde{\theta}_{\mathrm{r}}\sin\tilde{\theta}_{\mathrm{r}}(L_{\mathrm{d}}-L_{\mathrm{q}}) + i_{\mathrm{qe}}(L_{\mathrm{q}}\cos^2\tilde{\theta}_{\mathrm{r}} + L_{\mathrm{d}}\sin^2\tilde{\theta}_{\mathrm{r}})\right) - \omega_{\mathrm{r}}\psi_{\mathrm{m}}\sin\tilde{\theta}_{\mathrm{r}} \\
u_{\mathrm{qe}} &= Ri_{\mathrm{qe}} - \hat{\omega}_{\mathrm{r}}\left(-i_{\mathrm{de}}(L_{\mathrm{q}}\sin^2\tilde{\theta}_{\mathrm{r}} + L_{\mathrm{d}}\cos^2\tilde{\theta}_{\mathrm{r}}) - i_{\mathrm{qe}}\cos\tilde{\theta}_{\mathrm{r}}\sin\tilde{\theta}_{\mathrm{r}}(L_{\mathrm{d}}-L_{\mathrm{q}})\right) + \omega_{\mathrm{r}}\psi_{\mathrm{m}}\cos\tilde{\theta}_{\mathrm{r}}
\end{aligned}
\tag{3–33}
$$

where $\tilde{\theta}_{\mathrm{r}} = \theta_{\mathrm{r}} - \hat{\theta}_{\mathrm{r}}$. The voltages u_{de}, u_{qe} in (3–33) are the steady state outputs of the current controllers (voltage references). Motor parameters (R, L_{d}, L_{q}, ψ_{m}) are accurately known.

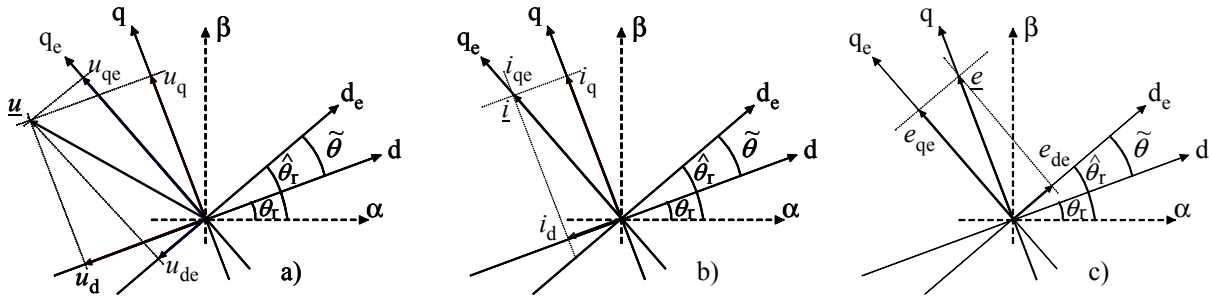

Fig. 3.5 Transformation between actual and estimated rotor reference frame: a) $\underline{u}$ b) $\underline{i}$ c) back-emf.

The position error $\tilde{\theta}_{\mathrm{r}}$ is unknown to the estimator algorithm. The software can calculate the steady state voltage by the following expression

$$
\begin{aligned}
\hat{u}_{\mathrm{de}} &= \hat{R}i_{\mathrm{de}} - \hat{\omega}_{\mathrm{r}}\hat{L}_{\mathrm{q}}i_{\mathrm{qe}} \\
\hat{u}_{\mathrm{qe}} &= \hat{R}i_{\mathrm{qe}} + \hat{\omega}_{\mathrm{r}}\hat{L}_{\mathrm{d}}i_{\mathrm{de}} + \hat{\omega}_{\mathrm{r}}\hat{\psi}_{\mathrm{m}}
\end{aligned}
\tag{3–34}
$$

The parameters used in (3–34) are estimates. Let us assume there are no parameter errors. The angular speed is estimated. In steady state the estimated speed is equal to the actual speed if the PLL algorithm is used. If (3–34) is subtracted from (3–33) it is possible to write the following voltage errors for the d and q axes.

$$
\begin{aligned}
u_{\mathrm{de}} - \hat{u}_{\mathrm{de}} = \tilde{u}_{\mathrm{de}} &= -\hat{\omega}_{\mathrm{r}}\sin\tilde{\theta}_{\mathrm{r}}\left((L_{\mathrm{d}}-L_{\mathrm{q}})(i_{\mathrm{de}}\cos\tilde{\theta}_{\mathrm{r}} + i_{\mathrm{qe}}\sin\tilde{\theta}_{\mathrm{r}})\right) - \omega_{\mathrm{r}}\psi_{\mathrm{m}}\sin\tilde{\theta}_{\mathrm{r}} \approx -\omega_{\mathrm{r}}\psi_{\mathrm{m}}\tilde{\theta}_{\mathrm{r}} \\
u_{\mathrm{qe}} - \hat{u}_{\mathrm{qe}} = \tilde{u}_{\mathrm{qe}} &= -\hat{\omega}_{\mathrm{r}}\sin\tilde{\theta}_{\mathrm{r}}\left((L_{\mathrm{d}}-L_{\mathrm{q}})(i_{\mathrm{de}}\sin\tilde{\theta}_{\mathrm{r}} - i_{\mathrm{qe}}\cos\tilde{\theta}_{\mathrm{r}})\right) + \omega_{\mathrm{r}}\psi_{\mathrm{m}}(\cos\tilde{\theta}_{\mathrm{r}} - 1)
\end{aligned}
\tag{3–35}
$$

$\tilde{u}_{\mathrm{de}}$ is the d axis component of the back-emf vector $\underline{e}$, Fig. 3.5c. $\tilde{u}_{\mathrm{de}}$ is a suitable error signal for PLL algorithm (3–12). Saliency has only a negligible effect because i_{de} and $\sin\tilde{\theta}_{\mathrm{r}}$ are controlled to zero in steady state. If the d axis error is compared to (3–12) the gain parameter K is now - $\omega_{\mathrm{r}}\psi_{\mathrm{m}}$.

In practice the input for PLL ($\tilde{u}_{\mathrm{de}}$) can be solved using the d axis voltage reference signal and (3–34). In steady state $u_{\mathrm{de}} = u_{\mathrm{de,ref}}$ (3–33). It can be seen from (3–35) that the voltage reference $u_{\mathrm{de,ref}} > \hat{u}_{\mathrm{de}}$ if $\tilde{\theta}_{\mathrm{r}} < 0$. If $\tilde{\theta}_{\mathrm{r}} > 0$, $u_{\mathrm{de,ref}} < \hat{u}_{\mathrm{de}}$. The d axis voltage can be estimated:

$-\hat{\omega}_r \hat{L}_q i_{qe} = \hat{u}_{de}$ (3–34) if i_{de} is controlled to zero in steady state. The d axis component of the back-emf can be approximated as

$$\tilde{u}_{de} \approx (-u_{de,ref} - \hat{\omega}_r \hat{L}_q i_{qe}) \text{sign}(\hat{\omega}_r) \quad (3–36)$$

The result must be multiplied by the sign of the rotor speed because the sign of the d axis component of the back-emf is dependent on the sign of ω_r (3–35).

The q axis voltage error (3–35) is not a suitable input for the PLL algorithm. However, $u_{q,ref}$ is proportional to ω_r. Thus it contains information which can be exploited in the speed estimation process.

3.4.3 Back-emf estimator with the phase locked loop structure

Matsui introduced in [Mat90] a simple estimator based on the voltage equation of the PMSM transformed to the estimated rotor frame (3–33). The rotor speed is estimated using two separate algorithms. The speed is estimated primarily by the direct method using the q axis voltage equation (3–24). As discussed in 3.4.1, direct speed estimators are sensitive for parameter errors. Matsui's novel idea was to correct the output of the direct estimator with a PLL type algorithm. The d axis voltage equation (3–33) in the estimated rotor reference frame, Fig. 3.5, contains information on the position error. The input signal for the PLL is calculated by (3–36). The output of the PLL is added to the direct estimate, $\hat{\omega}_2$ (3–24). Finally the position is estimated by integrating the sum of two speed estimates. The block diagram of the estimator is presented in Fig. 3.6.

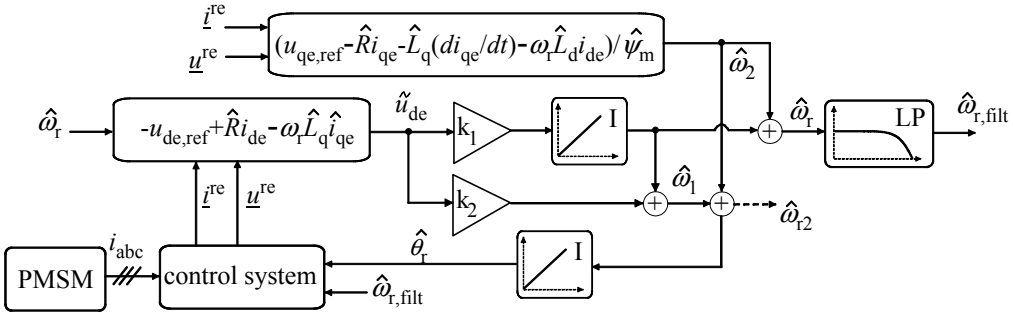

Fig. 3.6 Speed and position estimator with feedforward branch and PLL in synchronous frame. Matsui's voltage model method.

Matsui's original estimator is not equal to the Fig. 3.6. In [Mat90] the speed estimate used in the speed control was the sum of $\hat{\omega}_1$ and $\hat{\omega}_2$ ($\hat{\omega}_{r2}$ in Fig. 3.6). In this thesis the output of the integrator of the PLL was used as an speed estimate for speed control purposes due to the lower noise sensitivity.

In Fig. 3.6 the derivative of i_{de} is not included in the PLL input because i_{de} is held at zero and its amplitude is rather small in transients too. Therefore i_{de} can be completely omitted from the software implementation without significant impairment of the dynamic performance.

The model based algorithm introduced by Matsui has inspired several authors to publish methods closely related to [Mat90]. The PLL type voltage model estimator is studied also in [Har00], [Sak01], [Lee04a]. In [Har00], [Lee04a] the PLL algorithm was used without the direct speed estimator (3–24). In [Sak01] the position error signal was calculated by arctan method as in [Kim97], (3–30). The signal was input for the PLL algorithm. No direct speed estimator was used. These methods utilise only the d axis back-emf information.

[Mat90] is studied in detail in this thesis because it utilises the information of both the real and imaginary axes of the estimated back-emf. Compared to state observers it has a rather simple structure. The steady state speed error is zero even if the motor parameters are not accurately known. In the following sections [Mat90] is called Matsui's voltage model method.

Matsui's estimator in stationary reference frames

The author presented a "novel" voltage model based estimator in [Esk03]. In fact, this estimator method is a direct counterpart to [Mat90] in the stationary reference frame. The block diagram is illustrated in Fig. 3.7. In [Esk03] the estimator was proposed for PMSMs with a saliency ratio close to unity ($L_d = L_q = L$). The fundamental frequency voltage equation of the PMSM (3–32) can be written in stationary reference frame as

$$\begin{aligned} \underline{u}^{\mathrm{s}} &= R\underline{i}^{\mathrm{s}} + \frac{\mathrm{d}\underline{\psi}^{\mathrm{s}}}{\mathrm{d}t} = R\underline{i}^{\mathrm{s}} + L\frac{\mathrm{d}\underline{i}^{\mathrm{s}}}{\mathrm{d}t} + \mathrm{j}\omega_{\mathrm{r}}\psi_{\mathrm{m}} \cdot e^{\mathrm{j}\theta_{\mathrm{r}}} \\ \Rightarrow \hat{\omega}_{\mathrm{r}} &= \frac{\mathrm{d}\hat{\theta}_{\mathrm{r}}}{\mathrm{d}t} = \underbrace{(\underline{u}^{\mathrm{s}}_{\mathrm{ref}} - \hat{R}\underline{i}^{\mathrm{s}} - \hat{L}\frac{\mathrm{d}\underline{i}^{\mathrm{s}}}{\mathrm{d}t})}_{\underline{y}} \cdot \underbrace{e^{\mathrm{j}(\hat{\theta}_{\mathrm{r}}+\pi/2)}}_{\underline{w}} \cdot \frac{1}{\hat{\psi}_{\mathrm{m}}}. \end{aligned} \tag{3–37}$$

$\underline{y}$ is a back-emf phasor whose length is proportional to the angular speed and its angle leads the d axis $\pi/2$ rad. $\underline{w}$ is a phasor with a length of 1 and it leads the estimated rotor position by $\pi/2$ rad. If the imaginary part of the product $\underline{y}\underline{w}^*$ (cross product of vectors) is zero, the phasors $\underline{w}$ and $\underline{y}$ are in phase and the estimated position angle is correct, provided that the parameters are known. The angle increment is mainly composed of $\mathrm{Re}\{\underline{y}\underline{w}^*\}$. $\mathrm{Im}\{\underline{y}\underline{w}^*\}$ is an error signal which is an input for the PLL algorithm.

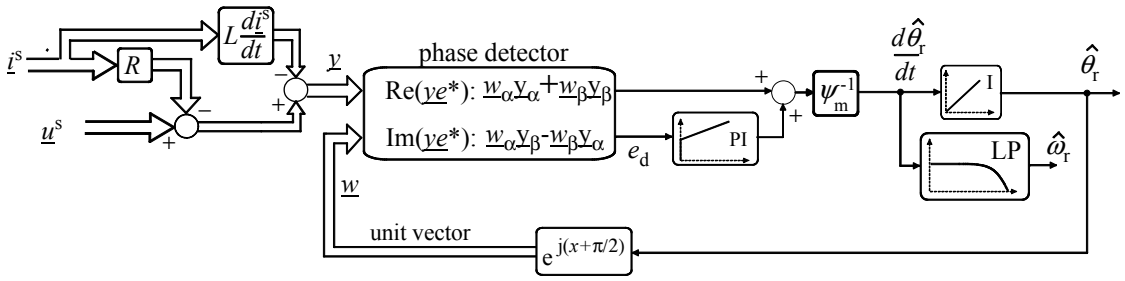

Fig. 3.7 Back-emf estimator with feedforward branch in the stationary reference frame.

Other papers applying stationary frame equations have also been published. In [Yin02] the position was estimated in stationary frame using three-phase equations. [Yin02] was improved using PLL structure in [Yin03] which is a three phase counterpart of [Esk03].

3.4.3.1 Estimation of the speed and position using only the phase locked loop

The direct branch of the speed estimation process was discussed in Section 3.4.1. In this section the PLL branch of the Matsui's voltage model method is studied. Equations for the gains of the PI controller are presented and parameter sensitivity is analysed.

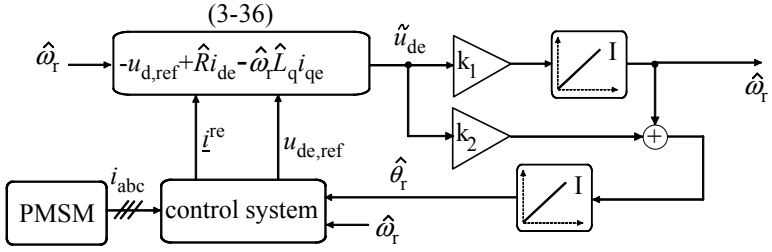

Fig. 3.8 Block diagram of the back-emf estimator in the rotor reference frame.

The gain parameter K of the PLL (3–12) is speed dependent ($-\omega_r \psi_m$) as discussed. This is a drawback because the gains k_1 and k_2 of the PI controller, Fig. 3.6, Fig. 3.8 must be a function of the estimated speed if the bandwidth of the PLL is kept constant. In the original paper [Mat90] constant gains were used. Because K is proportional to speed the gains k_1 and k_2 must be inversely proportional to the estimated speed. This leads to infinite gains at zero speed. Gains k_1 and k_2 are limited when the estimated speed approaches zero [Har00]. Thus the bandwidth of the speed control loop is reduced at low speeds. The following gains are used in this thesis

$$\text{If } |\hat{\omega}_r| > \omega_{low}: \quad k_1 = \frac{\rho^2}{\hat{\omega}_r \hat{\psi}_m}, \; k_2 = \frac{2\rho}{\hat{\omega}_r \hat{\psi}_m} \tag{3–38a}$$

$$\text{If } |\hat{\omega}_r| \le \omega_{low}: \quad k_1 = \frac{\text{sign}(\hat{\omega}_r)\rho^2}{\omega_{low} \hat{\psi}_m}, \; k_2 = \frac{\text{sign}(\hat{\omega}_r)2\rho}{\omega_{low} \hat{\psi}_m} \tag{3–38b}$$

The pure PLL estimator has some drawbacks. The rate of convergence at low speeds is decreased because the gains k_1 and k_2 must be limited. If the inertia of the drive is small and fast accelerations are required, the PLL is easily pulled out of phase lock. To prevent this the poles of the PLL algorithm must be placed far from the imaginary axis. This increases k_1 and k_2, which means the noise is more heavily amplified.

In [Wal05] the transient performance of the PLL was improved by boosting the input of the integrator, Fig. 3.9. The output of the PLL was subtracted from the speed estimate achieved directly from the length of the estimated back-emf. The result was amplified and added to the input of the integrator. However, Matsui's voltage method, Fig. 3.6, Fig. 3.7, is faster because the direct estimate is not fed through the integrator.

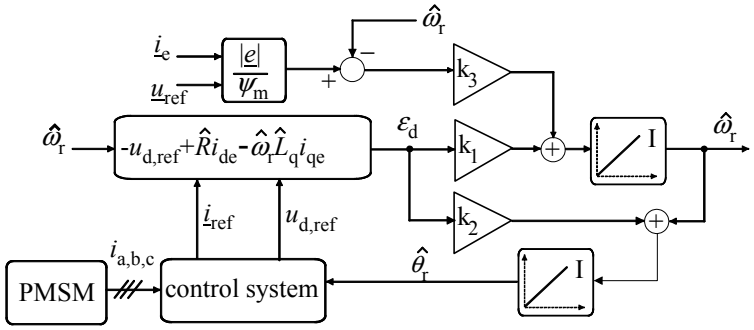

Fig. 3.9 Improved PLL estimator [Wal05].

The effect of parameter errors

In steady state the derivative of the speed of the PMSM is zero. The steady state speed error $\tilde{\omega}_r$ is also zero when PLL type algorithm is used. Derivatives of the estimates of speed (3–13) and position (3–14) are subtracted from the derivatives of the actual quantities. After subtraction the speed and position error derivatives can be written [Har00]:

$$\begin{cases} \dfrac{d\tilde{\omega}_r}{dt} = -k_1\varepsilon = 0 \Rightarrow \varepsilon = 0 \\ \dfrac{d\tilde{\theta}_r}{dt} = \tilde{\omega}_r - k_2\varepsilon = 0 \end{cases} \tag{3–39}$$

Thus the d axis voltage error signal (3–35) is zero in steady state conditions.

In Section 3.4.2 the equation of the d axis voltage error (position error signal) was obtained by subtracting the estimator's u_{de} (3–34) from the actual u_{de} (3–33). Now the same subtraction is made with parameter errors, $\hat{R} \neq R$ and $\hat{L}_q \neq L_q$. The steady state voltage error signal of d axis can be written:

$$\tilde{u}_{de} = \omega_r \tilde{L}_q i_{qe} - \tilde{R} i_{de} - \omega_r \left((L_q - L_d)(i_{de}\cos\tilde{\theta}_r + i_{qe}\sin\tilde{\theta}_r) - \psi_m \right) \sin\tilde{\theta}_r = 0 \;|_{\omega=\hat{\omega}} \tag{3–40}$$

where $\tilde{L}_\mathrm{q} = L_\mathrm{q} - \hat{L}_\mathrm{q}$ and $\tilde{R} = R - \hat{R}$. i_de is assumed to be zero. The position error solved from (3–40) is

$$\tilde{\theta} = \begin{cases} \sin^{-1}\left(\dfrac{-1+\sqrt{1+4(L_\mathrm{q}-L_\mathrm{d})i_\mathrm{qe}^2\tilde{L}_\mathrm{q}\psi_\mathrm{m}^{-2}}}{-2(L_\mathrm{q}-L_\mathrm{d})i_\mathrm{qe}}\psi_\mathrm{m} \right) & L_\mathrm{q} \neq L_\mathrm{d} \\ -\sin^{-1}(\tilde{L}_\mathrm{q} i_\mathrm{qe}\psi_\mathrm{m}^{-1}) & L_\mathrm{q} = L_\mathrm{d} \end{cases} \quad (3\text{–}41)$$

If i_de is controlled to zero, the effect of the resistance error vanishes. PM flux ψ_m is not used in the estimation process. Thus the L_q is the only error source in steady state if the speed and the position are estimated using only the PLL, Fig. 3.8. The position error is proportional to i_qe (3–41). It should be noted that i_qe is also a function of position error. However, in the case of tolerable errors $i_\mathrm{qe} \approx i_\mathrm{q}$.

3.4.3.2 Discrete time implementation

The equations of the back-emf estimator must be converted into discrete time form before they can be implemented with a microcontroller. In this study the backward Euler approximation [Åst97] is used. Discrete time transfer function is obtained by replacing the Laplace variable *s* by (z-1)/zt_s. The discrete time algorithm of the PI controller of the PLL, Fig. 3.6, Fig. 3.8, can be written

$$\omega_1(\mathrm{k}) = \omega_1(\mathrm{k}-1) + \frac{k_\mathrm{p}t_\mathrm{s}}{t_\mathrm{i}}\tilde{u}_\mathrm{de}(\mathrm{k}) + k_\mathrm{p}\tilde{u}_\mathrm{de}(\mathrm{k}) = \omega_1(\mathrm{k}-1) + \tilde{u}_\mathrm{de}(\mathrm{k})k_1 t_\mathrm{s} + \tilde{u}_\mathrm{de}(\mathrm{k})k_2 \quad (3\text{–}42)$$

where t_s, t_i and k_p are sample time, integration time and gain respectively.

The calculation of $\hat{\omega}_2$ contains the derivative of i_q. The discrete derivative is (i_qe(k) - i_qe(k-1))/t_s. After LP filtering of the derivative $\hat{\omega}_2$ is calculated by the q axis voltage equation (3–24). The position estimate is updated by the following integral algorithm.

$$\hat{\theta}_\mathrm{r}(k) = \hat{\theta}_\mathrm{r}(k-1) + t_\mathrm{s}\left(\omega_1(k) + \omega_2(k)\right) \quad (3\text{–}43)$$

In practice the estimated speed must be filtered before it can be used in the speed control loop. The first order LP filter can be written in discrete form as follows.

$$\hat{\omega}_{\mathrm{r,filt}}(\mathrm{k}) = \frac{\tau}{\tau + t_\mathrm{s}}\hat{\omega}_{\mathrm{r,filt}}(\mathrm{k}-1) + \frac{t_\mathrm{s}}{\tau + t_\mathrm{s}}\hat{\omega}_\mathrm{r}(\mathrm{k}) \quad (3\text{–}44)$$

$\hat{\omega}_\mathrm{r} = \hat{\omega}_1 + \hat{\omega}_2$ and τ is an inverse of -3 dB corner frequency, $\tau = 1/(2\pi f_{\text{-3dB}})$

3.4.4 Back-emf estimator based on the current tracking

Matsui also introduced another interesting model based estimator [Mat92], Fig. 3.10. The estimator was compared to [Mat90] in [Mat96] where it was called a current model estimator. "Current model" is a somewhat misleading name because the estimation is based on the same equations (3–32) as Matsui's "voltage model" method. The idea of [Mat92] is to estimate ω_r and θ_r by tracking the measured currents in the estimated synchronous reference frame.

If the basic rotor frame voltage equation (3–32) is transformed to the estimated rotor reference frame (3–33), the derivatives of i_{de} and i_{qe} can be written

$$\begin{aligned}\frac{di_{de}}{dt} &= \frac{1}{L_d}\left(u_{de} - Ri_{de} + \hat{\omega}_r L_q i_{qe} + \underbrace{\omega_r \psi_m \sin\tilde{\theta}_r}_{e_{de}}\right)\\ \frac{di_{qe}}{dt} &= \frac{1}{L_q}\left(u_{qe} - Ri_{qe} - \hat{\omega}_r L_d i_{de} - \underbrace{\omega_r \psi_m \cos\tilde{\theta}_r}_{e_{qe}}\right)\end{aligned} \tag{3–45}$$

Some information is omitted when current derivatives (3–45) are solved from (3–33). A rather small position error is assumed. In that case $\sin(\tilde{\theta}_r)$ and the effect of saliency (L_d - L_q) are vanishing and can be excluded from (3–33) before (3–45) is written. e_{de} and e_{qe} are d and q axis components of the back-emf in the estimated synchronous reference frame.

If the derivative of current is known it is possible to write the following discrete time expression for the current at the next sampling period.

$$\begin{aligned}i_{de}(k+1) &= i_{de}(k) + t_s(di_{de}/dt)\\ i_{qe}(k+1) &= i_{qe}(k) + t_s(di_{qe}/dt)\end{aligned} \tag{3–46}$$

Voltage components e_{de} and e_{qe} are unknown in (3–45). Therefore the estimator must calculate the derivatives using the basic rotor frame voltage equation (3–32).

$$\begin{aligned}\frac{d\hat{i}_{de}}{dt} &= \frac{1}{\hat{L}_d}\left(u_{de} - \hat{R}i_{de} + \hat{\omega}_r \hat{L}_q i_{qe}\right)\\ \frac{d\hat{i}_{qe}}{dt} &= \frac{1}{\hat{L}_q}\left(u_{qe} - \hat{R}i_{qe} - \hat{\omega}_r \hat{L}_d i_{de} - \hat{\omega}_r \hat{\psi}_m\right)\end{aligned} \tag{3–47}$$

In the case of Equation (3–47) the current components predicted by the estimator software are

$$\begin{aligned}\hat{i}_{\mathrm{de}}(\mathrm{k}+1) &= i_{\mathrm{de}}(\mathrm{k}) + t_{\mathrm{s}}(d\hat{i}_{\mathrm{de}}/dt)\\ \hat{i}_{\mathrm{qe}}(\mathrm{k}+1) &= i_{\mathrm{qe}}(\mathrm{k}) + t_{\mathrm{s}}(d\hat{i}_{\mathrm{qe}}/dt)\end{aligned} \tag{3–48}$$

The parameters of (3–47) are assumed to be accurately known. If (3–48) is subtracted from (3–46) the error between measured and estimated current is

$$\begin{aligned}\tilde{i}_{\mathrm{de}}(\mathrm{k}+1) &= i_{\mathrm{de}}(\mathrm{k}+1) - \hat{i}_{\mathrm{de}}(\mathrm{k}+1) = \frac{t_{\mathrm{s}}}{L_{\mathrm{d}}} e_{\mathrm{de}}(\mathrm{k}) \approx \frac{t_{\mathrm{s}}\psi_{\mathrm{m}}}{L_{\mathrm{d}}}\omega_{\mathrm{r}}\tilde{\theta}_{\mathrm{r}}(\mathrm{k})\\ \tilde{i}_{\mathrm{qe}}(\mathrm{k}+1) &= i_{\mathrm{qe}}(\mathrm{k}+1) - \hat{i}_{\mathrm{qe}}(\mathrm{k}+1) = -\frac{t_{\mathrm{s}}}{L_{\mathrm{q}}}\left(e_{\mathrm{qe}}(\mathrm{k}) - \hat{\omega}_{\mathrm{r}}(\mathrm{k})\psi_{\mathrm{m}}\right) \approx -\frac{t_{\mathrm{s}}\psi_{\mathrm{m}}}{L_{\mathrm{q}}}\tilde{\omega}_{\mathrm{r}}(\mathrm{k})\end{aligned} \tag{3–49}$$

(3–49) is simplified by assuming small position error ($\sin\tilde{\theta}_{\mathrm{r}} = 0$ and $\cos\tilde{\theta}_{\mathrm{r}} = 1$). The d axis current error is proportional to the position error and q axis current error is proportional to the speed error.

The speed is estimated using q axis speed error information [Mat96], [Nah04]. This estimate is corrected using the d axis position error information.

$$\begin{aligned}\hat{\omega}_2(\mathrm{k}+1) &= \hat{\omega}_2(\mathrm{k}) - \mathrm{k}_1\tilde{i}_{\mathrm{qe}}(\mathrm{k}+1)\\ \hat{\omega}_{\mathrm{r}}(\mathrm{k}+1) &= \hat{\omega}_2(\mathrm{k}+1) + \mathrm{k}_2\tilde{i}_{\mathrm{de}}(\mathrm{k}+1)\end{aligned} \tag{3–50}$$

Gains k_1 and k_2 are tuning parameters. d axis current error is speed dependent (3–49) but constant gains were used in [Mat92], [Mat96], [Nah04]. The position estimate is obtained by integrating the speed estimate $\hat{\omega}_{\mathrm{r}}$. The structure of the estimator is illustrated in Fig. 3.10.

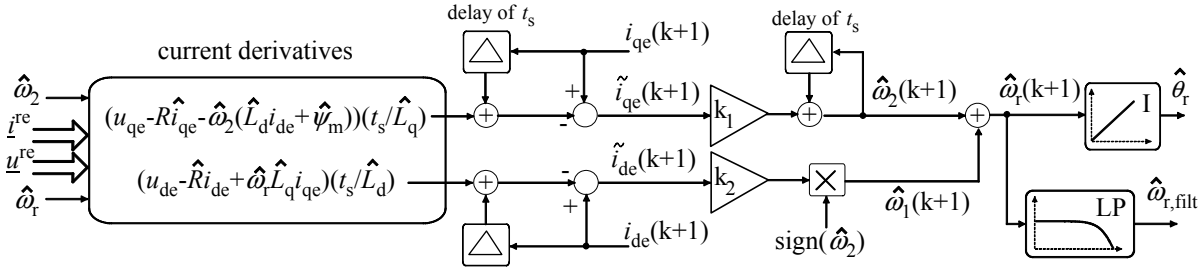

Fig. 3.10 Matsui's "current model" estimator in synchronous reference frame.

It should be noted that two different speeds are used inside the "current derivatives" block in Fig. 3.10. In the q axis algorithm (3–50) $\hat{\omega}_{\mathrm{r}}$ is replaced by $\hat{\omega}_2$. In the d axis algorithm the output of the speed estimator ($\hat{\omega}_{\mathrm{r}}$) is used. The q axis speed ω_2 must be independent of the final speed estimate. The reason is explained below.

If current error (3–49) is substituted into the estimator algorithm (3–50) the following non-linear control law can be written for the estimator

$$\hat{\omega}_2(\mathrm{k}+1) = \hat{\omega}_2(\mathrm{k})(1 + k_1 t_\mathrm{s}\psi_\mathrm{m} / L_\mathrm{q}) - \underbrace{\omega_\mathrm{r}(\mathrm{k})\cos\tilde{\theta}_\mathrm{r}\psi_\mathrm{m}}_{e_\mathrm{qe}}(k_1 t_\mathrm{s} / L_\mathrm{q}) \tag{3–51}$$

$$\hat{\omega}_\mathrm{r}(\mathrm{k}+1) = \hat{\omega}_2(\mathrm{k}+1) + \underbrace{\omega_\mathrm{r}(\mathrm{k})\psi_\mathrm{m}\sin\tilde{\theta}_\mathrm{r}}_{e_\mathrm{de}}(k_2 t_\mathrm{s} / L_\mathrm{d}) \tag{3–52}$$

(3–51) is a discrete time first order low pass filter with time constant $\tau = -(t_\mathrm{s} + L_\mathrm{q}/(k_1\psi_\mathrm{m}))$. Thus $\hat{\omega}_2$ converges to $\omega_\mathrm{r}\cos\tilde{\theta}_\mathrm{r}$. The bandwidth of the LP filter is a function of gain k_1. LP filtered speed $\hat{\omega}_2$ is corrected by the sine of the position error multiplied by the gain k_2, Fig. 3.11. k_2 must be multiplied by -1 if ω_r is negative, Fig. 3.10, because the sign of the d axis error signal is a function of the sign of ω_r (3–49).

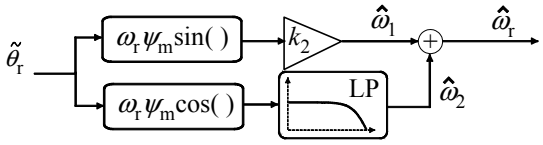

Fig. 3.11 Control law for the Matsui's current model method.

The position error is the input for the speed estimation process, Fig. 3.11, and it is the integral of the speed error $\omega_\mathrm{r} - \hat{\omega}_\mathrm{r}$. In steady state the output $\hat{\omega}_\mathrm{r}$ is constant. Thus the speed error must be zero in steady state operation. This also holds in the case of erroneous parameters.

The basic structure of the "current model" method is similar compared to the "voltage model" method, Fig. 3.6. The q axis voltage equation is used to give a fast direct estimate for the speed which is corrected by monitoring the d axis component of the back-emf. However, this method contains no PLL structure. Therefore parameter errors create large position errors.

Effect of parameter errors

The parameters R and ψ_m are not accurately known when the equation of current error is calculated (3–49). The q axis error can be written

$$\tilde{i}_\mathrm{qe}(\mathrm{k}+1) = -\frac{t_\mathrm{s}}{L_\mathrm{q}}\left(\omega_\mathrm{r}(\mathrm{k})\psi_\mathrm{m}\cos\tilde{\theta}_\mathrm{r} - \hat{\omega}_\mathrm{r}(\mathrm{k})\hat{\psi}_\mathrm{m} + \tilde{R}i_\mathrm{qe}\right) \tag{3–53}$$

When (3–53) is substituted into (3–50) the equation for $\hat{\omega}_2$ is

$$\hat{\omega}_2(\mathrm{k}+1) = \hat{\omega}_2(\mathrm{k})(1 + k_1 t_\mathrm{s}\hat{\psi}_\mathrm{m} / L_\mathrm{q}) - (k_1 t_\mathrm{s}\psi_\mathrm{m} / L_\mathrm{q})\left(\omega_\mathrm{r}(\mathrm{k})\cos\tilde{\theta} + \tilde{R}i_\mathrm{qe} / \psi_\mathrm{m}\right) \tag{3–54}$$

Equation (3–54) is a discrete LP filter with DC gain $\psi_\mathrm{m} / \hat{\psi}_\mathrm{m}$. Now the speed estimate $\hat{\omega}_2$ converges to

$$\hat{\omega}_2 = \left(\omega_\mathrm{r}\psi_\mathrm{m}\cos\tilde{\theta}_\mathrm{r} + \tilde{R}i_\mathrm{qe}\right)/\hat{\psi}_\mathrm{m} \tag{3–55}$$

Speed control is unstable if $\tilde{R}$ or $\tilde{\psi}_\mathrm{m}$ force the speed estimate (3–55) to be smaller than ω_r. Similar behaviour of the direct speed estimator using the q axis voltage model was discussed in Section 3.4.1. Thus the d axis algorithm must be used to correct the estimated speed (3–55). In steady state

$$\omega_\mathrm{r} = \hat{\omega}_1 + \hat{\omega}_2 = \sin\tilde{\theta}_\mathrm{r}(k_2\omega_\mathrm{r}t_\mathrm{s}\psi_\mathrm{m})/L_\mathrm{d} + \left(\omega_\mathrm{r}\psi_\mathrm{m}\cos\tilde{\theta}_\mathrm{r} + \tilde{R}i_\mathrm{qe}\right)/\hat{\psi}_\mathrm{m} \tag{3–56}$$

where $k_2\omega_\mathrm{r} \geq 0$. If small $\tilde{\theta}_\mathrm{r}$ is assumed: $\cos\tilde{\theta}_\mathrm{r} \approx 1$ and $\sin\tilde{\theta}_\mathrm{r} \approx \tilde{\theta}_\mathrm{r}$. Steady state position error can solved from (3–56).

$$\tilde{\theta}_\mathrm{r} \approx \frac{\omega_\mathrm{r}(1-\psi_\mathrm{m}/\hat{\psi}_\mathrm{m}) - (\tilde{R}/\hat{\psi}_\mathrm{m})i_\mathrm{qe}}{(\omega_\mathrm{r}k_2t_\mathrm{s}\psi_\mathrm{m})/L_\mathrm{d}} \tag{3–57}$$

A resistance error produces a position error proportional to load torque and inversely proportional to rotor speed. The error caused by an erroneous PM flux parameter is independent of the load torque. Increased k_2 enables a smaller position error but the system becomes more sensitive to noise.

Steady state position errors caused by erroneous L_d and L_q are small compared to the effect resistance and PM flux errors. However, in transient the q axis current error may temporarily be great. The q axis derivative equation is divided by L_q (3–47). Therefore L_q errors are not insignificant when the dynamic performance is studied.

3.4.5 Combined back-emf estimator

Matsui's voltage model estimator, Fig. 3.6, requires the derivative of i_qe. If all available information is to be exploited the derivative of i_de is also needed when the direct speed estimate $\hat{\omega}_2$ is calculated. Discrete derivative algorithms are subject to the noise and require additional LP filtering. The advantage of the method is the PLL structure enabling very small steady state position errors.

Matsui's "current model" estimator, Fig. 3.10, utilises all position error information contained in the fundamental frequency voltage equations without calculating any derivatives. This estimator is sensitive to resistance and PM flux errors which may cause great position errors at low speeds, (3–57). Both methods give zero steady state speed error.

The positive properties of Matsui's methods are combined in the present study. The discrete time algorithm of this combined estimator is illustrated in Fig. 3.12. The direct speed

estimate $\hat{\omega}_2$ is obtained by the LP filter type algorithm (3–51) of the current model method, (lowest part of Fig. 3.12). This estimate is corrected by the PLL structure of the voltage model method, Fig. 3.6, Fig. 3.8. The discrete version of the PLL, (3–42), is the upper part of Fig. 3.12. The current derivatives need not to be modelled.

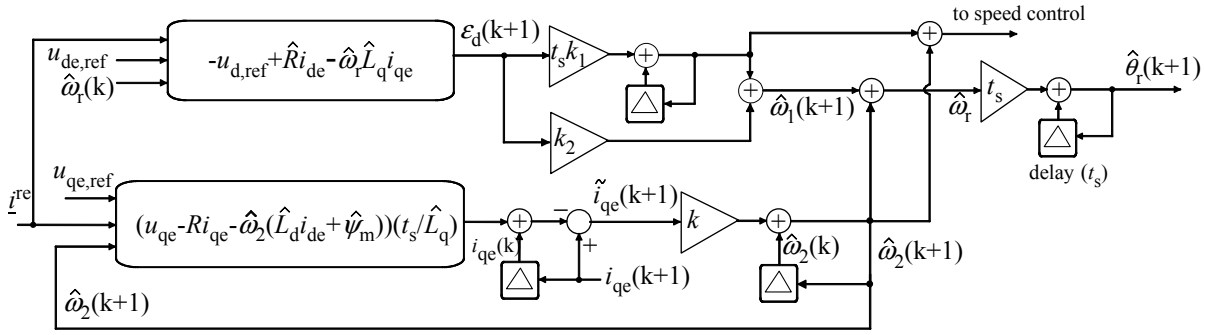

Fig. 3.12 Discrete time algorithm of the combined Matsui method.

3.5 Flux linkage estimators

This section deals with speed and position estimators where the primary estimated quantity is the stator flux linkage of the PMSM. Flux linkage estimators have been extensively studied in the literature because the flux linkage of the AC machine is the controlled quantity in direct torque control (DTC) drives.

Section 3.5 is organized as follows. In Section 3.5.1 the estimation of the flux linkage and the problems caused by parameter and measurement errors are briefly discussed. The speed and position estimator used in this thesis with flux linkage estimators is discussed in Section 3.5.2. Flux linkage estimators with a fairly simple structure are compared in Section 3.5.3.

3.5.1 Estimation of the flux linkage

The stator flux linkage of the PMSM can be estimated in stationary reference frame by solving the flux derivatives from the voltage equation.

$$\begin{aligned} u_\alpha &= Ri_\alpha + d\psi_\alpha / dt \\ u_\beta &= Ri_\beta + d\psi_\beta / dt \end{aligned} \Rightarrow \begin{aligned} \hat{\psi}_\alpha &= \int (u_\alpha - \hat{R}i_\alpha)dt \\ \hat{\psi}_\beta &= \int (u_\beta - \hat{R}i_\beta)dt \end{aligned} \qquad (3\text{–}58)$$

In practice the α and β components of the stator voltage vector are replaced by their reference values because the voltages are not measured.

The well known problem is the integral drift of (3–58), Fig. 3.13. Offsets in measured currents are inevitable. The integration process will integrate these DC signals, and unless reset, they will grow to large values leading to instability. Drift is also caused by voltage and

resistance errors. Resistance error is a serious problem at low speeds with high load torque. The voltage $\underline{u}^s$ then mainly consists of voltage drop over R and small errors in resistance can lead to fast integral drift. In this section methods to prevent the aforementioned problems are discussed briefly. More detailed description of methods preventing the integral drift is given in Section 3.5.3.

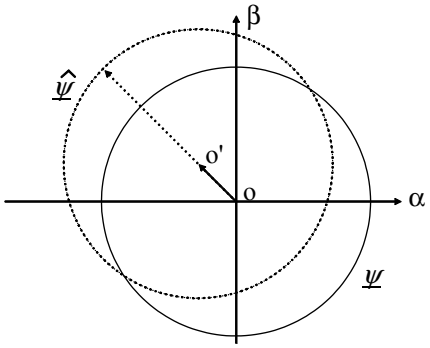

Fig. 3.13 Drift of the origin in the flux linkage estimation. O' denotes the drifted origin.

In early publications the integral drift was prevented by replacing the integrator by LP filter. In that case the waveforms of the estimated flux linkages are distorted. In [Wu91] the path of the flux linkage vector was observed at four points and after one fundamental period it is possible to detect the drift of the flux estimate by a simple geometric calculation. Low speeds are problematic because a large drift can occur before one electrical cycle is completed. In [Rah04] the pure integrator (3–58) is replaced by a three-stage cascaded LP filter. If the parameters of the filter are tuned properly as a function of ω_r, the algorithm acts as an integrator for the fundamental frequency and as an LP filter for other frequencies. When the fundamental frequency approaches zero, the gain and the filtering time constant of the modified LP filter approach infinity. Thus the algorithm can not be used in the zero speed region. In [You00] the offsets are removed by HP filters placed before and after the integrator algorithm. This method do not suffer the drawbacks of [Rah04] at low speeds.

The integral drift caused by measurement offsets is the easiest to compensate. High pass filtering [You00] can effectively remove the effect of DC signals. Voltage errors caused by the non-ideal converter and resistance error are more problematic. If the errors are not too large the system is stable in steady state but the origin of the estimated flux linkage vector is drifted and the amplitude is changed, Fig. 3.13. From the estimator's point of view the amplitude of the estimated flux linkage is a function of its angle. This periodic error creates torque and speed oscillation if the estimated flux linkage is used in a sensorless control system to estimate the rotor angle and speed. The aforementioned methods cannot remove these periodic errors because they only remove the effect of DC offsets.

Methods for trying to remove the effect of current measurement offsets and also the effect of erroneous voltage signal and the effect of inaccurate R are compared in Section 3.5.3.

3.5.2 Speed and position estimation

If the machine is loaded the angle of the stator flux linkage space-vector is not in alignment with the rotor d axis. The angle difference is called a load angle, denoted as δ, Fig. 3.14a. After the stator flux linkage has been estimated the rotor position can be determined by subtracting the estimated load angle from the angle of the estimated flux linkage [Con94], [Luu00]. Here the load angle is not directly estimated. The PLL algorithm is preferred when the speed and position are estimated. The estimation of the flux linkage is performed in the stationary reference frame. Therefore the PLL is tracking a rotating phasor which in the ideal case has the same angle, θ_r, as the rotor d axis. The structure of the speed and position estimation is illustrated in Fig. 3.15.

In Fig. 3.14a the PM flux vector is determined using d and q axis inductances and current vector components i_d and i_q. However, the measured current vector $\underline{i}^s$ need not to be transformed to the rotor reference frame to obtain the rotor position. In Fig. 3.14b the current vector is multiplied by L_q and subtracted from the estimated stator flux linkage. It can be seen in Fig. 3.14a that the load angle is a function of $L_q i_q$ only. The vector $\underline{\psi}^s$ - $L_q\underline{i}^s$ is in alignment with the rotor d axis if L_q is accurately known and $\underline{\psi}^s$, $\underline{i}^s$ contain no errors. The length of the estimated PM flux vector is $\psi_m + (L_d - \hat{L}_q)i_d$. An appropriate rotating phasor for position tracking can be calculated using only one inductance parameter even if $L_d < L_q$ and $i_d \neq 0$.

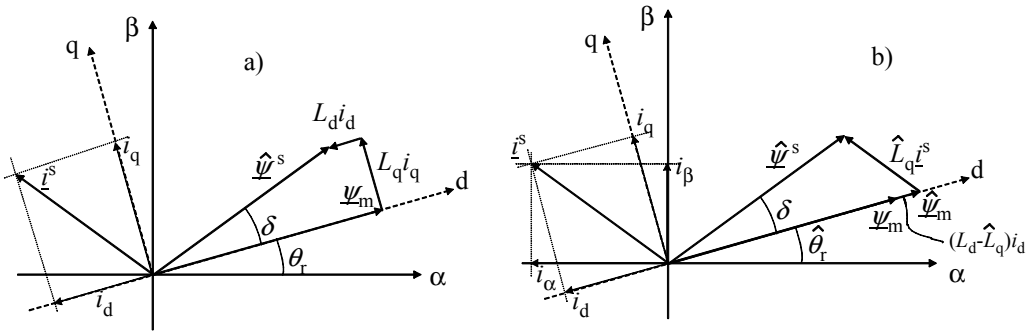

Fig. 3.14 a) Calculation of the PM flux vector using i_d, i_q and ideal parameters. b) Calculation of the PM flux vector by a simple vector subtraction using the current vector $\underline{i}^s$ and L_q.

In practice L_q is not accurately known. The position error caused by L_q estimate can be approximated as: $\arctan((i_q\tilde{L}_q)/\psi_m)$.

The speed and position estimator is illustrated in Fig. 3.15. The error signal of the PLL is

the difference between the angle of the estimated PM flux vector and the estimated rotor position. This operation requires one arctan operation. An other method is to form a rotating complex phasor using the sine and cosine of the estimated θ_r. In that case the error signal ε_d would be a cross product: $\psi_{m\beta}\cos\hat{\theta}_r - \psi_{m\alpha}\sin\hat{\theta}_r$.

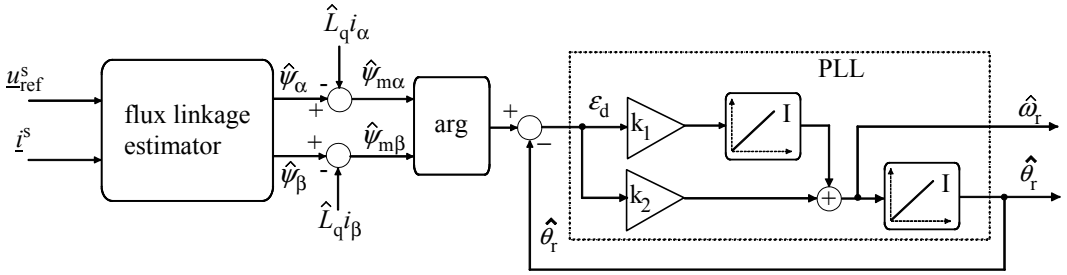

Fig. 3.15 Speed and position estimator. The input of the PLL is the angle difference between the estimated PM flux vector and the position output of the PLL.

3.5.3 Drift correction methods

In Sections 3.5.3.1 and 3.5.3.2 the flux linkage is estimated using only the voltage model, (3–58). These methods need the inductance information only when the rotor position is estimated, Fig. 3.15. Section 3.5.3.3 deals with estimators where the integral drift is prevented using a current model. The current model estimates the same flux linkage as (3–58) using PM flux information and flux linkage components $L_d i_d$ and $L_q i_q$.

3.5.3.1 Hu & Wu method, modified integrator

The modified integrator presented in [Hu98] is a well known method to prevent problems of the flux linkage estimation. If the amplitude of the estimated flux linkage exceeds the limit value the algorithm acts as an LP filter. Otherwise the algorithm is a pure integrator. The transfer function of the modified integrator is

$$y(s) = \frac{1}{s+\omega_c}x(s) + \frac{\omega_c}{s+\omega_c}z(s) \qquad (3–59)$$

The algorithm is illustrated in Fig. 3.16. If y exceeds limit L, $z = L$, otherwise $z = y$.

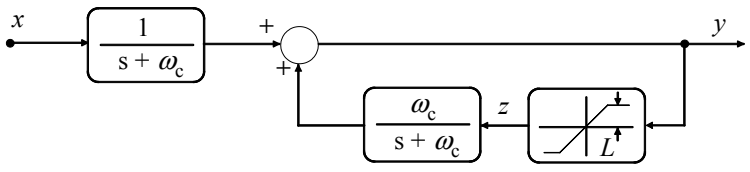

Fig. 3.16 Modified integrator with a saturable feedback.

The problem of the algorithm in Fig. 3.16 is the proper selection of the limiting constant L.

A wrong limit value distorts the estimated flux. In [Hu98] an improved algorithm is introduced which is suitable for AC drives where the flux linkage is not constant. The improved method exploits the fact that the flux linkage and its back-emf are orthogonal. If a drift occurs this orthogonal relation is lost and can be detected from non-zero scalar product between the flux linkage estimate and its back-emf, Fig. 3.17. The scalar product is divided by the amplitude of the estimated flux linkage and it is amplified by the PI controller.

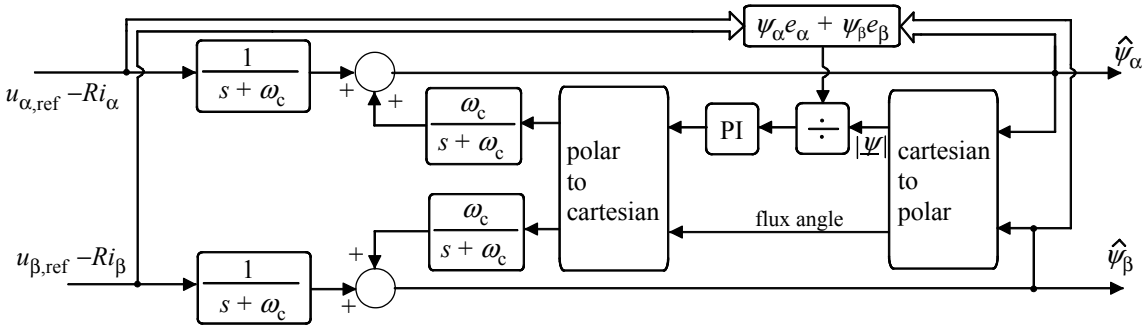

Fig. 3.17 Modified algorithm with adaptive flux linkage limit [Hu98].

PI controller output is the compensation signal amplitude suitable for the present flux linkage value.

Compared to many other drift correction methods the basic structure of the improved Hu&Wu algorithm, Fig. 3.17, is rather complex. In [Luu00] the structure is simplified by limiting the flux linkage amplitude directly in the cartesian coordinates. In that case the trigonometric operations are not needed.

In [Nie99] the drift of the flux linkage estimate is prevented by using a simpler algorithm. Hu&Wu algorithm and [Nie99] are compared in [Luu00]. Performance of the algorithm presented in [Nie99] is better. This simple method is studied in the next section. Hu&Wu algorithm is not further discussed here.

3.5.3.2 Niemelä estimator

It is easy to see from Fig. 3.13 that the maximum value of the flux linkage estimate is achieved in the direction of the drifted origin. The drift is detected by monitoring the modulus of the estimated flux linkage vector, $|\underline{\psi}|^2 = \psi_\alpha^2 + \psi_\beta^2$, Fig. 3.18. The average is removed by subtracting the modulus from its LP filtered value and the result is denoted as ε. It was shown in [Nie99] that the direction of the drifted origin is approximately the same as the direction of the flux linkage estimate when ε is at maximum. ε is amplified by a gain g and multiplied by the flux linkage estimate. The result is a correction vector which is added to the integration algorithm (3–58). Now the integral of $\underline{u}^s - R\underline{i}^s$ can be written in discrete form:

$$\hat{\psi}_\alpha(\mathrm{k}+1) = \hat{\psi}_\alpha(\mathrm{k}) + t_\mathrm{s}(u_\alpha(k) - Ri_\alpha(k)) + \psi_{\alpha,\mathrm{corr}}$$
$$\hat{\psi}_\beta(\mathrm{k}+1) = \hat{\psi}_\beta(\mathrm{k}) + t_\mathrm{s}(u_\beta(k) - Ri_\beta(k)) + \psi_{\beta,\mathrm{corr}} \qquad (3\text{–}60)$$

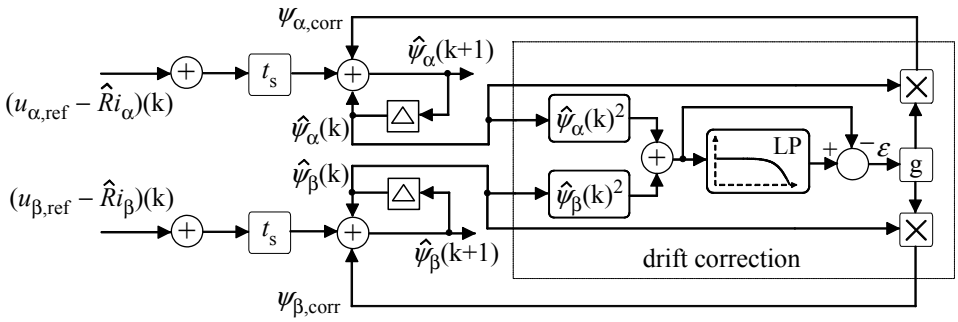

Fig. 3.18 Correction of the integral drift by monitoring the modulus of the estimated flux linkage [Nie99].

In [Nie99] the LP filter is a simple first order algorithm. The time constant of the LP filter is twice the fundamental frequency of the flux linkage. Therefore the time constant τ is inversely proportional to the estimated angular speed ω_r. To keep the effect of the drift correction equal over the speed range of the PMSM the gain g should be proportional to ω_r. In [Nie99] $g = t_\mathrm{s}/\tau$.

Modified LP filter

If the conventional first order LP filter is used the correction term ε, Fig. 3.18, may grow to a large value during a torque transient. After a transient the flux linkage estimate may oscillate when the system tries to remove the effect of the overgrown correction term. In [Luu00] the conventional LP filter, Fig. 3.18, is replaced by the following discrete-time algorithm where y and u denote output and input.

$$y(\mathrm{k}+1) = y(\mathrm{k}) + \frac{t_\mathrm{s}}{\tau}\big(u(\mathrm{k}) - y(\mathrm{k})\big) + g_\mathrm{LP}\big(u(\mathrm{k}) - u(\mathrm{k}-1)\big) \qquad (3\text{–}61)$$

If the tuning gain g_LP is zero, (3–61) is a conventional first order LP filter. Increased gain g_LP decreases the damping of higher frequencies. (3–61) becomes a unity gain if $g_\mathrm{LP} = 1 - t_\mathrm{s}/\tau$.

The gain g_LP may be constant or an adaptive coefficient. In [Luu00] the torque estimate is high pass filtered. An absolute value of the HP filtered torque estimate is amplified by a constant gain and the result limited between zero and $(1 - t_\mathrm{s}/\tau)$ can be used as g_LP. In that case the LP filter (3–61) is a unity gain if the rate of change of the torque is high. In steady state (3–61) is a conventional or modified LP filter depending on the lower limit of g_LP. The torque estimate can be replaced by i_qe when g_LP is calculated, Fig. 3.19.

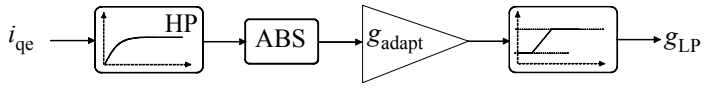

Fig. 3.19 Adaptive calculation of g_{LP}.

The modified LP filter decreases unnecessary large flux linkage corrections when the torque changes rapidly. If the gain g_{LP} is adaptive it is possible to completely disable the correction of the flux linkage estimate during torque steps.

In DTC drive this modification clearly improves the performance of the estimator [Luu00]. It also increases the number of the tuning parameters. The filtering time constant of the first order HP filter and the gain g_{adapt} must be appropriately selected.

3.5.3.3 Effect of parameter errors

The stator resistance is the only parameter needed in the flux linkage estimation, Fig. 3.18. In Fig. 3.20 the error between the actual input vector ($\underline{u}^s - R\underline{i}^s$) and the input of the estimator ($\underline{u}^s - \hat{R}\underline{i}^s$) is drawn in steady state. The drift is removed. It can be calculated from Fig. 3.20 that the angle error χ between vectors $\underline{u}^s - R\underline{i}^s$ and $\underline{u}^s - \hat{R}\underline{i}^s$ is

$$\chi = \arctan\left((\tilde{R}\left|\underline{i}^s\right|\sin\upsilon) / (\left|\underline{u}^s - R\underline{i}^s\right| - \tilde{R}\left|\underline{i}^s\right|\cos\upsilon) \right) \tag{3–62}$$

where $\upsilon = \varphi + \arctan(\ (|R\underline{i}^s|\sin\varphi\ ) / (|\underline{u}| - |R\underline{i}^s|\cos\varphi)\ )$, φ is an angle between the stator voltage and current vectors and $\tilde{R} = R - \hat{R}$.

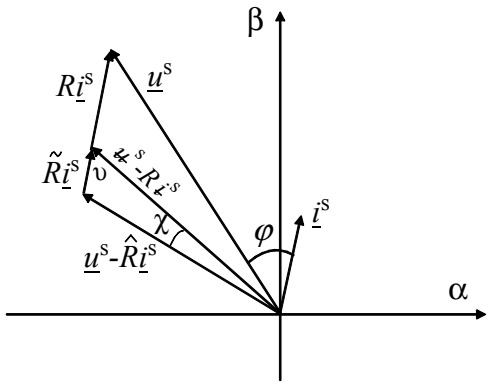

Fig. 3.20 Input error of the flux linkage estimator.

The amplitude of $\underline{u}^s - \hat{R}\underline{i}^s$ is

$$\left|\underline{u}^s - \hat{R}\underline{i}^s\right| = \sqrt{\left(\left|\underline{u}^s - R\underline{i}^s\right| - \tilde{R}\left|\underline{i}^s\right|\cos\upsilon\right)^2 + \left(\tilde{R}\left|\underline{i}^s\right|\sin\upsilon\right)^2} \tag{3–63}$$

υ is usually rather small in PMSMs because no magnetizing current is needed. Therefore

angle error (3–62) is small and the amplitude difference $\left|\underline{u}^{\mathrm{s}} - R\underline{i}^{\mathrm{s}}\right| - \left|\underline{u}^{\mathrm{s}} - \hat{R}\underline{i}^{\mathrm{s}}\right| \approx \widetilde{R}\left|\underline{i}^{\mathrm{s}}\right|$. After integration of the voltage error vector $|\underline{u}^{\mathrm{s}} - R\underline{i}^{\mathrm{s}}|$ - $|\underline{u}^{\mathrm{s}} - \hat{R}\underline{i}^{\mathrm{s}}|$ the angle of the flux error vector is (3–62) but the amplitude difference (3–63) is divided by ω_{r}.

$$\left|\underline{\psi}\right| - \left|\underline{\hat{\psi}}\right| \approx \widetilde{R}\left|\underline{i}^{\mathrm{s}}\right| / \omega_{\mathrm{r}} \tag{3–64}$$

3.5.3.3 Methods exploiting the current model

Some flux estimators also exploit the flux linkage information of so-called current model to prevent drift problems. In the literature a non-salient machine is often assumed. The stator flux linkage of the PMSM can be written:

$$\begin{aligned} \hat{\psi}_{\alpha,\mathrm{c}} &= \hat{\psi}_{\mathrm{m}} \cos\hat{\theta}_{\mathrm{r}} + \hat{L} i_{\alpha} \\ \hat{\psi}_{\beta,\mathrm{c}} &= \hat{\psi}_{\mathrm{m}} \sin\hat{\theta}_{\mathrm{r}} + \hat{L} i_{\beta} \end{aligned} \tag{3–65}$$

If this assumption is not done the flux linkage in the stationary reference frame is [And99]:

$$\begin{aligned} \hat{\psi}_{\alpha,\mathrm{c}} &= (\hat{\psi}_{\mathrm{m}} + \hat{L}_{\mathrm{d}} i_{\mathrm{d}}) \cos\hat{\theta}_{\mathrm{r}} - \hat{L}_{\mathrm{q}} i_{\mathrm{q}} \sin\hat{\theta}_{\mathrm{r}} \\ \hat{\psi}_{\beta,\mathrm{c}} &= (\hat{\psi}_{\mathrm{m}} + \hat{L}_{\mathrm{d}} i_{\mathrm{d}}) \sin\hat{\theta}_{\mathrm{r}} + \hat{L}_{\mathrm{q}} i_{\mathrm{q}} \cos\hat{\theta}_{\mathrm{r}} \end{aligned} \tag{3–66}$$

In [Fre96] the flux linkage is estimated by an algorithm which uses three-phase equations. This method also inherently estimates the rotor position. In the case of the voltage model methods discussed above the rotor position must be determined by an additional algorithm. However, the structure of [Fre96] is complicated compared to voltage model algorithms. In [Öst96] the structure of [Fre96] is simplified by using a space-vector presentation.

In [And99] the position is estimated and the drift is eliminated by comparing the voltage and current models, (3–58) and (3–66). This type of estimator is called a model reference adaptive system (MRAS). The angle difference between the flux linkage space-vectors ($\underline{\psi}_{\mathrm{c}}$, $\underline{\psi}_{\mathrm{u}}$) is used as an error signal for the PLL algorithm which calculates the position and speed estimates. The current model is corrected using the estimated position $\hat{\theta}_{\mathrm{r}}$. Therefore the current model is called an adaptive model. Voltage model is called a reference model.

The drift is corrected by adding a correction vector $\underline{u}_{\mathrm{corr}}$ to the integrator input $\underline{u}^{\mathrm{s}}$-$R\underline{i}^{\mathrm{s}}$, Fig. 3.21. $\underline{u}_{\mathrm{corr}}$ is achieved by amplifying α and β components of ($\underline{\psi}_{\mathrm{c}}$ - $\underline{\psi}_{\mathrm{u}}$) by PI controller. The structure of the algorithm is fairly simple, but due to the drift correction the voltage model is coupled with the position estimate, Fig. 3.21. Voltage model flux estimators, Fig. 3.17 and Fig. 3.18, do not need position information.

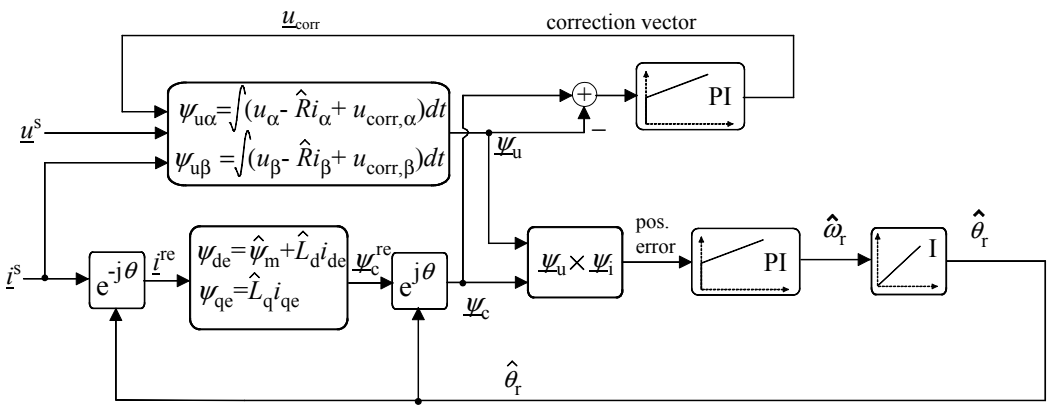

Fig. 3.21 Block diagram of the MRAS estimator with drift correction [And99].

[And99] was compared to the stationary frame version of [Mat90] by the author in [Esk03]. The low speed performance of Matsui's back-emf method was superior.

Also new approaches are published recently. In [Pii05] an interesting adaptive estimator is introduced where the estimation is performed in the estimated d,q frame instead of stationary frame. Now the reference model is the current model

$$\begin{aligned}\hat{\psi}_{cde} &= \psi_m + L_d i_{de}\\ \hat{\psi}_{cqe} &= L_q i_{qe}\end{aligned} \tag{3–67}$$

The adaptive model for flux linkage is the basic voltage equation (3–32) in the d,q frame

$$\begin{aligned}\hat{\psi}_{ude} &= \int\left(u_{de} - Ri_{de} + \hat{\omega}_r\hat{\psi}_{uqe} + k\tilde{i}_{de}\right)dt\\ \hat{\psi}_{uqe} &= \int\left(u_{qe} - Ri_{qe} - \hat{\omega}_r\hat{\psi}_{ude} + k\tilde{i}_{qe}\right)dt\end{aligned} \tag{3–68}$$

where k is a constant gain. The estimated speed is the parameter used to adjust the adaptive model in a manner which minimises the error between the adaptive and the reference model (3–67). The adaptive model also calcultates an estimate for the current: $\hat{i}_{de} = (\hat{\psi}_{ude} - \psi_m)/L_d$, $\hat{i}_{qe} = \hat{\psi}_{uqe}/L_q$. These current components are subtracted from i_{de} and i_{qe} and the error is used to correct the voltage model (3–68). The block diagram of the estimator is presented below.

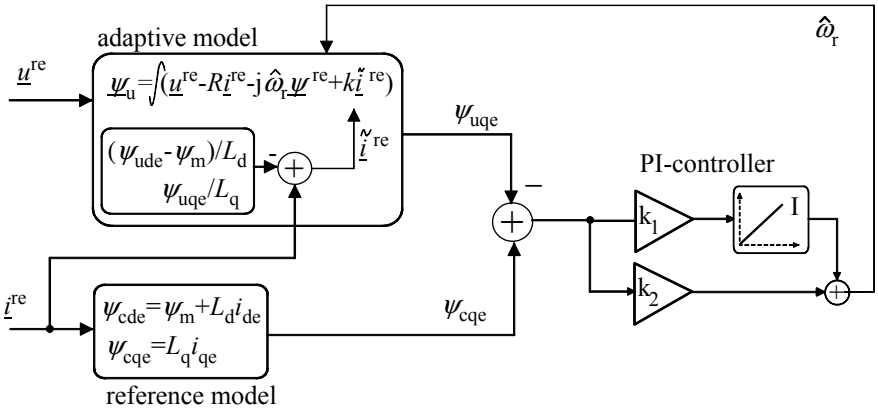

Fig. 3.22 Adaptive estimator in the estimated rotor reference frame, [Pii05].

In [Pii05] the model based method was assisted with a signal injection estimator. The result is a hybrid estimator which is stable also at zero speed region. This type of estimators are discussed in Chapter 4. Unfortunately, [Pii05] is not compared to other model based estimators in this study because it was published after the comparative study was completed.

Rasmussen estimator

In [Ras03] the drift of the flux linkage estimate is prevented by a simple scheme based on the current model. The block diagram of the discrete time algorithm is illustrated in Fig. 3.23. The flux linkage components $L_q i_\alpha$ and $L_q i_\beta$ are subtracted from the flux linkage estimated by the voltage model. The remaining vector represents the PM flux linkage in stationary reference frame. In [Ras03] a non-salient machine is assumed. Here the PM flux linkage is estimated using L_q of a salient machine. The estimated scalar ψ_m is subtracted from the length of the calculated PM flux linkage. If drift occurs the difference is nonzero. PM flux error is multiplied by gain g and transformed to the stationary reference frame. The resulting correction terms $u_{\alpha,corr}$ and $u_{\beta,corr}$ are added to the inputs of the integral algorithm. Now the rotor position estimation is included in the drift correction scheme, Fig. 3.23. This estimate can be directly used as an input for the PLL estimating the rotor speed and position, Fig. 3.15.

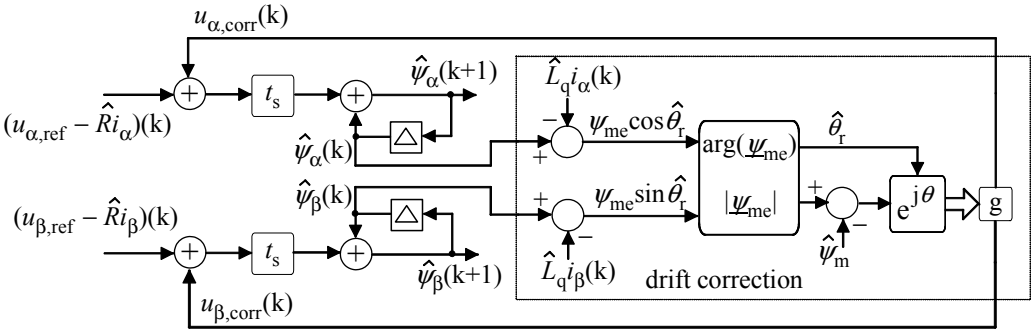

Fig. 3.23 Correction of the integral drift by estimating the permanent magnet flux [Ras03].

Parameter sensitivity of Rasmussen method

The effect of PM flux error was analysed in [Ras03]. The following analysis also contains the resistance and inductance error. As discussed in Section 3.5.2 the rotor position can be accurately calculated in the stationary reference frame using the current vector and one inductance parameter, Fig. 3.14. However, the estimated length of the PM flux vector, Fig. 3.23, is not correct if $L_d < L_q$ and $i_d \neq 0$. Therefore it is important to notice that the effect of the inductance error in the parameter sensitivity analysis below is valid only if the machine is non-salient or i_d is very small.

The estimated and real stator flux linkage derivatives can be written on the basis of Fig. 3.23 as follows

$$\frac{d}{dt}\underline{\hat{\psi}}^{\mathrm{s}} = \frac{d}{dt}\left(\psi_{\mathrm{me}} e^{j\hat{\theta}_{\mathrm{r}}} + \hat{L}_{\mathrm{q}}\underline{i}^{\mathrm{s}}\right) = \underline{u}^{\mathrm{s}} - \hat{R}\underline{i}^{\mathrm{s}} + g(\hat{\psi}_{\mathrm{m}} - \psi_{\mathrm{me}})e^{j\hat{\theta}_{\mathrm{r}}} \tag{3–69}$$

$$\frac{d}{dt}\underline{\psi}^{\mathrm{s}} = \frac{d}{dt}\left(\psi_{\mathrm{m}} e^{j\theta_{\mathrm{r}}} + L_{\mathrm{q}}\underline{i}^{\mathrm{s}}\right) = \underline{u}^{\mathrm{s}} - R\underline{i}^{\mathrm{s}} \tag{3–70}$$

where ψ_{me} is the length of the PM flux vector estimated by the algorithm, Fig. 3.23. $\hat{\theta}_{\mathrm{r}}$ is the angle of the estimated PM vector $\underline{\psi}_{\mathrm{me}}$ and also the estimated rotor position. Steady state operation is assumed: $d\hat{\theta}_{\mathrm{r}} / dt = d\theta_{\mathrm{r}} / dt = \omega_{\mathrm{r}}$. When (3–70) is subtracted from (3–69) and the result is transformed to estimated synchronous reference frame with angle $\hat{\theta}_{\mathrm{r}}$, the result is:

$$\frac{d}{dt}\left(\underline{\hat{\psi}}^{\mathrm{re}} - \underline{\psi}^{\mathrm{re}}\right) = \left(\frac{d}{dt} + j\hat{\omega}_{\mathrm{r}}\right)\left(\psi_{\mathrm{me}} - \psi_{\mathrm{m}} e^{j\tilde{\theta}_{\mathrm{r}}} - \tilde{L}_{\mathrm{q}}\underline{i}^{\mathrm{re}}\right) = \tilde{R}\underline{i}^{\mathrm{re}} + g(\hat{\psi}_{\mathrm{m}} - \psi_{\mathrm{me}}) \tag{3–71}$$

A small position error is assumed. Thus $\cos\tilde{\theta}_{\mathrm{r}} \approx 1$ and $\sin\tilde{\theta}_{\mathrm{r}} \approx \tilde{\theta}$. Let us denote: $X = (\psi_{\mathrm{me}} - \psi_{\mathrm{m}})/\ \psi_{\mathrm{m}}$ and $Y = (\hat{\psi}_{\mathrm{m}} - \psi_{\mathrm{m}})/\psi_{\mathrm{m}}$. Real and imaginary parts of (3–71) are

$$\begin{aligned}
&\mathrm{Re}: dX/dt - \frac{di_{\mathrm{de}}}{dt}\frac{\tilde{L}}{\psi_{\mathrm{m}}} + \hat{\omega}_{\mathrm{r}}\frac{\tilde{L}_{\mathrm{q}}}{\psi_{\mathrm{m}}} i_{\mathrm{qe}} + gX + \hat{\omega}_{\mathrm{r}}\tilde{\theta}_{\mathrm{r}} = \tilde{R} i_{\mathrm{de}}/\psi_{\mathrm{m}} + gY \\
&\mathrm{Im}: \hat{\omega}_{\mathrm{r}} X - d\tilde{\theta}_{\mathrm{r}}/dt - \hat{\omega}_{\mathrm{r}}\frac{\tilde{L}_{\mathrm{q}}}{\psi_{\mathrm{m}}} i_{\mathrm{de}} - \frac{di_{\mathrm{qe}}}{dt}\frac{\tilde{L}_{\mathrm{q}}}{\psi_{\mathrm{m}}} = \tilde{R} i_{\mathrm{q}}/\psi_{\mathrm{m}}
\end{aligned} \tag{3–72}$$

Components containing current derivatives or i_{de} are assumed to be zero. When the derivative operator is replaced by a Laplace operator s the position error is

$$\tilde{\theta}_{\mathrm{r}}(s) = \frac{g\hat{\omega}_{\mathrm{r}}}{s^2 + gs + \hat{\omega}_{\mathrm{r}}^2} Y(s) - \frac{(s+g)\tilde{R} + \hat{\omega}_{\mathrm{r}}^2 \tilde{L}_{\mathrm{q}}}{(s^2 + gs + \hat{\omega}_{\mathrm{r}}^2)\psi_{\mathrm{m}}} i_{\mathrm{q}}(s) \tag{3–73}$$

The steady state position error is approximately

$$\tilde{\theta}_{\mathrm{r}} \approx \frac{g(\hat{\psi}_{\mathrm{m}} - \psi_{\mathrm{m}})}{\hat{\omega}_{\mathrm{r}}\psi_{\mathrm{m}}} - \frac{1}{\psi_{\mathrm{m}}}\left(\frac{g\tilde{R}}{\hat{\omega}_{\mathrm{r}}^2} + \tilde{L}_{\mathrm{q}}\right) i_{\mathrm{qe}} \tag{3–74}$$

A low tuning parameter g produces a lower position error but the dynamic performance is impaired.

3.6 Comparison of the model based estimators by simulations

In this section Matsui's back-emf estimators are compared to flux linkage estimators in simulations. The simulations are carried out using Matlab Simulink program. The vector control system, Fig. 2.25, and speed & position estimators are modelled using the S-function property. S-function contains a text file where the discrete time algorithms are written using some common programming language. In this thesis Matlab's own language is used. The PMSM is modelled in the rotor reference frame using time continuous Simulink blocks. The model is presented in Fig. 3.24. It contains also the 6th harmonic of the inductance and the rotor flux linkage (2-22).

3.6.1 Simulations with ideal PMSM drive

In the first stage the frequency converter is assumed to be ideal. The stator voltage of the model is the voltage reference vector and the current measurement contains no errors. The PMSM model contains only the fundamental frequency components (L_{d}, L_{q} and ψ_{m} are constants). In Fig. 3.24 coefficients L6 (L_6 in (2-22)) and PM6 (ψ_{md6}, ψ_{mq6} in (2-22)) are set at zero. The parameters of the motor model and estimator algorithms are varied to compare the sensitivity for parameter errors.

Back-emf estimators (Matsui's methods) are modelled in synchronous reference frame and flux linkage estimators (Niemelä and Rasmussen methods) in stationary frame. The control system in rotor frame is illustrated in Fig. 2.25 and the counterpart in the stationary frame in Fig. 2.26. The discrete algorithm of the PI controllers is presented in Fig. 2.27. The control system parameters, Table 3.1, are similar in all simulations. The control and estimator algorithms are performed in 100 µs loop, which is also the calculation time of the experimental setup.

Table. 3.1 Parameters of the control system used in simulations.

	Gain k_p	Integration time t_i
Speed control	2	0.033 s
Current control	20	0.005 s

The PMSM used in simulations is a 3.5 kW 1500 rpm machine with surface mounted magnets. The number of pole pairs is 3. More detailed information is provided in Appendix A. With the parameters of the machine and Table 3.1 the closed loop bandwidth of the current control is approximately 300 Hz. The speed control bandwidth is approximately 60 Hz in the case of measured speed and position. The closed loop bandwidth is the frequency when the output is attenuated 3 dB compared to the sinusoidal reference value.

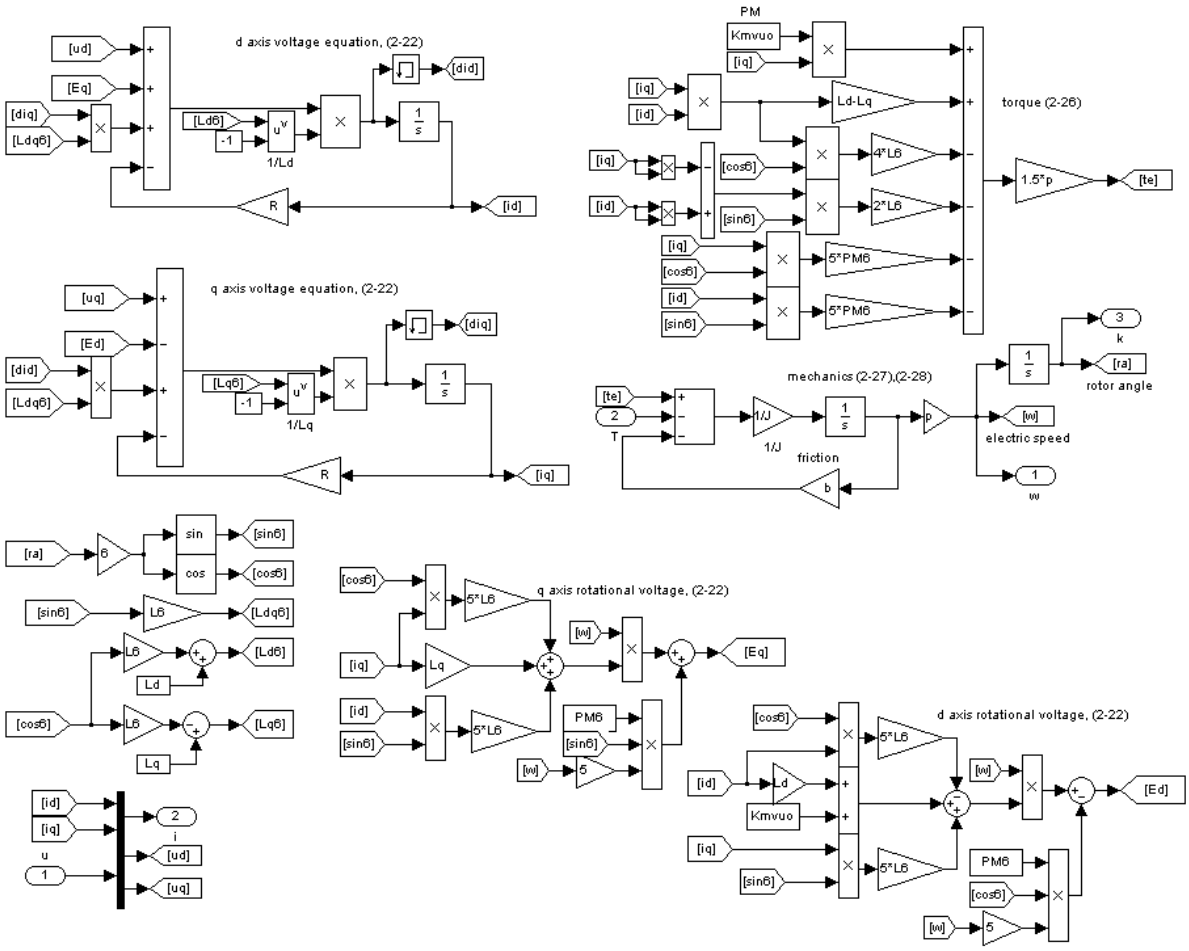

Fig. 3.24 Simulink model of the PMSM in the rotor reference frame.

The selected model based estimators are compared using the test sequence presented in Fig. 3.25. The load torque is nominal (22 Nm) and positive for 0 - 2.5 s. The speed reference signal is -1 p.u. during the first 0.5 s and the PMSM is then generating. For 0.5 - 1.5 s the speed reference is 1 p.u. and the PMSM power flows from the supply to the motor. At 1.5 s the speed reference is changed to 0.1. The direction of the rotation is changed at 2 s. The load

torque is changed from 100% to -100 % value at 2.5 s. In the last stage the PMSM is accelerated from speed -0.1 p.u. to speed 0.45 p.u. Per unit (p.u.) values are used throughout this study when simulated or measured rotor speeds are shown. 1 p.u. is the nominal speed given by the manufacturer. Nominal values of the PMSMs and per unit values for the parameters are given in Appendix A.

In all simulations the current was limited to 22 A which is approximately twice the nominal value. The simulation results presented in the following sections were obtained with nominal load. All simulations are also carried out without load and with medium load. The undesirable effects of the non-ideal PMSM drive and parameter errors are more serious in the case of nominal load. Therefore small load simulations are not presented.

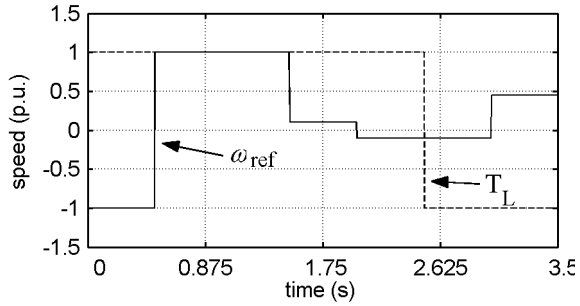

Fig. 3.25 The simulation sequence for comparing the parameter sensitivity of estimators.

3.6.1.1 Back-emf estimators

The tuning parameters of the back-emf estimators are presented in Table 3.2. In [Mat96], [Nah04] d axis correction gain k_2 was constant. However, the d axis total gain is proportional to speed (3–49), Fig. 3.11. If k_2 is suitable for a low speed range the total gain may become excessive around the nominal speed and the system is subjected to noise. In this thesis k_2 is linearly decreased when the rotor speed is over 0.15 p.u.

Table. 3.2 Tuning parameters of back-emf estimators.

	ρ (3–38)	ω_{low} (3–38)	k_1	k_2
"voltage model" (Fig. 3.6)	80/s	0.2 p.u. (94.2 rad/s)	–	–
"current model" (Fig. 3.10)	–	–	120	if ($\|\omega_r\| < 0.15$ p.u), $k_2 = 280$ else, $k_2 = 280\text{-}188*(\omega_{r(p.u)}\text{-}0.15)$
Combined method (Fig. 3.12)	80/s	0.2 p.u. (94.2 rad/s)	120	–

The tuning of the PI controller of the PLL of Matsui's "voltage model" estimator is presented in (3–38). The selection $\rho = 80$/s gives a rather narrow bandwidth (≈ 32 Hz) for the PLL. The narrow bandwidth is allowed because the speed is estimated mainly by the q axis branch, Fig. 3.6. The gain k_1 defines the bandwidth of the LP filter type direct speed estimator

(3–51). In the case of machine A the bandwidth of the LP filter is approximately 1.6 kHz.

Fig. 3.26 and Fig. 3.27 present the simulated speed and position error when Matsui's voltage method, Fig. 3.6, is used to estimate the speed and position. Fig. 3.28 and Fig. 3.29 show position errors when Matsui's current method, Fig. 3.10 and the combined method proposed by the present author, Fig. 3.12, are simulated. The voltage method and the combined method oscillate at low speeds. Matsui's current method also oscillates at nominal speed if there are no parameter errors.

The speed of the PMSM is mainly estimated by the direct estimator. As discussed earlier, the direct speed estimator is in the boundary of stable operation if parameter errors are zero. This can create a steady state oscillation if the inertia of the PMSM is rather low.

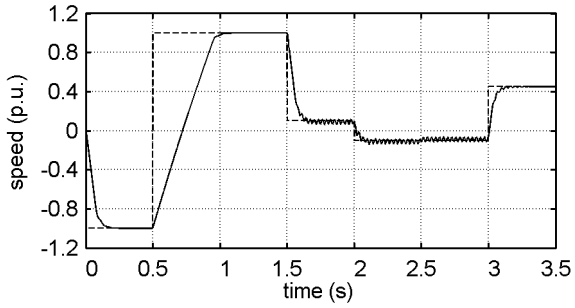

Fig. 3.26 Speed reference (--) and the speed (solid). Matsui voltage method, no parameter errors.

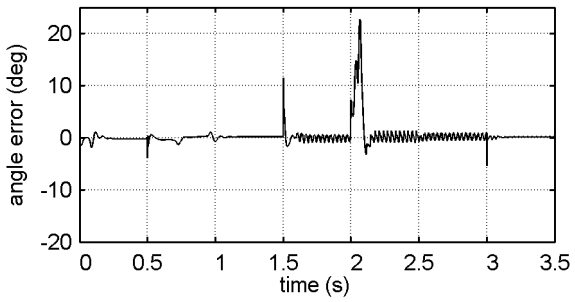

Fig. 3.27 Position error ($\theta_r - \hat{\theta}_r$). Matsui voltage method, no parameter errors.

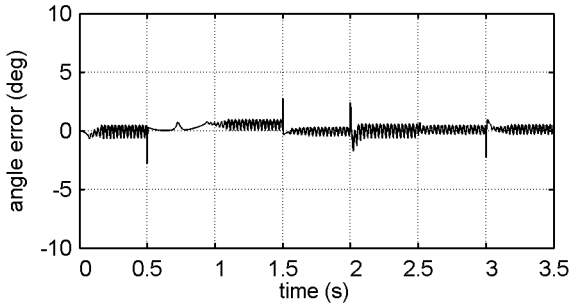

Fig. 3.28 Position error ($\theta_r - \hat{\theta}_r$). Matsui current method, no parameter errors.

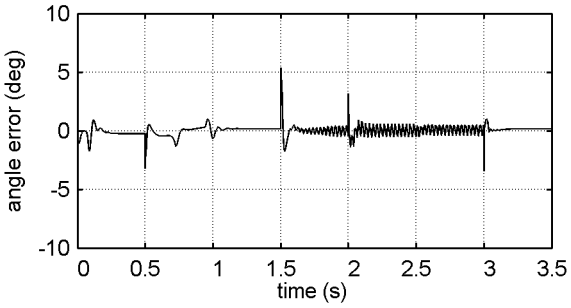

Fig. 3.29 Position error ($\theta_r - \hat{\theta}_r$). Combined Matsui estimator, no parameter errors.

Inductance error

The first parameter studied is the inductance L. Because the current vector lies approximately in the q axis direction only L_q error is considered. In Fig. 3.30 - Fig. 3.35 Matsui's voltage method, the current method and the combined method are simulated with nominal load. The estimated L_q was 10 mH, which is approximately 17% smaller than the actual L_q. The voltage method, Fig. 3.31, still oscillates after transients. The steady state position error is equal for all back-emf estimators and can be predicted by (3–41).

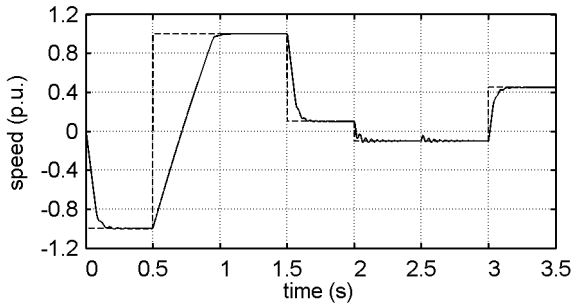

Fig. 3.30 Matsui voltage method. Simulated speed. $L_q - \hat{L}_q = 2$ mH (17 %).

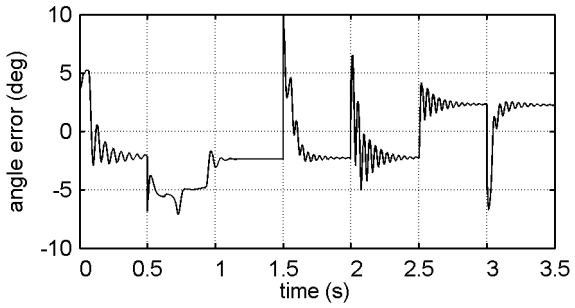

Fig. 3.31 Matsui voltage method. Position error ($\theta_r - \hat{\theta}_r$). $L_q - \hat{L}_q = 2$ mH (17 %).

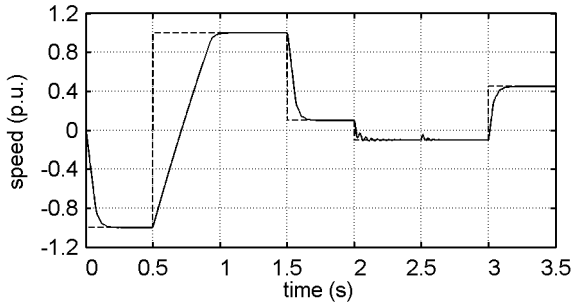

Fig. 3.32 Matsui current method. Simulated speed. $L_q - \hat{L}_q = 2$ mH (17 %).

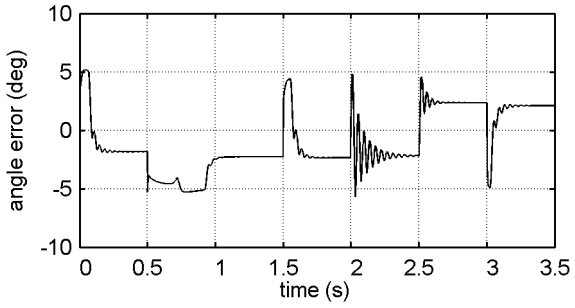

Fig. 3.33 Matsui current method. Position error. $L_q - \hat{L}_q = 2$ mH (17 %).

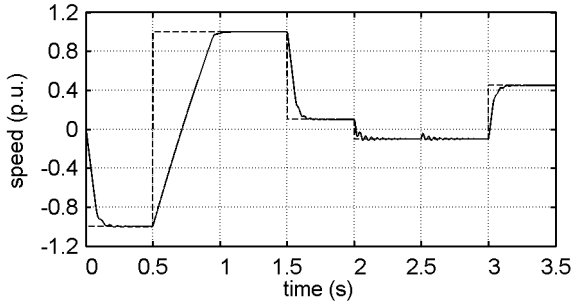

Fig. 3.34 Combined Matsui estimator. Simulated speed. $L_q - \hat{L}_q = 2$ mH (17 %).

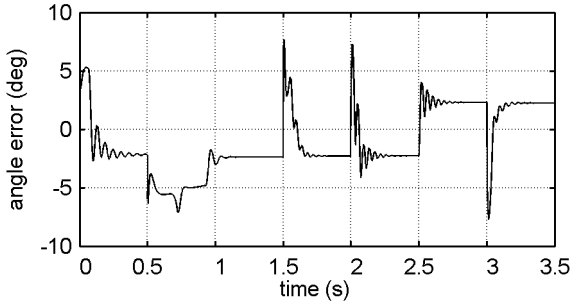

Fig. 3.35 Combined Matsui estimator. Position error. $L_q - \hat{L}_q = 2$ mH (17 %).

Resistance error

Fig. 3.36 - Fig. 3.41 show simulation results where the stator resistance is increased 30% compared to the R used in the estimator software. Other parameters are correct. All methods are stable. The voltage method still oscillates but the performance is improved compared to the case when resistance error is zero. As predicted by (3–41), the steady state position error is practically zero if R is the only incorrect parameter and the direct estimator is corrected by PLL, Fig. 3.36 - Fig. 3.41. In the current model method the speed error of the direct estimator is corrected by a P type controller, Fig. 3.11. It was shown that resistance and PM flux errors produce steady state position errors (3–57). This can be seen in Fig. 3.37.

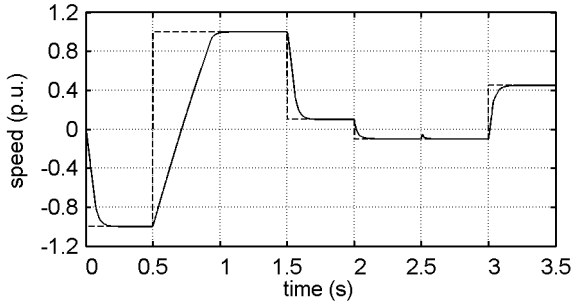

Fig. 3.36 Matsui current method. Simulated speed. $R - \hat{R} = 0.3\ \Omega$ (30%).

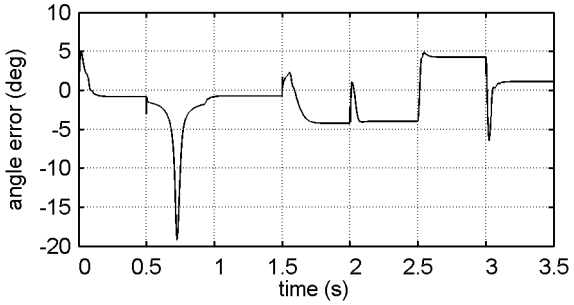

Fig. 3.37 Matsui current method, position error ($\theta_r - \hat{\theta}_r$). $R - \hat{R} = 0.3\ \Omega$ (30%).

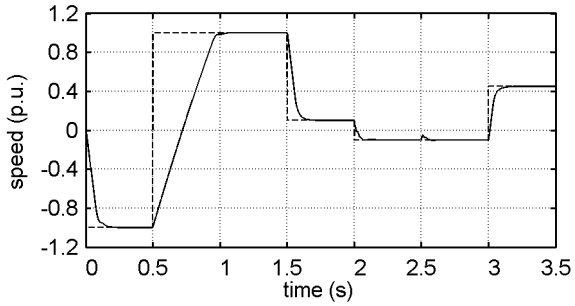

Fig. 3.38 Matsui voltage method. Simulated speed. $R - \hat{R} = 0.3\ \Omega$ (30%).

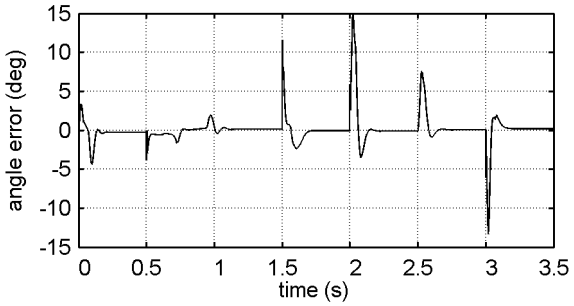

Fig. 3.39 Matsui voltage method, position error. $R - \hat{R} = 0.3\ \Omega$ (30%).

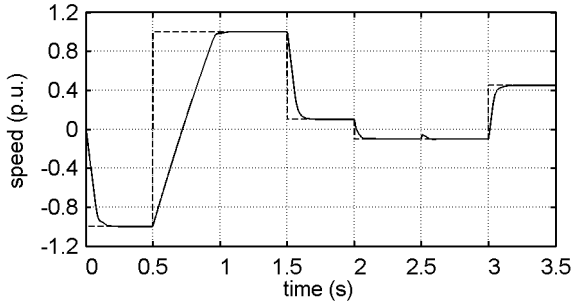

Fig. 3.40 Combined Matsui estimator. Simulated speed. $R - \hat{R} = 0.3\ \Omega$ (30%).

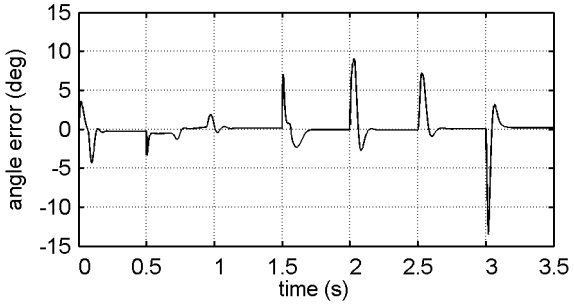

Fig. 3.41 Combined Matsui estimator, position error. $R - \hat{R} = 0.3\ \Omega$ (30%).

The positive resistance error improves the performance of the sensorless control system when the PLL type correction algorithms are applied. Steady state position error is practically zero if the other parameters have correct values. The ringing after transients, Fig. 3.27 - Fig. 3.35, disappears. Very large errors decrease the dynamic performance.

The combined method was tested with 100% resistance error and the system was stable with nominal load when the test sequence presented above was driven. The maximum position error was then approximately 40 degrees. If R of the PMSM is 30% smaller than the R in the software all three back-emf estimators studied are unstable. In that case the PLL algorithm is not capable of correcting the unstable direct speed estimator.

PM flux error

The flux of the permanent magnets decreases when the temperature of the PMSM rises [Hen94]. In Fig. 3.42 the combined estimator is simulated in the case when ψ_m is decreased by 15% compared to the nominal value, 0.5 Wb. A 15% drop is a large value which requires that the machine is approximately 100°C warmer than room temperature [Hen94].

Fig. 3.43 shows the position error in the case of the combined method. A rather large error occurs in the speed reversal but otherwise the effect of positive $\tilde{\psi}_m$ is not significant. The control system is unstable when Matsui's original methods are tested with the same error.

If the estimated PM flux is 15% smaller than the actual one the combined Matsui estimator is unstable. If L_q is also estimated to be too small the performance is improved. The oscillation in the nominal speed range is damped faster and the maximum position error is smaller.

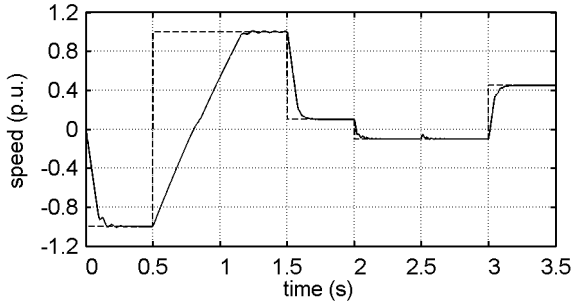

Fig. 3.42 Combined Matsui estimator. Simulated speed. $\psi_m - \hat{\psi}_m$ = -0.075 Wb (-15%).

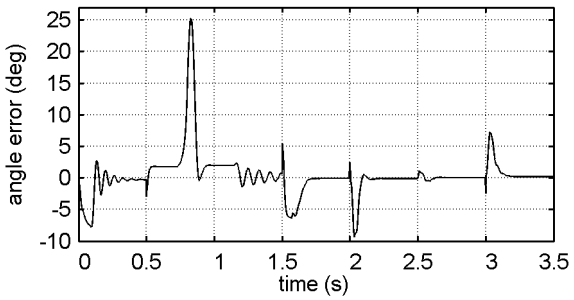

Fig. 3.43 Combined Matsui estimator, position error ($\theta_r - \hat{\theta}_r$). $\psi_m - \hat{\psi}_m$ = -0.075 Wb (-15%).

Comparison of back-emf methods

In the simulations presented above Matsui's voltage method [Mat90] is the poorest of the three candidates. The position errors after transients are higher compared to other candidates and the ringing is more intense, Fig. 3.27, Fig. 3.31. The oscillation is caused by the modelling of the derivative of i_q. The derivative algorithm is sensitive to noise and requires additional LP filtering. This affects the overall dynamic performance.

Matsui's current model method [Mat92] has a smoother transient performance. The absence of a PLL type correction algorithm creates greater steady state position errors than the voltage method, Fig. 3.37.

Matsui's original algorithms [Mat90], [Mat92] are not further studied by simulations in this thesis because it is possible to combine most of the positive properties of the Matsui's original estimators by using the combined algorithm presented in Fig. 3.12. In the simulations the combined estimator proved to be less sensitive to parameter errors than [Mat90] and

[Mat92]. In the following short list the combined method is compared to the best of Matsui's original estimators in each test.

- When the inductance was not correctly estimated the maximum position error of the combined method was two degrees higher compared to the current method. However, the oscillation of the combined estimator is attenuated faster, Fig. 3.33, Fig. 3.35.

- In the case of 30% resistance error the maximum position error was approximately seven degrees smaller than the maximum error in the case of Matsui's voltage model method Fig. 3.39, Fig. 3.41.

- The proposed combined estimator was stable when the PM flux was decreased by 15%. Matsui's original estimators were unstable.

3.6.1.2 Flux linkage estimators

In this Section [Nie99], Fig. 3.18, is compared to the Rasmussen estimator [Ras03], Fig. 3.23. These two methods are selected because they both have a rather simple structure and they can prevent the drift of the flux linkage estimate caused by parameter errors. The tuning parameters of the estimators used in the simulations are presented in Table 3.3.

In [Ras03] the gain g was constant. In this thesis g is proportional to rotor speed. This improves the performance at higher speeds. The correction voltage vector is added to $\underline{u}^s$ - $R\underline{i}^s$, Fig. 3.23, which is proportional to ω_r. Therefore the length of the correction vector is also proportional to ω_r. In the low speed region g is limited to 10.

The tuning of the PLL algorithm is straightforward compared to back-emf methods. The amplitude of the flux linkage is a function of load torque but can be considered a constant. Therefore the PLL tuning coefficients can be constant over the speed range. PLL can be tuned fast compared to back-emf estimators. The bandwidth of the PLL is approximately 300 Hz. Thus the dynamic performance of the estimator is mainly dependent on the flux linkage estimator.

Table. 3.3 Tuning parameters of flux linkage estimators.

	τ (time constant of LP filter)	g	PLL (Fig. 3.3a)
Niemelä estimator	$2/\omega_r$	t_s/τ (low limit 0.001)	$k_1 = 3000\text{^}2$, $k_2 = 6000$
Rasmussen estimator	–	ω_r /1.5 (low limit 10)	$k_1 = 3000\text{^}2$, $k_2 = 6000$

Simulations without parameter errors

In Fig. 3.44 - Fig. 3.45 the Niemelä method is simulated without parameter errors. In Fig. 3.46 - Fig. 3.49 the same simulation is carried out with the modified Niemelä estimator and with Rasmussen method. In the modified Niemelä estimator the filtering time constant of the

HP filter, is 0.5 ms and the gain g_{adapt} is 4, Fig. 3.19. These parameters are used in the following simulations.

Niemelä method oscillates as the back-emf estimators in the previous section. If the modified LP filter is used the performance is clearly improved, Fig. 3.47. The Rasmussen estimator has no problems with accurate parameters.

It can be seen in Fig. 3.45, Fig. 3.47 and Fig. 3.49 that there is a position error even if the parameters are accurately known. The flux linkage estimators are performed in the stationary reference frame. The steady state position error is created by the computation delays.

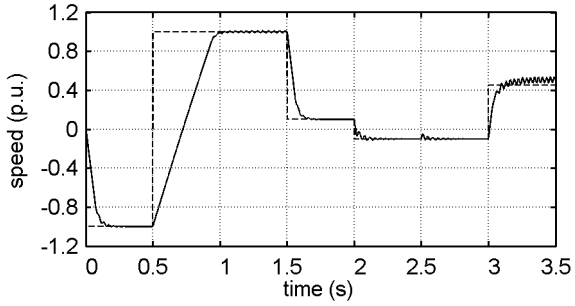

Fig. 3.44 Niemelä estimator. No parameter errors. Simulated speed.

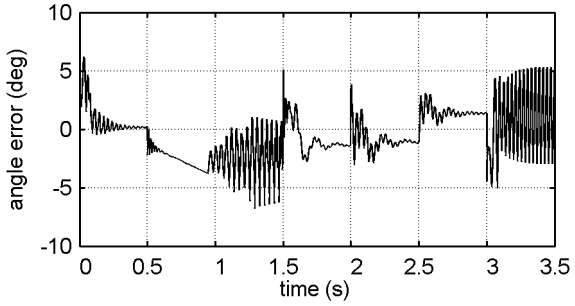

Fig. 3.45 Niemelä estimator. No parameter errors. Position error ($\theta_r - \hat{\theta}_r$).

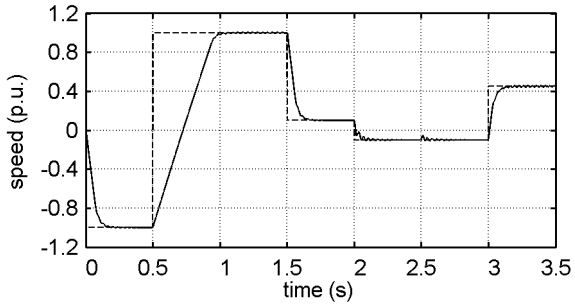

Fig. 3.46 Modified Niemelä estimator. No parameter errors. Simulated speed.

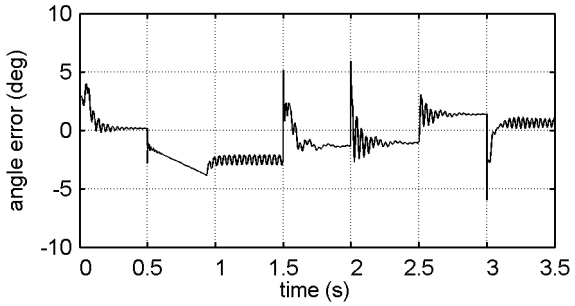

Fig. 3.47 Modified Niemelä estimator. No parameter errors. Position error ($\theta_r - \hat{\theta}_r$).

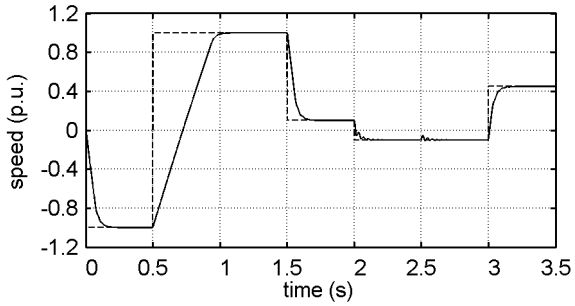

Fig. 3.48 Rasmussen estimator. No parameter errors. Simulated speed.

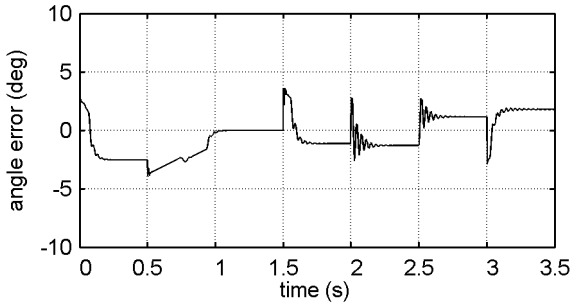

Fig. 3.49 Rasmussen estimator. No parameter errors. Position error ($\theta_r - \hat{\theta}_r$).

Inductance error

Fig. 3.50 - Fig. 3.53 show the simulations where the L_q in the estimator software was 0.01 mH, 17% smaller than L_q in the motor model. Both flux linkage methods show rather similar performance. The position errors are comparable to those presented in the previous section. Negative L_q error causes heavy oscillation in the case of both flux linkage estimators.There is no significant difference between the estimators when L_q is not accurately known.

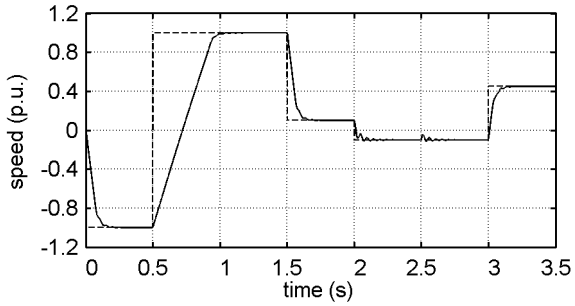

Fig. 3.50 Modified Niemelä estimator. Simulated speed. $L_q - \hat{L}_q = 2$ mH (17 %).

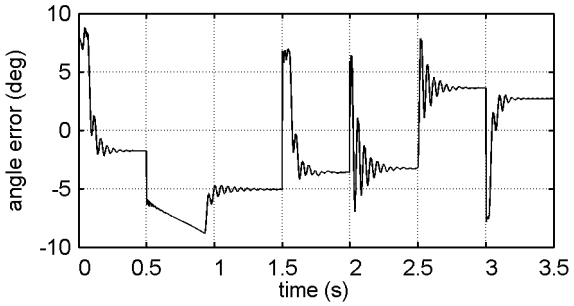

Fig. 3.51 Modified Niemelä estimator, position error ($\theta_r - \hat{\theta}_r$). $L_q - \hat{L}_q = 2$ mH (17 %).

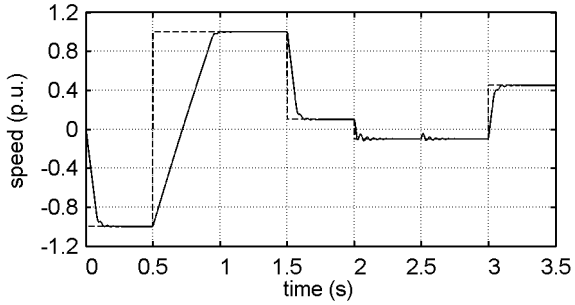

Fig. 3.52 Rasmussen estimator. Simulated speed. $L_q - \hat{L}_q = 2$ mH (17 %).

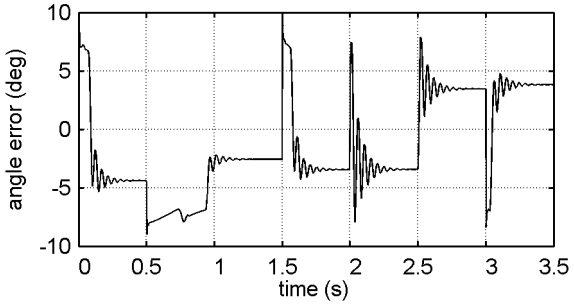

Fig. 3.53 Rasmussen estimator, position error. $L_q - \hat{L}_q = 2$ mH (17 %).

Resistance error

Fig. 3.54 - Fig. 3.58 show simulation results where the stator resistance is increased 30% compared to the R used in the estimator software. The other parameters are correct.

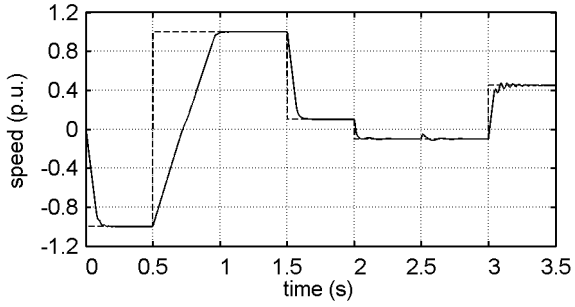

Fig. 3.54 Rasmussen estimator. Simulated speed. $R - \hat{R} = 0.3\ \Omega$ (30%).

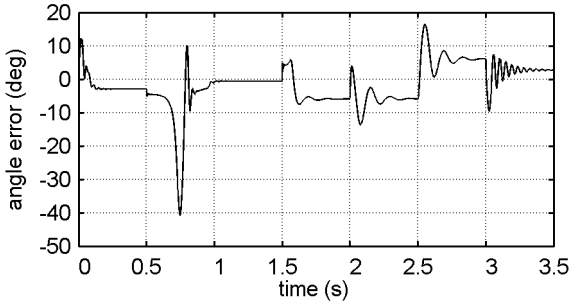

Fig. 3.55 Rasmussen estimator, position error. $R - \hat{R} = 0.3\ \Omega$ (30%).

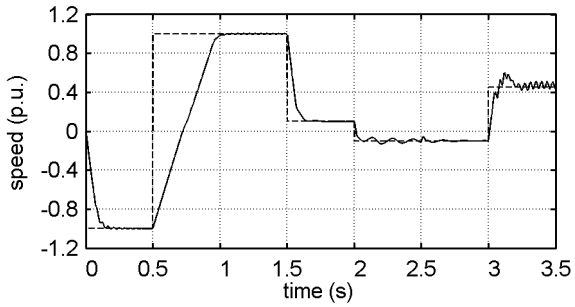

Fig. 3.56 Modified Niemelä estimator. Simulated speed. $R - \hat{R} = 0.3\ \Omega$ (30%).

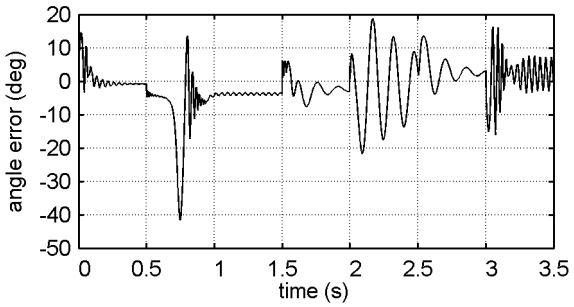

Fig. 3.57 Modified Niemelä estimator, position error. $R - \hat{R} = 0.3\ \Omega$ (30%).

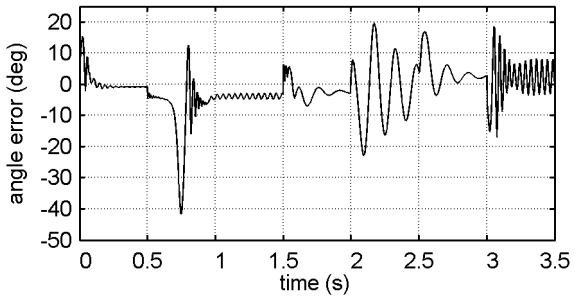

Fig. 3.58 Niemelä estimator (basic algorithm), position error. $R - \hat{R} = 0.3\ \Omega$ (30%).

The Rasmussen method is stable, but position errors are large compared to back-emf methods. There are also steady state position errors at low speeds, Fig. 3.55. This can be predicted by (3–74).

The modified Niemelä estimator oscillates after the speed is reversed from 0.1 p.u. speed to -0.1 p.u. and in the end of the simulation period. In the case of the 30% resistance error there is no significant difference between the original [Nie99] and the modified estimator, Fig. 3.57, Fig. 3.58. Both Rasmussen and Niemelä methods are unstable in the low speed region if the estimated resistance is 30% larger than the actual one.

PM flux error

PM flux error is tested only in the case of the Rasmussen estimator because ψ_m need not to be known if [Nie99] is applied. In Fig. 3.59 and Fig. 3.60 the flux of the permanent magnets is decreased by 15%. Simulator software uses the nominal value 0.5 Wb. In Fig. 3.61 and Fig. 3.62 ψ_m of the motor model is 0.5 Wb and $\hat{\psi}_m = 0.425$ Wb. The Rasmussen estimator is not sensitive to the PM flux error.

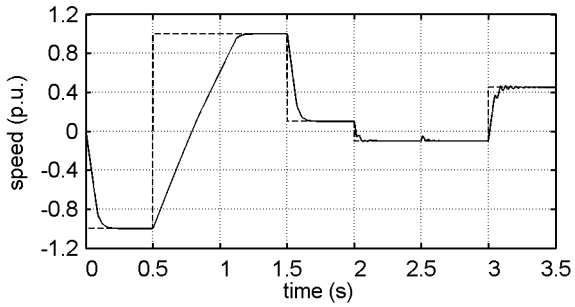

Fig. 3.59 Rasmussen estimator. Simulated speed. $\psi_m - \hat{\psi}_m$ = -0.075 Wb (-15%).

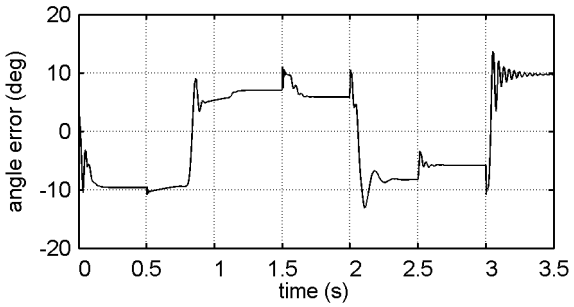

Fig. 3.60 Rasmussen estimator, position error $\theta_r - \hat{\theta}_r$. $\psi_m - \hat{\psi}_m$ = -0.075 Wb (-15%).

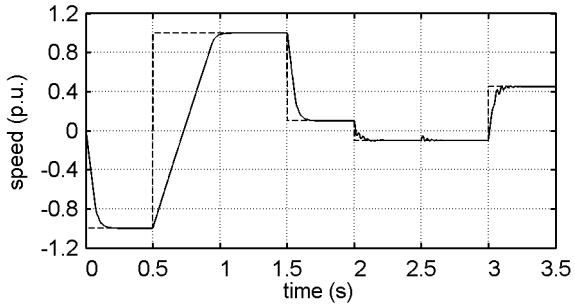

Fig. 3.61 Rasmussen estimator. Simulated speed. $\psi_m - \hat{\psi}_m$ = 0.075 Wb (15%).

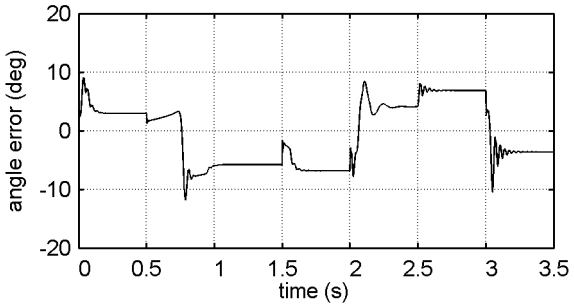

Fig. 3.62 Rasmussen estimator, position error. $\psi_m - \hat{\psi}_m$ = 0.075 Wb (15%).

The simulation results presented above show that [Ras03] is less sensitive to resistance errors. With accurate parameters and inductance error no remarkable differences were found. Niemelä method tends to oscillate after transients. This phenomenon was stronger compared to Rasmussen method even if the improved filtering was applied. In addition to parameters shown in Table 3.3 the flux linkage estimator presented by Niemelä was also tested with many other values of τ and g. However, results were always poorer compared to [Ras03]. Therefore [Ras03] is selected to the final simulations with the combined Matsui estimator. In the next section they are studied in the case of a non-ideal PMSM drive.

3.6.2 Simulations with non-ideal PMSM drive

The following non-ideal properties of the PMSM drive are modelled in simulations: flux linkage harmonics, effect of the main circuit of the frequency converter and non-ideal current measurement.

3.6.2.1 Non-ideal PMSM

In this chapter machine A (Appendix A) is modelled using (2-22) with 6th harmonics in inductances and flux linkages. The parameters of the model are selected using measured motor quantities. Fig. 3.63 shows the measured back-emf from phase A. Fig. 3.64 shows the spectrum of the measured voltage. Harmonics with multiples of three disappear from the

model after transformation to rotor reference frame because they are common for all phases.

The 5th harmonic is approximately 1% of the main rotor flux ψ_m and the 7th harmonic is negligible. Using (2-21): $\psi_{md,6} = -\psi_{mq,6} = \psi_{m,5}$ if $\psi_{m,7} = 0$. This amplitude of the 6th PM flux linkage harmonic is denoted as PM6 in the PMSM model, Fig. 3.24. The value of PM6 is 0.005 Wb.

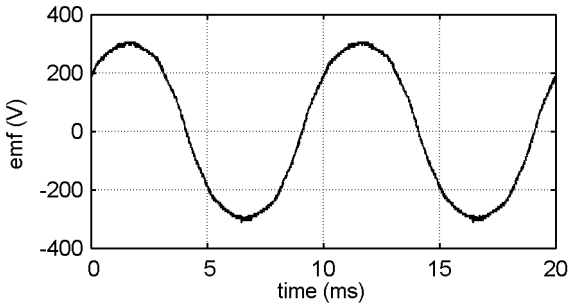

Fig. 3.63 Measured back-emf (phase A) of the PMSM. Mechanical rotor speed is 2000 rpm.

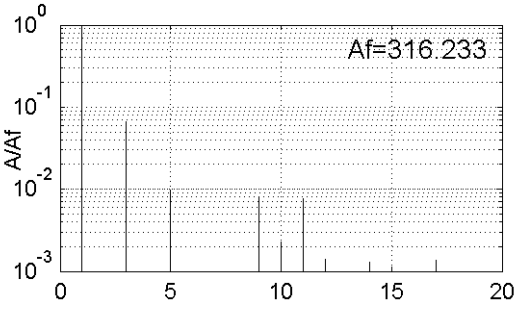

Fig. 3.64 Back-emf spectrum.

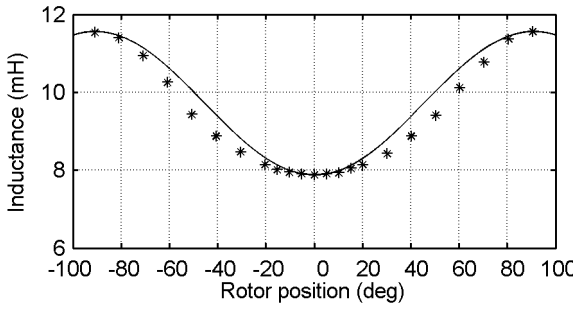

Fig. 3.65 Measured phase inductance (phase A) as a function of the rotor position θ_r. Ideal saliency (solid line).

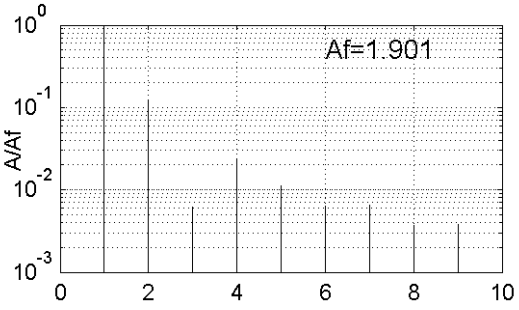

Fig. 3.66 Spectrum of the phase inductance.

Fig. 3.65 shows the measured phase inductance with several rotor positions. Inductance was measured using the following setup [Vas93]. Phases B and C were connected to the common point. A sinusoidal 300 Hz voltage signal was generated over this point and phase A. The device feeding the circuit was a controllable AC voltage source ELGAR SW5250A. The voltage generated by ELGAR SW5250A and the current of the phase A were measured and the data was analysed using Matlab. Inductance was determined using the fundamental frequency components of the voltage and the current. If the rotor d axis is in alignment with the phase A the measured inductance is L_d. The angle $\pi/2$ rad between the rotor d axis and the phase A gives the quadrature axis inductance L_q.

The spectrum of the saliency curve is illustrated in Fig. 3.66. The first order component is the main saliency. The second order component, $n = 2$ in (2-15) and (2-16), is clearly the dominant harmonic ($\approx$ 11 %). The amplitude of the main saliency $(L_q - L_d)/2$ is approximately 1.9 mH, Fig. 3.65. Thus L_6 (2-22) in the simulation model is 0.2 mH.

The effect of a non-ideal PMSM is compared by steady state simulations. The load is nominal and simulations are performed at 4% speed and 30% speed. Fig. 3.67 shows the speed and position error when the combined Matsui estimator is studied. The speed reference signal is set at 4% of nominal speed. The results of at 30% speed are presented in Fig. 3.68. In Fig. 3.69 and Fig. 3.70 the same simulations are performed with the Rasmussen estimator.

As presented in Chapter 3.5, the steady state position error is greater in the case of the flux linkage estimator. At speed 0.04 p.u. the peak-to-peak amplitudes of the simulated speed oscillations are: 0.011 p.u. (Matsui) and 0.019 p.u. (Rasmussen). At speed 0.3 p.u. the amplitudes are practically the same. The conclusion is that the combined Matsui estimator is less sensitive to flux linkage harmonics in the low speed region.

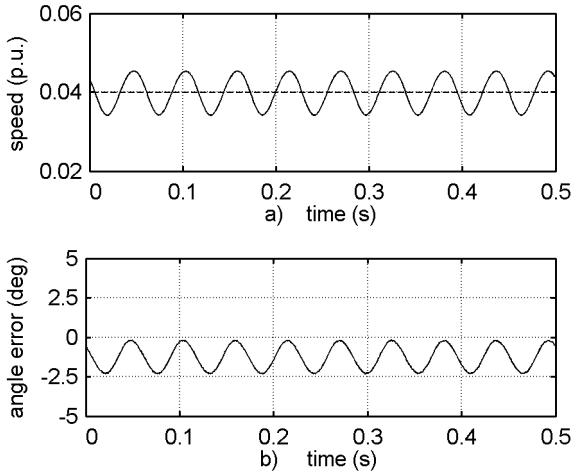

Fig. 3.67 Non-ideal PMSM, combined Matsui estimator, full load, 0.04 p.u. speed reference. a) simulated speed, b) position error.

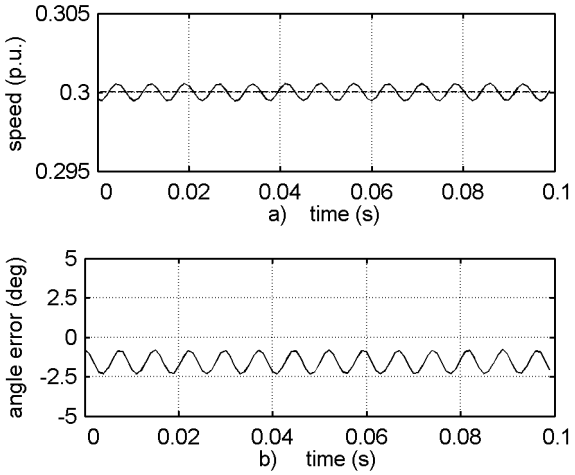

Fig. 3.68 Non-ideal PMSM, combined Matsui estimator, full load, 0.3 p.u. speed reference. a) simulated speed, b) position error.

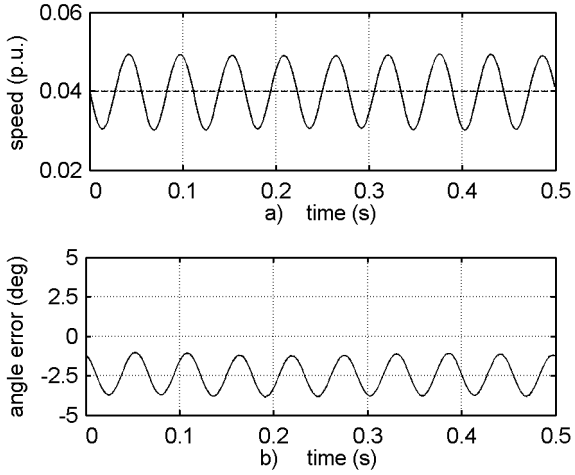

Fig. 3.69 Non-ideal PMSM, Rasmussen, full load, 0.04 p.u. speed reference. a) simulated speed, b) position error.

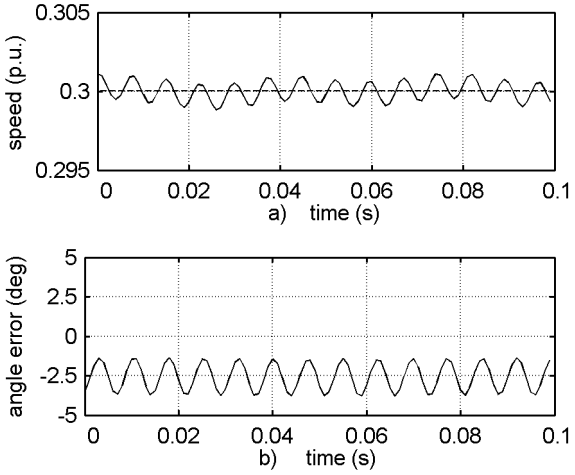

Fig. 3.70 Non-ideal PMSM, Rasmussen, full load, 0.3 p.u. speed reference. a) simulated speed, b) position error.

The speed ripple consisting of multiples of 6th harmonics is clearly damped when the speed is increased from 0.04 p.u to 0.3 p.u. The frequency of the disturbance is then outside

the closed loop bandwidth of the speed control. If the speed control is tuned faster the low speed oscillation increases.

3.6.2.2 Effect of the non-ideal frequency converter

The effect of the non-ideal frequency converter is studied by adding an error voltage vector to the input of the PMSM model, Fig. 3.24. The error voltage vector is the non-linear part of (2-43). The voltage error equation of the VSI is used because it is the most simple one to model. The threshold voltage and the effect of dead times are equal to those used in Fig. 2.18. The amplitude of the error voltage for one phase in the simulations is 1.9 V. In the simulations of this section the model of the PMSM is ideal.

In Fig. 3.71 the combined Matsui estimator is simulated with 0.04 p.u. speed and nominal load. Fig. 3.72 presents the steady state simulation at 0.3 p.u. speed. Fig. 3.73 and Fig. 3.74 show the same simulations with the Rasmussen estimator.

The oscillation is stronger when the back-emf estimator is applied, Fig. 3.71. The amplitude difference can be explained by the structure of the estimators. The voltage reference vector is a sum of the actual stator voltage and the voltage drop over the semiconductors of the frequency converter. The voltage drop creates non-linear error voltage (2-44) which is included in the input of the flux estimator (3–58). The integrator attenuates the error signal. In the back-emf estimator, where PLL is used to estimate the speed and position, the effect of the inverter bridge is amplified by the PI controller. In this thesis the direct amplifier branch of the PI controller does not take part in composing the signal used in speed control, Fig. 3.6. If the full output of the PI controller is used the transient performance is improved but the system becomes sensitive to disturbances created by the non-ideal VSI.

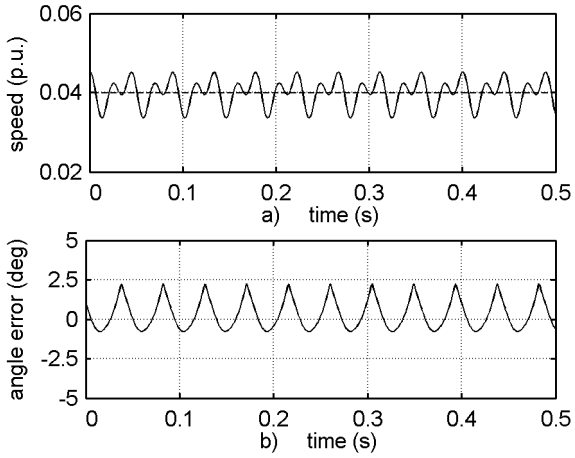

Fig. 3.71 Non-ideal VSI, combined Matsui estimator, $U_{dead}+U_{th}$= 1.92 V, full load, 0.04 p.u. speed reference a) speed, b) position error.

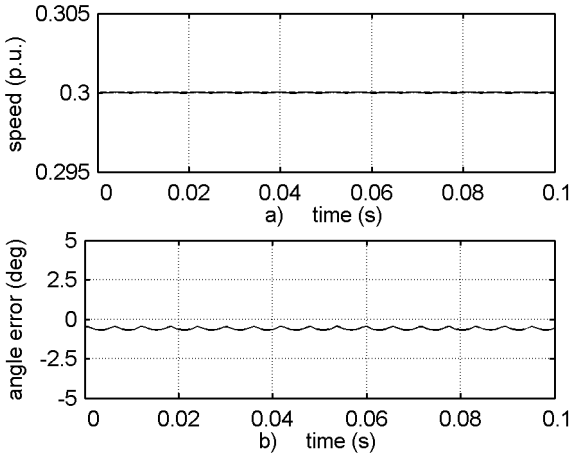

Fig. 3.72 Non-ideal VSI, combined Matsui estimator, $U_{dead}+U_{th}$= 1.92 V, full load. 0.3 p.u. speed reference a) speed, b) position error.

In the case of the Rasmussen method the voltage error generates an additional position error in the low speed region, Fig. 3.73. When the back-emf method is simulated the average steady state position error is not affected by the voltage errors generated by the inverter bridge Fig. 3.71.

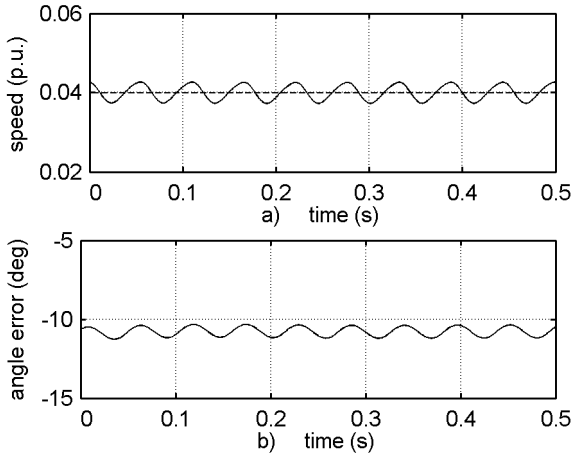

Fig. 3.73 Non-ideal VSI, Rasmussen estimator, $U_{dead}+U_{th}$= 1.92 V, full load, 0.04 p.u. speed reference. a) speed, b) position error.

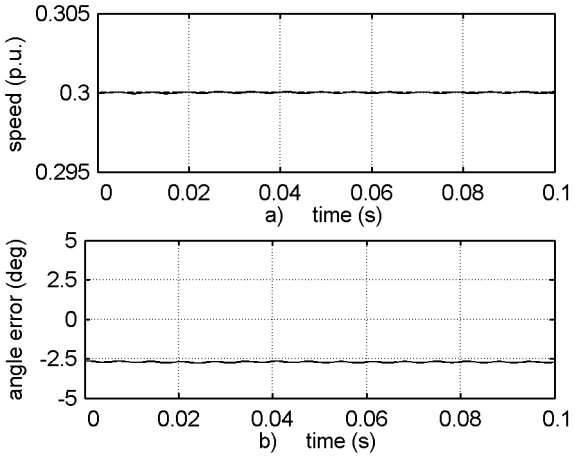

Fig. 3.74 Non-ideal VSI, Rasmussen estimator, $U_{dead}+U_{th}$= 1.92 V, full load, 0.3 p.u. speed reference. a) speed, b) position error.

3.6.2.3 Effect of non-ideal current measurements

Fig. 3.75 - Fig. 3.78 show simulations where the current measurement of phase A contains a 0.2 A (≈1.9%) offset. A quantization error of 10 bit A/D conversion is also simulated. Simulink's quantizer blocks with 50 mA interval are used. In the simulations of this section the model of the PMSM is ideal.

The offset creates a speed oscillation at the fundamental frequency [Qia04]. The flux linkage estimator is more sensitive to the offset error, Fig. 3.75 - Fig. 3.78. Current offset can be removed by careful tuning of the measurement system. High pass filters can also be used to remove DC levels.

In Fig. 3.79 - Fig. 3.80 the effect of gain unbalance of current measurement is simulated. Gain errors create the 2nd harmonic in speed and torque [Qia04]. The current of phase A is multiplied by 0.95. Other phases have unity gain. The simulations are performed at 0.04 p.u. speed. The load torque is nominal. The back-emf estimator is slightly more sensitive for gain unbalance when tuning parameters of Tables 3.2 and 3.3 are used. However, the differences are not remarkable.

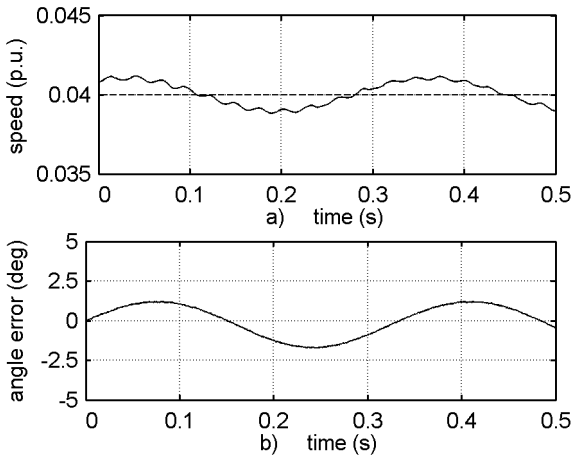

Fig. 3.75 Combined Matsui estimator, current offset 0.2 A in one phase, full load, 0.04 p.u. speed reference. a) speed, b) position error.

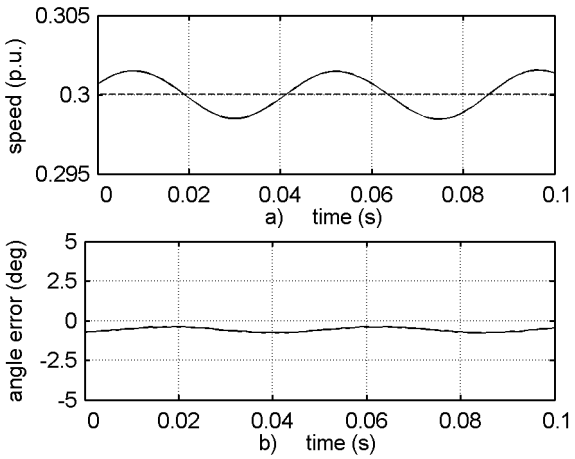

Fig. 3.76 Combined Matsui estimator, current offset 0.2 A in one phase, full load, 0.3 p.u. speed reference. a) speed, b) position error.

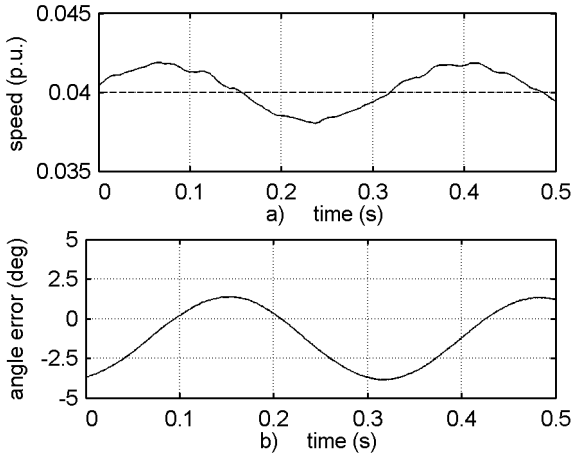

Fig. 3.77 Rasmussen estimator, current offset 0.2 A in one phase, full load, 0.04 p.u. speed reference. a) speed, b) position error.

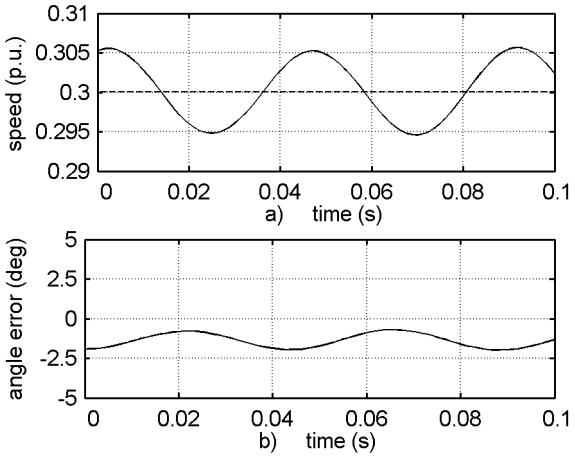

Fig. 3.78 Rasmussen estimator, current offset 0.2 A in one phase, full load, 0.3 p.u. speed reference. a) speed, b) position error.

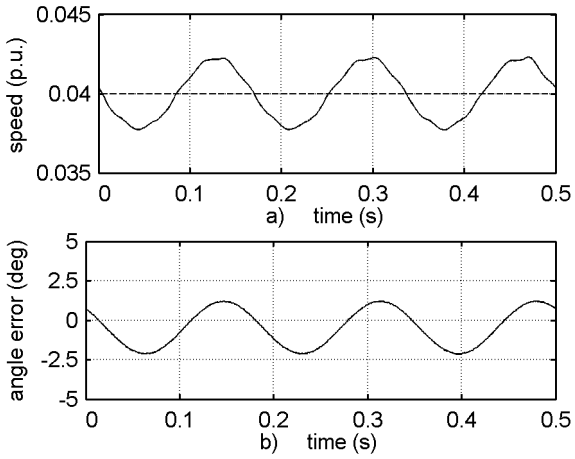

Fig. 3.79 Combined Matsui estimator, 0.95 gain in phase A, full load. a) speed, b) position error.

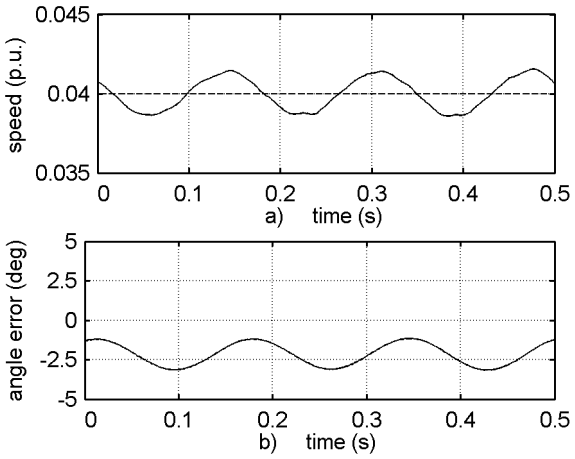

Fig. 3.80 Rasmussen estimator, 0.95 gain in phase A, full load. a) speed, b) position error.

3.6.3 Conclusions of simulations

In Section 3.6 model based estimators were compared in simulations. Two methods were based on the flux linkage estimation in the stationary reference frame [Nie99], [Ras03]. Three estimators were based on the back-emf information in the estimated rotor reference frame [Mat90], [Mat92]. The third back-emf method was proposed by the present author. It is a combination of the estimators presented by Matsui.

All the simulated methods are based on the PMSM voltage model (2-12). The flux linkage estimators are based on the voltage model in the stationary reference frame. No information on the mechanical parameters is needed. All the simulated methods have a fairly simple structure. The average steady state speed estimation error is zero with all simulated methods, also in the case of parameter errors, non-ideal PMSM and frequency converter. However, there were also differences between the estimators studied in the simulations.

Estimators were compared with erroneous parameters and non-ideal PMSM drive. The drawbacks and strengths revealed in the parameter sensitivity simulations are presented in Table 3.4. In the simulations where the parameter sensitivity was studied the combined Matsui estimator, Fig. 3.12, had a better performance than Matsui's original algorithms. The Rasmussen estimator [Ras03] performed better than the Niemelä method [Nie99]. Thus [Ras03] was chosen for the last simulations with the combined Matsui estimator, where they were compared in the case of non-ideal PMSM drive.

There were no significant differences between the combined Matsui method and Rasmussen method when the effects of non-ideal PMSM, frequency converter and current measurement system were studied. At low speeds the speed oscillation caused by the flux linkage harmonics of the PMSM was stronger in the case of Rasmussen estimator. The error voltages created by the non-ideal frequency converter caused a stronger oscillation in the case of the combined Matsui method. On the other hand the voltage errors increased the position error of the Rasmussen estimator. It was also slightly more affected by the offsets in the measured current signals.

Table 3.4 Comparison of the parameter sensitivity.

	Drawbacks	Strengths
Matsui's voltage method [Mat90], Fig. 3.6.	- Derivative of i_q must be modelled - Tends to oscillate - Very sensitive to parameter errors which create too small direct speed estimate.	- $\tilde{R}$ and $\tilde{\psi}_m$ do not create a position error in steady state - Zero steady state position error if $\tilde{L}_q = 0$
Matsui's current method [Mat92], Fig. 3.10.	- $\tilde{R}$ and $\tilde{\psi}_m$ create position errors in the low speed region - Very sensitive to parameter errors which create too small direct speed estimate	- Smooth behaviour even with large paramer errors
Combined Matsui estimator, Fig. 3.12.	- Very sensitive to parameter errors which create too small direct speed estimate	- Same as [Mat90] plus improved dynamic performance compared to [Mat90] without modelling the current derivatives
Niemelä estimator [Nie99], Fig. 3.18.	- Poor dynamic performance in the low speed region compared to back-emf methods - Very sensitive to negative resistance ($R < \hat{R}$) and inductance errors	- PM flux information is not needed. - Very simple algorithm. Only one tuning parameter
Rasmussen estimator [Ras03], Fig. 3.23.	- $\tilde{R}$ and $\tilde{\psi}_m$ create position errors in the low speed region. - Sensitive to negative resistance and inductance errors.	- PM flux information is needed but the method tolerates large errors - Less sensitive to negative resistance and inductance errors than the back-emf methods.

The combined Matsui estimator was selected for the experimental tests. The first reason is an easy implementation. The algorithm is performed in the synchronous reference frame where the current control is easier to implement. Computation delays do not create additional steady state position errors if the algorithm deals with DC signals. The other reason is the slight novelty of the back-emf estimator. Although it is based directly on the ideas of Matsui, some improvements are achieved if the algorithm proposed by the present author is applied.

4 Signal injection estimators

This chapter deals with signal injection estimators. At the beginning of the chapter a short introduction is given to the injection methods presented in the literature. The rest of the chapter concentrates on the comparison of high frequency and low frequency methods. At the end of the Chapter 4 a hybrid estimator where injection and model based algorithms are combined is discussed.

4.1 Introduction to signal injection estimators

4.1.1 Injection estimators based on the saliency of the PMSM

If a PMSM is magnetically asymmetric (salient), $L_q > L_d$. This is usually the case even if magnets are mounted on the rotor surface because the PM flux saturates the stator iron in the d axis direction. This increases the effective air gap and decreases the inductance in that direction. Thus the phase inductances are not equal. The direction of the saliency is the rotor d axis only if the PMSM is not loaded. The saturation of the iron is strongest in the direction of the stator flux linkage. If the load angle δ is significant the minimum inductance direction is shifted away from the d axis direction.

If $L_q \neq L_d$ and the stator voltage vector length of the three-phase machine changes, the direction of the resulting current vector is not the same. The exception is the case when the voltage vector derivative is aligned or perpendicular to the saliency. All the signal injection estimators discussed in Section 4.1.1 are based on this simple phenomenon. The estimators exploiting magnetic anisotropy are also called high frequency estimators. The frequency of the injected signal is clearly higher than the nominal angular speed ω_1.

The type of the high frequency excitation is one property which differentiates the methods. The types of signal processing used to track the rotor position and the angular speed also vary. The basic properties of high frequency injection estimators are briefly discussed in the following sections.

4.1.1.1 Periodic injection signal created by the modified PWM

One of the first signal injection methods presented was the INFORM method (INdirect Flux evaluation by Online Reactance Measurement). The INFORM method was reported for

the first time in 1988 [Sch88]. During the last fifteen years several improvements have been proposed to the method by the inventor, Professor Manfred Schröedl and his colleagues. INFORM is also used in commercial applications and can be considered to be a quite mature method.

The basic idea of detecting the position angle is quite simple. The control system is the vector control. Signal injection is performed by modifying the PWM operation. At constant intervals the normal PWM is stopped and a test voltage vector is injected into the motor. The changes of the phase currents during the test voltage injection are measured. The voltage and current information are used to determine a reactance vector in a complex plane. This "INFORM reactance" contains the information on the rotor position of the PMSM [Sch96]. INFORM has been tested with all AC motor types and it can also be used with induction motors and PMSM with surface mounted magnets [Sch96]. However, there are induction motors where the INFORM effect is too small for applicable solutions. The INFORM estimator needs an additional model based algorithm to determine a proper estimate for the angular speed. The estimator may be a Kalman filter [Sch96], for example, or a simple state observer [Sch02].

In [Jia97] and [Hol98] the position angle of a cage induction motor was estimated using instantaneous measurement of the total leakage reactance. The estimator needs measurements from phase voltages. Compared to INFORM this method requires only slight modification of the PWM switching and no additional estimator algorithms are required. The method exploits the magnetic anisotropy caused by the rotor slots. Thus this simple method cannot be applied to synchronous motors.

So-called "burst injection" was introduced in [Sta99]. This method is also suitable only for cage induction motors. In [Sta99] the periodic injection signal burst is applied to the stator voltages at only every half cycle. The rest of the time the voltage reference signals are sinusoidal. The bandwidth of this method is quite narrow.

Four requirements for a good sensorless control system were stated in Section 3.1.2. The signal injection methods referred above do not meet requirement 2. In this thesis methods which do not require modified PWM software are preferred. Periodic injection methods are discussed here no further.

4.1.1.2 Continuous signal superimposed on the fundamental frequency excitation signals

Compared to the estimators based on the modified PWM switching continuous injection signal estimators have been widely studied. Continuous injection methods do not need any

modifications of the PWM software. A high frequency voltage or current signal is superimposed on the fundamental frequency excitation signals (voltage or current reference signals). The waveform of the injected signal is usually sinusoidal. Naturally the injection signal is not literally sinusoidal because it is generated by a limited number of voltage vectors. Frequencies may vary from a few hundred hertz to the kilohertz region. In most of the papers presented the injected signal is a voltage. The amplitudes of resulting high frequency currents are modulated by the machine anisotropies. The position information is extracted from the measured stator current or the stator voltage waveforms. Continuous injection estimators can be divided into two subcategories by the reference frame in which the signal is injected.

Injection of a revolving signal, α,β -injection

A high frequency rotating voltage vector with a constant amplitude is added to the fundamental frequency voltage reference vector in the stationary α,β-reference frame [Jan95], [Lor00], [Sil03], [Tes01], [Con01], [Con03]. Thus the injected voltage vector has a constant angular speed and amplitude if it is observed from motor terminals. The resulting current vector naturally has a constant angular speed ω_i but the amplitude is modulated by the saliency of the motor. Current components with injection frequency are extracted from measured currents using band-pass filters or moving average filters. The extracted current vector $\underline{i}_i$ contains the position error information. A phase locked loop type tracking algorithms or simple arctan-function [Sil03] is used to form the speed and position estimate on the basis of the error information extracted from the measured currents (or voltages).

In [Con01] the principle of the α,β injection estimator is very simple. The position is estimated by detecting minimum and maximum values of the high frequency current vector $\underline{i}_i$ and comparing it to the angle of the carrier voltage vector at the same moment. The rotor position can be solved because the amplitude of $\underline{i}_i$ is a trigonometric function of the angle difference, θ_i-θ_r. θ_i is the angle of the injection voltage vector. The PLL algorithm is not necessary. However, this method does not estimate the angular speed of the rotor. It is also mentioned in [Lin03a] that measuring an accurate time instant for minimum and maximum $\underline{i}_i$ is difficult in the noisy environment.

In most of the papers a carrier signal is added to the voltage reference signals. In [Rib98] the voltage and current signal injections are compared. The voltage injection was recommended because the current control does not interfere with the high frequency signal added to the output of the current controllers. If the carrier signal is added to the current references the bandwidth of the current control limits the performance of position estimator.

The other approach is to measure stator voltages instead of currents and probe the zero voltage term (sum of the phase voltages) [Con00], [Con03]. The saliency of the AC motor also modulates the injection frequency component in the zero voltage. The position and speed signal can be extracted from zero voltage using the same signal processing methods as in the case of estimators using measured currents. In this thesis these methods are not further discussed. Voltage measurements are not difficult to implement but usually voltages are not measured in industrial applications. Thus the estimators presented in [Con00] and [Con03] do not fulfill the requirements given in Chapter 3.

Injection of an alternating signal, d,q -injection

A constant amplitude sinusoidal high frequency voltage signal is added to the voltage reference vector in the estimated rotor reference frame [Cor98], [Lin02], [Lin03a], [Jan03]. This method is also called pulsating injection because the injected voltage vector has both positive and negative sequence components. The idea of a pulsating injection signal was introduced in [Bla96] where a saturated induction machine was studied. The signal processing used to extract position and the speed information is rather similar to the α,β-injection methods. The carrier is usually injected into the estimated d axis direction [Lin02], [Lin03a], [Jan03]. In [Ha99], [Jan01] the carrier signal is injected into the 45° direction in d,q-frame. The α,β injection and d,q injection both fulfill the requirements of good speed and position estimator when the measured quantity is the stator current.

4.1.2 Injection estimators based on mechanical oscillation

In [Kim94] the initial rotor position was solved by injecting a rotating current vector into the PMSM. The frequency of the injected current was 65 Hz. The saliency ratio was assumed to be unity. It was found that the voltage reference vector with injection frequency moves along an ellipse if the rotor oscillates. The major axis of the ellipse is the direction of the rotor reference frame d axis. In [Lep03] the application was an induction motor drive. In addition to standstill, the low frequency estimator was successfully used in the low speed region. In this study these methods are called low frequency estimators. The injection frequency is in the same range as the nominal supply frequency.

In [Lep03] the sinusoidal injection signal was superimposed on the d axis current reference in the estimated rotor reference frame. Thus the injection current does not rotate in the stationary reference frame but pulsates as in the high frequency d,q injection discussed above. If the estimate of the rotor position is not correct there is also a torque producing q axis

component, which causes a mechanical oscillation. Oscillation can be detected from the estimated back-emf provided that the inertia is not too high. The oscillating back-emf signal is used to drive the position error to zero. The the low frequency estimator uses the motor model but is somewhat insensitive to parameter errors.

The low frequency estimator can also be applied in the case of PMSM [Ker03], [Esk05]. In [Ker03] the low frequency method is analysed in the case of a symmetric PMSM ($L_d = L_q$) and tested by simulations. The saliency of the motor is a distortion for the low frequency estimator method. In high frequency methods the saliency is a necessary condition for the estimator. In [Esk05] the effect of the saliency of the PMSM in the case of low frequency injection was discussed for the first time in the literature. The saliency effect was analysed theoretically and verified by measurements. A simple compensation method was proposed to prevent large steady state position errors. Key questions of the theoretical analysis of [Ker03] and [Esk05] are presented in Section 4.3. The method presented by Leppänen fulfills the requirements given in Chapter 3 at least in the low speed region.

4.2 Estimators using continuous high frequency signal injection

In this section d,q and α,β injection methods are briefly presented.

4.2.1 d,q injection (alternating injection)

The first task is to find a suitable voltage vector $\underline{u}_i$ which is injected into the PMSM. Quantities with frequency ω_i are denoted with the subscript i. In most papers and also here the injection is performed in the d axis direction. If only the d axis flux linkage oscillates the acoustic noise is minimized because no torque is produced. There is also another reason why d axis direction is preferred which will be explained later.

Let us assume that the sinusoidal signal is injected only in the direction of the actual d axis. Then $\tilde{\theta}_r = \theta_r - \hat{\theta}_r = 0$. Higher order flux linkage harmonics (2-22) are ignored. The injected space-vector is: $\underline{u}_i = v_i \cos(\omega_i t) + j0$, where v_i is the amplitude of the signal. If the injection frequency is in the kHz region R is negligible compared to $\omega_i L$. Therefore the PMSM (2–12) can be modelled as pure inductive load for quantities with frequency ω_i.

$$u_{\mathrm{id}} \approx L_{\mathrm{d}} \frac{di_{\mathrm{id}}}{dt} - \omega_{\mathrm{r}} L_{\mathrm{q}} i_{\mathrm{iq}}$$
$$u_{\mathrm{iq}} \approx L_{\mathrm{q}} \frac{di_{\mathrm{iq}}}{dt} + \omega_{\mathrm{r}} L_{\mathrm{d}} i_{\mathrm{id}} \quad + (\omega_{\mathrm{r}} \psi_{\mathrm{m}}) \tag{4–1}$$

$\omega_{\mathrm{r}} \psi_{\mathrm{m}}$ is a DC signal and therefore omitted.

It can be seen in (4–1) that the d and q axis equations are coupled if $\omega_{\mathrm{r}} \neq 0$. The q axis current also oscillates if the rotor rotates even if no injection signal is added to the q axis voltage reference. This should be avoided because the goal is that only the d axis current (and flux) oscillate when the position error is zero. The coupling can be removed by also adding a suitable signal in q axis direction. If the q axis flux does not oscillate with the frequancy ω_{i}, then $i_{\mathrm{iq}} = 0$. If zero i_{iq} is substituted into (4–1), i_{id} can be written: $i_{\mathrm{id}} = v_{\mathrm{i}} \sin(\omega_{\mathrm{i}} t) / (\omega_{\mathrm{i}} L_{\mathrm{d}})$. Now u_{iq} can be solved and the voltage reference space-vector which compensates the speed coupling is

$$u_{\mathrm{ide}} = v_{\mathrm{i}} \cos(\omega_{\mathrm{i}} t)$$
$$u_{\mathrm{iqe}} = v_{\mathrm{i}} \frac{\omega_{\mathrm{r}}}{\omega_{\mathrm{i}}} \sin(\omega_{\mathrm{i}} t) \tag{4–2}$$

Now the subscript "id" is replaced by "ide" (4–2) because in practice the injection is performed in the estimated d,q frame. If the signal injection estimator is used only in the low speed region ($\omega_{\mathrm{i}} >> \omega_{\mathrm{r}}$), zero value for u_{iqe} (4–2) can be used without significant errors. This has usually been done in the literature and also in this thesis.

When the voltages of (4–1) are replaced by (4–2) the high frequency flux vector in the estimated reference frame can be written

$$\psi_{\mathrm{ide}} = \frac{v_{\mathrm{i}}}{\omega_{\mathrm{i}}} \sin(\omega_{\mathrm{i}} t)$$
$$\psi_{\mathrm{iqe}} = 0. \tag{4–3}$$

In Chapter 2 the flux linkage equation (2-11) in the rotor reference frame was achieved by transforming (2-2) to the rotor reference frame. In stationary reference frame the equations of flux components with frequency ω_{i} are

$$\psi_{\mathrm{i}\alpha} = (L_0 + L_2 \cos 2\theta_{\mathrm{r}}) i_{\mathrm{i}\alpha} + L_2 \sin 2\theta_{\mathrm{r}} i_{\mathrm{i}\beta}$$
$$\psi_{\mathrm{i}\beta} = L_2 \sin 2\theta_{\mathrm{r}} i_{\mathrm{i}\alpha} + (L_0 - L_2 \cos 2\theta_{\mathrm{r}}) i_{\mathrm{i}\beta} \tag{4–4}$$

where $L_0 = (L_{\mathrm{d}} + L_{\mathrm{q}})/2$ and $L_2 = (L_{\mathrm{d}} - L_{\mathrm{q}})/2$. $\mathrm{i}_{\mathrm{i}\alpha}$ and $i_{\mathrm{i}\beta}$ are injection frequency components of the measured current vector. PM flux linkages are omitted. If (4–3) is transformed to the

stationary reference frame the flux linkage components are

$$\begin{aligned}\psi_{\mathrm{i}\alpha} &= \frac{v_\mathrm{i}}{\omega_\mathrm{i}}\sin(\omega_\mathrm{i}t)\cos\hat{\theta}_\mathrm{r} \\ \psi_{\mathrm{i}\beta} &= \frac{v_\mathrm{i}}{\omega_\mathrm{i}}\sin(\omega_\mathrm{i}t)\sin\hat{\theta}_\mathrm{r}\end{aligned} \tag{4–5}$$

When (4–4) and (4–5) are combined the components of the stationary frame current vector can be written

$$\begin{aligned}i_{\mathrm{i}\alpha} &= \sin(\omega_\mathrm{i}t)\frac{v_\mathrm{i}}{2\omega_\mathrm{i}}\left(\frac{L_\mathrm{d}+L_\mathrm{q}}{L_\mathrm{d}L_\mathrm{q}}\cos\hat{\theta}_\mathrm{r} - \frac{L_\mathrm{d}-L_\mathrm{q}}{L_\mathrm{d}L_\mathrm{q}}\cos(2\theta_\mathrm{r}-\hat{\theta}_\mathrm{r})\right) \\ i_{\mathrm{i}\beta} &= \sin(\omega_\mathrm{i}t)\frac{v_\mathrm{i}}{2\omega_\mathrm{i}}\left(\frac{L_\mathrm{d}+L_\mathrm{q}}{L_\mathrm{d}L_\mathrm{q}}\sin\hat{\theta}_\mathrm{r} - \frac{L_\mathrm{d}-L_\mathrm{q}}{L_\mathrm{d}L_\mathrm{q}}\sin(2\theta_\mathrm{r}-\hat{\theta}_\mathrm{r})\right)\end{aligned} \tag{4–6}$$

(4–6) is the injection current vector measured by A/D converters. Real and imaginary parts contain a sinusoidal component whose amplitude is modulated by the actual rotor position θ_r and the estimated position $\hat{\theta}_r$.

The next step is to transform (4–6) to the estimated rotor frame where the control and estimator algorithms are performed, Fig. 4.1.

$$\underline{i}_\mathrm{i}^{\mathrm{re}} = (i_{\mathrm{i}\alpha} + j i_{\mathrm{i}\beta})e^{-\mathrm{j}\hat{\theta}_\mathrm{r}} \Rightarrow \begin{aligned} i_{\mathrm{ide}} &= \frac{v_\mathrm{i}}{2\omega_\mathrm{i}}\sin(\omega_\mathrm{i}t)\left(-\frac{L_\mathrm{d}+L_\mathrm{q}}{L_\mathrm{d}L_\mathrm{q}} - \frac{L_\mathrm{d}-L_\mathrm{q}}{L_\mathrm{d}L_\mathrm{q}}\cos 2\tilde{\theta}_\mathrm{r}\right) \\ i_{\mathrm{iqe}} &= -\frac{v_\mathrm{i}}{2\omega_\mathrm{i}}\sin(\omega_\mathrm{i}t)\frac{L_\mathrm{d}-L_\mathrm{q}}{L_\mathrm{d}L_\mathrm{q}}\sin 2\tilde{\theta}_\mathrm{r} \approx -\underbrace{\frac{v_\mathrm{i}}{\omega_\mathrm{i}}\frac{L_\mathrm{d}-L_\mathrm{q}}{L_\mathrm{d}L_\mathrm{q}}}_{K_\mathrm{inj}}\sin(\omega_\mathrm{i}t)\tilde{\theta}_\mathrm{r}\end{aligned} \tag{4–7}$$

Now it can be seen that the q axis component of the injection current vector is a suitable error signal for the PLL type algorithm. If the rotor position is not accurately known the measured q axis current contains sinusoidal component with frequency ω_i. A current vector with injection frequency (4–7) is extracted from the measured i_qe by a band pass filter, Fig. 4.1. After filtering (4–7) must be demodulated. In [Lin02] (4–7) was transformed to the synchronous reference frame with angle $\omega_\mathrm{i}t$ and the demodulation was performed for the transformed current vector. In [Jan03] the demodulation process is simplified. Because the q axis equation contains all the essential information i_ide is omitted (4–7). i_iqe is multiplied by $\sin(\omega_\mathrm{i}t)$, Fig. 4.1. The result is a pulsating DC signal whose sign and amplitude are proportional to the position error. This error signal is LP filtered and the result is the input

signal of the PLL algorithm. The structure of the estimator is illustrated in Fig. 4.1.

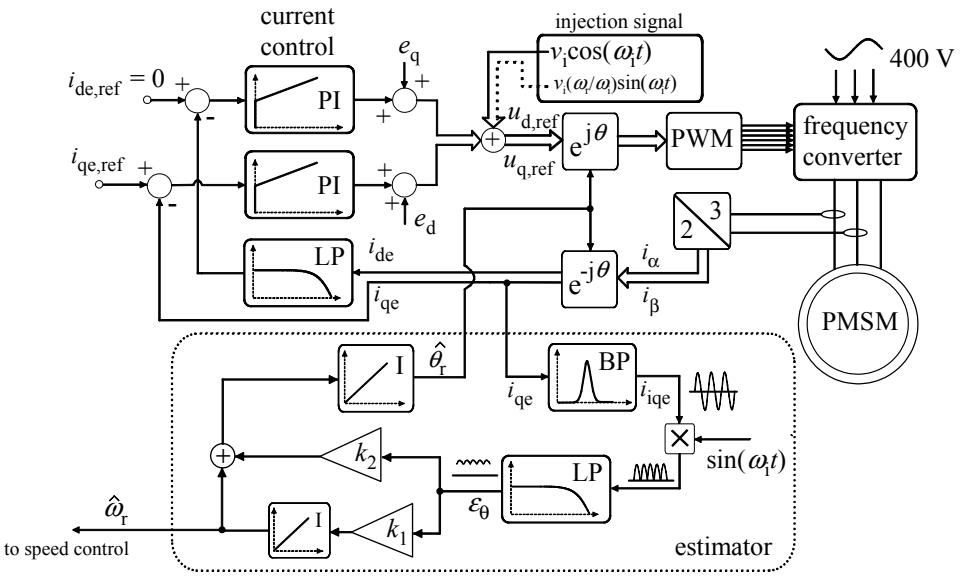

Fig. 4.1 Injection in the synchronous reference frame. The estimator is surrounded by a dotted line.

In this study the q axis injection signal is zero because injection methods are applied only at low speeds. In [Jan03] the PI controller of the PLL was replaced by a hysteresis controller which is faster but also produces more noise. Therefore the PLL structure is preferred.

4.2.2 α,β injection (revolving injection)

Instead of the pulsating signal (4–1) the injected voltage can be a rotating vector given by

$$\begin{aligned} u_{i\alpha} &= -v_i \sin(\omega_i t) \\ u_{i\beta} &= v_i \cos(\omega_i t) \end{aligned} \tag{4–8}$$

The injection current vector in stationary frame can be written [Deg98]

$$\begin{aligned} i_{i\alpha} &= \frac{v_i}{2\omega_i}\left(\frac{L_d + L_q}{L_d L_q}\cos(\omega_i t) - \frac{L_d - L_q}{L_d L_q}\cos(2\theta_r - \omega_i t)\right) \\ i_{i\beta} &= \frac{v_i}{2\omega_i}\left(\frac{L_d + L_q}{L_d L_q}\sin(\omega_i t) - \frac{L_d - L_q}{L_d L_q}\sin(2\theta_r - \omega_i t)\right) \end{aligned} \tag{4–9}$$

The injection current consists of two vectors rotating in opposite directions. Only the negative sequence vector ($2\theta_r$-$\omega_i t$) contains position information, Fig. 4.2. (4–9) can be extracted from the measured current by high pass or BP filtering. After filtering the positive sequence component is removed from (4–9) by "synchronous filtering" [Deg98]. (4–9) is transformed to the synchronous reference frame with angle $\omega_i t$, Fig. 4.2. After coordination

transformation the positive sequence components are DC signals easy to remove with HP filters. The filtered signals are transformed back to stationary frame. The result is a rotating vector.

$$\underline{i}_{\mathrm{i}}^{s} = \frac{v_{\mathrm{i}}}{2\omega_{\mathrm{i}}}\left(-\frac{L_{\mathrm{d}}-L_{\mathrm{q}}}{L_{\mathrm{d}}L_{\mathrm{q}}}\cos(2\theta_{\mathrm{r}}-\omega_{\mathrm{i}}t)-\mathrm{j}\frac{L_{\mathrm{d}}-L_{\mathrm{q}}}{L_{\mathrm{d}}L_{\mathrm{q}}}\sin(2\theta_{\mathrm{r}}-\omega_{\mathrm{i}}t)\right)=\frac{v_{\mathrm{i}}(L_{\mathrm{d}}-L_{\mathrm{q}})}{2\omega_{\mathrm{i}}L_{\mathrm{d}}L_{\mathrm{q}}}e^{\mathrm{j}(2\theta_{\mathrm{r}}-\omega_{\mathrm{i}}t)} \quad (4\text{–}10)$$

The position information is contained in the angle of the vector. The length of the vector is proportional to the saliency ratio. The error signal which drives the PLL algorithm is formed by taking the cross-product between the measured negative sequence vector (4–10) and an estimated unit vector, Fig. 4.2.

$$\mathrm{Im}\left\{-\frac{v_{\mathrm{i}}(L_{\mathrm{d}}-L_{\mathrm{q}})}{2\omega_{\mathrm{i}}L_{\mathrm{d}}L_{\mathrm{q}}}e^{j(2\theta_{\mathrm{r}}-\omega_{\mathrm{i}}t)}e^{-\mathrm{j}(2\hat{\theta}_{\mathrm{r}}-\omega_{\mathrm{i}}t)}\right\}=-\frac{v_{\mathrm{i}}(L_{\mathrm{d}}-L_{\mathrm{q}})}{2\omega_{\mathrm{i}}L_{\mathrm{d}}L_{\mathrm{q}}}\sin 2\tilde{\theta}_{\mathrm{r}}\approx-\frac{v_{\mathrm{i}}(L_{\mathrm{d}}-L_{\mathrm{q}})}{\omega_{\mathrm{i}}L_{\mathrm{d}}L_{\mathrm{q}}}\tilde{\theta} \quad (4\text{–}11)$$

The error signal amplitude is equal to (4–7). The stationary reference frame injection estimator is illustrated in Fig. 4.2. PLL is not the only option for forming the position estimate. In [Sil03] the position was determined directly from (4–10) by arctan operator.

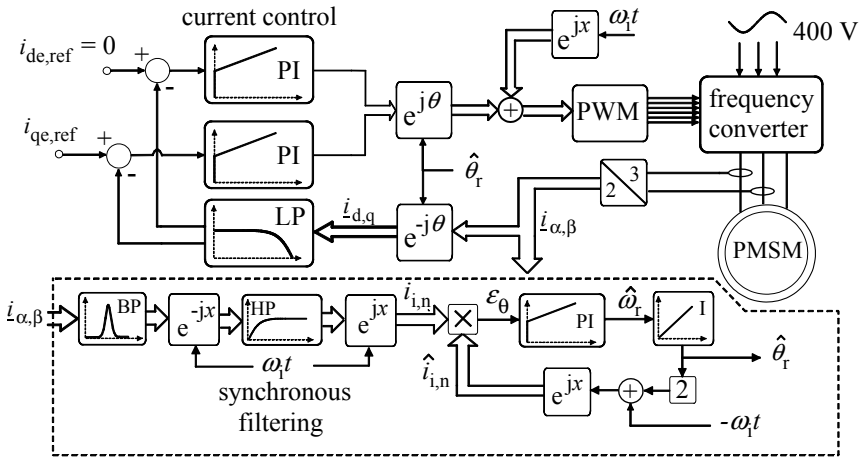

Fig. 4.2 Injection in the stationary reference frame.

4.2.3 The effect of non-ideal drive

4.2.3.1 Non-ideal frequency converter

In the literature the α,β injection, Fig. 4.2, and the d,q injection, Fig. 4.1, have both been widely studied. As stated above, the error signal formed by these estimators is equal in the case of an ideal machine. However, when the PMSM is fed by a real frequency converter the performances are not equal. Here the d,q injection method is preferred because it is shown in

[Lin03a], [Lin03b] that the d,q injection is less sensitive to disturbances created by the frequency converter.

The voltage distortion model of the frequency converters was discussed in Section 2.4. This modelling is also valid for high frequency injection. Fig. 4.3 illustrates the behaviour of the voltage and current vectors in the boundary between the current sectors I and II when the α,β injection is applied. The current sector is changed when one of the phase currents crosses zero. When the fundamental component of the current vector $\underline{i}^s$ is close to the sector boundary the high frequency current component $\underline{i}_i$ causes high frequency sector transitions. When the sector is changed the error voltage caused by the converter also changes (2–44) , Fig. 4.3. The maximum influence between both sectors can be expected when the fundamental current angle is 30° + n·60°. The high frequency error voltage vector transitions distort the estimator algorithm. Fig. 4.3 presents the distortion in the case of VSI. As discussed in Chapter 2, the error voltage waveforms of IMC and DMC are more complicated. However, the strongest voltage transitions occurs in the current sector boundary, also in the case of MC, Fig. 2.21 and Fig. 2.22.

Fig. 4.4 illustrates the behaviour of the current and voltage vectors when the d,q injection is performed. Now the current component with the injection frequency pulsates approximately in the direction of the d-axis because $u_{d,ref}$ oscillates, Fig. 4.1. The sector transitions mainly distort the d axis voltage. As presented in Section 4.2.1, the q axis current is used for speed and position tracking. Therefore the voltage distortion is less harmful

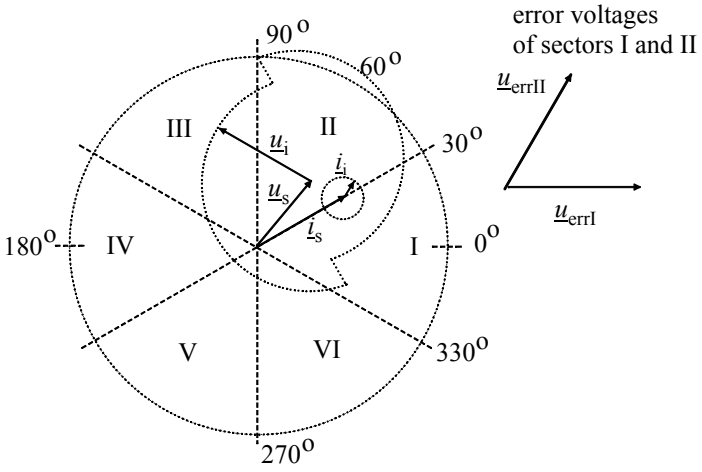

Fig. 4.3 Voltage and current vector trajectories on the boundary between two sectors, α,β injection.

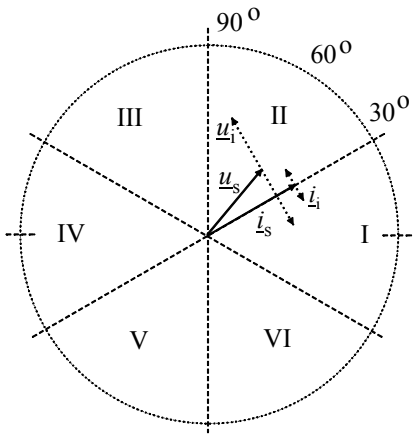

Fig. 4.4 Voltage and current vector trajectories on the boundary between two sectors, d,q injection.

The effect of the frequency converter is also illustrated in Fig. 4.5 (α,β) and Fig. 4.6 (d,q). The PMSM A (Appendix A) is driven in the Simulink model with direct speed and position

feedback. Thus $\hat{\theta}_r$ is replaced by θ_r in the estimator algorithms. Injection signals are superimposed on the voltage reference signals as presented in Fig. 4.1 and Fig. 4.2. The model of the non-ideal frequency converter is the same as in the simulations in Chapter 3. The error signal ε_θ, which is the input for the PLL, is clearly more distorted in the case of α,β injection, Fig. 4.5. Six sector transitions during the one fundamental period create the sixth harmonic component to the torque and speed of the PMSM if the signal ε_θ is used to track the rotor position. Therefore d,q injection is preferred.

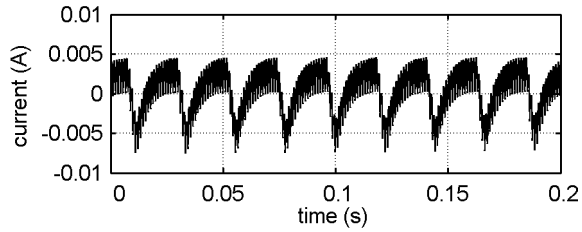

Fig. 4.5 Error signal ε_θ, α,β injection. Nominal load, 0.1 p.u. speed.

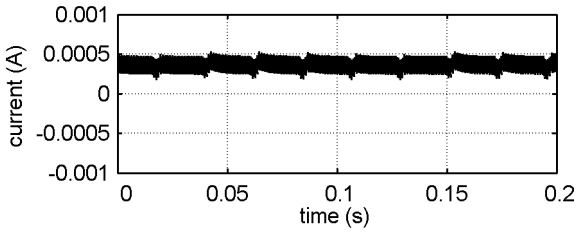

Fig. 4.6 Error signal ε_θ, d,q injection. Nominal load, 0.1 p.u. speed.

4.2.3.2 Higher order saliencies and current measurement errors

The estimator algorithms presented in the previous sections are based on the fundamental frequency model, where L_d and L_q are constants. As presented in Chapter 2, the flux equations contain multiples of the 6th harmonic of the fundamental motor supply frequency when they are transformed to the rotor reference frame. Therefore the error signal (4–7), (4–11) contains multiples of 6^{th} harmonics and the same frequencies can be found in the torque produced by the PMSM.

Errors of current measurement create effects similar to those presented in the simulations in Section 3.6.2. Offsets create speed and torque oscillation at fundamental frequency [Qia04]. Gain errors create 2nd harmonic. In general, an injection estimator is more sensitive to current measurement errors than a model based estimator. Position error is tracked from the signal with rather small amplitude compared to the fundamental frequency current. The measured result may be distorted if A/D conversion is performed close to the time point when the active vectors of the converter are changed. The distortion may be insiginicant for current control and a model based estimator, but the relative error may be large when $\underline{i}_i$ is concerned. In this thesis A/D conversions are executed at the end of the modulation period. In the low speed region, the end of t_{mod} is reserved for a zero vector with relatively long duration because the fundamental voltages are small. Thus the current oscillations should have decayed.

4.2.3.3 Effect of the armature reaction

The air gap flux of the PMSM is affected by the flux created by the stator current and inductances of the PMSM. This is called an armature reaction. The direction of the minimum inductance is a function of the load torque. Especially in the case of the SPMSM the armature reaction can produce significant position errors because the saliency is mainly created by the air gap flux. The armature reaction is illustrated in Fig. 4.7. Fig. 4.8 shows the measured steady state position error at zero speed (Machine A, Appendix A) when d,q injection is used to estimate the rotor position. No attempt was made to compensate the effect of load. The position error was quite linearly dependent on the load torque. Thus the position error created by the load effect is fairly easy to compensate.

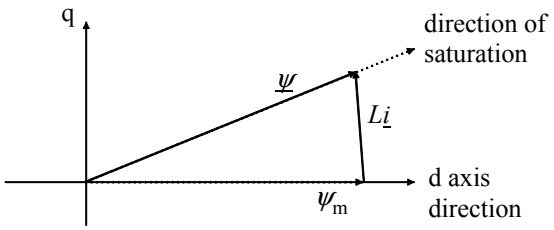

Fig. 4.7 Armature reaction.

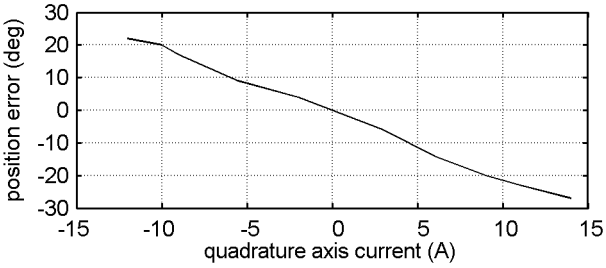

Fig. 4.8 Measured steady state position error at zero speed (Machine A). The effect of the armature reaction has not been compensated.

The armature reaction also makes the compensation of the higher order saliencies of the PMSM more difficult. In Chapter 2 the higher order saliencies are tied to the rotor position θ_r. In (2-21) zero θ_r means that $L_{dd,6n}$ and $L_{qq,6n}$ have their maximum and the effect of cross coupling inductance $L_{dq,6n}$ is zero. In practice there is a load dependent phase shift between the higher order saliencies and their reference frames $6n\theta_r$ where n = 1,2,3… More information on the effects of the main flux saturation will be found in [Vas92]. Higher order saliencies are studied in [Deg98], [Lor00].

The author tried to compensate the sixth harmonic produced by the PMSM by adding a suitable sinusoidal signal to the input of the PLL, ε_θ in Fig. 4.1, having the same amplitude and frequency as the sixth harmonic in the error signal ε_θ but an opposite phase. The results were not encouraging. The amplitude of the 6th harmonic of ε_θ, Fig. 4.1, was a function of i_q. A more serious problem was the phase shift between 6th harmonic and θ_r. It was possible to reduce the torque oscillation in one operating point. However, if the load was changed the compensation was no longer effective and in some cases the results were even worse than with no compensation.

4.2.4 Compensation of disturbances and other practical aspects

As discussed above, the frequency converter and additional saliencies of the PMSM create multiples of the 6th harmonic in to the torque and speed of the PMSM. Compensation of the dead time effect of the frequency converter is not crucial if d,q injection is applied. In the case of α,β injection dead times must be taken into account [Sil02], [Sil03]. The effect of additional saliencies of the PMSM still remains. In [Sil03] a so-called space modulation profile is used to remove unwanted signals from the input of the PLL. The method is based on the predefined tables. The commissioning of the tables is done off-line with data captured during sensored operation. Measured position is used to form compensation signals which remove harmonics from the input signals of the estimator. The initialization sequence is performed with various load torques. The result is a two-dimensional look-up table giving suitable compensation signals. In [Sil03] α,β injection is used, but a similar idea can be applied in the case of d,q injection. The experimental results are quite promising. The drawback of this method is the need for the sensor during the "teaching sequence". Kalman filter based heavy algorithms are also used to remove selected harmonics from a signal [Car03]. In this thesis compensation methods are not studied in detail.

4.2.4.1 Initial angle detection

When the system is started the estimator finds the direction of the d-axis. However, there is an uncertainty in the rotor position of 180 degrees since there are two inductance minima, one in 0° direction and other in 180° direction. The simple method to check the direction of the estimated d axis is to use a short drive sequence where the motor is fed by a constant q axis current after the estimator has tracked the minimum inductance. The direction of rotation is detected. If the estimated angle increases during the sequence with positive current the estimator has found the correct d axis direction.

Rotating of the rotor is not always possible. A more sophisticated method is to exploit the saturation of the stator iron. One method is to inject voltage pulses into both directions of the estimated d axis. When the pulse causes a flux in the same direction as the PM flux the stator iron becomes more saturated. This decreases the inductance. If the pulse causes opposite flux the saturation decreases and the inductance increases. If the voltage pulses are strong enough the inductance difference can be measured. A fairly comprehensive list of initial angle detection methods based on the signal injection is given and a new method is developed in [Kim04]. In this thesis initial angle detection methods are not studied.

4.2.4.2 Selection of the frequency and the amplitude of the injection signal

The tuning of the high frequency injection estimator requires the selection of parameters affecting the performance of the system. These parameters are: injection voltage (amplitude and frequency), parameters of the selected signal processing method used to extract the useful information from the measured currents and tuning of the PLL. Tuning of the PLL and filter algorithms of the high frequency injection estimator will be described in Section 4.2.5.

The main principle is to select a injection frequency as high as possible. A higher frequency means a faster estimator. The magnitude of the position error is known after half of the injection signal period, Fig. 4.1. If ω_i is high enough it does not affect the performance of the current control because the injection components are outside the bandwidth of the control. However, two factors restrict the maximum frequency. First, increased ω_i decreases i_{iq} which decreases the accuracy of the system because the resolution of the current measurement is limited. Very high ω_i would require injection voltages which are not acceptable in practice. Secondly, ω_i is limited by the modulation frequency. If ω_i is too high, one injection voltage period is realised using only a few active voltage vectors. This increases the harmonics of the i_{iqe} and current measurements may be distorted due to the large voltage transients.

In this study one injection voltage period is composed of eleven voltage values. Therefore the injection frequency is 909 Hz (1/(11*100 μs)). This frequency is clearly outside the bandwidth of the current control. Frequencies 1 kHz, 1.111 kHz were also tested but the performance of the estimator was impaired. Frequencies lower than 909 Hz did not improve the results in the low speed region where injection methods were applied. In the literature, [Jan03], [Sil03], [Wal04a], the injection frequency usually varies between 500 Hz and 1 kHz. In [Cor98], [Lin02] the injection frequency was 2 kHz.

In matrix converter drives (Machine A) the amplitude of $\underline{u}_i$ was 40 V. In VSI drive (Machine B) the amplitude was 80 V. In the matrix converter drive the amplitude of the i_{id} was approximately 1.1 A (10% of the nominal). In the VSI drive the amplitude was 3 A. The resolution of the current measurement of the MC drive was 50 mA and 250 mA in the case of the VSI drive with Machine B.

The amplitudes of the injection currents are higher than would be expected on the basis of the inductance values of Appendix A. Inductances are smaller for the higher frequencies because it is more difficult for high frequency flux components to penetrate the iron parts of the rotor and the permanent magnets. Thus leakage inductances become more dominant when frequency is increased.

4.2.5 Tuning of the signal injection estimator

The high frequency injection estimator, Fig. 4.1, includes signal processing algorithms not needed in the basic PLL applied in the model based estimators. In this thesis, Fig. 4.1, the injection frequency component is separated from the measured i_{qe} by a second order band-pass (BP) filter. The filter type is Butterworth. When the PLL is analysed the amplitude of the i_{iqe} (4–7) is replaced by a DC signal. The PB filter is then replaced by a first order LP filter which gives the envelope of the BP filter, Fig. 4.10. The block diagram of the PLL in the frequency domain is illustrated in Fig. 4.9. Now the PLL is a third order system. The LP filter used for the smoothing of the demodulated signal, Fig. 4.1, is not concerned because its time constant may be one tenth of τ in Fig. 4.9. The step responses of the BP filter used in this thesis and the "equivalent" LP filter are shown in Fig. 4.10. The magnitude response and the discrete transfer function of the BP filter are shown in Fig. 4.11. The time constant τ is 2.2 ms. The application specific gain K_{inj} was introduced in (4–7).

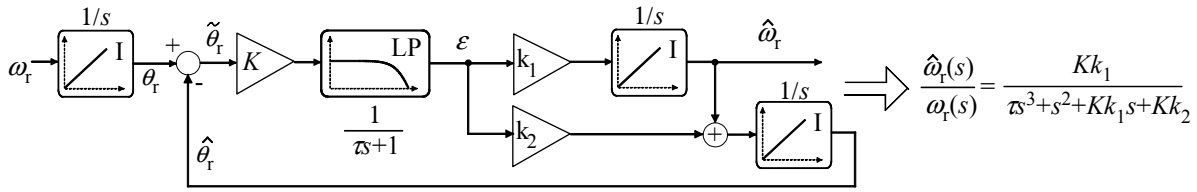

Fig. 4.9 Relation between ω_i and estimated speed in the PLL used for speed and position estimation.

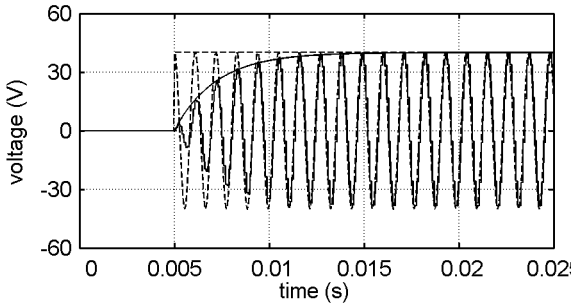

Fig. 4.10 Step response of the BP filter and "equivalent" LP filter. Input signals are dashed.

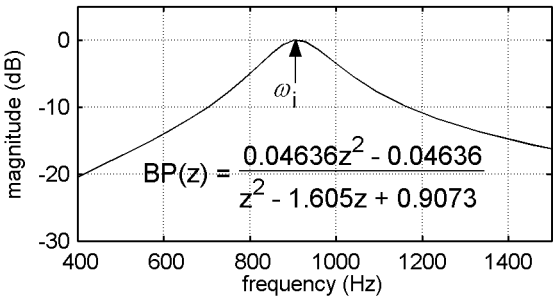

Fig. 4.11 Amplitude response and the transfer function of the BP filter.

Filtering naturally narrows the bandwidth of the PLL. Thus the filter should be as fast as possible. A fast filter means that the amplitude of the filter output i_{iqe} rapidly follows the changes of the position error. The drawback is the lesser damping of the frequencies around ω_i. In fast current transients other frequencies pass the filter and disturb the estimation process. Heavy damping around the injection frequency gives a "clean" signal but the performance of the speed control is impaired.

The BP filter is not the only algorithm used to extract i_{iqe} from i_{qe}. In [Wal04a] high-pass

filters with very low bandwidths were used to remove the DC-level of the measured current. These filters are sensitive to disturbances and serious problems may occur during transients, especially in servo drives, where mechanical time constants are small. In [Lep03], [Pii04] the DC-level is removed by using moving average (MA) and trend removing alogorithms. [Lep03] concentrated on low frequency injection but the idea of the estimator is similar to high frequency methods. In a MA filter n samples of data are stored and the sum of samples is divided by n. In every calculation period the oldest sample is replaced by the newest. The filter can remove frequency multiples of $1/(nt_s)$, where t_s is the sample time.

In this thesis a BP filter is preferred because it has better properties in fast current transients. In Fig. 4.12 a signal with a frequency of 1 kHz is extracted from the input signal by a BP filter and the MA algorithm where the MA of 1 ms (n = 10) is subtracted from the input signal. In steady state both algorithms give similar results. If the DC level of the input signal is rapidly changed the output of the MA algorithm is more heavily distorted. The MA filter removes only certain frequencies as explained above. On the other hand the MA filter is faster and does not contain the LP filter type delay presented in Fig. 4.10, when the magnitude of the position error changes rapidly. Because a MA algorithm filters effectively only the multiples of $1/(nt_s)$ the signal may require stronger LP filtering after the demodulator compared to the case when a BP filter is used, Fig. 4.1

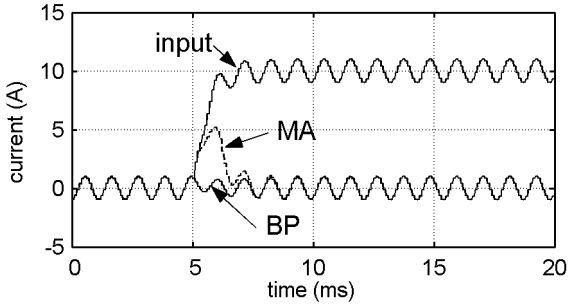

Fig. 4.12 Comparison of responses of the band-pass filter (BP) and the moving average filter (MA).

The estimated speed (output of the PLL) must be filtered to prevent the amplification of distubances in the speed control loop. Here a second order Butterworth type LP filter was used. The filter has a double pole in –400/s. Let us assume that a second order LP filter is tuned to attenuate a certain frequency by the same amount as a first order filter. The step response of the higher order filter is clearly faster. The bandwidth of the speed control loop is therefore increased. In this thesis a second order LP filter was used to filter the speed estimate in the simulations and measurements.

The benefits of second order filters are clear in the case of machine A, which is a small

servomotor. Machine B has a long mechanical time constant J/b. In that case the speed filter is of only minor importance and a first order filter can be used.

4.3 Low frequency signal injection estimator

In Section 4.3 the position and speed estimation of the PMSM using a low frequency signal injection are studied. The method was presented for an induction motor in [Lep03]. In [Esk05] the same method was applied for a synchronous machine drive. In Section 4.3.1 the basic functionality of the method is explained. In Section 4.3.2 the steady state behaviour is analysed in a case of salient ($L_d < L_q$) PMSM. Saliency is a disturbance which may generate a significant position error. In Section 4.3.3 a simple compensation method is proposed and the performance is verified with an experimental example.

4.3.1 Low frequency d,q injection

The fundamental frequency voltage model of the PMSM in the rotor reference frame was given in Equation (2-12) and is shown here again:

$$\begin{aligned} u_d &= Ri_d + L_d \frac{di_d}{dt} - \omega_r L_q i_q \\ u_q &= Ri_q + L_q \frac{di_q}{dt} + \omega_r (\psi_m + L_d i_d) \end{aligned} \tag{4–12}$$

where ψ_m is the PM flux. In the low frequency injection estimator studied in this thesis a sinusoidal low frequency signal, $i_i\cos(\omega_i t)$, is added to the d-axis current reference, Fig. 4.13. In that case the d and q axis currents contain DC components (i_d and i_q) and sinusoidal components (i_{id} and i_{iq}) with the injection angular frequency ω_i. The equation of the torque and the equation of the motion are

$$T_e = 3p/2\left(\psi_m (i_q + i_{iq}) + (\Delta L)(i_d + i_{id})(i_q + i_{iq})\right) \tag{4–13}$$

$$\omega_r = \frac{p}{J}\int (T_e - T_L)dt \tag{4–14}$$

where $\Delta L = L_d - L_q$. The friction coefficient b in (2-27) is assumed to be insignificant.

The basic idea of the low frequency method is first explained by assuming a completely non-salient machine, $\Delta L = 0$ [Ker03]. In that ideal case the torque produced by the PMSM is a function of the q axis current only. If the estimated position angle of the rotor is not correct the sinusoidal current is also injected in q axis direction, which creates a mechanical

oscillation. The actual q axis current oscillating with frequency ω_i can be written

$$i_\mathrm{iq} \approx \mathrm{Im}\left\{\left(\underbrace{i_\mathrm{i}\cos(\omega_\mathrm{i}t)}_{i\mathrm{ide,ref}} + j0\right)\mathrm{e}^{-\mathrm{j}\tilde{\theta}_\mathrm{r}}\right\} \approx -i_\mathrm{i}\cos(\omega_\mathrm{i}t)\sin\tilde{\theta}_\mathrm{r} \tag{4–15}$$

The equation of i_iq is an approximation, because the actual currents do not follow their references perfectly. (4–15) is substituted into the equation of torque (4–13). The oscillating torque is substituted into (4–14). The load torque T_Load is assumed to be constant, and it can thus be omitted because it does not contain any components with injection frequency. Now it is possible to write an expression for the back-emf oscillating with the injection frequency ω_i.

$$e_\mathrm{iq} = -\omega_\mathrm{r}\psi_\mathrm{m} = \frac{3p^2\psi_\mathrm{m}^2 i_\mathrm{i}}{2J}\sin\tilde{\theta}_\mathrm{r}\int\cos(\omega_\mathrm{i}t)dt = \sin(\omega_\mathrm{i}t)\frac{3p^2\psi_\mathrm{m}^2 i_\mathrm{i}}{2J\omega_\mathrm{i}}\sin\tilde{\theta}_\mathrm{r} \tag{4–16}$$

Finally the actual oscillating q axis back-emf (4–16) is transformed into the estimated d,q frame with angle $\hat{\theta}_\mathrm{r}$. The oscillating back-emf component in the reference frame of the control system is

$$e_\mathrm{iqe} = \mathrm{Im}\{\mathrm{j}e_\mathrm{iq}\mathrm{e}^{\mathrm{j}\tilde{\theta}_\mathrm{r}}\} = \cos\tilde{\theta}_\mathrm{r}\sin(\omega_\mathrm{i}t)\frac{3p^2\psi_\mathrm{m}^2 i_\mathrm{i}}{2J\omega_\mathrm{i}}\sin\tilde{\theta}_\mathrm{r} \approx \sin(\omega_\mathrm{i}t)\frac{3p^2\psi_\mathrm{m}^2 i_\mathrm{i}}{2J\omega_\mathrm{i}}\tilde{\theta}_\mathrm{r} \tag{4–17}$$

(4–17) is a suitable error signal for a PLL type algorithm. Equation (4–17) has a similar form to the error equation of the high frequency estimator, (4–7). The amplitude of the oscillating back-emf e_iqe is proportional to the square of the number of pole pairs and inversely proportional to the inertia J.

Estimator structure

The estimate of the oscillating back-emf in the q direction (4–17) is obtained using the basic voltage equation in the estimated rotor reference frame (4–12).

$$u_\mathrm{qe} = Ri_\mathrm{qe} + L_\mathrm{q}\frac{di_\mathrm{qe}}{dt} + \omega_\mathrm{r}(L_\mathrm{d}i_\mathrm{de} + \psi_\mathrm{m}) \Rightarrow e_\mathrm{qe} = -u_\mathrm{qe} + \hat{R}i_\mathrm{qe} + \hat{L}_\mathrm{q}\frac{di_\mathrm{qe}}{dt} + \hat{\omega}_\mathrm{r}\hat{L}_\mathrm{d}i_\mathrm{de} \tag{4–18}$$

A BP filter is used to extract e_iqe from the estimated back-emf e_qe (4–18). In [Lep03] the filtering is achieved by removing the trend and average from e_qe. The position error is demodulated by multiplying the extracted signal by $\sin(\omega_\mathrm{i}t)$, Fig. 4.13.

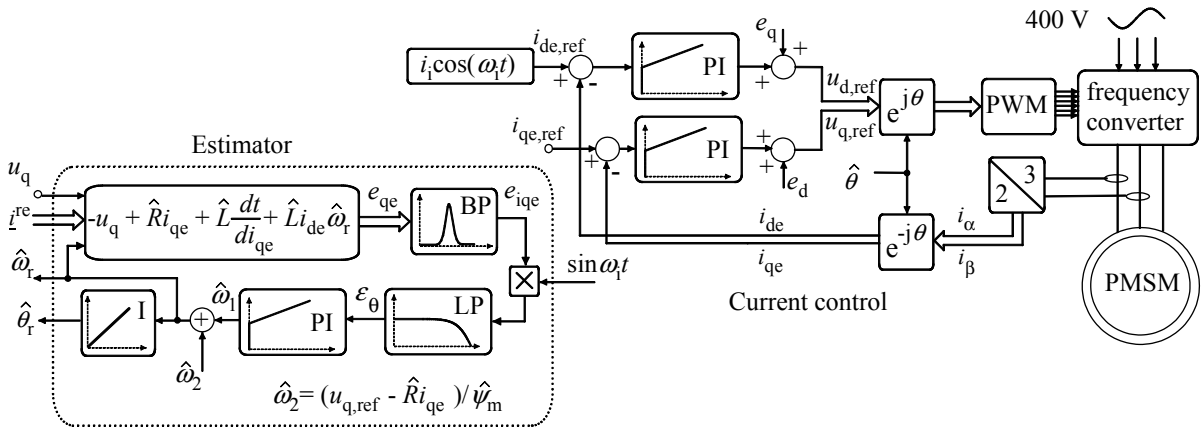

Fig. 4.13 Basic structure of the current control and low frequency estimator.

If the motor is symmetric and the rotor speed is close to zero the PLL algorithm drives the position error to zero in steady state operation. In practice there is always some saliency even in the case of surface magnet motors. The effect of saliency and interaction between speed and oscillating current components may cause severe errors in the estimated position if they are not properly compensated.

The dynamic performance of the low frequency signal injection is rather poor because the position error information is extracted from a low frequency signal. The injection frequency ω_i varies between a few Hz and a few hundred Hz depending on p^2/J ratio (4–17). The dynamic performance of the estimator can be improved by also exploiting the speed information of the average component of e_{qe} [Lep03]. In Fig. 4.13 the output of the direct speed estimator is denoted as $\hat{\omega}_2$.

4.3.2 Analysis of the steady state behaviour

If the PMSM is loaded and there is an error between the actual and the estimated position the current seen by the control system is

$$\underline{i}^{re} = e^{j\tilde{\theta}_r}\,\underline{i}^{r} \Leftrightarrow i_{de} = i_d\cos\tilde{\theta}_r - i_q\sin\tilde{\theta}_r,\; i_{qe} = i_d\sin\tilde{\theta}_r + i_q\cos\tilde{\theta}_r \qquad (4\text{–}19)$$

The current control drives the average of i_{de} to zero. Thus in steady state

$$i_d = i_q\tan\tilde{\theta}_r\,. \qquad (4\text{–}20)$$

i_q is dependent on the load and on the position error. If the position error is within an acceptable range: $i_q \approx 2T_{Load}/3p\psi_m$. The BP filter, Fig. 4.13, removes from e_{qe} (4–18) all but the frequencies ω_i. Therefore the DC component ($i_d i_q$) and the component with frequency $2\omega_i$ ($i_{id} i_{iq}$) are omitted from the equation of the torque (4–13). Using (4–13) and (4–14) the speed

in steady state is

$$\omega_{\mathrm{r}} = \omega_{\mathrm{r0}} + \omega_{\mathrm{ir}} = \omega_{\mathrm{r0}} + \frac{p}{J}\int T_{\mathrm{ie}}dt = \omega_{\mathrm{r0}} + \underbrace{\frac{3p^2}{2J}\int\left(\psi_{\mathrm{m}} i_{\mathrm{iq}} + \Delta L(i_{\mathrm{d}} i_{\mathrm{iq}} + i_{\mathrm{q}} i_{\mathrm{id}})\right)dt}_{\omega_{\mathrm{ir}}}, \qquad (4\text{–}21)$$

where ω_{r0} is the average speed and ω_{ir} is the oscillating speed with frequency ω_{i}. Now we can write the voltage equation (4–12) in the actual synchronous reference frame. Only the components with frequency ω_{i} are included.

$$\begin{aligned} u_{\mathrm{id}} &= R i_{\mathrm{id}} + L_{\mathrm{d}} \frac{di_{\mathrm{id}}}{dt} - L_{\mathrm{q}}(\omega_{\mathrm{r0}} i_{\mathrm{iq}} + \omega_{\mathrm{ir}} i_{\mathrm{q}}) \\ u_{\mathrm{iq}} &= R i_{\mathrm{iq}} + L_{\mathrm{q}} \frac{di_{\mathrm{iq}}}{dt} + L_{\mathrm{d}}(\omega_{\mathrm{r0}} i_{\mathrm{id}} + \omega_{\mathrm{ir}} i_{\mathrm{d}}) + \psi_{\mathrm{m}} \omega_{\mathrm{ir}} \end{aligned} \qquad (4\text{–}22)$$

Using (4–19) - (4–22) we can built a model in a more convenient form for the steady state analysis of the low frequency estimator, Fig. 4.14. This model contains the current control, PMSM and the block calculating the oscillating back-emf e_{iqe}. The "e" block of Fig. 4.14 is simplified by omitting the derivative of i_{q}. This can be done because the steady state performance is analysed and the i_{q} reference contains no component with frequency ω_{i}. For the same reason the speed control is excluded.

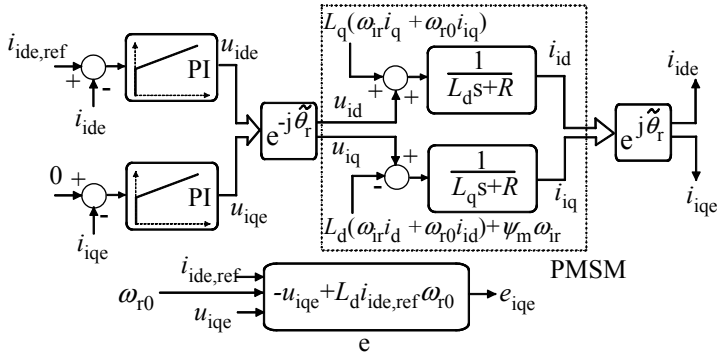

Fig. 4.14 Simplified structure of the control system and low frequency estimator.

Using Fig. 4.14 it is possible to write a transfer function between the back-emf e_{iqe} and i_{ide} reference [Esk05].

$$G_{\mathrm{e}}(s) = \frac{e_{\mathrm{iqe}}(s)}{i_{\mathrm{ide,ref}}(s)} = \frac{-(K_{\mathrm{p}}s + K_{\mathrm{i}})^2 \left(\frac{\Delta L \sin(2\tilde{\theta}_{\mathrm{r}})}{2} s^2 + \omega_{\mathrm{r0}}(L_{\mathrm{d}} \cos^2 \tilde{\theta}_{\mathrm{r}} + L_{\mathrm{q}} \sin^2 \tilde{\theta}_{\mathrm{r}})s + A \right)}{(L_{\mathrm{d}} L_{\mathrm{q}} s^4 + (K_{\mathrm{p}} + R)(L_{\mathrm{d}} + L_{\mathrm{q}})s^3 + Bs^2 + Cs + D)s} + \hat{L}_{\mathrm{d}} \omega_{\mathrm{r0}}$$

(4–23)

where

$$A = -\frac{3p^2 \sin(2\tilde{\theta}_\mathrm{r})}{4J}(\Delta L(\psi_\mathrm{q} i_\mathrm{q} + \psi_\mathrm{d} i_\mathrm{d}) + \psi_\mathrm{m}\psi_\mathrm{d}) + \frac{3p^2}{2J}(\psi_\mathrm{q} \sin^2 \tilde{\theta}_\mathrm{r}(\psi_\mathrm{m} + \Delta L i_\mathrm{d}) + \Delta L \psi_\mathrm{d} i_\mathrm{q} \cos^2 \tilde{\theta}_\mathrm{r})$$

$$B = \left(\omega_{\mathrm{r}0}^2 L_\mathrm{d} L_\mathrm{q} + (K_\mathrm{p} + R)^2 + K_\mathrm{i}(L_\mathrm{d} + L_\mathrm{q}) + \frac{3p^2}{2J}(\psi_\mathrm{m}\psi_\mathrm{d} L_\mathrm{d} + \Delta L \psi_\mathrm{d} L_\mathrm{d} i_\mathrm{d} - \Delta L \psi_\mathrm{q} L_\mathrm{q} i_\mathrm{q}) \right)$$

$$C = (K_\mathrm{p} + R)\left(2K_\mathrm{i} + \frac{3p^2}{2J}(\psi_\mathrm{m}\psi_\mathrm{d} - \Delta L \psi_\mathrm{q} i_\mathrm{q} + \Delta L \psi_\mathrm{d} i_\mathrm{d}) \right) + \frac{\omega_{\mathrm{r}0} 3p^2}{2J}(\Delta L(\psi_\mathrm{d} L_\mathrm{q} i_\mathrm{q} + \psi_\mathrm{q} L_\mathrm{d} i_\mathrm{d}) + L_\mathrm{d}\psi_\mathrm{m}\psi_\mathrm{q})$$

$$D = K_\mathrm{i}^2 + \frac{3p^2 K_\mathrm{i}}{2J}(\Delta L \psi_\mathrm{d} i_\mathrm{d} - \Delta L \psi_\mathrm{q} i_\mathrm{q} + \psi_\mathrm{m}\psi_\mathrm{d})$$

In (4–23) K_p is the gain of the PI controller and K_i is the gain K_p divided by the integration time t_i. ψ_d and ψ_q are flux linkage components ($\psi_\mathrm{m} + L_\mathrm{d} i_\mathrm{d}$) and $L_\mathrm{q} i_\mathrm{q}$. If the rotor speed is near zero and the PI controller gains (K_i, K_p) are large the denominator of (4–23) approaches $s(K_\mathrm{p}s + K_\mathrm{i})^2$. If this approximation is used we can write a simplified expression for the gain and phase of (4–23). The simplified model does not take the tuning of the PI controllers into account.

$$\begin{aligned} \mathrm{Gain}\big(G_\mathrm{e}(s)\big) &\approx \sqrt{\omega_{\mathrm{r}0}^2 (L_\mathrm{d} \cos^2 \tilde{\theta}_\mathrm{r} + L_\mathrm{q} \sin^2 \tilde{\theta}_\mathrm{r})^2 + \left(-\frac{\Delta L \sin(2\tilde{\theta}_\mathrm{r})}{2}\omega_\mathrm{i} + \frac{A}{\omega_\mathrm{i}} \right)^2} \\ \mathrm{Phase}\big(G_\mathrm{e}(s)\big) &\approx \tan^{-1}\left(\frac{\left(-\frac{\Delta L \sin(2\tilde{\theta}_\mathrm{r})}{2}\omega_\mathrm{i} + \frac{A}{\omega_\mathrm{i}} \right)}{-\omega_{\mathrm{r}0}(L_\mathrm{d} \cos^2 \tilde{\theta}_\mathrm{r} + L_\mathrm{q} \sin^2 \tilde{\theta}_\mathrm{r})} \right) \end{aligned} \qquad (4–24)$$

The effect of saliency at zero speed

First the position error $\tilde{\theta}_\mathrm{r}$ is assumed to be zero. The only nonzero component in the gain is $3p^2 \Delta L \psi_\mathrm{d} i_\mathrm{q} / 2J$ inside the coefficient A, (4–24). The phase shift is approximately $-\pi/2$. This can be concluded from (4–24) because the denominator of the lower expression is very small (the speed $\omega_{\mathrm{r}0}$ is near zero). In the demodulation process, Fig. 4.13, e_iqe is multiplied by a signal with $-\pi/2$ phase lag compared to $i_\mathrm{ide,ref} = i_\mathrm{i}\cos(\omega_\mathrm{i} t)$. Thus the e_iqe has a non-zero amplitude and is in phase with the demodulation signal. The error signal ε_θ is larger than 0. The estimated position increases. The next important operating point is the position error where the torque oscillation with the angular frequency ω_i is zero. This is the case when the coefficient A is zero. However, the position estimate still increases because the saliency

dependent component $-\Delta L\sin(2\tilde{\theta}) < 0$ (4–24). Finally the position error stabilizes when $-0.5\Delta L\sin(2\tilde{\theta}_r)\omega_i^2 + A = 0$ (4–24). The gain equation (4–24) is simplified further by excluding all coefficients smaller than 10% of the largest one. The following expression can be written for position error in steady state.

$$\tilde{\theta}_{SS} \approx \tan^{-1}\left(\frac{C + \sqrt{4\Delta L^2\omega_i^4 J^2 + 3p^2\psi_m^2(4\Delta L\omega_i^2 J + 3p^2\psi_m^2 + 12p^2\Delta L^2 i_q^2)}}{6p^2\Delta L\psi_m i_q}\right) \quad (4\text{–}25)$$

where $C = -2J\Delta L\omega_i^2 - 3p^2\psi_m^2$

The steady state position error as a function of saliency, inertia, injection frequency and the load torque is illustrated in Fig. 4.15, [Esk05] (Appendix A, Machine B). The results achieved by (4–23) and the simplified case (4–25) are compared to the results from the full Simulink model with the speed control loop. The simple model gives accurate results if the position error is smaller than 15°. The analysis shows that quite small saliencies can lead to significant steady state errors in position. Thus the effect of the saliency must be compensated.

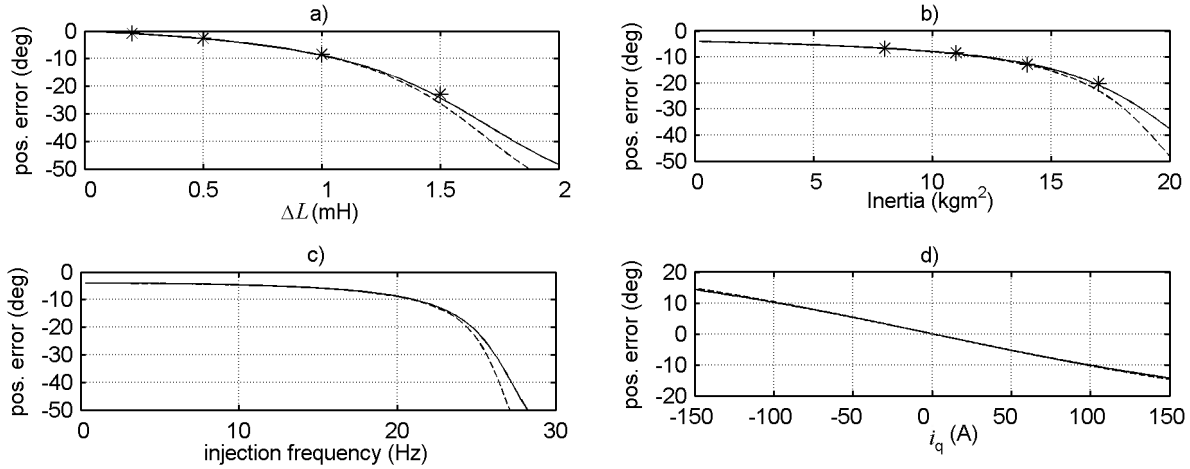

Fig. 4.15 Zero speed steady state position error $\theta - \hat{\theta} = \tilde{\theta}$ of the PMSM (B). In a) ΔL varies while other parameters are correct and the load is nominal, L_d = 8.5 mH. In b), c) and d) the variable quantities are inertia, injection frequency and i_q. The steady state error is calculated by (4–23) (solid line) and (4–25) (dashed line). Results from the full Simulink model are marked by *. Nominal values are: J = 11 kgm^2, ΔL = -1 mH, i_q = 85 A and $\omega_i = 40\pi$ rad/s.

Effect of speed

In Fig. 4.15 angular speed ω_{r0} is assumed to be zero. If the speed is nonzero it interacts with i_{id} and i_{iq} (4–22). $\omega_{r0}L_d i_{id}$ is the dominant oscillating flux component. The current controller tries to compensate it (i_{iq} reference = 0). If the PI controller, Fig. 4.14, is not extremely fast, there will remain some sinusoidal q axis voltage, which causes an additional

error to e_{iqe}. It can be seen in (4–24) that non-zero ω_{r0} changes the amplitude and the phase shift of e_{iqe}. The steady state error is now clearly dependent on the tuning of the current control. Thus the simple model (4–24) gives accurate results only if the angular frequency ω_{r0} is zero or very low. Fig. 4.16 shows the error when the speed varies between -10% and 10% speed. The results are calculated with three t_i using (4–23). If t_i is kept constant and K_p varies the results are very similar. Increased inertia and saliency increase the speed dependent error. However, this speed error also exists when $L_d = L_q$.

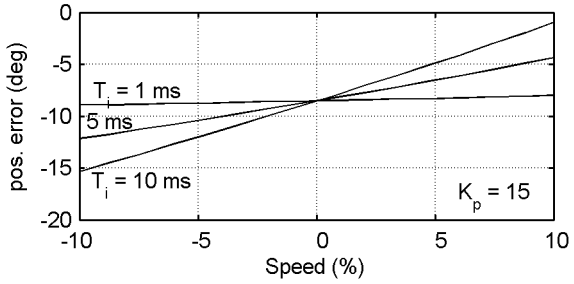

Fig. 4.16 Steady state position error as a function of speed. Load and the other parameters are nominal.

4.3.3 Compensation of the steady state position error

A major steady state error in the position estimate can be prevented by injecting a convenient low frequency signal in the q axis direction. The idea is to cancel the reluctance component from the equation of the torque. Let us assume that $i_{iqe,ref} \neq 0$. Now i_{id} and i_{iq} are: $(i_{id} + \mathrm{j}i_{iq}) \approx (i_{ide,ref} + \mathrm{j}i_{iqe,ref})e^{-j\tilde{\theta}_r}$. i_{id} and i_{iq} are are substituted into the equation of the torque (4–13). There is no torque oscillation with frequency ω_i if the position error is zero and

$$i_{iqe,ref} = -\frac{i_{ide,ref} i_q \Delta L}{\psi_m + \Delta L i_d} \tag{4–26}$$

The reference signal in the q direction is in phase with the main injection signal $i_{ide,ref}$. Even if the position error is not zero the injection of (4–26) compensates the effect of the reluctance torque with good accuracy. In practice the non-ideal current controllers cause a small error. The saliency ratio, inertia and other parameters restrict the use of this compensation method. Even if injecting (4–26) removes the other coefficients with ΔL from the numerator of (4–23) there remains a component $0.5\Delta L \sin(2\tilde{\theta}_r)$. If it increases faster than the coefficient A (4–23) when the position error increases the system is unstable or at least the steady state error becomes considerable. If the slopes of these two coefficients are studied

around the zero position error the following condition can be written for the inertia and saliency ΔL.

$$\Delta L \omega_{\mathrm{i}}^2 + \frac{3p^2\psi_{\mathrm{m}}^2}{2J} > 0 \tag{4–27}$$

The performance of the low frequency estimator is studied experimentally with a 23 kW axial flux machine [Esk05]. The selected PMSM is challenging due to its high inertia. The PMSM is not very salient: $L_{\mathrm{d}}/L_{\mathrm{q}} \approx 0.9$. When the machine was driven in steady state with 65% load the position error was approximately 20 degrees [Esk05]. Fig. 4.17 shows the measured speed when the load is nominal and the effect of saliency is corrected by (4–26). The measured position error is presented in Fig. 4.18.

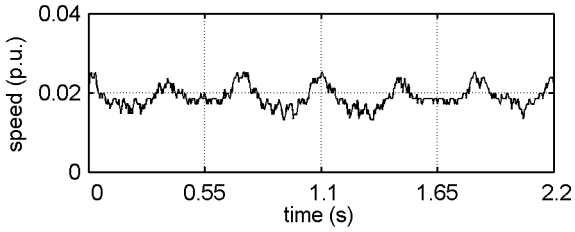

Fig. 4.17 Measured angular speed. The load is nominal and the speed reference is 0.02 p.u.

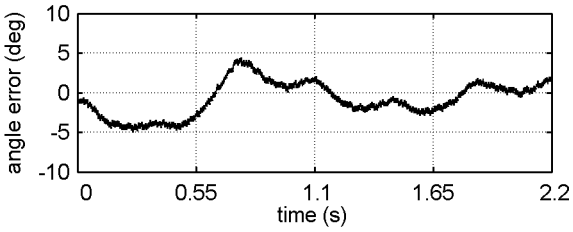

Fig. 4.18 Measured position error. The load is nominal and the speed reference is 0.02 p.u.

The low frequency estimator is not immune to the disturbances which create multiples of the 6th harmonic to the torque. The sixth harmonic is clearly visible in Fig. 4.17.

The low speed estimator was also tested in transients. In [Esk05] the drive was stable in 30% torque step tests. The drive was unstable in the case of nominal torque steps and fast speed reversals with nominal load.

The performance of the low frequency estimator is clearly poorer than the performance of the high frequency d,q injection estimator (when it is possible to use HF method). The low frequency estimator is suitable for special cases when the saliency ratio is close to unity. Then the low frequency method may be the only way to obtain stable operation around the zero speed. Low frequency injection methods are not further discussed here.

4.4 Hybrid estimator

In this thesis the goal is to find a position and speed estimator which is stable over the nominal speed region. The requirements for a good estimator were given in Section 3.1. Model based estimators cannot be applied alone because they cannot operate properly at low speeds. High frequency methods are stable at zero speed region and they can also be used in

the nominal speed region [Lin03b]. However, at higher speeds model based methods have attractive features, hence the motivation for a hybrid estimator.

The main drawbacks of high frequency injection estimators are:

- Need for injection voltage. Injection creates additional acoustic noise and power losses,
- Modulation index greater than unity may be demanded by the control if the machine is operating with nominal speed and an injection voltage with high amplitude is added to the voltage references,
- Higher demands for the performance of the current measurement system.

In Chapters 3 and 4 several model based estimators and injection estimators were discussed. The model based estimator presented in Section 3.4.5 is used at higher speeds. In the low speed region d, q injection is applied.

An important issue is the change of the method. It cannot be done suddenly because it would cause unwanted oscillation if the drive operates near the border speed. In [Wal04a] the transition between the model based and the injection estimator is made by linear transition functions, Fig. 4.19. This method is also used here.

The position error signal is calculated by the voltage model, Fig. 3.12, and the injection method, Fig. 4.1. Both error signals are multiplied by their transition function and added together. If $|\omega_r| > \omega_h$ the estimator is completely model based. If $|\omega_r| < \omega_l$, the position error is corrected using only the signal injection method. When $|\omega_r| > \omega_h$ the amplitude of the injection signal v_i is decreased linearly toward zero as a function of $|\omega_r|$.

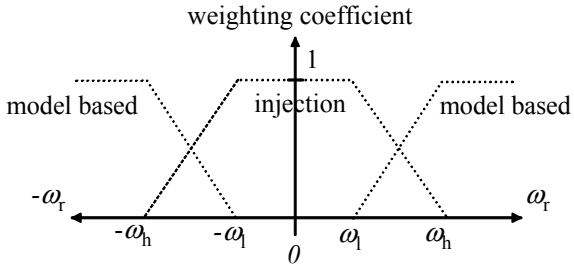

Fig. 4.19 Transition function providing smooth transition between estimation methods.

Fig. 4.20 shows the hybrid estimator used in this study. The estimator is the same as that presented in Fig. 3.12 (combined Matsui estimator). The only addition is the "filtering and demodulation" block from Fig. 4.1. The direct speed estimator (lower branch in Fig. 4.20 with output $\hat{\omega}_2$) is always active. It was found that the performance of the estimator is improved at low speeds if the signal injection estimator is assisted by the simple model based speed estimator.

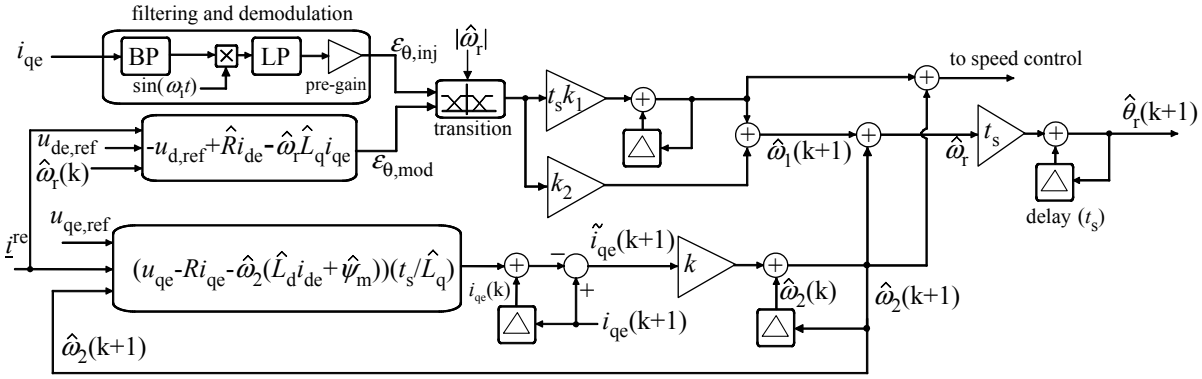

Fig. 4.20 Discrete time implementation of the hybrid estimator.

In [Pii05] the injection estimator does not directly take part in calculating the speed estimate. The injection branch has its own PI controller and the output of the PI algorithm is used to correct the speed estimate which adjusts the adaptive model. When $|\omega_t|$ increases the effect of injection is reduced by linearly decreasing the amplitude of v_i and gains of the PI controller.

4.5 Simulations of injection and hybrid estimators

The modelling of the d,q injection estimator and the hybrid estimator is performed in the Matlab Simulink environment. The tuning of the speed controller, current controllers and estimator algorithms are presented in Table 4.1. The motor parameters are from Appendix A (Machine A).

Simulations are carried out with d,q injection estimator alone Fig. 4.1 and with the hybrid estimator Fig. 4.20. When d,q injection is not assisted by the model based algorithm the gains of the PLL are constants because the application specific gain K (3-12) is not speed dependent. Poles are placed at the real axis as explained in Section 3.3.

In the hybrid estimator the model based estimator is the combined Matsui method presented in Section 3.4.5. As discussed in Section 3.4.3, the gains of the PLL vary as a function of speed ω_t when a back-emf estimator is applied (3-38). When $\omega_t < \omega_{low}$ the gains k_1 and k_2 are constants, Table 4.1. The gain ($K_{inj} = v_i(L_d\text{-}L_q)/\omega_t L_d L_q$) of the injection estimator (4–7) is clearly smaller than the gain $\omega_t \psi_m$ (3-35) of the model based estimator when $\omega_t < \omega_{low} = \omega_n$. Gains of the PLL are constants when the estimated ω_t is below ω_{low} (3–38). Therefore the output of the injection branch, Fig. 4.20, is multiplied by a "pre-gain" $(\omega_{low}\psi_m)/K_{inj}$ This ensures that the error signals $\varepsilon_{\theta,inj}$ and $\varepsilon_{\theta,mod}$ are approximately equal when the injection branch is active. In the case of motor A (Appendix A), pre-gain is approximately

70. The border frequencies ω_l and ω_h of the hybrid estimator are 0.09 p.u and 0.18 p.u. respectively, Fig. 4.19. The 2nd order LP filter in speed feedback has a double pole in -400/s.

Table 4.1 Parameters of the control system and estimators.

	k_p	t_i	PLL of the estimator	ω_{low}	k
Speed control	1.8	0.03 s			
Current control	20	0.005 s			
Model based in hybrid			$k_1 = \rho^2/K$, $k_2 = 2\rho/K$ (ρ = 80/s and $K = \omega_r \psi_m$)	0.18 p.u.	120
d,q injection in hybrid			same as above (K always (0.18*471) ψ_m)		
d,q injection alone			$k_1 = 700^2$, $k_2 = 2*700$		

4.5.1 Low speed simulations

First the pure injection estimator and hybrid estimator are compared. The speed is changed from zero to 0.05 p.u. and then the sign of the speed reference is changed. After the machine has been decelerated to zero speed the sign of the nominal load torque is changed from 100% to -100% value at 0.75 s. Fig. 4.21 and Fig. 4.22 show the simulated speed and position error. Fig. 4.23 and Fig. 4.24 illustrate the same sequence in the case of the hybrid estimator. Because the speed estimate is under 0.09 p.u. the signal $\varepsilon_{d,mod}$ is not used to correct the estimated position. However, the direct speed estimator of the hybrid estimator with output $\hat{\omega}_2$ is active, Fig. 4.20.

The overshoot of the simulated speed is significant. The reason is not the tuning of the speed controller. The current transient disturbs the injection estimator. For a short period after the transient the estimated speed increases into a wrong direction.

The performance of the hybrid estimator is better even if the slower PLL tuning is used compared to the pure d,q injection version, Table 4.1. This is an advantage because the estimator is less sensitive to disturbances if the gains of the PLL can be decreased.

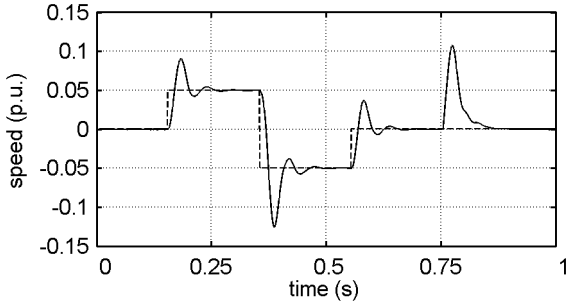

Fig. 4.21 d,q injection, speed reference and simulated speed, nominal load.

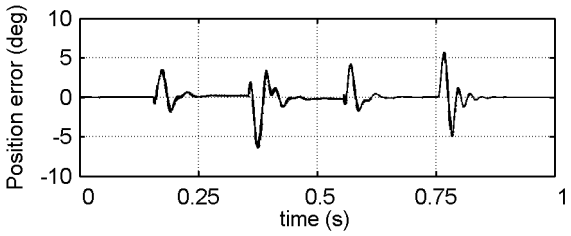

Fig. 4.22 d,q injection, position error ($\theta_r - \hat{\theta}_r$), nominal load.

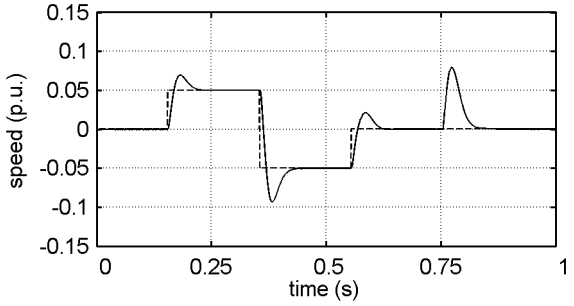

Fig. 4.23 Hybrid estimator, speed reference and simulated speed, nominal load.

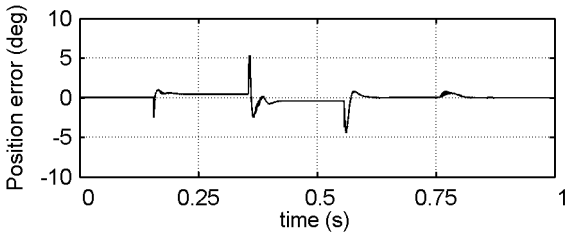

Fig. 4.24 Hybrid estimator, position error, nominal load.

If gains of the pure injection estimator are decreased from the values of Table 4.1 the overshoot and oscillation of the speed increase. In the hybrid estimator, Fig. 4.23, the parameters R, ψ_m and L were accurate. The response of the hybrid estimator is slower if significant parameter errors occur.

Fig. 4.25 and Fig. 4.26 show the simulated speed and position errors in the case of a non-ideal PMSM when the pure d,q injection is used. The results of the hybrid estimator are presented in Fig. 4.27 and Fig. 4.28. The speed reference was 0.02 p.u. and the load was nominal. The non-idealities were discussed in Section 3.6.2.1.

There are no significant differences between the d,q injection estimator and the hybrid estimator where the d,q method was assisted by a direct speed estimator, Fig. 4.20. In the case of pure d,q method, Fig. 4.25, the amplitude of the 12th harmonic is more visible. Errors generated by the frequency converter are not considered because they have no significant effect when the d,q injection is simulated. The effect of current measurement errors was simulated in Chapter 3.

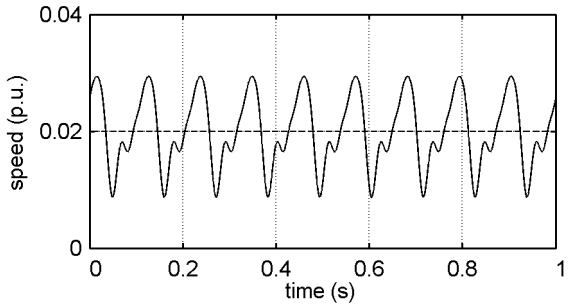

Fig. 4.25 d,q injection. 6th harmonic included in inductances, simulated speed, nominal load. 0.02 p.u. speed reference (dashed line).

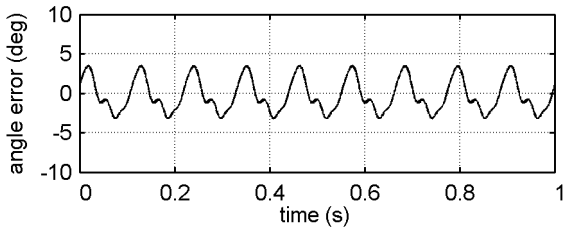

Fig. 4.26 d,q injection. Position error.

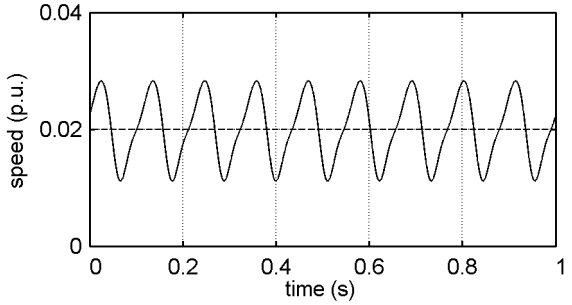

Fig. 4.27 Hybrid estimator. 6th harmonic included in inductances, simulated speed, nominal load. 0.02 p.u. speed reference (dashed line).

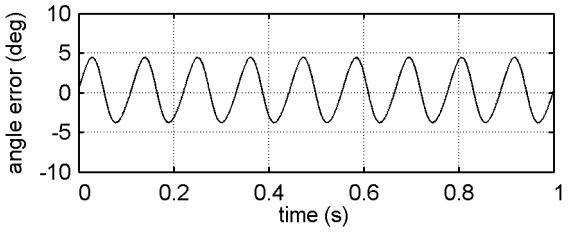

Fig. 4.28 Hybrid estimator. Position error.

4.5.2 Nominal speed simulations

Fig. 4.29 - Fig. 4.34 show simulations where the PMSM is driven from side to side of the nominal speed range and the rotor position and the angular speed are calculated by the hybrid estimator. The PMSM is accelerated from zero to nominal negative speed. The PMSM regenerates when ω_r is negative. After speed reversal the PMSM is decelerated to low speed region and finally the speed reference is changed to value 0.5 p.u.

Fig. 4.29 and Fig. 4.30 show the angular speed and position error when the parameter errors are zero and the load is nominal. The next two figures show the same simulation without load. In Fig. 4.33 and Fig. 4.34 the load is nominal and the parameters R, L_d and L_q are not accurately known. The resistance of the PMSM is 30% higher than the R used in the estimator software. The estimator also uses only one inductance value $L = (L_d + L_q)/2$. The position error is increased but otherwise parameter errors do not significantly reduce the performance of the estimator.

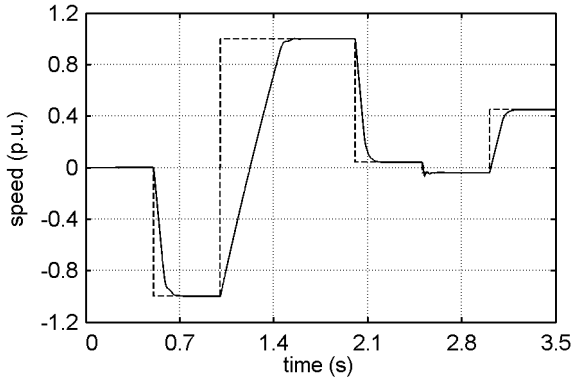

Fig. 4.29 Hybrid estimator. Reference and simulated speed. Nominal load, accurate parameters.

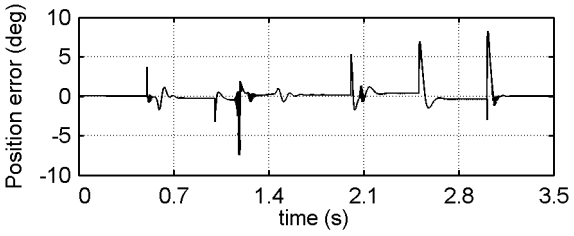

Fig. 4.30 Hybrid estimator. Position error, nominal load, accurate parameters.

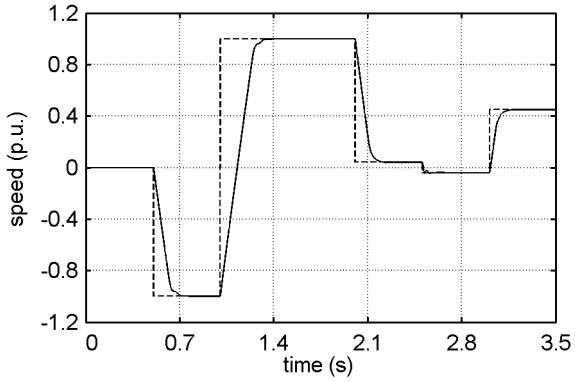

Fig. 4.31 Hybrid estimator. Reference and simulated speed. No load, accurate parameters.

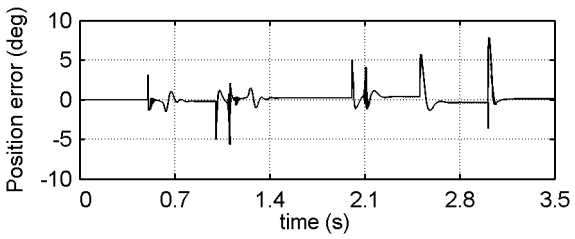

Fig. 4.32 Hybrid estimator. Position error, no load, accurate parameters.

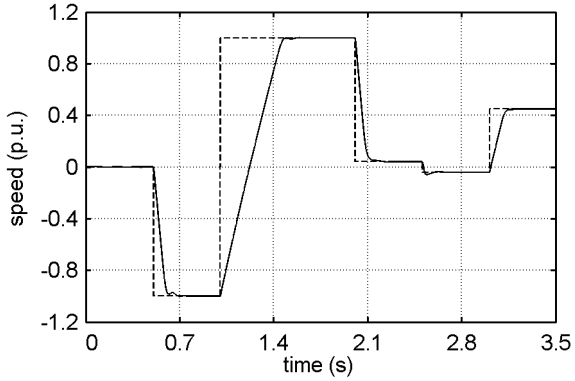

Fig. 4.33 Hybrid estimator. Simulated speed. Nominal load, $R - \hat{R} = 0.3\ \Omega$ (30%). $\hat{L} = 0.01$ H.

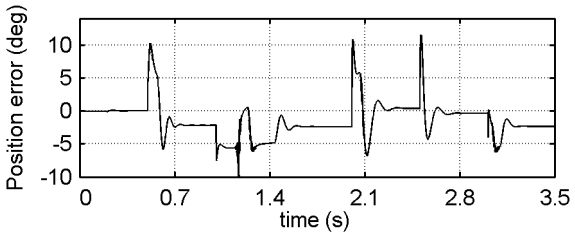

Fig. 4.34 Hybrid estimator, position error, nominal load. $R - \hat{R} = 0.3\ \Omega$ (30%). $\hat{L} = 0.01$ H.

In the step response tests above the estimated ω_r rapidly crosses the speed range between ω_l and ω_h, Fig. 4.19. In the next two figures the load torque is nominal and the speed is reversed by using a rather slow ramp reference signal. The parameter errors are same as above, Fig. 4.33. The position error, Fig. 4.36, contains a small steady state error but otherwise the behaviour of the system is good. The steady state error is created by parameter errors. In that case the incorrent q axis inductance estimate produces a position error (3-41).

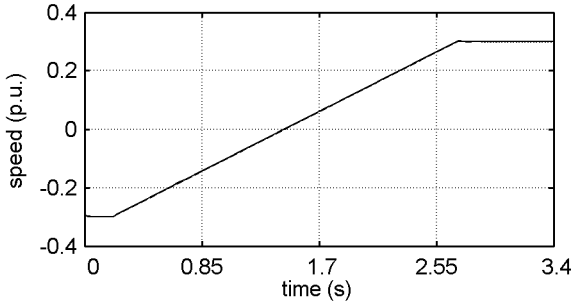

Fig. 4.35 Hybrid estimator. Simulated speed. Nominal load, $R - \hat{R} = 0.3\ \Omega$, $\hat{L} = 0.01$ H.

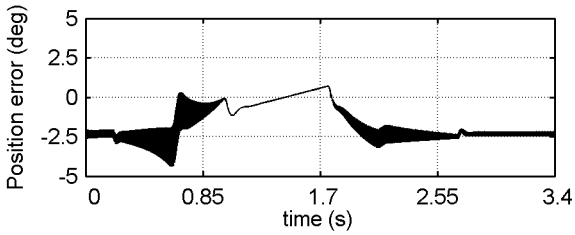

Fig. 4.36 Hybrid estimator, position error. Nominal load, $R - \hat{R} = 0.3\ \Omega$, $\hat{L} = 0.01$ H.

5. Realisation of the experimental setup

5.1 Experimental VSI drive

Fig. 5.1 illustrates a schematic diagram of the VSI drive used in this thesis. A 23 kW axial flux PMSM (machine B in Appendix A) is fed by a voltage source frequency converter, Appendix B. The rectifier is a three-phase diode bridge. In the DC link two 3300 µF 350 V electrolytic capacitors are connected in series. The rated power of the frequency converter is 50 kW. The load machine is a 50 kW separately excited DC machine fed by a thyristor rectifier (ABB, DCS500). The power transmission between the PMSM and the DC-machine is implemented with a cogged belt. A photograph of the setup will be found in Appendix A.

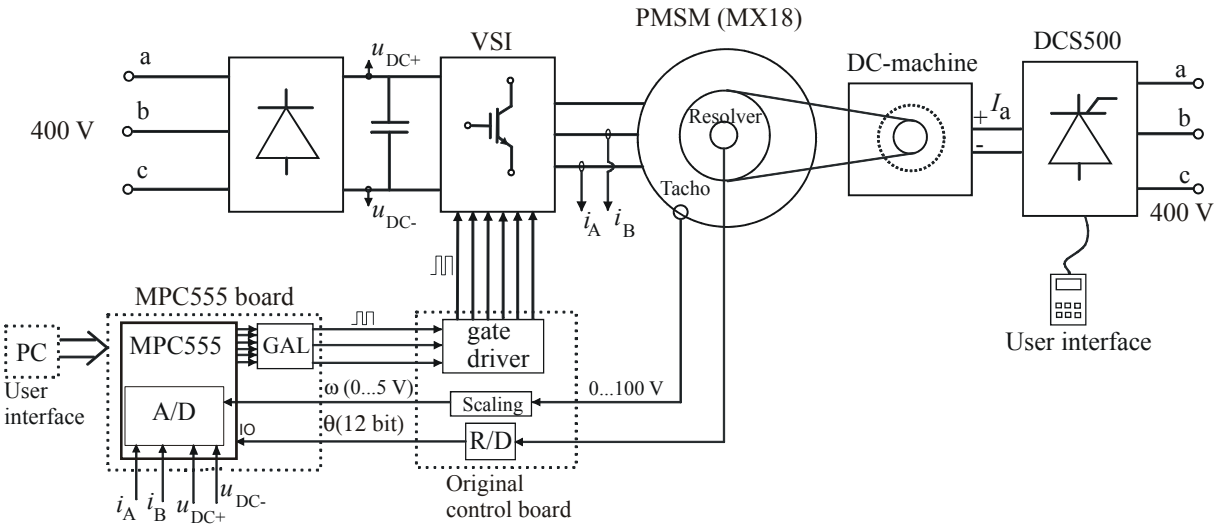

Fig. 5.1 Schematic diagram of the VSI drive.

The original control board of the frequency converter is replaced by an MPC555 control board, designed at the Institute of Power Electronics (TUT). The heart of the control board is the MPC555 microcontroller. The board also contains the auxiliary circuits needed by the peripherals of MPC555 and the GAL circuits (generic array logic) needed for modulation and protection purposes. The GAL circuits create switching signals (0…5 V) for each inverter leg. A positive signal means that the upper IGBT is conducting. Dead time generation is done by an IXYS IXDP631 circuit in the original gate driver board. The user interface is a PC with Matlab. The PC and MPC555 communicate via RS-232 serial interface. DCS500 has its own control panel.

Measurements

The quantities measured are two load currents for the control system and the estimator, the DC link voltage for the modulator, the rotor angular speed and the rotor position angle for analytical purposes. Current measurements of phases A and B are made with Hall-effect based LEM LA100-P current transducers. The current signal is converted into 0…5 V voltage signal where -130 A, 0 A, and 130 A correspond 0 V, 2.5 V and 5 V respectively. The voltage signal is the input of the 10 bit A/D converters of MPC555, Fig. 5.1. Thus the resulting current resolution is approximately 250 mA. The DC link voltage is scaled by a resistance circuit into level 0…5 V where 750 V corresponds to 5 V.

The angular speed is measured with a tachometer (Radio-Energie, RE.0444 L1B) and the voltage is scaled to 0…5 V level with the circuits of the original control board before being transformed to the digital form in the MPC555. The rotor position is measured with a resolver (Smartsyn). The analogue sine and cosine signals are converted to a digital form by the resolver to digital (R/D) converter (Analog Devices, AD2S81A). The resolution of the position measurement is 12 bit. The R/D converter and MPC555 communicate via general purpose I/O pins of MPC555. The measured speed and position are used as references when the performance of the sensorless operation is verified.

Protection

The experimental setup of Fig. 5.1 contains two overcurrent and overvoltage protection systems. The control software disables the VSI (all switches are opened) if too high current or voltage is detected. The MPC555 board also includes a hardware protection which disables the VSI bridge when any of the input voltages of the A/D converters exceeds a predetermined level. The fault signal is routed to the MPC555 and also to the logic circuitry (GAL). Thus the VSI can be disabled even if the software operation fails.

5.2 Experimental matrix converter drive

The structure of the matrix converter setup is described in Fig. 5.2, where the MC can be the indirect or the direct topology. The matrix converter feeds the 3.5 kW radial flux PMSM, Appendix A. The load is a 6.3 kW separately excited DC machine fed by a thyristor rectifier (Siemens, Simoreg K 6RA24). The rated power of the MC prototypes is 5 kVA. Photographs of the setup will be found in Appendix B.

The current and voltage measurements will be discussed in the following sections. The rotor angular speed and the rotor position angle are measured for analytical purposes. The

speed is measured with a tachometer (Hübner GT 7.08L/420) which creates 20 mV/rpm. The voltage of the tachometer is scaled to 0…5 V signal by a simple external board. The rotor position is measured with an absolute encoder (Stegmann AG612 XSRS). The encoder gives 4096 pulse/revolution. Thus the resolution is 12 bit. Before the position signal is routed to the MPC555 the serial form signal is transformed to the parallel form by a Stegmann SPA3 device.

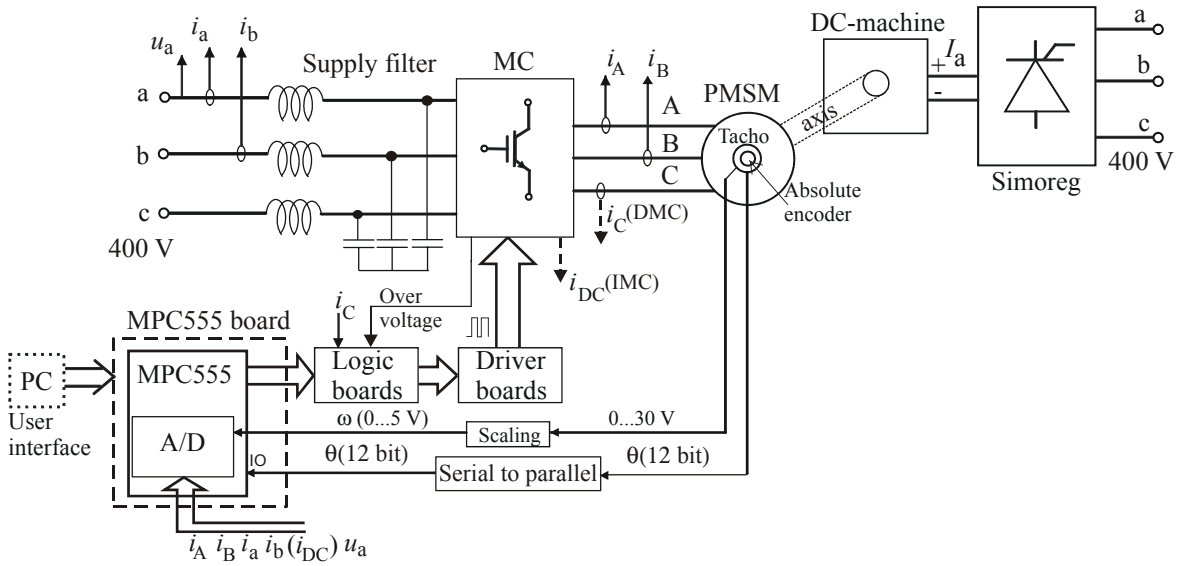

Fig. 5.2 Schematic diagram of the matrix converter drive.

5.2.1 Indirect matrix converter prototype

Sections 5.2.1 and 5.2.2 give a summary of the matrix converter prototypes tested in this thesis. A comprehensive presentation of these MCs will be found in [Jus05].

Main circuit

The main circuit of the IMC with clamp circuits for overvoltage protection is presented in Fig. 5.3 [Jus03]. The load bridge is an IGBT module containing a whole inverter bridge (Semikron SKM40GD123D). The voltage and current ratings of the module are 1200 V and 40 A. The line bridge consists of twelve discrete IGBTs with integrated antiparallel diodes (Semikron SKM75GAL123D). The voltage and current ratings of the modules are 1200 V and 75 A.

The inductances of the supply LC filter, Fig. 5.3, are 2.3 mH. The capacitors are 10 μF and they are Y-connected. For the output power of 5 kVA these values mean 0.023 p.u. and 0.1 p.u. respectively. The resonance frequency of the LC filter is approximately 1049 Hz.

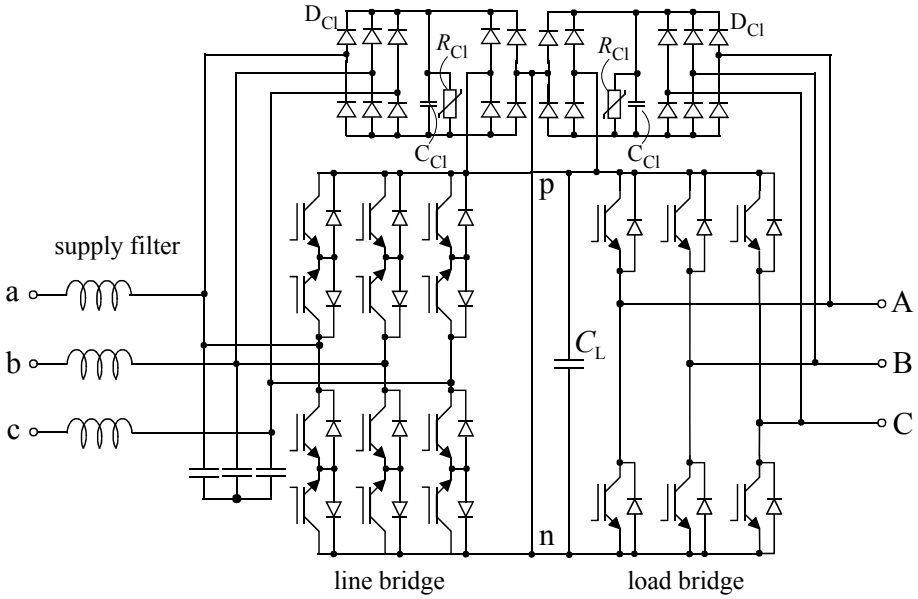

Fig. 5.3 IMC implementation with clamp circuits (overvoltage protection).

Measurements and protection

Five measurements are needed, Fig. 5.2: 1. Zero crossing of the supply phase voltage (phase a), 2. Two supply currents, 3. DC link current, 4. Two load currents, 5. DC voltage of the clamp circuit of the line bridge. The first is needed to synchronise the input current reference vector to the input phase voltages. The second is needed for protection purposes only. The third is needed to detect the directions of the line bridge currents. This measurement is required by the four-step commutation of the line bridge and is also needed for protection. The fourth measurement is required by the vector control of the PMSM and the speed and position estimator. It is also used for overcurrent protection. The fifth measurement is made only for protection purposes. If overvoltage occurs, a fault bit is routed to the logic board, Fig. 5.2. The logic board sets switches at zero vector state until the fault is over.

The current measurements are made with LEM LA55-P current transducers. In the load current measurement -25 A and 25 A correspond 0 V and 5 V respectively in the MPC555 board. Thus the resulting current resolution is approximately 50 mA.

Clamp circuits, Fig. 5.3, include two diode circuits to protect the bridges against overvoltages. The voltage rating of the diodes (D_{Cl}) is 1200 V and the voltage rating of both varistors (R_{Cl}) is 700 V. The capacitors (C_{Cl}) are formed by connecting three 22 μF (400 V) capacitors in series.

Control and driver boards

The microcontroller board used in MC prototypes is similar to that discussed in Section

5.1. Therefore the measurements and protection functions are carried out in the same way as in the VSI drive, Fig. 5.1. The modulation is performed in the external logic board with GAL circuits.

The block “Driver boards” in Fig. 5.2 consists of three gate driver circuit boards. Each of them has six isolated outputs. One unit drives the load bridge and the others drive the line bridge. The driver boards also generate the required operating voltages for electronics of the prototype. The driver boards were designed and made at the Institute of Power Electronics, TUT.

5.2.2 Direct matrix converter prototype

Main circuit

The main circuit with the overvoltage protection circuit is presented in Fig. 5.4 [Jus05]. The main circuit of the DMC prototype consists of nine bi-directional switches. Three of them have a common collector configuration and six have a common emitter configuration. Switches are composed of six SKM75GAL123D modules and six SKM75GBL123D modules. The first contains one IGBT and diode connected antiparallel. In SKM75GBL123D two pieces of the IGBT/diode configuration of SKM75GAL123D are connected in series. In Fig. 5.4. parts of the SKM75GBL123D modules are surrounded and connected by a line. The voltage and current ratings of the modules are 1200 V and 75 A. The supply LC filter is equal to the filter of the IMC prototype.

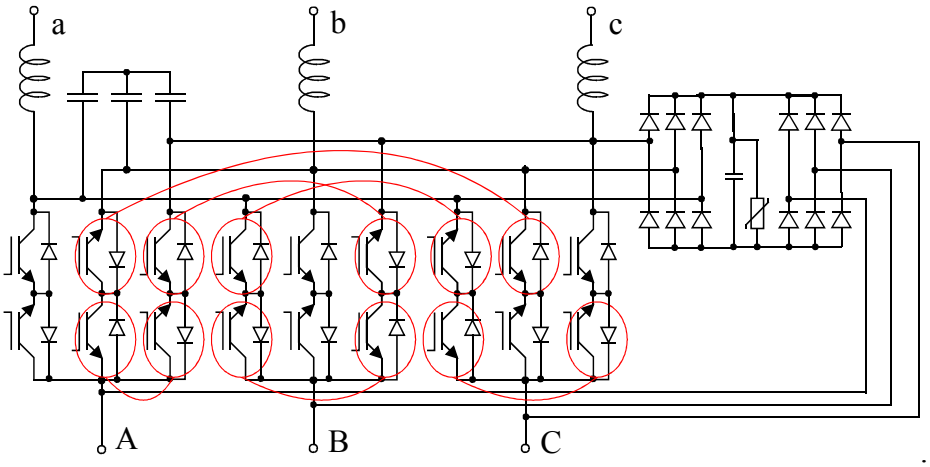

Fig. 5.4 DMC implementation with clamp circuit.

Other properties

The measurement systems of the DMC and IMC prototypes are almost equal. Naturally, the DC link current measurement is not needed in the DMC. However, all output currents of

the DMC prototype are measured. The four-step commutation of the DMC requires accurate knowledge of the output current directions [Jus05]. The information of the sign of i_C is routed only to the logic board, Fig. 5.2. Current transducers are similar in both prototypes (LEM LA55-P). The same MPC555 microcontroller board and driver boards are used in both prototypes. The modulator software is the same in both prototypes and the auxiliary logic boards use similar GAL circuits.

5.3 Software implementation

In the experimental tests the operation of the MC prototypes and the VSI were controlled by a Motorola MPC555 32 bit single-chip microcontroller [Mot00]. The main features of the MPC555 are: PowerPC core with floating point unit, 40 MHz operation, 448 kilobytes on-chip flash EEPROM, 26 kilobytes on-chip RAM, two 10 bit A/D converter modules with 16 input channels total, two time processor units (TPU). Floating-point operations are possible but only fixed point operations were used.

The microcontroller implementation includes A/D conversions of the measured quantities, software based overcurrent protection, computation of the control system algorithms (speed and current control, estimator and modulator) and the communication between the user interface (Matlab) via RS-232. These operations are executed at every interrupt interval of 100 μs.

Two A/D converter modules of MPC555 operate independently. Therefore two phase currents of the PMSM can be measured simultaneously. A third phase current can be calculated on the basis of the measured currents because the PMSMs are Y-connected. In the MCs two line currents are measured for protection purposes. The measured voltages are the DC link voltage of the VSI (for the modulator algorithm) and the input voltage u_a of the MCs. The angle of the synchronous reference frame of the supply network is updated by a PLL algorithm [Sal02], [Jus05] which needs the information of the zero crossings of u_a.

The control system and estimator algorithms were introduced in Chapters 2, 3 and 4. Coordinate transformations and generation of injection signals require sine and cosine functions. In this study predetermined tables are used. Sine and cosine tables are generated in the initialisation process of the software with resolution 0.176° (90°/512).

The implementation of the modulator algorithms of the VSI and the MCs is beyond the scope of this thesis. The theory and implementation of the space-vector modulator of the VSI are presented in [Rou05]. Implementations of the modulators of the IMC and the DMC are presented in detail in [Jus05]. The time processor units of the MPC555 are the interface

between the modulator software and external electronics. The TPUs enable the state of an external pin to be changed at a predetermined time once per interrupt interval. The time instants are calculated by the modulator software. The output pins of the TPUs control the external GAL circuits, Fig. 5.2, which give the signals for the driver circuits.

6 Operation of the sensorless PMSM drives

Chapter 6 is organized as follows. In Section 6.1 the model based estimator presented in Section 3.4.5 is tested with the machine A (Appendix A) fed by the IMC. In Section 6.2.1 the IMC and VSI are compared when the speed and rotor position of the machine A are estimated using the d,q injection. In Section 6.2.2 the performance of the hybrid estimator is verified. DMC and IMC are compared and the PMSM drive is tested in steady state and dynamic conditions. Some test runs are also performed with the machine B (Appendix A), Fig. 5.1. The results are discussed in Section 6.3.

6.1 Model based estimator

In all the measurements in this section 6.1 the following motor parameters are used in the software: R = 0.95 Ω, ψ_m = 0.5 Wb and $L_d = L_q$ = 0.01 H. The tuning of the second order LP filter used in the speed feedback is the same as in the simulations: the continuous time filter transformed into discrete form has a double pole in –400/s. The tuning of the estimator, speed control and current control are same as those used in the simulations described in Section 4.5.

In Fig. 6.1 - Fig. 6.10 the back-emf estimator presented in Section 3.4.5 is tested. Fig. 6.1 shows the result of the speed reference step test. The test sequence is similar to that in the simulations in Section 3.6. The measured transient position errors, Fig. 6.2, are significantly greater than the simulated errors. This is common for all measured speed step tests. Otherwise the model based estimator can operate in the speed range 0.1 – 1 p.u. without problems.

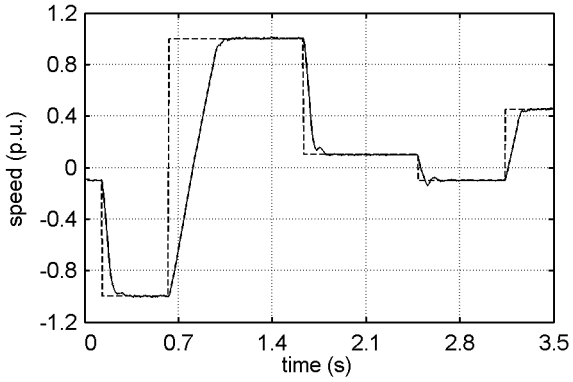

Fig. 6.1 IMC. Model based estimator. Measured speed and reference signal, nominal load.

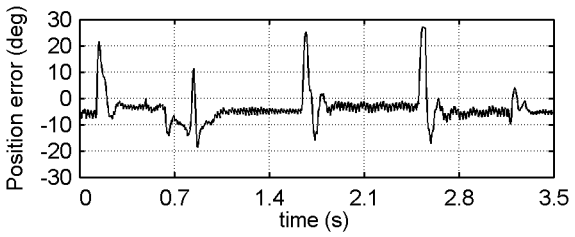

Fig. 6.2 IMC. Model based estimator. Measured position error (electric degrees), nominal load.

In Fig. 6.3 and Fig. 6.4 the PMSM is rotated at speed 0.05 p.u. with nominal load. The sixth harmonic created by the non-ideal motor and the frequency converter can be seen in the measured speed and position error. Fig. 6.5 shows the measured phase current and the spectrum of the current is shown in Fig. 6.6. Fig. 6.7 and Fig. 6.8 show the measured current and its spectrum in the case of 0.1 p.u. speed. The quality of the torque is clearly not at an acceptable level if the speed is under 10% of nominal. The steady state performance can be easily improved by selecting a lower gain and a longer integration time of the speed controller. However, the dynamic performance is then decreased. The other option to decrease the 6th harmonic is to model the non-ideal properties, but this leads to complex estimator algorithms.

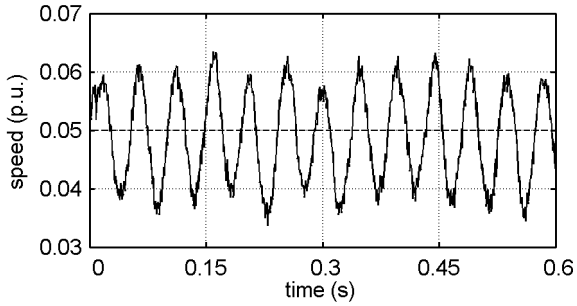

Fig. 6.3 IMC. 0.05 p.u. speed reference. Measured speed, nominal load.

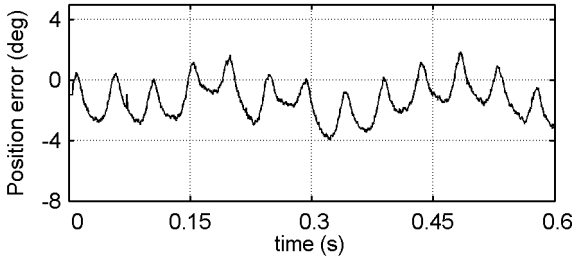

Fig. 6.4 IMC. Position error (electric degrees), nominal load.

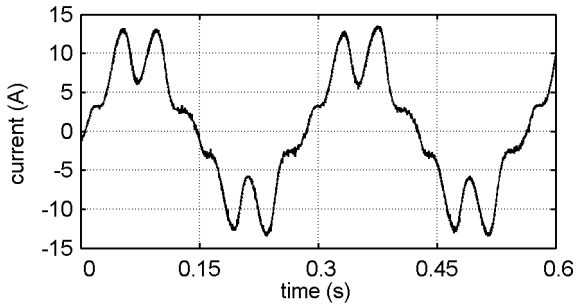

Fig. 6.5 IMC. Measured i_a, 0.05 p.u. speed reference, nominal load.

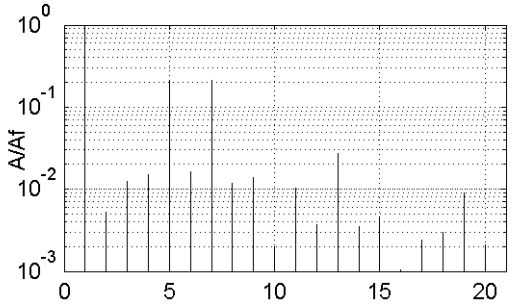

Fig. 6.6 IMC. Spectrum of i_a, nominal load, 0.05 p.u. speed reference.

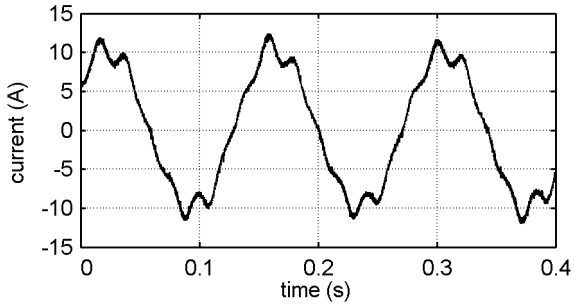

Fig. 6.7 IMC. Measured i_a, 0.1 p.u. speed refeence, nominal load.

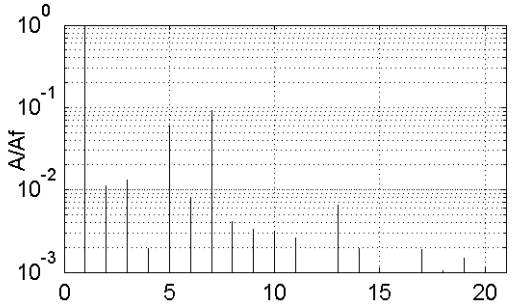

Fig. 6.8 IMC. Spectrum of i_a, nominal load, 0.1 p.u. speed refeence.

6.2 Injection and hybrid estimators

6.2.1 Comparison of VSI and IMC, d,q injection

The armature reaction discussed in Section 4.2.3 is compensated by adding a correction term linearly proportional to i_q reference to the input of the PLL, ε_θ in Fig. 4.1. In Fig. 6.9 - Fig. 6.20 the performance of IMC and VSI are compared. The estimator method is d,q injection. These results were originally presented in [Esk04]. In these tests the tuning of the speed controller is slower than in other measurements. The gain is 0.25. The main reason for the lower gain is the type of the PI controller of the PLL. In [Esk04] the speed estimate was taken from the output of the PI controller, Fig. 3.3b. This structure is more sensitive to disturbances. In other tests results presented here the speed estimate is taken from the integral branch, Fig. 3.3a, Fig. 4.20.

First the PMSM is rotated at speed 0.01 p.u. with nominal load. The measured current vector trajectories of IMC and VSI are shown in Fig. 6.9 and Fig. 6.10. The spectra of the currents are presented in Fig. 6.11 and Fig. 6.12. The measured speeds are shown in Fig. 6.13 and Fig. 6.14. In both cases the 6th harmonic can be seen in the measured speed. In the spectra it is seen as dominant 5th and 7th harmonics.

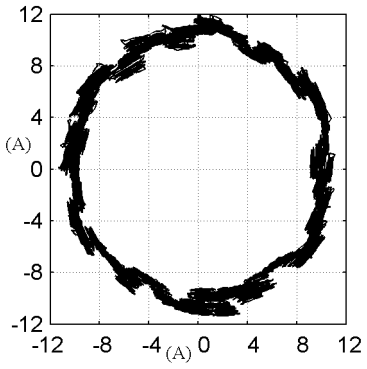

Fig. 6.9 IMC. Current vector trajectory, nominal load, 0.01 p.u. speed reference.

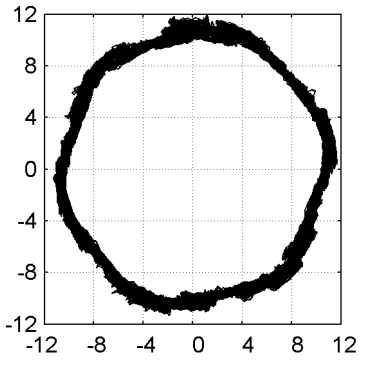

Fig. 6.10 VSI. Current vector trajectory, nominal load, 0.01 p.u. speed reference.

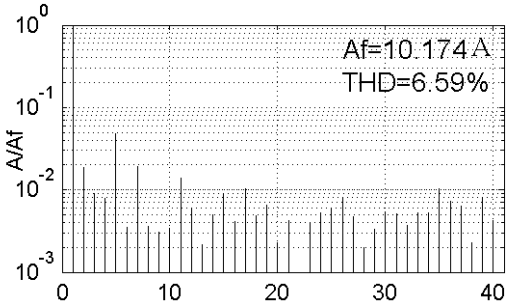

Fig. 6.11 IMC. Frequency spectrum of phase current, 0.01 p.u. speed reference..

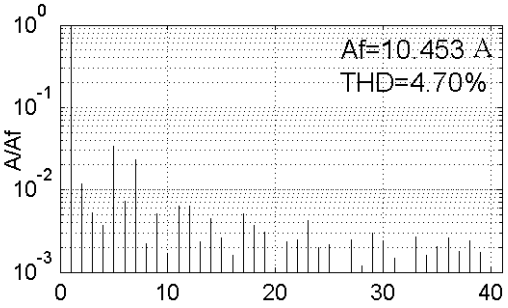

Fig. 6.12 VSI. Frequency spectrum of phase current, 0.01 p.u. speed reference..

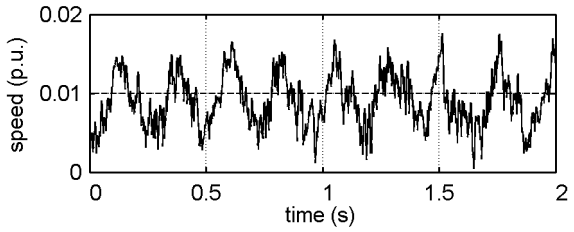

Fig. 6.13 IMC. Measured speed, The reference is 0.01 p.u. Loas is nominal.

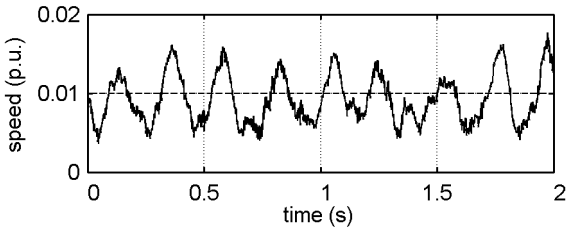

Fig. 6.14 VSI. Measured speed. The reference is 0.01 p.u. Load is nominal.

The current produced by the IMC contains more ripple at higher frequencies than the current of the VSI.

The d,q injection is also tested in the nominal frequency range. The current spectra and measured speeds are shown in Fig. 6.15 - Fig. 6.18. At nominal speed the 12th harmonic is dominant. Again the current spectrum of the matrix converter contains more harmonics of higher order. In [Esk04] the IMC was tested in transients, too, and there was no significant difference between the VSI and the IMC.

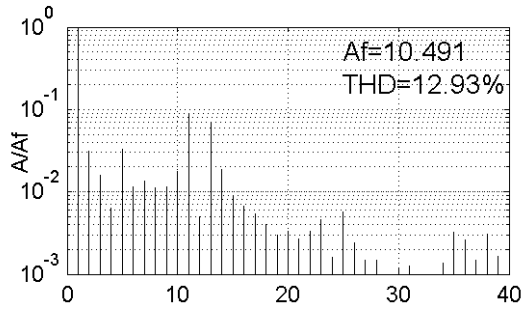

Fig. 6.15 IMC. Frequency spectrum of the phase current, nominal speed (1 p.u.), nominal load.

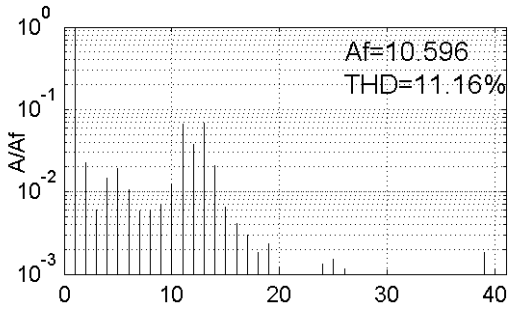

Fig. 6.16 VSI. Frequency spectrum of the phase current, nominal speed (1 p.u.), nominal load.

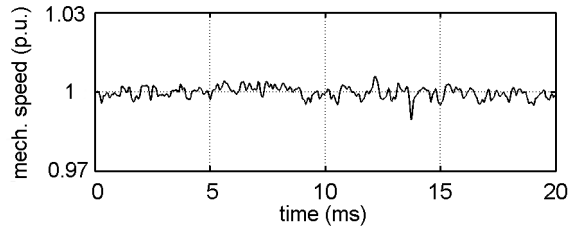

Fig. 6.17 IMC. Measured speed. Nominal load.

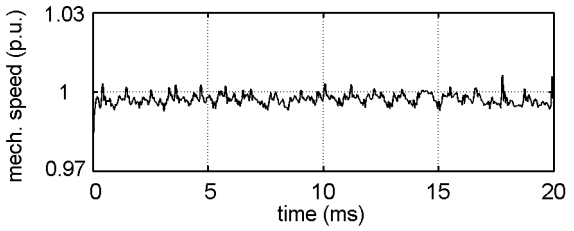

Fig. 6.18 VSI. Measured speed. Nominal load.

6.2.2 Hybrid estimator

In this section the performance of the hybrid estimator is verified. The IMC and the DMC topologies are compared. Some measurements were also performed with the machine B. In that case the PMSM is fed by a 50 kW VSI, Fig. 5.1.

In all tests the tuning of the speed control, current control and hybrid estimator are the same as in the simulations, Table 4.1. In the measurements of this section the following motor parameters are used in the estimator software.

Table 6.1 Parameters used in the estimator software.

	Matrix converters (machine A)	VSI (machine B)
R (Ω)	0.95	0.25
ψ_m (Wb)	0.5	1.1
$L_d = L_q$ (H)	0.01	0.0085

6.2.2.1 Steady state tests

IMC and DMC

In Fig. 6.19 - Fig. 6.24 the speed reference signal is 2% of nominal (supply frequency was 1.5 Hz). The load torque is nominal. The measured speeds are presented in Fig. 6.19 and Fig. 6.20. Position errors ($\theta_r - \hat{\theta}_r$) are shown in the next two figures. There is no clear difference between the two different topologies. No load results in the case of IMC are presented in Fig. 6.23 and Fig. 6.24. The results shown in Fig. 6.19 - Fig. 6.28 are clearly better than those presented in [Esk04], where only the d,q injection estimator was applied.

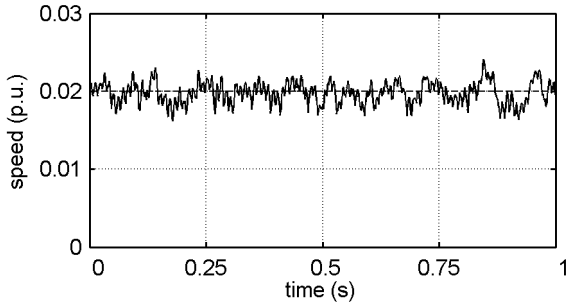

Fig. 6.19 IMC. Measured speed, speed reference is 0.02 p.u. Load is nominal.

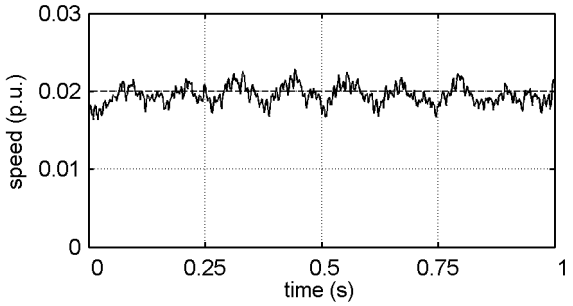

Fig. 6.20 DMC. Measured speed, speed reference is 0.02 p.u. Load is nominal.

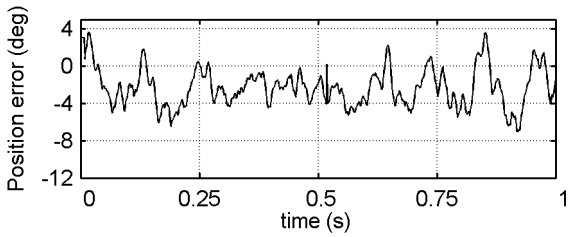

Fig. 6.21 IMC. Position error, speed is 0.02 p.u.

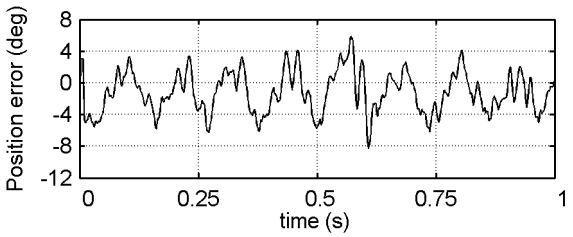

Fig. 6.22 DMC. Position error, speed is 0.02 p.u.

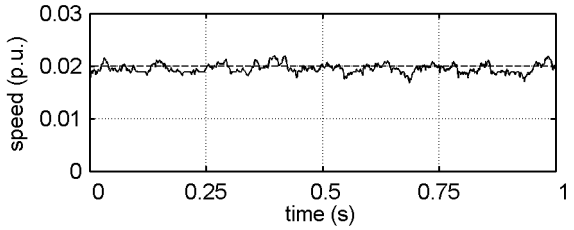

Fig. 6.23 IMC. Measured speed, no load.

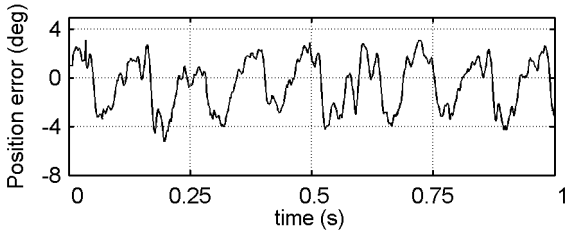

Fig. 6.24 IMC. Measured position error, no load.

The measured phase currents are presented in Fig. 6.25 (IMC) and Fig. 6.26 (DMC). Their

spectra are shown in Fig. 6.27 and Fig. 6.28. 5th and 7th components are the most significant ones. The amplitudes of lower harmonics were higher in the case of the DMC.

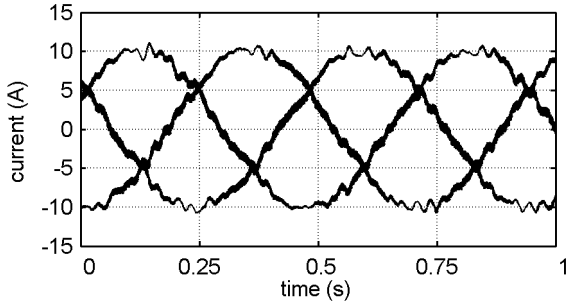

Fig. 6.25 IMC. Phase currents, speed is 0.02 p.u and load is nominal.

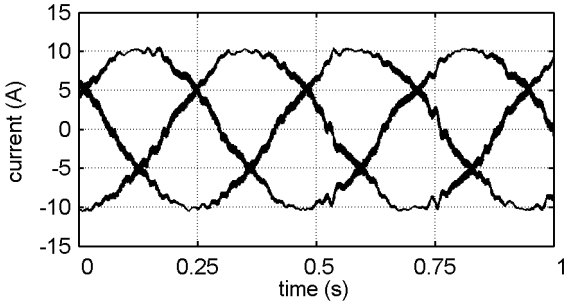

Fig. 6.26 DMC. Phase currents, speed is 0.02 p.u. and load is nominal.

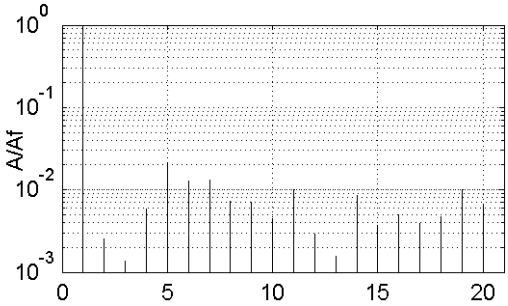

Fig. 6.27 IMC. Spectrum of i_a, speed is 0.02 p.u, nominal load.

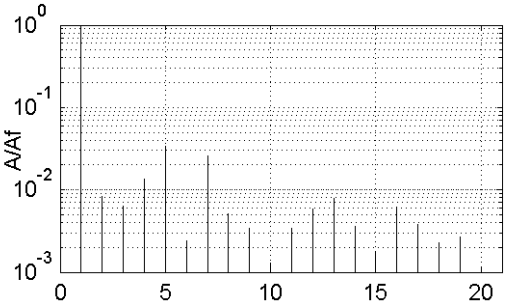

Fig. 6.28 DMC. Spectrum of i_a, speed is 0.02 p.u, nominal load.

In Fig. 6.29 - Fig. 6.36 IMC and DMC are compared at the nominal operating point. The measured speed of the IMC contains slightly more ripple but the position errors are practically identical. The steady state position error is caused by an inductance error. Again, DMC creates more lower harmonics.

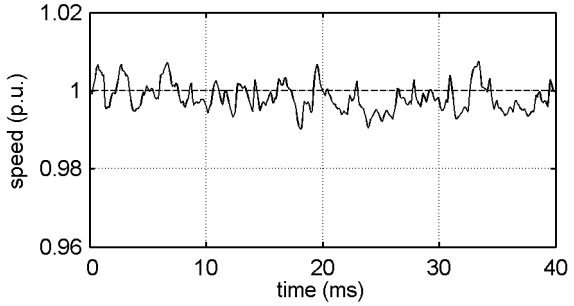

Fig. 6.29 IMC. Measured speed, nominal load.

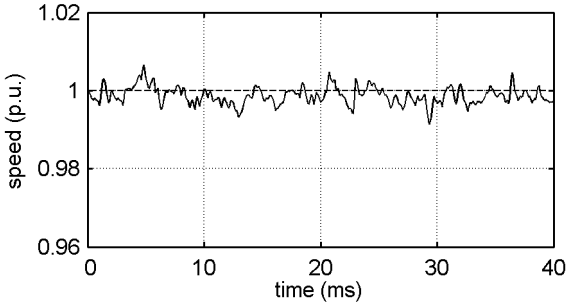

Fig. 6.30 DMC. Measured speed, nominal load.

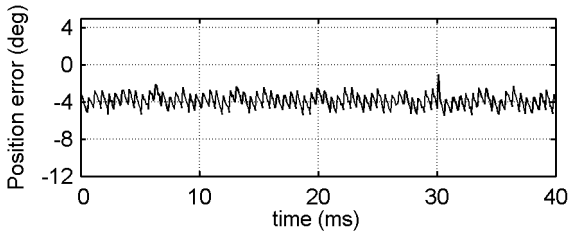

Fig. 6.31 IMC. Position error, nominal speed.

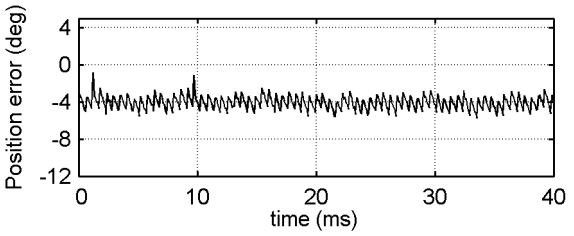

Fig. 6.32 DMC. Position error, nominal speed.

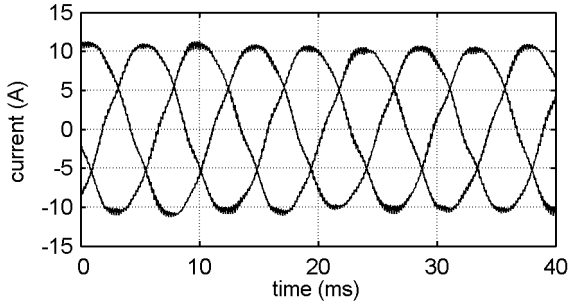

Fig. 6.33 IMC, Phase currents, speed is 1 p.u.

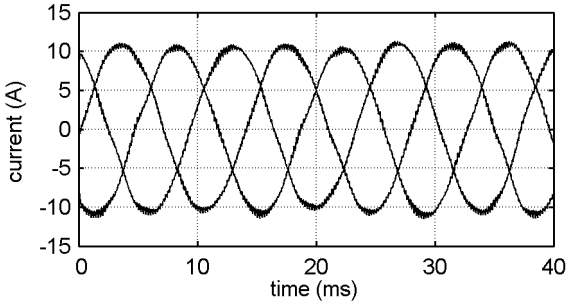

Fig. 6.34 DMC. Phase currents, speed is 1 p.u.

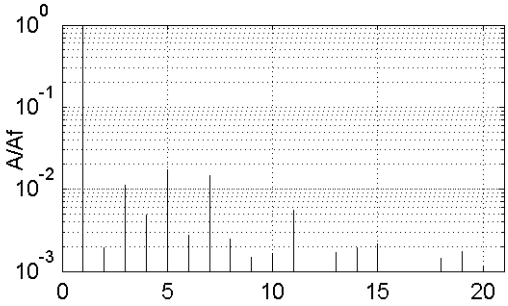

Fig. 6.35 IMC, spectrum of i_a.

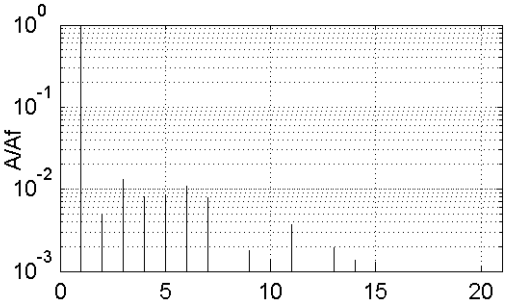

Fig. 6.36 DMC. spectrum of i_a.

VSI

In Fig. 6.37 - Fig. 6.40 the 50 kW VSI drive is tested in steady state with nominal load and without load. The speed reference is 2% of nominal (supply frequency is 0.47 Hz).

The measured phase currents are presented in Fig. 6.41. The spectrum of the one phase current is shown in Fig. 6.42. The harmonics of higher order also exists and now the 5th and 7th harmonics are not the dominant ones.

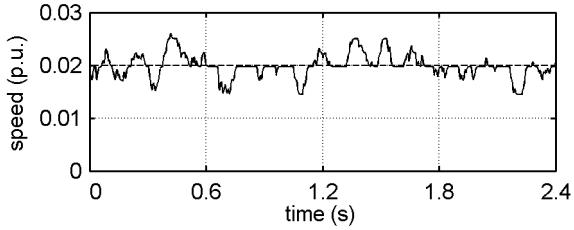

Fig. 6.37 VSI. Measured speed. Speed reference is 0.02 p.u. Load is nominal.

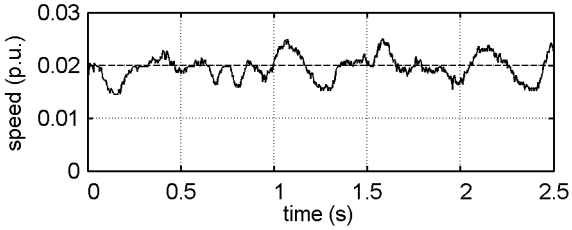

Fig. 6.38 VSI. Measured speed. Speed reference is 0.02 p.u. No load.

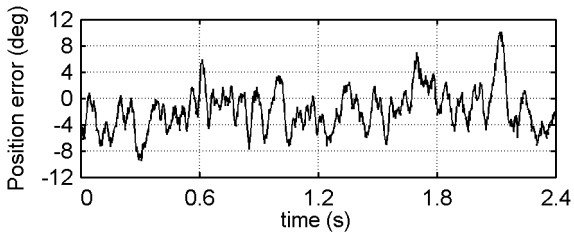

Fig. 6.39 VSI. Position error. Load is nominal.

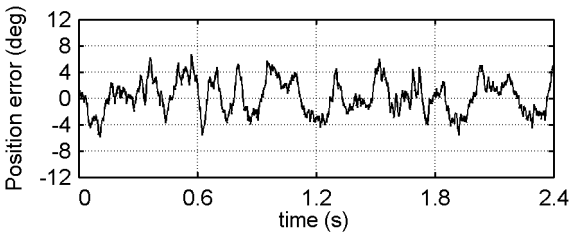

Fig. 6.40 VSI. Position error. No load.

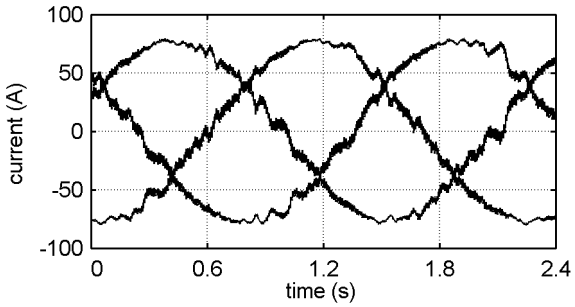

Fig. 6.41 VSI. Phase currents, speed is 0.02 p.u and load is nominal.

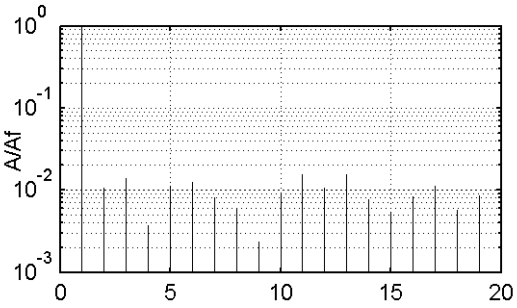

Fig. 6.42 VSI. Spectrum of i_a, speed is 0.02 p.u, nominal load.

6.2.2.2 Ramp and step responses

IMC

Fig. 6.43 and Fig. 6.44 show the speed response when the speed reference is a ramp from -0.3 to 0.3 p.u. speed. In Fig. 6.43 the load torque is nominal and zero in Fig. 6.44. Fig. 6.45 and Fig. 6.46 show the measured position errors.

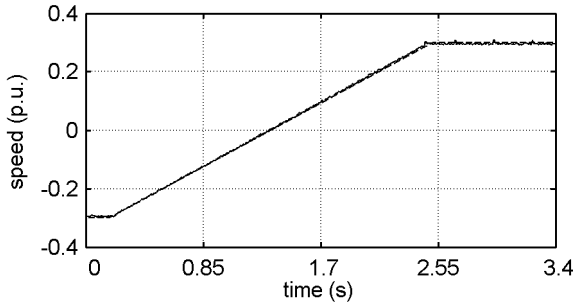

Fig. 6.43 IMC. Ramp response, nominal load. Measured speed (solid), reference (dashed).

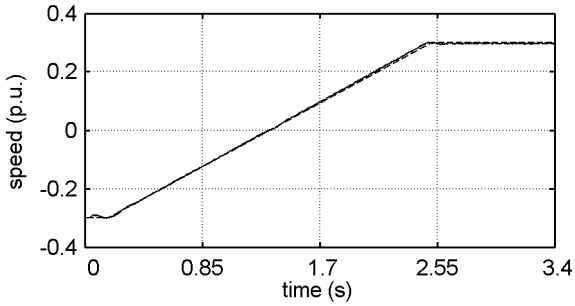

Fig. 6.44 IMC. Ramp response, no load. Measured speed (solid), reference (dashed).

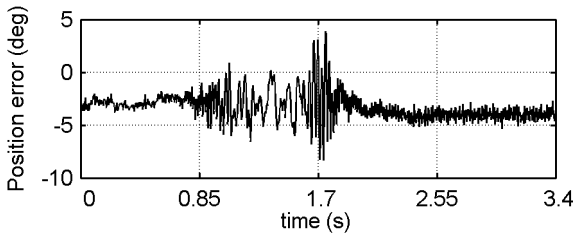

Fig. 6.45 IMC. Position error, nominal load.

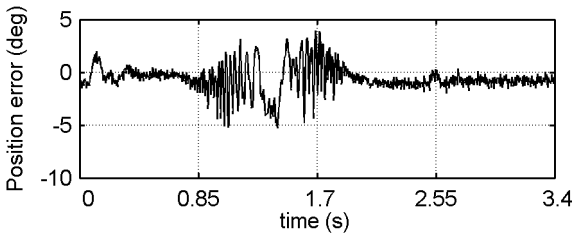

Fig. 6.46 IMC. Position error, $\theta_r - \hat{\theta}_r$, no load.

The results of the speed step response test are presented in Fig. 6.47 - Fig. 6.52. The behaviour of the measured speed is comparable to the simulations with and without load. The position errors are again rather large during transients, Fig. 6.49, Fig. 6.50. Measured i_d and i_q are shown in Fig. 6.51 and Fig. 6.52.

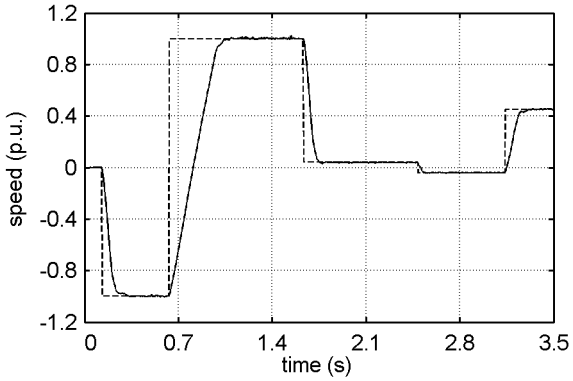

Fig. 6.47 IMC. Step test, nominal load. Measured speed (solid), reference (dashed).

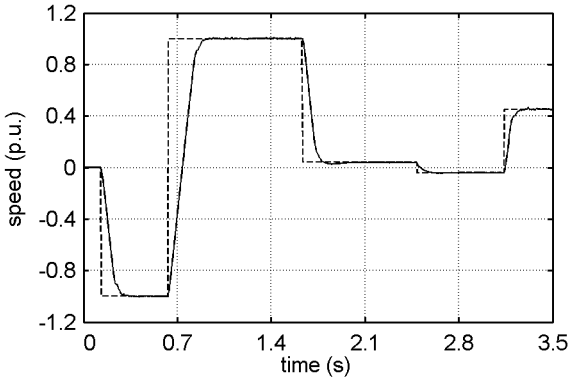

Fig. 6.48 IMC. Step test, no load. Measured speed (solid), reference (dashed).

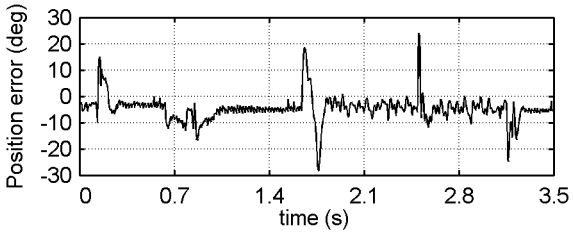

Fig. 6.49 IMC. Step response test. Position error, nominal load.

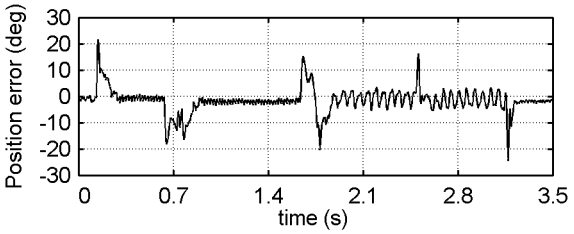

Fig. 6.50 IMC. Step response test. Position error, no load.

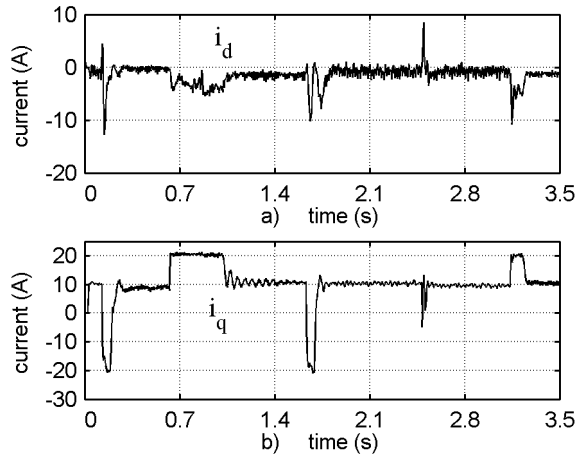

Fig. 6.51 IMC. Step response test, nominal load a) i_d, b) i_q.

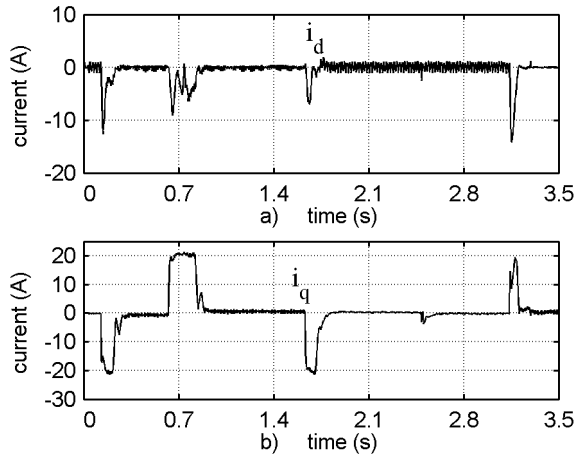

Fig. 6.52 IMC. Step response test, no load a) i_d, b) i_q.

Torque step

In the torque step test the speed reference signal is constant. The torque reference signal of the load DC machine is changed by step signal from zero to 1.5 times the nominal value and back to zero. The test is performed at zero speed, Fig. 6.53 and Fig. 6.55, and at speed 0.15 p.u., Fig. 6.54 and Fig. 6.56. The latter test verifies that the performance of the estimator is not decreased when both estimators are operating simultaneously. Measured i_d and i_q are shown in Fig. 6.57 and Fig. 6.58.

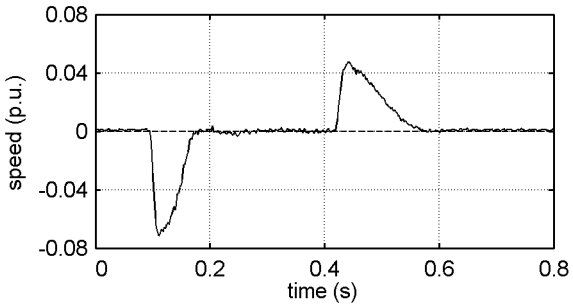

Fig. 6.53 IMC, Torque step, zero speed. Measured speed (solid), reference (dashed).

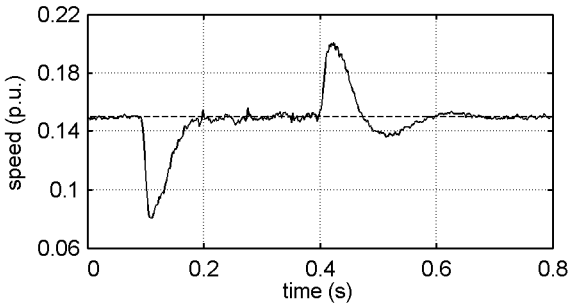

Fig. 6.54 IMC, Torque step, 0.15 p.u. speed reference. Measured speed (solid), reference (dashed).

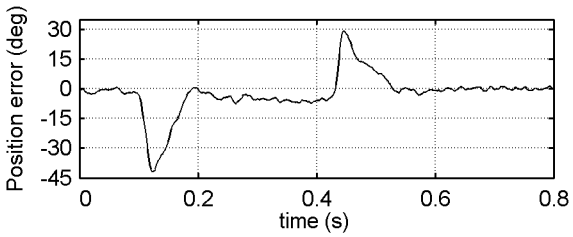

Fig. 6.55 IMC, Torque step at zero speed. Position error.

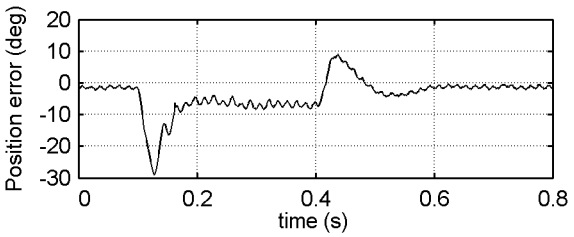

Fig. 6.56 IMC, Torque step, 0.15 p.u. speed reference. Position error.

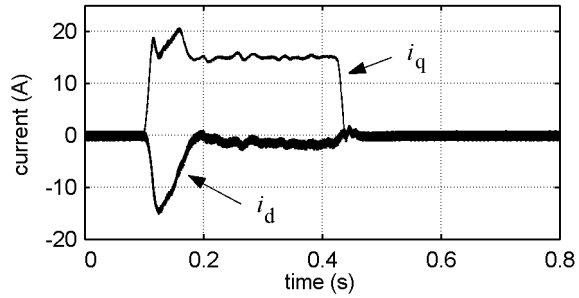

Fig. 6.57 IMC, torque step at zero speed, i_q and i_d.

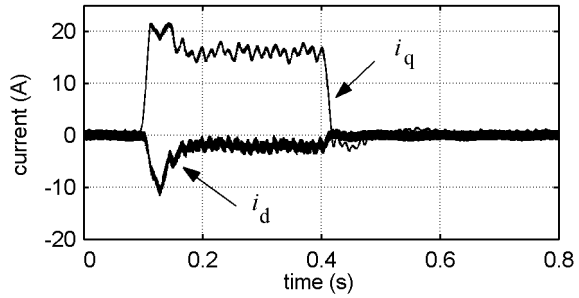

Fig. 6.58 IMC, torque step, 0.15 p.u. speed reference., i_q and i_d.

VSI

Fig. 6.59 shows the measured speed response when the speed reference is a ramp from -0.3 to 0.3 p.u. speed. The load torque is nominal. The position error is shown in Fig. 6.60. Compared to the MCs the results are poorer. The position error is larger and the speed fluctuates during the transient.

Motor B is magnetically more symmetric than the machine A (Appendix A). Therefore the performance of the d,q injection is decreased. When the model based estimator operates alone the ripple disappears.

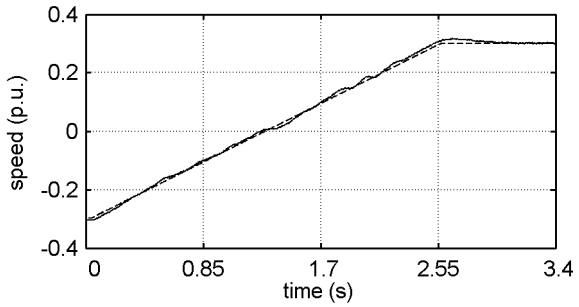

Fig. 6.59 VSI. Ramp response test, nominal load. Measured speed (solid), reference (dashed).

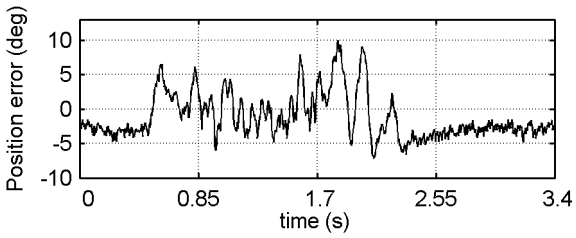

Fig. 6.60 VSI. Ramp response test, nominal load. Position error.

6.3 Summary of the results

The model based algorithms of the hybrid estimator need information on the motor parameters. The parameter estimator or other additional correction algorithms were not used in the experimental tests. The control system was stable in all tests. Changing the estimator method from injection to model based did not create any problems. This was verified by speed ramp tests and torque steps in the speed range where both estimator algorithms were working simultaneously. In the experimental tests the most difficult cases were fast speed reference and torque steps. In those tests the maximum momentary position errors were significant. In the worst case the error was approximately 40 electrical degrees, Fig. 6.55.

During fast transients the measured position errors were larger than the simulated errors. Otherwise the measured results are in agreement with the simulations. Non-ideal current measurements may be one reason for the rather large measured position errors. Current was measured only once during every 100 µs control period. No attempt was made to optimize the time instant of the measurement. The accuracy of the A/D conversions of the setup (10 bit) is also rather low for a high performance control system.

The matrix converter topologies were compared experimentally. There were no remarkable differences between IMC and DMC. On the basis of the analysis of Chapter 2 it was expected that DMC would give a slightly better current waveform in steady state tests. However, in the measurements with the hybrid estimator the THD of the current was slightly smaller in the case of IMC, Fig. 6.27 and Fig. 6.28. Both MCs are prototypes which may cause some imprecision in the results.

In [Esk04] IMC and VSI were compared and some of the results were presented in this chapter. The torque produced by the IMC contained more higher order harmonics and the THD was slightly higher in all steady state tests. This was expected, because disturbances

between input and output are not filtered due to the absence of the DC-link with an energy storage. In the dynamic tests the performance of IMC and VSI was similar.

The experimental results presented in Section 6.2 show that the sensorless control of the PMSM can be realised using the proposed speed and position estimator. The system was stable over the nominal speed range in steady state and various transient conditions. It can be concluded from the measurements that the main drawbacks of the estimator method tested are:

- The speed control gain must be rather low or else the disturbances generated by the PMSM and the converter are amplified. This decreases the dynamic performance.
- The position errors may be rather large during transient. More attention should be paid to the implementation of the hardware and the software.

Steady state at 2% speed (0.02 p.u.) and the speed reversals were tested also with the machine B fed by the VSI. This axial flux machine is magnetically more symmetric than the machine A. Therefore the performance was not satisfactory at low speeds where also the signal injection was applied. When the motor was accelerated there was some oscillation in the speed range where the model based and the injection estimators were used simultaneously, Fig. 6.59.

The flux linkage harmonics are small compared to the machine A. In [Esk03] the machine B was driven at low speeds using a model based estimator. The ripple in the speed and torque was clearly smaller than in the results shown in Fig. 6.3 where the machine A was driven using the proposed model based estimator. In [Esk03] the PMSM was succesfully decelerated to 3% speed (0.03 p.u.) with nominal load. This test may lead to instable operation in the case of machine A. Therefore the speed range where the d,q injection estimator is applied could be decreased when the axial flux motor (B) is driven. These tests show that it is difficult to find the parameters which provide an optimal performance for various machines.

PMSMs are still an emerging technology and they are not yet widely used in standard industrial drives. Therefore it is difficult to say for what application area the performance of the proposed estimator would be appropriate. On the basis of the experimental tests the high performance servo drives might be too demanding, but industrial drives with moderate dynamics are surely achievable. Such applications are, for example direct drive applications where the PMSM is mounted directly on the rotating part of the machinery.

7 Conclusions

The vector control of synchronous machine requires knowledge of the rotor position and angular speed. The presence of sensors measuring these quantities implies several disadvantages in addition to the extra cost; a greater number of connections between the motor and the control board and reduced robustness. For these reasons several strategies to detect the speed and position without sensors have been developed over the last twenty years.

The first goal of this study was to find optimal methods to estimate the angular speed and position of the PMSM. Requirements for a good sensorless control system were given in Chapter 3. No modification of the basic frequency converter hardware was allowed. The estimator should be a simple algorithm without a parameter estimator. Stable operation over the speed range was also required.

In Chapter 3 several model based estimators (state observers, back-emf and flux linkage estimators) were compared on the basis of a survey of the literature. The methods selected for the comparative simulations all fulfilled the requirements excluding stable operation around zero speed. On the basis of simulations a back-emf estimator based on the work of Matsui was selected for experimental tests. The theory of phase locked loop was also briefly presented in Chapter 3. This simple tracking algorithm is a basic structure of many position and speed estimators and was also applied in this thesis.

The requirement of a stable zero speed operation was fulfilled by using the signal injection estimator in the low speed range. Signal injection methods were analysed in Chapter 4. d,q injection was selected because it is fairly immune to disturbances generated by the frequency converter. The final speed and position estimator was a combination of model based back-emf estimator and the d,q injection estimator. The injection method was used in the low speed region and when the rotor angular speed increased, the weighting of the model based estimator was gradually increased. The transition between the model based and the injection estimators was explained in Chapter 4. The transition from one estimator to another was quite a simple task because both methods had a phase locked loop structure. At the end of Chapter 4 the performance of the injection estimator and of the hybrid method were studied by simulations.

The other goal was to study the suitability of the matrix converter for the sensorless PMSM drives. Matrix converter topologies were presented in Chapter 2. The theory of the vector

modulation of the matrix converter was explained. Some non-ideal properties of the VSI and the MCs were compared.

In Chapter 6 the performance of the proposed hybrid estimator was verified by measurements. The PMSM was fed by the IMC and the DMC. The requirements laid down in Chapter 3 were fulfilled. The measurements also proved that matrix converters can be used in sensorless drives. The IMC and the DMC showed quite similar performance in all tests. The IMC was also compared to the VSI, the widely used solution for variable speed drives. In dynamic conditions there was no difference between the IMC and the VSI. In steady state tests the THD of the current produced by the IMC was slightly higher. This was expected, because the disturbances between the supply network and the output of the MC are not filtered due to the absence of the DC-link with an energy storage. In general the low output voltage of the matrix converters restricts their use with standard motors.

There is still work to be done if the sensorless control method presented is to be applied in industry. More attention should be paid on the measurement of currents. A/D converters with better accuracy should be used and several measurements during one control period should be taken to remove the effect of single distortions. The back-emf estimator is an optimal choice when parameters are not estimated. If parameter estimators can be applied the flux estimators (Niemelä and Rasmussen methods or their combination) might also have a good performance.

In the measurements of this thesis the performance of the speed control was not very high. If a faster speed control is required the effect of non-ideal properties of the PMSM and the frequency converter should be removed more effectively.

References

[And99] G.D. Andreescu, “Position and speed sensorless control of PMSM drives based on adaptive observer,” EPE’99, Lausanne, Switzerland,1999.

[Apa03] M. Apap, J.C. Clare, P.W. Wheeler and K.J. Bradley**. “**Analysis and comparison of AC-AC matrix converter control strategies,” IEEE PESC’03, June 2003, Vol. 3, pp. 1287-1292.

[Ari04] A. Arias, R. Filka, G. asher and M. Sumner, “Application of the matrix converter for the sensorless control of permanent magnet AC machines using high frequency injection,” 11th international Power Electronics and Motion Control Conference, EPE-PEMC, Riga, Latvia, 2004.

[Bat00] T.D. Batzerl and K.Y. Lee, “Slotless permanent magnet syncronous motor operation without a high resolution rotor angle sensor,” IEEE Transactions on Power Conversion, Vol. 15, No. 4, December 2000, pp.366-371.

[Bla96] F. Blaschke, J. van der Burgt and A. Vandenput, “Sensorless direct field orientation at zero flux frequency,” in Proceedings of IEEE Industrial Applications Society Annual Meeting, October, 1996.

[Bol99] S. Bolognani, R. Oboe and M. Zigliotto, “Sensorless full-digital PMSM drive with EKF estimation of speed and rotor position,” IEEE Transactions on Industrial Electronics, Vol. 46, No. 1, February 1999, pp. 184-191.

[Bol01] S. Bolognani, M. Zigliotto and M. Zordan, “Extended-range PMSM sensorless speed drive based on stochastic filtering,” IEEE Transactions on Power Electronics, Vol. 16, No. 1, January 2001, pp. 110-117.

[Bol03] S. Bolognani, L. Tubiana and M. Zigliotto, “Extended Kalman filter tuning in sensorless PMSM drives,” IEEE Transactions on Industry Applications, Vol. 39, No. 6, November/December 2003, pp.1741-1747.

[Bro91] W.L. Brogan, *Modern control theory*, 3rd ed., Prentice-Hall, Englewood Cliffs, NJ, 1991, 653 p.

[Bru01] M. Bruckmann. O. Simon, W. Springmann, M. Münzer and M. Loddenkötter, “Application of a new IGBT module for matrix converter,” 9th European Conference on Power Application, EPE2001.

[Bur89] N. Burány, “Safe control of four-quadrant-switches,” IEEE, IAS Annual Meeting, Conference record, 1989, Vol. 1, pp. 1190-1194.

[Car03] C. Caruana, G. Asher, K. Bradley and M. Woolfson, “Flux position estimation in cage induction machines using synchronous HF injection and Kalman filtering,” IEEE Transactions on Industry Applications Vol. 39, No. 5, Sep/Oct 2003, pp.1372-1378.

[Cas02] D. Casadei, G. Serra, A. Tani and L. Zarri, “Matrix converter modulation strategies: a new general approach based on space-vector representation of the switch state,” IEEE Transactions on Industrial Electronics, Vol. 49, April 2002, pp. 370 – 381.

[Cha03] H.J. Cha and P.N. Enjeti, “An Approach to reduce common-mode voltage in matrix converter,” IEEE Transactions on Industry Applications, Vol. 39, No. 4, July/August 2003, pp. 1151-1159.

[Col99] F. Colamartino, C. Marchand and. A Razek, “Torque ripple minimization in permanent magnet synchronous servodrive,” IEEE Transaction on Energy Conversion, Vol. 14, No. 3, September 1999, pp. 616-621.

[Con94] A. Consoli, S. Musumeci, A. Raciti and A. Testa, “Sensorless vector and speed control of brushless motor drives,” IEEE Transactions on Industrial Electronics, Vol. 41, No. 1, February 1994, pp.91-96.

[Con00] A. Consoli, G. Scarcella and A. Testa, “A New zero frequency flux detection approach for direct field oriented control drives,” IEEE Transactions in Industry. Applications, Vol.36, No.3, May/June 2000, pp. 797 – 804.

[Con01] A. Consoli, G. Scarcella and A. Testa, “Industry application of zero-speed sensorless control techniques for PM synchronous motors,” IEEE Transactions on Industry Applications, Vol.37, No.2, March/April 2001, pp. 513-521.

[Con03] A. Consoli, G. Scarcella, “An alternative to high frequency current detection techniques for zero speed sensorless control of AC motor drives,” EPE Journal, Vol. 13, No. 3, August 2003, pp. 30 – 35.

[Cor98] M.J. Corley and R.D. Lorenz, “ Rotor position and velocity estimation for a salient-pole permanent magnet synchronous machine at standstill and high speeds,” IEEE Transactions on Industry Applications, Vol. 34 , No. 4, 1998, pp. 784 - 789.

[Deg98] M.W. Degner and R.D. Lorenz, “Using multiple saliencies for the estimation of flux, position, and velocity in AC machines,” IEEE Transactions on Industry Applications, Vol. 34, No. 5, September/October, 1998, pp. 1097-1104.

[Dha91] R. Dhaouadi, N. Mohan and L. Norum, “Design and implementation of an extended Kalman filter for the state estimation of a permanent magnet synchronous motor,” IEEE Transactions on Power Electronics, Vol. 6, No. 3, July 1991, pp. 491-497.

[Du95] T. Du, P. Vas and F. Stonach, “Design and application of extended observers for joint state and parameter estimation in high-performance AC drives,” IEE Proceedings of Electric Power Applications, Vol. 142, No. 2, March 1995, pp. 71-77.

[Elm96] C. Elmas and H.Z. De La Parra, “Application of a full-order extended Luenberger observer for a position sensorless operation of a switched reluctance motor drive,” IEE Proc.-Control Theory Applications, Vol. 143, No. 5, September 1996, pp. 401-408.

[Emp98] L. Empringham, P.W. Wheeler and J.C. Clare, “Intelligent commutation of matrix converter bi-directional switch cells using novel gate drive techniques,” IEEE, PESC’98, Conference Record, May 1998, Vol. 1, pp. 707 – 713.

[Esk02] M. Eskola, *Tahtikoneen takaisinkytkemättömien säätömenetelmien vertailu*, Licentiate thesis, Tampere University of Technology, Finland, 2002, 103 p.

[Esk03] M. Eskola and H. Tuusa, "Comparison of MRAS and novel simple method for position estimation in PMSM drives," IEEE Power Electronics Specialist Conference, PESC'03, Vol. 2, June 2003, pp. 550 – 555.

[Esk04] M. Eskola, M. Jussila and H. Tuusa, "Indirect matrix converter fed PMSM - sensorless control using carrier injection," IEEE, Power Electronics Specialists Conference, PESC'04, Aachen, Germany, 2004.

[Esk05] M. Eskola and H. Tuusa, "Sensorless control of salient pole PMSM using a low-frequency signal injection," Conference record of EPE2005, Dresden, Germany, 2005.

[Fre96] C. French and P. Acarnley, "Control of permanent magnet motor drives using a new position estimation technique," IEEE Transactions on Industry Applications, Vol. 32, No. 5, September/October 1996, pp. 1089-1097.

[Gre93] M.S. Grewal and A.P. Andrews, *Kalman filtering, theory and practice.* New Jersey, Prentice Hall, 1993, 381 p.

[Guc01] Z. Guchuan, A. Kaddouri, L-A Dessaint and O. Akhrif, "A Nonlinear state observer for the sensorless control of a permanent-magnet AC machine," IEEE, Transactions on Industrial Electronics, Vol. 48, No. 6. December, 2001, pp. 1098-1108.

[Gyu76] L. Gyugyi and B.R. Pelly, *Static power frequency changers - theory, performance, and application*, A John Wiley & Sons, New York, 1976, 442 p.

[Ha99] J.-I. Ha and S.-K. Sul, " Sensorless field orientation control of an induction machine by high frequency signal injection," IEEE Transactions on Industry Applications, Vol. 35. No. 1, Jan./Feb. 1999.

[Har00] L. Harnefors and H.-P. Nee, "General algorithm for speed and position estimation of AC motors," IEEE Transactions on Industrial Electronics, Vol. 47, No. 1. February 2000, pp 77-83.

[Hen94] J.R. Hendershot and T.J.E. Miller, *Design of Brushless Permanent-Magnet Motors*, Oxford, U.K.: Magna Physics Publishing and Clarendon Press, 1994.

[Hol96] J. Holtz and L. Springob, "Identification and compensation of torque ripple in high-precision permanent magnet motor drive," IEEE Transactions on Industrial Electronics, Vol. 43, No. 2, April 1996, pp. 309-320.

[Hol98] J. Holtz, "Sensorless position control of induction motors -an emerging technology," IEEE Transactions on Industrial Electronics, Vol. 45, No. 6. December, 1998 pp. 840 – 851.

[Hol02] J. Holtz and J. Quan, "Sensorless vector control of induction motors at very low speed using a nonlinear inverter model and parameter identification," IEEE Transactions on Industry Application, Vol. 38, No. 4, July/August 2002, pp. 1087-1095.

[Hol03] D.G. Holmes and T.A. Lipo, *Pulse width modulation for power converters*, 2003. IEEE Press, A John Wiley & Sons, USA, 2003.

[Hsi96] G-C. Hsieh and J.C. Hung, "Phase-locked loop techniques-A survey," IEEE Transactions on Industrial Electronics, vol. 43, No. 6, December 1996, pp. 609-615.

[Hu98] J. Hu and B. Wu, "New integration algorithms for estimating motor flux over a wide speed range," IEEE Transactions on Power Electronics, Vol. 13, No. 5, September 1998, pp. 969-977.

[Hub95] L. Huber and D. Borojević, "Space vector modulated three-phase to three-phase matrix converter with input power factor correction," IEEE Transactions on Industry Applications, vol. 31, Nov./Dec. 1995, pp. 1234–1246.

[Iim97] K. Iimori, K. Shinohara, O. Tarumi, Z. Fu and M. Muroya, "New current controlled PWM rectifier- voltage source inverter without DC link components," Power Conversion Conference, Nagaoka, Aug. 1997, Vol 2, pp. 783 – 786.

[Isi85] A. Isidori, *Nonlinear control systems*, 2nd ed., Springer-Verlag, Berlin, 1985, 479 p.

[Ito04] J-I Itoh, I. Sato, A. Odaka, H. Ohguchi, H. Kodatchi and N. Eguchi, **"**A novel approach to practical matrix converter motor drive system with reverse blocking IGBT," Proceedings of Conf. Rec., IEEE PESC'04, June 2004, Vol. 3, pp. 2380 – 2385.

[Jah86] T. Jahns, G. Kliman, and T. Neumann, "Interior permanent-magnet synchronous motors for adjustable-speed drives," IEEE Transactions on Industry Applications, vol. 22, no. 4, July/Aug. 1986, pp. 738–747.

[Jan95] P.L. Jansen and R.D. Lorenz, "Transducerless position and velocity estimation in induction and salient AC machines," IEEE Transactions on Industry Applications, Vol. 31, No. 2, March/April 1995. pp. 204-207.

[Jan01] J.-H. Jang, J-I. Ha and S.-K. Sul, " Vector control of surface mounted permanent magnet synchronous motor without any rotational transducer," Proceedings of IEEE Applied Power Electronics Conference (APEC), USA, 2001.

[Jan03] J.-H. Jang, S.-K. Sul, J.-I. Ha, K. Ide and M. Sawamura, " Sensorless drive of surface-mounted permanent-magnet motor by high-frequency signal injection based on magnetic saliency," IEEE Transactions on Industry Applications, Volume 39, No. 4, July/August 2003, pp. 1031-1039.

[Jia97] J. Jiang and J. Holtz, "Accurate estimation of rotor position and speed of induction motor near standstill," in Proc. IEEE Conference of Power Electronics and Drive Systems, (PEDS'97), Singapore, 1997.

[Jon89] L.A. Jones and J.H. Lang, "A state observer for the permanent-magnet synchronous motor," IEEE Transactions on Industrial Electronics, Vol. 36, No. 3, August 1989, pp. 374-382.

[Jus03] M. Jussila, M. Salo and H. Tuusa, "Implementation of a three-phase indirect matrix converter with an indirect vector modulation method applying a microcontroller," Proc. Conf. Rec. PCIM, 2003.

[Jus05] M. Jussila, *Suoran ja epäsuoran matriisikonvertterin vertailu*, Licentiate thesis, Tampere University of Technology, Finland, 2005, 116 p.

[Jus06] M. Jussila, M. Eskola and H. Tuusa, "Characteristics and comparison of output voltage non-idealities of direct and indirect matrix converters," International Review of Electrical Engineering, IREE, Praise Worthy Prize, Volume 0, No. 0, Jan/Feb 2006, pp. 74-82.

[Ker03] T. Kereszty, V-M Leppänen and J. Luomi, "Sensorless control of surface magnet synchronous motors at low speeds using low-frequency signal injection," Conference record of the 29th Annual Conference of the IEEE Industrial Electronics Society, IECON'03, Roanoke, VA, 2-6, November 2003.

[Kim94] J-S Kim and S-K Sul, "New stand-still position detection strategy for PMSM drive without rotational transducers," APEC'94. Conference Proceedings, Vol 1, 13-17 February, 1994.

[Kim97] J-S Kim and S-K Sul, "New approach for high performance PMSM drives without rotational position sensors," IEEE Transactions on Power Electronics, Vol. 12, No. 5, September 1997, pp. 904-911.

[Kim04] H. Kim, K-K Huh, R. D. Lorenz and T. M. Jahns, "A novel method for initial rotor position estimation for IPM synchronous machine drives," IEEE Transactions on Industry Applications, Vol. 40, No. 5, September/October 2004, pp. 1369-1378.

[Kra02] P.C. Krause, O. Wasynczuk and S.D. Sudhoff, *Analysis of electric machinery and drive systems*, 2nd edition, New York, IEEE Press: Wiley, 2002.

[Kol02] J.W. Kolar, M. Baumann, F. Schafmeister and H. Ertl, "Novel three-phase AC-DC-AC sparse matrix converter," Proc. Conf. Rec. IEEE APEC, 2002, Vol. 2. pp. 777-791.

[Lee04a] J-K Lee, J-K Seok and D-C Lee, "Sensorless speed control of non-salient permanent magnet synchronous motor using rotor position tracking PI controller," 35th annual IEEE Power Electronics Specialists Conference, Aachen, Germany, 2004. pp. 4024-4029.

[Lee04b] K-B. Lee and F. Blaabjerg, "Performance improvement of sensorless vector control for induction motor drives fed by matrix converter using nonlinear model and disturbance observer," 35th annual IEEE Power Electronics Specialists Conference, Aachen, Germany, 2004. pp. 1341-1347.

[Lep03] V-M. Leppänen, *A Low-Frequency signal-injection method for speed sensorless vector control of induction motors*, Thesis for the degree of doctor of science in technology, Helsinki University of Technology, Institute of Intelligent Power Electronics, Espoo, 2003.

[Lin01] A. Lindemann, "A new IGBT with reverse blocking capability," EPE 2001, Proc. Conf. Record, Graz, Austria 2001.

[Lin02] M. Linke, R. Kennel and J. Holtz, "Sensorless position control of permanent magnet synchronous machines without limitation at zero speed," *28th Annual Conference of the IEEE Industrial Electronics Society IECON'02,* Sevilla/Spain, Nov. 5-8, 2002.

[Lin03a] M. Linke, R. Kennel and J. Holtz, "Sensorless speed and position control of synchronous machines using alternating carrier injection," *IEEE International Electric Machines and Drives Conference IEMDC'03*, Madison/Wi., USA, June 1-4, 2003.

[Lin03b] M. Linke, *Injektion alternierender Trägersignale zur sensorlosen Regelung von Drehfeldmaschinen*, Thesis for the degree of doctor of technology, University of Wuppertal, Germany, 2003, 103 p.

[Liu03] T-H. Liu, S-H. Chen and D-F. Chen, " Design and implementation of a matrix converter PMSM drive without a shaft sensor," IEEE Transactions on Aerospace and Electronic systems, Vol. 39, Issue 1, January 2003, pp. 228 – 243.

[Lor00] R. D. Lorentz, "Sensorless, drive control methods for stable, high performance, zero speed operation," 9th International Conference on Power Electronics and Motion Control, EPE-PEMC, Kosice, 2000.

[Low90] T-S. Low, K.J. Tseng, T-H. Lee, K.W. Lim and K.S. Lock, "Strategy for the instantaneous torque control of permanent-magnet brushless DC drives," IEE Proceedings, Vol. 137, Pt. B, No. 6, November 1990, pp. 355-363.

[Low93] T-S. Low, T-H. Lee and K-T. Chang, "A Nonlinear speed observer for permanent magnet synchronous motors," IEEE Transactions on Industrial Electronics, Vol. 40, No. 3, June 1993, pp. 307-316.

[Low96] T-S. Low, C. Bi and K-T. Chang, "Motor "identity"-A Motor model for torque analysis and control," IEEE Transactions on Industrial Electronics, Vol. 43, No. 2, April 1996, pp. 285-291.

[Lue71] D.G. Luenberger, "An Introduction to observers," IEEE Transaction on Automatic Control, Vol. 16, No. 6, December, 1971, pp.596-602.

[Luu00] J. Luukko, *Direct torque control of permanent magnet synchronous machines – analysis and implementation*, Thesis for the degree of doctor of technology, Lappeenranta University of Technology, 2000, 172 p.

[Mat90] N. Matsui and M. Shigyo, "Brushless DC motor control without position and speed sensors," IEEE Industry Applications Society, Conference Record, 1990 pp. 448 – 453.

[Mat92] N. Matsui, T Takeshita and K. Yasuda, "A new sensorless drive of brushless DC motor," in proc. IECON'92, 1992, pp. 430-435.

[Mat96] N. Matsui, "Sensorless PM brushless DC motor drives," IEEE Transactions on Industrial Electronics, Vol. 43, No. 2, April 1996, pp. 300-308.

[Min93] Minari, Y., Shinohara, K., Ueda, R., PWM-rectifier/voltage-source inverter without dc –link components for induction motor drive, IEE Proceedings-B – Electric power applications, vol. 140, Nov. 1993, pp. 363–368.

[Mot00] Motorola Inc., MPC555 User's Manual, Revised 15 October 2000.

[Mun99] A.R. Muñoz and T.A. Lipo, "On-line dead-time compensation technique for open-loop PWM-VSI drives," IEEE Transactions on Power Electronics, Vol. 14, No. 4, July 1999, pp. 683-689.

[Mur01] M. Muroya, K. Shinohara, K. Iimori, and H. Sako, "Four-step commutation strategy of PWM rectifier of converter circuit without DC link components for induction motor drives," *Proc. Conf. Rec. IEEE IEMDC*, 2001, pp. 770–772.

[Nah04] B. Nahid-Mobarakeh, F. Meibody-Tabar and F-M Sargos, "Mechanical sensorless control of PMSM with online estimation of stator resistance," IEEE Transactions on Industry Application, Vol. 40, No. 2, March/April 2004, pp. 457-471.

[Nie96] P. Nielsen, F. Blaabjerg and J.K. Pedersen, "Space vector modulated matrix converter with minimized number of switchings and a feedforward compensation of input voltage unbalance," Proc. Conference Record, PEDES, 1996, Vol. 2, pp. 833-839.

[Nie99] M. Niemelä, Position sensorless electrically excited synchronous motor drive for industrial use based on direct flux linkage and torque control, Thesis for the degree of doctor of technology, Lappeenranta University of Technology, 1999, 144 p.

[Nov00] D.W. Novotny and T.A. Lipo, *Vector control and dynamics of AC drives*, Oxford, Clarendon Press, 2000.

[Oll93] J. Ollila, *Analysis of PWM-converters using space vector theory-application to a voltage source rectifier*, Thesis for the degree of doctor of technology, Tampere, University of Technology, Finland, 1993, 167 p.

[Orl89] T. Orlowska-Kowalska, "Application of extended Luenberger observer for flux and rotor time-constant estimation in induction motor drives," IEE Proceedings, Vol. 136, Pt. D. No. 6, November 1989, pp. 324-330.

[Pet01] V. Petrovic, A.M. Stankovic, "Modeling of PM synchronous motors for control and estimation tasks, in Proc. of the 40th IEEE Conference on Decision and Control, Vol. 3, Dec. 2001 pp. 2229 – 2234.

[Pii04] A. Piippo, M. Hinkkanen and J. Luomi, "Sensorless control of PMM drives using a combination of voltage model and HF siganl injection," IEEE, 39th IAS Annual Meeting, Conference Record, Vol. 2, 2004, pp. 964 – 970.

[Pii05] A. Piippo and J. Luomi, "Adaptive observer combined with HF signal injection for sensorless control of PMSM drives," IEEE, International conference on Electric Machines and Drives, May, 2005, pp. 674 – 681.

[Pro03] A.B. Proca, A. Keyhani, A. EL-Antably, W. Lu and M. Dai, "Analytical model for permanent magnet motors with surface mounted magnets," IEEE Transaction on Energy Conversion, Vol. 18, No. 3, September 2003, pp. 386-391.

[Qia04] W. Qian, S.K. Panda and J-X. Xu, "Torque ripple minimization in PM synchronous motors using iterative learning control," IEEE Transactions on Power Electronics, Vol. 19, No. 2, March 2004, pp. 272-279.

[Rah04] M.F. Rahman, E. Haque, L. Tang and L. Zhong, "Problems associated with the direct torque control of an interior permanent-magnet synchronous motor drive and their remedies," IEEE Transactions on Industrial Electronics, Vol. 51, No. 4, August 2004, pp. 799-809.

[Ras03] H. Rasmussen, P. Vadstrup and H. Borsting, "Sensorless field oriented control of a PM motor including zero speed," in Proc. IEEE IEMDC'03, Vol. 2, Madison, USA, 2003, pp. 1224-1228.

[Rib98] L.A.S. Ribeiro, M.W. Degner, F. Briz and R.D. Lorenz, "Comparison of carrier signal voltage and current injection for the estimation of flux angle or rotor position," Industry Applications Conference, IEEE-IAS Annual Meeting,Vol. 1, 1998.

[Rou05] M. Routimo, *Digitaalisesti säädetyn rinnakkaisaktiivisuotimen virtakompensoinnin parantaminen*, Licentiate thesis, Tampere University of Technology, Finland, 2005, 112 p.

[Row86] T. Rowan and R. Kerkman, “A new synchronous current regulator and an analysis of current regulated PWM inverters,” IEEE Transaction on Industrial Applications, Vol. 22, No. 4, July/August 1986, pp. 678-690.

[Sak01] K. Sakamoto, Y. Iwaji, T. Endo and Y. Takakura, “Position and speed sensorless control for PMSM drive using direct position error estimation,” 27. Annual Conference of the IEEE Industrial Electronics Society, Denver, USA, November, 2001, pp.1680-1685.

[Sal02] M. Salo, *Microcontroller based control of current-source PWM converter applications*, Thesis for the degree of doctor of technology, Tampere, University of Technology, Finland, 2002, 150 p.

[Sch88] M. Schrödl, “Detection of the rotor position of a permanent magnet synchronous machine at standstill,” proceedings of ICEM’88, Pisa, Italy, 1988.

[Sch96] M. Schrödl, “Sensorless control of AC machine at low speed and standstill based on the “INFORM” method ,” IEEE Industry Applications Conference, IAS'96, Vol. 1, 1996.

[Sch02] M. Schrödl, M. Lambeck and E. Robeischl, “Implementaltion of the INFORM method in a commercial converter for sensorless PM synchronous drives,” International Conference on Power Electronics, PCIM, 2002.

[Sep92] R.B. Sepe and J.H. Lang, “Real-time observer-based (adaptive) control of a permanent-magnet synchronous motor without mechanical sensors,” IEEE Transactions on Industry Applications, Vol. 28, No. 6, Nov/Dec 1992, pp. 1345-1352.

[Sil02] C. Silva, G. Asher and M. Sumner, “Influence of dead-time compensation on rotor position estimation in surface mounted PM machines using HF voltage injection,” Power Conversion Conference, Osaka, Japan, 2002.

[Sil03] C. Silva, G. Asher, M. Sumner, K.J. Bradley, “Sensorless control in a surface mounted PM machine using rotating injection,” EPE Journal, Vol. 13, No. 3, August 2003, pp. 12-18.

[Sol95] J. Solsona, M.I. Valla and C. Muravchik, “State estimation of a permanent magnet synchronous motor with unknown load torque,” IFAC Low Cost Automation, Buenos Aires, Argentina, 1995.

[Sol96] J. Solsona, M.I. Valla and C. Muravchik, “A nonlinear reduced order observer for permanent magnet synchronous motors,” IEEE Transactions on Industrial Electronics, Vol. 43, No. 4, August 1996, pp. 492-497.

[Sol00] J. Solsona, M.I. Valla and C. Muravchik, “Nonlinear control of a permanent magnet synchronous motor with disturbance torque estimation,” IEEE Transactions on Energy Conversion, Vol. 15, No. 2, June 2000, pp.163-168.

[Son00] J. Song, K-B Lee, J.H. Song, I. Choy and K-B Kim, “Sensorless vector control of induction motor using a novel reduced-order extended Luenberger observer,” IEEE, Industry Application Conference, Vol. 3, 2000, pp. 1828-1834.

[Sta99] C.S. Staines, G.M. Asher and K.J. Bradley, "A periodic burst injection method for deriving rotor position in saturated cage-salient induction motors without a shaft encoder," IEEE Transactions on Industry Applications, Vol. 35, No. 4, July/August, 1999, pp. 851 – 858.

[Ste97] J.L. Stensby, *Phase-locked loops: Theory and applications*, Boca Raton, FL: CRC Press,1997.

[Tak86] I. Takahashi and T. Noguchi, "A new quick-response and high-efficiency control strategy of an induction machine," IEEE Transactions on Industry Applicatations, vol. 22, September./October, 1986, pp. 820–827.

[Ued75] R. Ueda, H. Takata, S. Nakagaki and S. Takata, "On the estimation of transient state of power system by discrete nonlinear observer," IEEE Transactions on Power Apparatus and systems, Vol. PAS-94, No. 6, Nov./Dec., 1975, pp. 2135-2140.

[Vas92] P. Vas, *Electrical machines and drives*, New York, Oxford University Press, 1992.

[Vas93] P. Vas, *Parameter estimation, condition monitoring, and diagnosis of electrical machines*, Oxford University Press, 1993, 360 p.

[Vas98] P. Vas, *Sensorless vector and direct torque control*, New York, Oxford University Press, 1998, 729 p.

[Vas99] P. Vas, Artificial-intelligence-based electrical machines and drives: application of fuzzy, neural, fuzzy-neural and genetic-algorithm-based techniques, Oxford University Press, 1999, 625 p.

[Ven80] M. Venturini and A. Alesina, "The generalized transformer: A new bidirectional sinusoidal waveform frequency converter with continuously adjustable input power factor," in Proc. IEEE, PESC, 1980, pp. 242-252.

[Wal04a] O. Wallmark, L. Harnefors and O. Carlson, "Sensorless control of PMSM drives for hybrid electric vehicles," 35th Annual IEEE Power Electronics Specialists Conference, Aachen, Germany, 2004.

[Wal04b] O. Wallmark, *On Control of Permanent-Magnet Synchronous Motors in Hybrid-Electric Vehicle Applications*, Licentiate thesis, Chalmers University of Technology, Sweden, 2004.

[Wal05] O. Wallmark, L. Harnefors and O. Carlson, "An improved speed and position estimator for salient permanent-magnet synchronous motors," IEEE Transactions on industrial electronics, Vol. 52, No. 1, February 2005, pp. 255-262.

[Wei01] L. Wei and T.A. Lipo, "A novel matrix converter topology with simple commutation," IEEE, IAS Annual Meeting, Conference Record, Volume 3, Oct. 2001, pp. 1749 – 1754.

[Whe94] P.W. Wheeler, H. Zhang and D.A. Grant, "A theoretical and practical consideration of optimised input filter design for a low loss matrix converter," Fifth International Conference on Power Electronics and Variable-Speed Drives October 1994, pp. 363-367.

[Whe02] P.W. Wheeler, J. Rodríguez, J.C. Clare, L. Empringham and A. Weinstein, "Matrix converters: a technology review," IEEE Transactions on Industrial. Electronics, vol. 49, April 2002, pp. 276–288.

[Whe04] P.W. Wheeler, J.C. Clare and L. Empringham, "Enhancement of matrix converter output waveform quality using minimized commutation times," IEEE Transactions on Industrial Electronics, Vol. 51, Issue 1, February 2004, pp. 240 – 244.

[Wu91] R. Wu and G.R. Slemon, "A permanent magnet motor drive without a shaft sensor," IEEE Transactions on Industry Applications, Vol. 27, No. 5, September/October 1991, pp. 1005-1011.

[Yin02] L. Ying and N. Ertugrul, "A new algorithm for indirect position estimation in permanent magnet AC motors," IEEE, Power Electronics Specialists Conference, PESC'02, 2002.

[Yin03] L. Ying and N. Ertugrul, "A novel, robust DSP-based indirect rotor position estimation for permanent magnet AC motors without rotor saliency," IEEE Transactions on Power Electronics, Vol. 18, No. 2, March 2003, pp. 539-546.

[You00] D. Yousfi, M. Azizi and A Saad, "Robust position and speed estimation algorithm for permanent magnet synchronous drives," IEEE, Industry Applications Conference, Conference Record, Vol. 3, 2000, pp. 1541 – 1546.

[Åst97] K.J. Åström and B. Wittenmark, *Computer controlled systems*, 3rd ed. Upper Saddle River, Prentice Hall Inc., 1997, 555 p.

[Öst96] S. Östlund and M. Brokemper, "Sensorless rotor-position detection from zero to rated speed for an integrated PM synchronous motor drive," IEEE Transactions on Industry Applications, Vol. 32, No. 5, September/October 1996, pp. 1158-1165.

Appendix A

PMSMs used in experimental tests and simulations

Machine A:

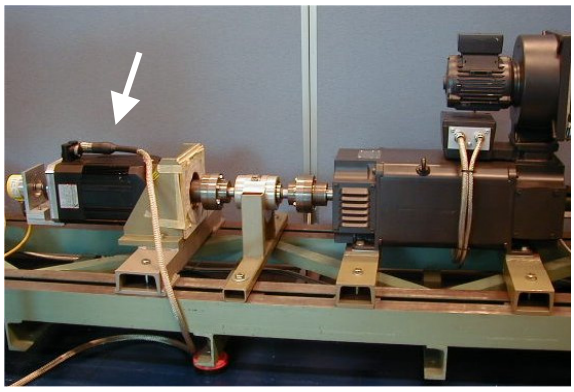

Nominal values

	absolute	p.u.
torque	22 Nm	
speed	1500 rpm	
phase current	7.5 A (RMS)	
PM flux	0.5 Wb	1
stator resistance	0.95 Ω	0.043
fundamental frequency inductances: L_d, L_q	8 mH, 12 mH	0.18, 0.25
number of pole pairs	3	
Inertia (PMSM + DC machine)	0.04 kgm^2	

Machine B:

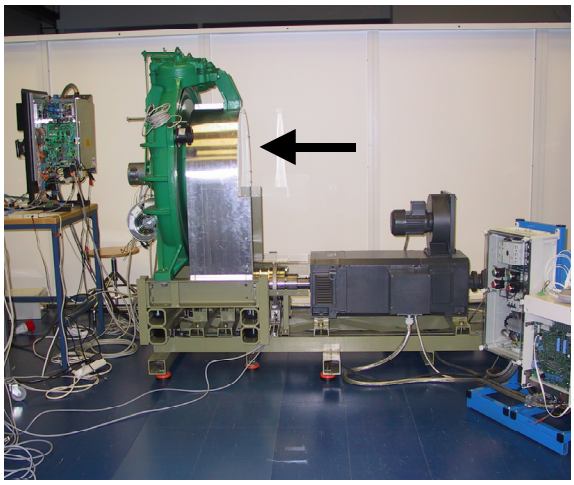

Nominal values

	absolute	p.u.
torque	1800 Nm	
speed	120 rpm	
phase current	60 A (RMS)	
PM flux	1.2 Wb	1
Stator resistance	0.3 Ω	0.14
Fundamental frequency inductances: L_d, L_q	8.5 mH, 9.5 mH	0.6, 0.69
number of pole pairs	12	
Inertia (PMSM + DC machine)	33 kgm^2	

Base values

Current	$i_b = \sqrt{2}\, I_n$
Voltage	$u_b = \psi_m \omega_n$
Impedance	$z_b = u_b / i_b$
Inductance	$L_b = z_b / \omega_{rn}$

Appendix B

Matrix converter prototypes used in experimental tests

Indirect Matrix Converter

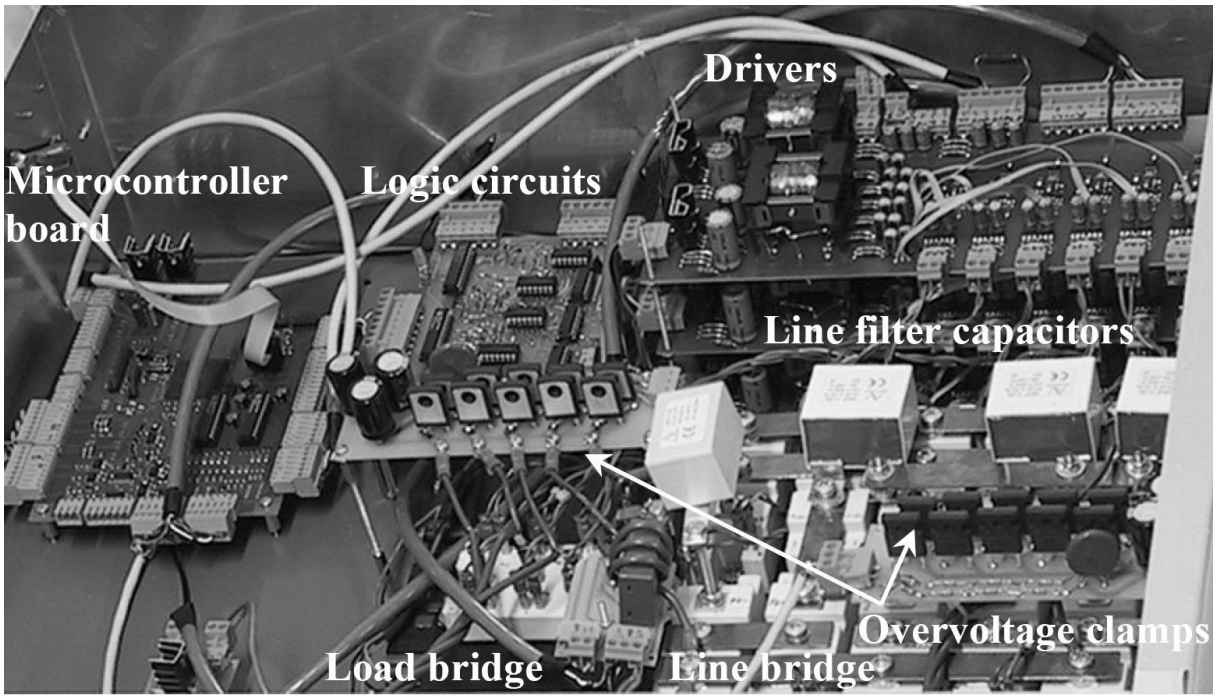

Direct Matrix Converter

Tampereen teknillinen yliopisto
PL 527
33101 Tampere

Tampere University of Technology
P.O. Box 527
FIN-33101 Tampere, Finland